GOA UNIVERSITY

NANOSTRUCTURED BASED CATALYSTS FOR DETOXIFICATION OF CARBON MONOXIDE GAS

THESIS

Submitted to the

GOA UNIVERSITY

For the degree of

DOCTOR OF PHILOSOPHY

IN CHEMISTRY

By

Mr. ROHAN K. KUNKALEKAR

DEPARTMENT OF CHEMISTRY

GOA UNIVERSITY

GOA 403 206 INDIA

July 2011

DECLARATION

I hereby declared that the work incorporated in the thesis entitled "**Nanostructured based catalysts for detoxification of carbon monoxide gas**" is the result of investigation carried out by me under the guidance of Prof. A. V. Salker and it has not previously formed basis for any other titles.

In keeping with the general practice of reporting scientific observations, due acknowledgement has been made wherever the work described is based on the findings of other investigators.

Mr. Rohan K. Kunkalekar
Research student
Department of Chemistry
Goa University
Goa 403206, India

July 2011

EXAMINED BY

06.01.12

(G. D. YADAV)
6th January, 2012

CERTIFICATE

As required under the University ordinance, I certify that the thesis entitled **"Nanostructured based catalysts for detoxification of carbon monoxide gas"** submitted by Mr. Rohan K. Kunkalekar, for the award of Doctor of Philosophy in Chemistry is a record of research done by the candidate during the period of study under my guidance and that it has not previously formed the basis for the award to the candidate of any degree, diploma, associateship, fellowship or other similar titles.

Prof A. V. Salker

Research guide,

Department of Chemistry

Goa University

Goa 403206, India

July 2011

ACKNOWLEDGEMENT

First and foremost, I would like to thank my respectable advisor Prof. A. V. Salker for making my time at Goa University enjoyable, productive and beneficial. I also thank him for his valuable guidance, innovative ideas, generous support and encouragement through out my Ph. D. work.

I offer my sincere thanks to the Vice-chancellor of Goa University for allowing me to work in this institute. I am very much thankful to Prof. A. V. Salker (Head, Department of Chemistry), Prof. Desa (Dean), Prof. J. B. Fernandes (Ex-Head and Ex-Dean), Prof. S. P. Kamat (Ex-Head) and Prof. K. S. Rane (Ex-Dean) for providing all the necessary facilities to carry out my research work.

I am also thankful to Dr. V. M. S. Verenkar, Prof. B. R. Srinivasan, Prof. S. G. Tilve, Prof. K. S. Rane and Prof. B. D. Desai for their constant encouragement and useful advises.

I am grateful to all the teaching and non-teaching staff of the Department of Chemistry who has helped me directly or indirectly during my research work. I acknowledge the Librarian and the staff members of Library of Goa University for their constant help. I am also thankful to Mr. Jaiprakash of USICA for timely help.

My special thanks to Dr. Satyanarayana, Dr. Gopinath and the research students of heterogeneous catalysis Lab. NCL-Pune, Mr. Prabhu and Mr. Khedekar of NIO-Goa, Dr. Rahul Mohan of NCAOR-Goa and Dr. Ghosh and Mr. B. Naik of BITS Pilani-Goa for instrumental facilities. Also I am grateful to IIT SAIF and TIFR-Mumbai for analysis.

My sincere thanks are due to the authorities of Goa University for providing all the necessary facilities.

Financial assistance from the University Grant Commission (UGC) New Delhi and Goa University is gratefully acknowledged, which allowed me to pursue my full time research.

I am at loss of words to thank all my friends for their help and support during the entire period of my thesis work. Notably among these are Satish, Lactina, Shrikant, Santosh, Vinod, Prakash, Mahesh, Rupesh, Rajesh, Bhanudas, Shambhu, Chinmaya, Umesh,

Priyanka, Kashinath, Hari, Sandesh, Puzy, Reshma, Siddhali, Prachi, Sonia, Kiran, Rajashree, Sifali, Divya, Ratan, Ashish, Milind, Pramod, Jose, Savia, Sulaksha, Sagar, Prajesh, Deeptesh and James. Their untiring company, suggestions and constant encouragement always boosted my morale enabling me to give my investigation the present shape and making my stay enjoyable over here. I am also very much thankful to Amit, Gayatri, Swati and Pranay for their constant help.

It gives me immense pleasure to express my deep sense of gratitude to all the people who have directly or indirectly helped me in various capacities in the successful completion of the thesis.

I am greatly indebted to my parents and family members for morale support, encouragement, valuable suggestions, great affection and selfless sacrifice. Without their constant support and inspiration, it would have been impossible for me to be where I am at present.

I close with thanks giving to the Almighty for the showers of blessing during the hours of trial.

Mr. Rohan K. Kunkalekar

CONTENTS

CHAPTER 3

3. PREPARATION AND INSTRUMENTAL TECHNIQUES

CHAPTER 4

4. SOLID STATE AND SPECTROSCOPIC STUDIES

LIST OF ABBRIVATIONS

BE	Binding energy
BET	Brunauer-Emmett-Teller
COHb	Carboxyhaemoglobin
CTAB	Cetyltrimethyl ammonium bromide
DMF	Dimethyl formamide
DRS	Diffuse reflectance spectroscopy
FID	Flame ionization detector
FTIR	Fourier transform infrared
GC	Gas chromatograph
OMS	Octahedral molecular sieves
OSC	Oxygen storage capacity
PROX	Preferential oxidation
PVA	Polyvinyl alcohol
PVP	Polyvinyl pyrolidone
RT	Room Temperature
SEM	Scanning electron microscopy
TEM	Transmission electron microscopy
TG/DTA	Thermogravimetry/Differential thermal analysis
TPD	Temperature programmed desorption
TOS	Time on stream
TCD	Thermal conductivity detector
UV	Ultraviolet
UV-Vis	Ultraviolet- Visible
WHSV	Weight hour space velocity
XRD	X-ray diffraction

CHAPTER 1

INTRODUCTION

INTRODUCTION

Gaseous air pollutants are a cause of major health and environmental concern today and more so because of the impending threat of "Global Climate Change". Toxic gases such as CO, HC, NO_x etc. which are emitted as by-products of combustion process from industrial, transportation and domestic activities are well known to cause environmental and health hazards. In view of this, a lot of research and development has been centered towards reducing these emissions, particularly carbon monoxide, the most toxic and hazardous among them.

Carbon monoxide (CO) generally produced and released from industrial, transportation and domestic activities. It causes potential harmful effects on the environment and the public health. Thus complete elimination or abatement below the permissible levels fixed by environmental regulations is a major concern. CO is highly stable up to a temperature of 700 ^{o}C and remains in atmosphere for several weeks. Catalytic oxidation of carbon monoxide is one of the pivotal reactions [1-10] owing to its application in indoor air cleaning, automotive exhaust treatment, CO_2 lasers, breathing apparatus, and fuel cells, besides to cope with environmental regulations. The reason for tremendous interest in low-temperature CO oxidation is due to the demand for low-temperature automobile and industrial exhaust catalysts. These catalysts are expected to be resistant to sintering and sustain its activity at steady-state working temperature of the exhaust system within cost-effective barriers.

Nanotechnology has gained substantial popularity recently due to the rapidly developing techniques both to synthesize and characterize materials and devices at the nano-scale, as well as the promises that such technology offers to substantially expand the

achievable limits in many different fields including medicine, electronics, chemistry, and engineering. In the literature, there are constant reports of new discoveries of unusual phenomena due to the small scale and new applications. Nano-size noble metal particles have occupied a central place in heterogeneous catalysis for many years, long before the recognition of nanotechnology. Over the past two decades, gold nanoparticles have made important and widely recognized contributions to various industrially and environmentally important reactions such as CO oxidation, NO*x* reduction, water–gas shift reaction, NH_3 oxidation, hydrogenation reactions etc [11-15]. Thus, it is fitting to critically evaluate the impact of such development on heterogeneous catalysis [16,17].

Oxidation to CO_2 is a major solution to CO abatement in air depollution treatments. The development of catalytic converters led to an extraordinary high number of publications on metal catalysts during the last fifty years. Many different catalysts have been prepared and tested for the low temperature carbon monoxide oxidation activity. Precious metals such as Au, Ag, Pt etc. are active catalyst for CO conversion reaction [18-22]. They generally allow low operating temperatures and higher space velocities than the transition metal oxide based catalysts. However due to the high cost of noble metals and their less availability as well as sublimation and sintering problems, considerable part of the research has been devoted to the development of suitable catalyst among the transition metal oxides [23-26]. Appropriate combination of oxides and some mixed metal oxides exhibit greater activity and thermal stability than the single oxides. Combination of noble metals with transition metal oxides result in materials with high catalytic activity, stability and also require less quantity of noble metals [27-31]. Due to the increasing price of noble metals and the remarkable progress in oxide syntheses, catalytic oxidation of carbon monoxide over oxide catalysts has recently gained interest, even if some oxides are known to present significant activity since the beginning of the 20^{th} century.

Manganese oxides (MnO_x) have long been used as highly active, durable, low cost and environmental friendly catalysts for combustion of various volatile organic substances [32-36]. They have superior ability to activate and supply oxygen which is helpful in oxidation reactions. They are non-stoichiometric compound and have many crystalline forms [37,38]. The properties of MnO_x are influenced significantly by its structure, morphology and preparative methods. Great deal of attention has been paid to the preparation of MnO_x with different crystallographic structures and morphologies. It is known that structural factors, size and orientation of crystallites, dispersity of the material, presence of various kinds of defects and extent to which the composition of compounds deviates from the stoichiometry, determine its chemical properties [39,40]. Manganese oxide in combination with other metal serve as highly active thermally stable catalyst for oxidation reactions and can operate at a temperature significantly lower than the noble metal-based catalysts. Various types of manganese oxides, mixed manganese oxides, noble metal doped/supported Mn oxides [41-45] are used for CO oxidation reaction. When combined with noble metal such as gold nanoparticles, significantly enhanced activity has been reported for low temperature CO oxidation [46-48]. The basic building block of most of the manganese oxide is MnO_6 octahedra, these octahedra are connected in different ways by sharing their edges and corners into variety of different structural arrangements [38,40].

Highlights of the Thesis

- Preparation of nano-sized doped MnO_2 and doped Mn_2O_3 catalysts by co-precipitation method and preparation of supported catalysts by impregnation method were undertaken.
- Prepared catalysts have been characterized by different instrumental techniques such as X-ray diffraction (XRD), FTIR spectroscopy, scanning electron

microscopy (SEM) for the surface morphology of the sample, transmission electron microscopy (TEM) and BET surface area.

- Solid state and spectroscopic studied such as DC electrical resistivity, magnetic susceptibility, thermal analysis (TG/DTA), diffuse reflectance spectroscopy (DRS), XPS analyses were carried out.
- Catalytic oxidation of carbon monoxide was carried out over all the catalysts. Time on stream studies were carried out on the selected catalysts. The effect of increase in partial pressure of oxygen in the feed mixture was studied. The influence of moisture on catalytic activity was also studied on some of the preferred catalysts.

Organization of the Thesis

Chapter 1

Brief introduction, the aim and objectives of the research work.

Chapter 2

Literature survey

Chapter 3

Experimental details, preparation of different catalysts and instrumental techniques for the characterization.

Chapter 4

Solid state and spectroscopic studies.

Chapter 5

The catalytic activity studies for CO oxidation reaction over all the catalysts are reported here.

Chapter 6

Summary and conclusions

CHAPTER 1

INTRODUCTION

CHAPTER 2

LITERATURE SURVEY

LITERATURE SURVEY

2.1 Carbon monoxide

Carbon monoxide (CO), also called carbonous oxide, is an odorless, tasteless, colorless, nonirritating gas with a melting point of -205.02 °C and a boiling point of -191.5 °C [1]. The atmospheric concentration of CO is generally below 0.001 percent, but it may be higher in urban areas or enclosed environments. It is highly toxic to humans and animals in higher quantities, although it is also produced in normal animal metabolism in low quantities, and is thought to have some normal biological functions.

Carbon monoxide consists of one carbon atom and one oxygen atom, connected by a triple bond which consists of two covalent bonds as well as one dative covalent bond. It is the simplest oxocarbon. In coordination complexes the carbon monoxide ligand is called carbonyl.

Carbon monoxide is a "combustion pollutant"—a gas (or particle) that comes from burning carbon-based materials. Carbon monoxide is produced from the partial oxidation of carbon-containing compounds; it forms when there is not enough oxygen to produce carbon dioxide (CO_2), such as when operating a stove or an internal combustion engine in an enclosed space. In the presence of oxygen, carbon monoxide burns with a blue flame, producing carbon dioxide. The most common sources of carbon monoxide are gas stoves, furnaces, automobiles and house fires. Carbon monoxide poisoning has also resulted from breathing the exhaust from electrical generators, gasoline-powered high pressure washers and house boats. Worn or poorly adjusted and maintained combustion devices (e.g., boilers, furnaces) can be significant sources.

Carbon monoxide binds to haemoglobin with an affinity 210-280 times greater than oxygen, forming a compound called carboxyhaemoglobin (COHb). It also causes the haemoglobin to hold onto oxygen more tightly than normal, thus preventing the release of oxygen to the tissues. This means that if both carbon monoxide and oxygen are inhaled, carbon monoxide will preferentially bind to haemoglobin. This reduces the amount of haemoglobin available to bind to oxygen, so the body and tissues become starved of oxygen. The end result is tissue hypoxia. The areas most affected are those which have high oxygen demands, especially the brain and the heart. Hypoxia does not explain all of the toxicity associated with CO. Carbon monoxide also diffuses into cells and binds to cytochromes in the oxidative phosphorylation system. This inhibits the generation of energy and also leads to the production of oxygen free radicals (O^-, OH^-, H_2O_2) which lead to further tissue damage. When exposed to CO, white blood cells adhere to the vascular endothelium. When these white blood cells are later re-exposed to oxygen, they release cytokines which cause lipid peroxidation of cell membranes. This lipid peroxidation has been shown in animals to be responsible for the permanent and delayed effects of CO on the central nervous system.

The most common symptoms of carbon monoxide poisoning may resemble other types of poisonings and infections, including symptoms such as headache, nausea, vomiting, dizziness, fatigue and a feeling of weakness. Infants may be irritable and feed poorly. Neurological signs include confusion, disorientation, visual disturbance, syncope and seizures [49]. Some descriptions of carbon monoxide poisoning include retinal hemorrhages, and an abnormal cherry-red blood hue. In most clinical diagnoses these signs are seldom seen.

Carbon monoxide binds to other molecules such as myoglobin and mitochondrial cytochrome oxidase. Exposures to carbon monoxide may cause significant damage to the

heart and central nervous system, especially to the globus pallidus [50], often with long-term sequelae. Carbon monoxide may have severe adverse effects on the foetus of a pregnant woman.

2.1.1 Molecular properties

The bond length between the carbon atom and the oxygen atom is 112.8 pm [51]. This bond length is consistent with a triple bond, as in molecular nitrogen (N_2) which has a similar bond length and nearly the same molecular mass. Carbon-oxygen double bonds are significantly longer, 120.8 pm in formaldehyde, for example. The boiling point (82 K) and melting point (68 K) are very similar to those of N_2 (77 K and 63 K respectively). The bond dissociation energy of CO (1072 kJ/mol) is stronger than that of N_2 (942 kJ/mol) and represents the strongest chemical bond known. The ground electronic state of carbon monoxide is a singlet state since there are no unpaired electrons.

2.1.2 Bonding and dipole moment

Carbon and oxygen together have a total of 10 valence electrons in carbon monoxide. To satisfy the octet rule for the carbon, the two atoms form a triple bond, with six shared electrons in three bonding molecular orbitals, rather than the usual double bond found in organic carbonyl compounds. Since four of the shared electrons come from the oxygen atom and only two from carbon, one of the bonding orbitals is occupied by two electrons from oxygen, forming a dative or dipolar bond. This causes a polarization of the molecule, with a small negative charge on carbon and a small positive charge on oxygen. The other two bonding orbitals are each occupied by one electron from carbon and one from oxygen, forming (polar) covalent bonds, and a reverse polarization is produced by the greater electronegativity of oxygen, with a small negative charge on oxygen. In the free carbon

monoxide, a net negative charge δ- remains at the carbon end and the molecule has a small dipole moment of 0.122 D [52].

Oxygen has more electron density, but also more positive charge. Because most electron density is located between the atoms, the molecule has a net positive charge on the oxygen end. By contrast, the isoelectronic dinitrogen molecule has no dipole moment. If carbon monoxide acts as a ligand, the polarity of the dipole may reverse with a net negative charge on the oxygen end, depending on the structure of the coordination complex.

2.1.3 Resonance structures and oxidation state

Different Lewis structures can be drawn for carbon monoxide. In the structure with three covalent bonds, the octet rule is satisfied, but the electropositive carbon has a negative formal charge. The structure with two covalent bonds would be consistent with the very low dipole moment of the molecule if the bonds were nonpolar. The structure with one covalent bond expresses the greater electronegativity of oxygen and the calculated net atomic charges. None of them do exactly meet the real electronic structure. Calculations with natural bond orbitals show that the structure with a triple bond is the most important Lewis structure (for the free molecule); this structure is the best approximation of the real distribution of electron density, with maximal occupation of bonding orbitals and lone pair orbitals [53]. This is in accordance with other theoretical and experimental studies which show that, despite the greater electronegativity of oxygen the dipole moment points from the more negative carbon end to the more positive oxygen end [54]. The three bonds, however, are in fact polar covalent bonds that are strongly polarized. The calculated polarization towards the oxygen atom is 71 % for the σ-bond and 77 % for both π-bonds. The oxidation state of carbon in carbon monoxide is 2+ in each of

these structures. It is calculated by counting all the bonding electrons as belonging to the more electronegative oxygen. Only the two non-bonding electrons on carbon are assigned to carbon. In this count carbon then has only two valence electrons in the molecule compared to four in the free atom.

Resonance structure of carbon monoxide

2.1.4 Industrial production

A major industrial source of CO is producer gas, a mixture containing mostly carbon monoxide and nitrogen, formed by combustion of carbon in air at high temperature when there is an excess of carbon. In an oven, air is passed through a bed of coke. The initially produced CO_2 equilibrates with the remaining hot carbon to give CO. The reaction of O_2 with carbon to give CO is described as the Boudouard equilibrium. Above 800 °C, CO is the predominant product:

$$O_2 + 2\ C \rightarrow 2\ CO\ (\Delta H = -221\ kJ/mol)$$

Another source is "water gas", a mixture of hydrogen and carbon monoxide produced via the endothermic reaction of steam and carbon:

$$H_2O + C \rightarrow H_2 + CO\ (\Delta H = +131\ kJ/mol)$$

Other similar "synthesis gases" can be obtained from natural gas and other fuels.

Carbon monoxide is also is a byproduct of the reduction of metal oxide ores with carbon, shown in a simplified form as follows:

$$MO + C \rightarrow M + CO$$

Since CO is a gas, the reduction process can be driven by heating, exploiting the positive (favorable) entropy of reaction.

Finally, oxidation into CO_2 is a major solution to CO abatement in air depollution treatments. The development of catalytic converters led to an extraordinary high number of publications on metal catalysts during the last fifty years. Due to the increasing price of noble metals and to remarkable progresses in oxide syntheses, catalytic oxidation of carbon monoxide over oxide catalysts has recently gained interest, even if some oxides are known to present remarkable activity since the beginning of the 20^{th} century.

2.2. Catalysis

Ask the average person in the street what a catalyst is, and he or she will probably tell that a catalyst is what one has under the car to clean up the exhaust. Indeed, the automotive exhaust converter represents a very successful application of catalysis; it does a great job in removing most of the pollutants from the exhaust leaving the engines of cars. However, catalysis has a much wider scope of application than abating pollution.

Catalysis is the change in rate of a chemical reaction due to the participation of a substance called a catalyst. Unlike other reagents that participate in the chemical reaction, a catalyst is not consumed by the reaction itself. A catalyst may participate in multiple chemical transformations. Catalysts that speed the reaction are called positive catalysts. Substances that interact with catalysts to slow the reaction are called inhibitors (or negative catalysts). Substances that increase the activity of catalysts are called promoters, and substances that deactivate catalysts are called catalytic poisons.

Catalytic reactions have a lower rate-limiting free energy of activation than the corresponding uncatalyzed reaction, resulting in higher reaction rate at the same temperature. However, the mechanistic explanation of catalysis is complex. Catalysts may affect the reaction environment favorably, or bind to the reagents to polarize bonds, e.g. acid catalysts for reactions of carbonyl compounds, or form specific intermediates that are not produced naturally, such as osmate esters in osmium tetroxide-catalyzed dihydroxylation of alkenes, or cause lysis of reagents to reactive forms, such as atomic hydrogen in catalytic hydrogenation.

Kinetically, catalytic reactions are typical chemical reactions; i.e. the reaction rate depends on the frequency of contact of the reactants in the rate-determining step. Usually, the catalyst participates in this slowest step, and rates are limited by amount of catalyst and its "activity". In heterogeneous catalysis, the diffusion of reagents to the surface and diffusion of products from the surface can be rate determining. Analogous events associated with substrate binding and product dissociation apply to homogeneous catalysts.

Although catalysts are not consumed by the reaction itself, they may be inhibited, deactivated, or destroyed by secondary processes. In heterogeneous catalysis, typical secondary processes include coking where the catalyst becomes covered by polymeric side products. Additionally, heterogeneous catalysts can dissolve into the solution in a solid-liquid system or evaporate in a solid-gas system.

Let us consider the catalytic reaction between two molecules A and B to give a product P. The cycle starts with the bonding of molecules A and B to the catalyst ***C***. A and B then react within this complex to give a product P, which is also bound to the catalyst. In the

final step, P separates from the catalyst ***C***, thus leaving the reaction cycle in its original state.

$$A + B + \boldsymbol{C} \rightarrow AB\boldsymbol{C} \qquad (1)$$

$$AB\boldsymbol{C} \rightarrow \boldsymbol{C}P \qquad (2)$$

$$\boldsymbol{C}P \rightarrow \boldsymbol{C} + P \qquad (3)$$

Although the catalyst is consumed by reaction 1, it is subsequently produced by reaction 3, so for the overall reaction:

$$A + B \rightarrow P \qquad (4)$$

As a catalyst is regenerated in a reaction, often only small amounts are needed to increase the rate of the reaction. In practice, however, catalysts are sometimes consumed in secondary processes.

To see how the catalyst accelerates the reaction, we need to look at the potential energy diagram in Fig. 2.1, which compares the non-catalytic and the catalytic reaction. For the non-catalytic reaction, the figure is simply the familiar way to visualize the Arrhenius equation: the reaction proceeds when A and B collide with sufficient energy to overcome the activation barrier in Fig. 2.1. The change in Gibbs free energy between the reactants, A + B, and the product P is ΔG.

The catalytic reaction starts by bonding of the reactants A and B to the catalyst, in a spontaneous reaction. Hence, the formation of this complex is exothermic, and the free energy is lowered. Then there follows the reaction between A and B while they are bound to the catalyst. This step is associated with activation energy; however, it is significantly lower than that for the uncatalyzed reaction. Finally, the product P separates from the

catalyst in an endothermic step. Note that the uncatalyzed reaction has to overcome a substantial energy barrier, whereas the barriers in the catalytic route are much lower.

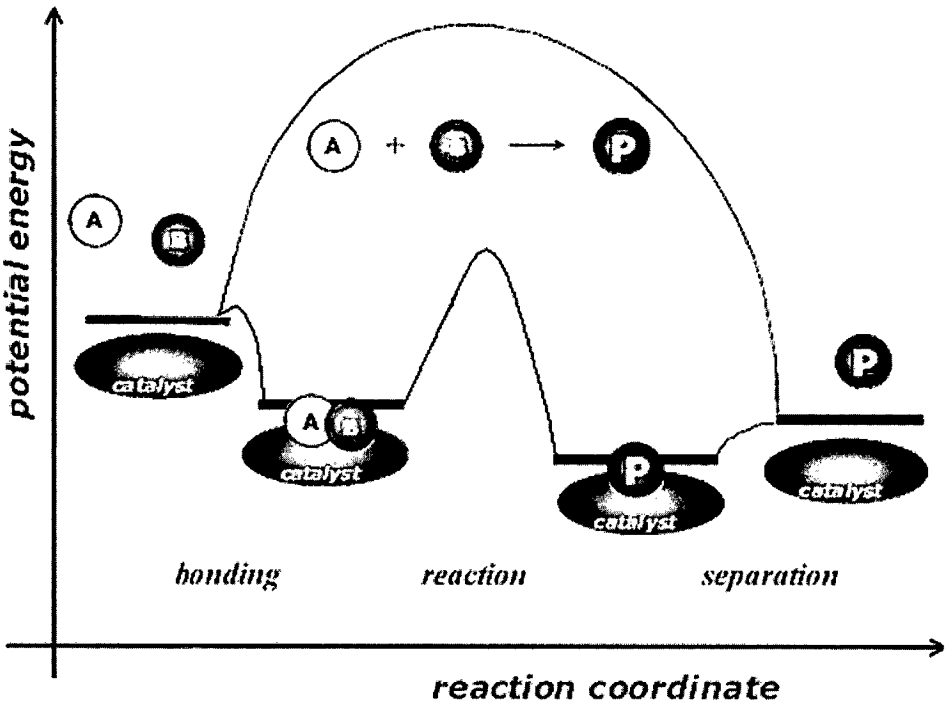

Fig. 2.1 Potential energy diagram of a heterogeneous catalytic reaction, with gaseous reactants and products and a solid catalyst.

The energy diagram of Fig. 2.1 illustrates several important points:

- The catalyst offers an alternative path for the reaction, which is obviously more complex, but energetically much more favorable.
- The activation energy of the catalytic reaction is significantly smaller than that of the uncatalyzed reaction; hence, the rate of the catalytic reaction is much higher.
- The overall change in free energy for the catalytic reaction equals that of the uncatalyzed reaction. Hence, the catalyst does not affect the equilibrium constant for the overall reaction of A + B to P. Thus, if a reaction is thermodynamically

unfavorable, a catalyst cannot change this situation. A catalyst changes the kinetics but not the thermodynamics.

- The catalyst accelerates both the forward and the reverse reaction to the same extent. In other words, if a catalyst accelerates the formation of the product P from A and B, it will do the same for the decomposition of P into A and B.

Thus far it is immediately evident that there are also cases in which the combination of catalyst with reactants or products will not be successful:

- If the bonding between reactants and catalyst is too weak, there will be hardly any conversion of A and B into products.

- Conversely if the bond between the catalyst and one of the reactants, say A, is too strong, the catalyst will be mostly occupied with species A, and B is not available to form the product. If A and B both form strong bonds with the catalyst, the intermediate situation with A or B on the catalyst may be so stable that reaction becomes unlikely. In terms of Fig. 2.1, the second level lies so deep that the activation energy to form P on the catalyst becomes too high. The catalyst is said to be poisoned by (one of) the reactants.

- In the same way, the product P may be too strongly bound to the catalyst for separation to occur. In this case the product poisons the catalyst.

2.2.1 Types of catalysis

Catalysts can be either heterogeneous or homogeneous, depending on whether a catalyst exists in the same phase as the substrate. Biocatalysts (enzymes) are often seen as a separate group.

2.2.1.1 Homogeneous Catalysis

In homogeneous catalysis, both the catalyst and the reactants are in the same phase, i.e. all are molecules in the gas phase, or, more commonly, in the liquid phase. One of the simplest examples is found in atmospheric chemistry. Ozone in the atmosphere decomposes, among other routes, via a reaction with chlorine atoms:

$$Cl + O_3 \rightarrow ClO_3$$

$$ClO_3 \rightarrow ClO + O_2$$

$$ClO + O \rightarrow Cl + O_2$$

or overall

$$O_3 + O \rightarrow 2O_2$$

Ozone can decompose spontaneously, and also under the influence of light, but a Cl atom accelerates the reaction tremendously. As it leaves the reaction cycle unaltered, the Cl atom is a catalyst. Because both reactant and catalyst are in the same phase, namely the gas phase, the reaction cycle is an example of homogeneous catalysis.

Industry uses a multitude of homogenous catalysts in all kinds of reactions to produce chemicals. The catalytic carbonylation of methanol to acetic acid by $[Rh(CO)_2I_2]^-$ complexes in solution is one of many examples. In homogeneous catalysis, often aimed at the production of delicate pharmaceuticals, organometallic complexes are synthesized in procedures employing molecular control, such that the judicious choice of ligands directs the reacting molecules to the desired products.

$$CH_3OH + CO \rightarrow CH_3COOH$$

2.2.1.2 Biocatalysis

Enzymes are nature's catalysts. For the moment it is sufficient to consider an enzyme as a large protein, the structure of which results in a very shape-specific active site. Having shapes that are optimally suited to guide reactant molecules (usually referred to as substrates) in the optimum configuration for reaction, enzymes are highly specific and efficient catalysts. For example, the enzyme catalase catalyzes the decomposition of hydrogen peroxide into water and oxygen at an incredibly high rate of up to 10^7 hydrogen peroxide molecules per second.

$$2\ H_2O_2 \rightarrow H_2O + O_2$$

Enzymes often match the shape of the substrates they bind to, or the transition state of the reaction they catalyze. Enzymes are highly efficient catalysts and represent a great source of inspiration for designing technical catalysts.

Enzymes allow biological reactions to occur at the rates necessary to maintain life, such as the build up of proteins and DNA, or the breakdown of molecules and the storage of energy in sugars. An example with, perhaps, some special appeal to students is the breakdown of alcohol to acetaldehyde inside the body by the enzyme alcohol dehydrogenase. The acetaldehyde in turn is converted into acetate by aldehyde hydrogenase. Some people cannot tolerate alcohol (as revealed by facial flushing after drinking a small amount) because they lack the form of the enzyme that breaks down acetaldehyde.

2.2.1.3 Heterogeneous catalysts

Heterogeneous catalysts act in a different phase than the reactants. Most heterogeneous catalysts are solids that act on substrates in a liquid or gaseous reaction mixture. Diverse

mechanisms for reactions on surfaces are known, depending on how the adsorption takes place (Langmuir-Hinshelwood, Eley-Rideal, and Mars-van Krevelen). The total surface area of solid has an important effect on the reaction rate. The smaller the catalyst particle size, the larger the surface area for a given mass of particles.

For example, in the Haber process, finely divided iron serves as a catalyst for the synthesis of ammonia from nitrogen and hydrogen. The reacting gases adsorb onto "active sites" on the iron particles. Once adsorbed, the bonds within the reacting molecules are weakened, and new bonds between the resulting fragments form in part due to their close proximity. In this way the particularly strong triple bond in nitrogen is weakened and the hydrogen and nitrogen atoms combine faster than would be the case in the gas phase, so the rate of reaction increases.

Heterogeneous catalysts are typically "supported," which means that the catalyst is dispersed on a second material that enhances the effectiveness or minimizes their cost. Sometimes the support is merely a surface on which the catalyst is spread to increase the surface area. More often, the support and the catalyst interact, affecting the catalytic reaction. Supports are porous materials with a high surface area, most commonly alumina or various kinds of carbon.

The chemical industry of the 20th century could not have developed to its present status on the basis of non-catalytic, stoichiometric reactions alone. Reactions can in general be controlled on the basis of temperature, concentration, pressure and contact time. Raising the temperature and pressure will enable stoichiometric reactions to proceed at a reasonable rate of production, but the reactors in which such conditions can be safely maintained become progressively more expensive and difficult to make. In addition, there are thermodynamic limitations to the conditions under which products can be formed, e.g.

the conversion of N_2 and H_2 into ammonia is practically impossible above 600 °C. Nevertheless, higher temperatures are needed to break the very strong N≡N bond in N_2. Without catalysts, many reactions that are common in the chemical industry would not be possible, and many other processes would not be economical.

Catalysts accelerate reactions by orders of magnitude, enabling them to be carried out under the most favorable thermodynamic regime, and at much lower temperatures and pressures. In this way efficient catalysts, in combination with optimized reactor and total plant design, are the key factor in reducing both the investment and operation costs of a chemical processes.

2.3 Nanotechnology in catalysis

The catalysis is of vital importance in our society and constitutes a cornerstone of life from biological processes to large scale production of bulk chemicals. The availability of plentiful and inexpensive chemicals relies on industrial catalytic processes. Other technologies also depend on catalysis, including production of pharmaceuticals, means of environmental protection, and production and distribution of sustainable energy. Much technological advancement required to render alternative energy carriers to fossil fuels an economically viable option such as sunlight and hydrogen relies on optimizing a catalytic process.

A major goal in catalysis research is to design catalysts that can achieve perfect selectivity and desirable activity. Between activity and selectivity, it is commonly accepted that the latter is much more difficult to achieve and control. A reaction of perfect selectivity would generate no waste products, thereby reduce energy and process

requirements for separation and purification. For catalyst synthesis research, investigators for years have attempted to develop techniques to custom design catalysts for this purpose.

One of the most important properties of a catalyst is its active surface where the reaction takes place. The active surface increases when the size of the catalysts is decreased, smaller the catalysts particles, the greater the ratio of surface to volume. The higher is the catalysts active surface, the greater is the reaction efficiency. Research has shown that the spatial organization of the active sites in a catalyst is also important. Both properties nanoparticle size and molecular structure/distribution can be controlled using nanotechnology.

In nature, biological enzymes operate with very high selectivity. An enzyme is made of protein. The specific order of amino acids in the protein generates functionalities critical for the operation of the enzyme. Like other catalysts, an enzyme has an active site where chemical transformation takes place, such as bond breaking and forming. What distinguishes an enzyme from many other catalysts is the environment of the active site. Often the active site is in a cavity formed by the protein. Along the wall of the cavity are functional groups that help bind the reactant and product. One interesting and perhaps critical characteristic is the fact that the protein is flexible [55], such that the cavity, the active site, and the binding sites move during the course of the reaction to accommodate the adsorption and release of the reacting species. The geometrical and electronic structures of nanoscale catalysts particles play a major role in selectively. Thus, a synthetic method to obtain highly controlled particle size distribution is desirable. The combination of selectively and lower temperature needed for a reaction to occur make heterogeneous catalysis a prime energy saving technology.

The manufacturing of structures on the nanometer scale has been a central issue in catalysis research and development for decades. This fact relates to the structure of a heterogeneous catalyst, which requires control of materials ranging from macroscopic dimensions down to the nanoscale. Heterogeneous catalysis therefore has in a sense always had a nanoscience component. Since catalytic action takes place at a surface, and catalytic materials are often very expensive, the goal for chemists has always been to fabricate catalysts with as high surface to volume ratio as possible, so to maximize the surface exposed to the reaction and minimize the amount of catalyst required. A typical heterogeneous catalyst consists of few nanometer wide catalytically active nanoparticles dispersed on a highly porous support material which can have much higher surface areas up to 250 m^2g^{-1}.

Application of nanotechnology concepts in catalysis is already beginning to show a great industrial impact. The detailed understanding of the chemistry of nanostructures and the ability to control materials on the nanometer scale will ensure a more rational and cost efficient development of new and improved catalysts for chemical production.

2.3.1 Active sites for metals

It is now accepted that for metallic catalysts, control at the atomic level is needed to design active sites because the chemical and catalytic properties of atoms at terraces, corners, and edges of a metal crystallite are different, and can be different from atoms at the metal-support interface. In addition, the location of the metal cluster on the support may be important also if its properties are affected by its proximity to the support defects [56].

A much studied method attempting to generate metal clusters with atomic control is to use well-defined organometallic complexes as precursors. In recent years, uniform clusters

of identifiable geometry up to five or six metal atoms can be synthesized [57]. Extension of this method to larger clusters, however, is limited by the availability of precursor complexes.

When considering controlling metal clusters at the atomic level, it is important to keep in mind that the clusters may be dynamic, that is, the location of the atoms may respond to the environment. For example, there is direct observation using high resolution electron microscopy that the surface layer of a Pd crystallite restructures [58] and the shape of the crystallite changes [59] upon exposure to oxygen. A thorough understanding of the dynamic behavior of the atoms in a metal crystallite during catalysis would be greatly beneficial to establishing the limit and desirability of atomic control in these systems.

2.3.2 Active sites for oxides

Among oxides, zeolite is the most studied and best understood. For zeolite acids, the active sites are associated with the trivalent substituents in the zeolite framework. Other functionality, such as framework titanium for epoxidation and framework Co for oxidation, are also established. Extra framework active sites, including those introduced by ion-exchange and those synthesized by the ship-in-a-bottle techniques can be readily characterized.

For other oxides, however, the nature of the active site is less well defined. It is common that coordination unsaturation of a cation in the surface is necessary for catalytic activity. The general method to generate coordination unsaturation is by high temperature dehydroxylation of an oxide, which generates a wide range of surface sites. The preparation method plays important role in the metal oxide preparation. Method such as sol-gel and precursor produces metal oxide particles of nano-sized with different

morphologies and structures which are highly active [1]. More the finer size of particles more is the active surface for the adsorption of the reactant molecules.

2.3.3 Reaction engineering

Nanotechnology could also have an impact in reaction engineering. One area is combinatorial catalysis or high-throughput testing. Here, nanotechnology can help miniaturize the equipment and develop analytical methods that can detect trace quantities of products or occurrence of reactions reliably and rapidly. A different but potentially promising area is nano-sized reactors, those that will be orders of magnitude smaller than the various demonstrated forms of microchannel reactors. If nano-sized reactors can be manufactured, new application areas including biomedical applications may become possible.

Researchers have successfully modified enzymes to effect on-off switching of catalytic activity. For example, by incorporating a polymer whose conformation responds to small changes in temperature into an enzyme near the active site, it was possible to switch on and off the enzyme reversibly by a small temperature swing [60]. Extending this concept to catalysts in general, it should be possible to design catalyst systems where there is a movable segment, controlled by a hinge, that brings a blocking group to or retrieve it from an active site, thereby turning the catalyst off and on.

2.4 Manganese oxides

Manganese oxides are of special interest because of variable oxidation states and their wide applications in batteries, catalysis and chemical synthesis [61-72]. The characteristics of manganese oxide particles such as mean size, crystal structure, morphology, and surface

area are important to their applications. Nano-sized manganese oxide particles are expected to exhibit good performance because of their large surface area and high reactivity [38,73].

Manganese exists in variable oxidation state from 2+ to 7+. Manganese oxides present in MnO, MnO_2, Mn_2O_3, Mn_3O_4 and Mn_2O_7 depending on the preparation conditions.

2.4.1 Structural properties

All MnO_2 structures can be described as a close-packed network of oxygen atoms in which Mn^{4+} cations (ionic radius of 0.53 Å) are differently distributed. These distributions are conveniently described by filled [MnO_6] octahedra sharing opposite octahedral edges to form endless chains, which can in turn be linked to neighboring octahedral chains by sharing corners or edges. The manganese dioxides can be classified according to the number of MnO_6 units and the number of MnO_6 octahedral chains between two basal layers to form tunnel (Tm,n) openings. The $T_{1,n}$ group includes two chemically pure forms: the pyrolusite β-MnO_2 ($T_{1,1}$) and the ramsdellite R–MnO_2 ($T_{1,2}$). The $T_{m,\infty}$ group includes the layered phyllomanganates such as birnessite, buserite, and rancieite. Fig. 2.2 shows the schematic representation of the various manganese dioxide frameworks showing the variation in the chain and tunnel (m×n) structures: (a) pyrolusite ($T_{1,1}$), (b) ramsdellite ($T_{1,2}$), (c) hollandite ($T_{2,2}$), (d) birnessite ($T_{1,\infty}$), (e) romanechite ($T_{2,3}$), (f) spinel ($T_{1,1}$), (g) nsutite ($T_{1,1/1,2}$) and (h) vernadite ($T_{1,\infty}$) [37,38,74-76].

The stable form of MnO_2 is the mineral pyrolusite or β-MnO_2. It has the tetragonal rutile structure (*P*42/*mnm* space group) containing single chains running along the *c*-axis, sharing only corners with adjacent chains. All octahedral are equivalent but distorted with an average Mn–O distance of 1.86 Å. However, the bridging Mn–O distance within a chain is shorter than the apical Mn–O distance within the basal planes. The MnO_6 units

build up strings of edge sharing octahedra extending along the crystallographic *c* axis. These chains are linked with neighboring chains by sharing common corners, resulting in formation of (1×1) channels in β-MnO_2 structure.

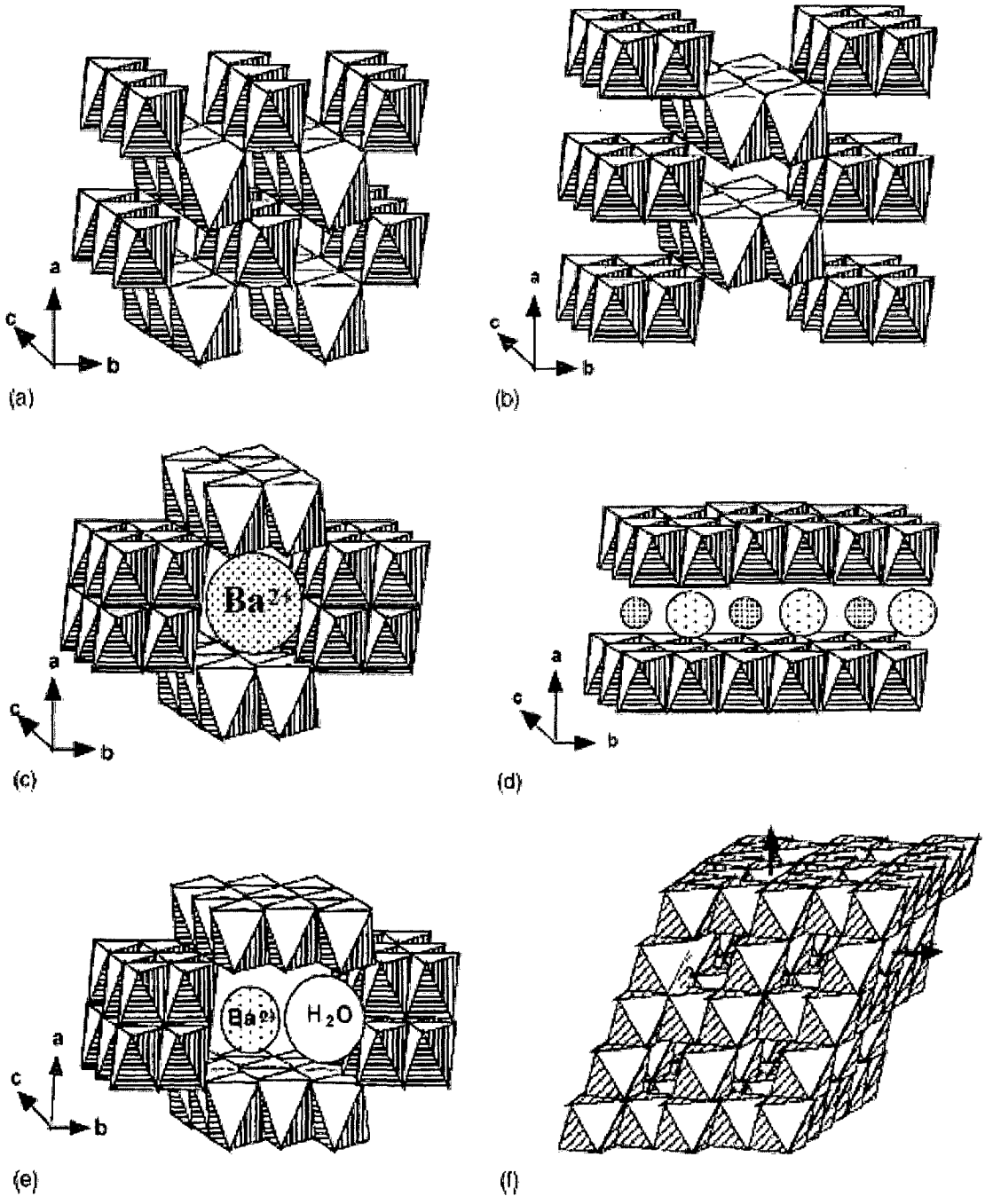

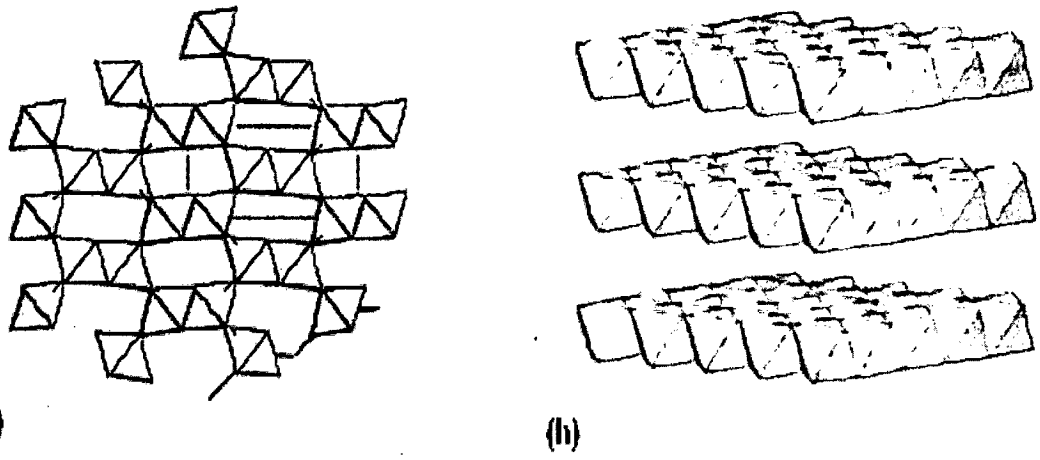

Fig. 2.2 Schematic representation of the various manganese dioxide frameworks showing the variation in the chain and tunnel ($m \times n$) structures: (a) pyrolusite (1×1), (b) ramsdellite (1×2), (c) hollandite (2×2), (d) birnessite (1×8), (e) romanechite (2×3), (f) spinel (1×1), (g) nsutite (1×1) (1×2) and (h) vernadite ($1 \times \infty$).

The orthorhombic ramsdellite R-MnO_2 (*Pbnm* space group) contains double chains formed by edge-sharing [MnO_6] octahedra. It is a metastable form of MnO_2 containing (1×2) blocks of MnO_6 octahedra and empty channels of the same size. The crystal structure of ramsdellite is very similar to that of pyrolusite (β-MnO_2) except that the single chains of octahedra in pyrolusite are replaced by double chains in ramsdellite. Ramsdellite contains two kinds of oxygen atoms: one at the center of an almost equilateral triangle of cations Mn^{4+}, and the other at the apex of a trigonal pyramid of cations.

Another tetragonal form α-MnO_2 (*I4/m* space group) contains (2×2) open tunnels in a network of MnO_6 octahedra. These channels are formed by double chains of edge-sharing MnO_6 octahedra. Crystallographic data regarding the various structures of manganese oxide samples are presented in Table 1.

The structure of γ-MnO_2 is considered to be a random intergrowth of ramsdellite (2×1 channels) and pyrolusite (1×1 channels) structures. The structure of δ-MnO_2 is built up by sheets of edge-sharing MnO_6 octahedra, which are separated by layers of water molecules or hydroxide anions (OH^-). The oxygen atoms form a slightly distorted hexagonal closely packed array in the sheets of MnO. One of every six manganese sites in these layers is unoccupied, and Mn^{2+} and Mn^{3+} are considered to lie above and below these vacancies in a distorted octahedral arrangement formed by three oxygen atoms of the Mn-O layer and three hydroxide ions or water molecules of the intermediate layer.

The manganese sesquioxide bixbyite appears with two polymorphs, the α-Mn_2O_3 and the tetragonal γ-Mn_2O_3. α-Mn_2O_3 bixbyite (C-type structure) has a body-centered cubic lattice with space group *Ia*3.

Table 1 Crystallographic data of some Mn-O compounds

Compound	**Mineral**	**Crystal symmetry**	**Features**
β-MnO_2	Pyrolusite	Tetragonal (*P42/mnm*)	(1 × 1) Tunnel
R-MnO_2	Ramsdellite	Orthorhombic (*Pbnm*)	(1 × 2) Tunnel
α-MnO_2	Hollandite	Tetragonal (*I4/m*)	(2 × 2) Tunnel
$MnOx\cdot H_2O$	Birnessite	Tetragonal	(1 × ∞) Layer
λ-MnO_2	Spinel	Cubic (*Fd3m*)	(1 × 1) Tunnel
γ-MnO_2	Nsutite	Complex tunnel (hex)	(1 × 1)/(1 × 2)
δ-MnO_2	Vernadite	Hexagonal	(1 × ∞) Layer
α-Mn_2O_3	Bixbyite	Cubic (*Ia*3)	C-type
Mn_3O_4	Hausmannite	Tetragonal (*I*41/*amd*)	Spinel-like

2.5 Strategies for the preparation of manganese oxides

The various types of manganese oxides were prepared via variety of routes. Many of the materials with similar gross structural features nevertheless show a diversity of properties depending on the specific synthetic route. These differences can be attributed to variations in particle size and the type and the amount of defects in the structures. For this reason, small changes in the synthetic parameters can result in materials with novel catalytic, electrochemical and ion-exchange properties. By altering the method of preparation, by specific activation and by doping with transition metal cation either before or after crystallization can result in high catalytic material which works at low temperature. Some common preparative techniques for manganese oxide preparation are discussed in this section.

2.5.1 Co-precipitation method

By using co-precipitation method it is possible to achieve a high degree of homogenization together with a small particle size and thereby speed up the reaction rate. Manganese oxides with different morphologies and phases were prepared by co-precipitation method with different precipitants such as NaOH, KOH, NH_4OH, K_2CO_3, Na_2CO_3. These were added to the Mn salt solutions till the complete precipitation (pH = 8). Various manganese salts were used such as chloride, sulphates, acetate, nitrate etc [77-81]. The final brown coloured precipitate was then filtered and dried to get the final product. The co-precipitation route is the simplest, environmental friendly method for the preparation of manganese oxide.

The mixed copper manganese oxides in the form of hopcalite are found to be of great importance and are basically prepared by co-precipitation technique [82-85]. Suitable metal salts, typically nitrates are premixed and then a precursor is precipitated using

sodium carbonate. The experimental variables during the initial precipitation such as pH, temperature, Cu:Mn ratio and the precipitate ageing time, as well as the treatment of the initial precursor by calcination have all been shown to be crucial in their preparation which reflects in their applications and are widely use in catalysis. Cobalt manganese oxides, CeO_2-MnO_x mixed oxide were prepared by this method, these materials are used as catalyst for various reactions [86-89]. G. Qi et al. had prepared CeO_2-MnO_x by premixing the respective metal salts in distilled water, excess amount of ammonium carbonate was added with stirring [87]. The mixture was aged, filtered and finally calcined. Whereas, F. Arena et al. prepared $MnCeO_x$ oxide by new redox-precipitation route [88]. $KMnO_4$ solution was titrated with solution of Ce and Mn nitrate, at constant pH = 8 using KOH. After titration the solid was digested, filtered, dried and finally calcined.

Various noble metals supported and mixed manganese oxides were synthesized. Here the salts of noble metals (to be incorporated in MnO_x) were taken along with the Mn salt, dissolved in distilled water to get a clear solution. The simultaneous precipitation of noble metal along with MnO_x was carried out using precipitants such as KOH, NaOH, Na_2CO_3 and K_2CO_3 [90-93]. After being washed and dried the crushed precipitate was calcined. In some other cases as in platinum supported on MnO_2-CeO_2, the MnO_2-CeO_2 was prepared first by co-precipitation method and then the Pt was impregnated on MnO_2-CeO_2 according to the incipient wetness method using an aqueous solution of H_2PtCl_6 [94].

$KMnO_4$ was successfully utilized in the synthesis of Mg manganese oxide octahedral molecular sieve with todorokite type structure. Typical synthesis involve the addition of NaOH to the solution of Mn and Mg chloride to form a mixed slurry of $Mn(OH)_2$ and $Mg(OH)_2$, followed by the dropwise addition of $KMnO_4$ for the oxidation. The precipitate was washed with water till pH reached 6. This precipitate was then uses to prepare Mg-

todorokite by adding $MgCl_2$ solution to this slurry and was further given autoclave treatment. Resulting product was filtered, washed and dried [95].

$LaMnO_3$ and $LaCoO_3$ were prepared by dissolving stoichiometric quantities of La_2O_3, Mn or Co metal in Conc. HCl. NaOH was added till pH = 9, resultant precipitate was heated in water bath, oxidized by H_2O_2 with stirring. Finally filtered, washed, dried and calcined at 500-600 °C [8].

2.5.2 Sol – Gel method

The sol-gel method provides the capacity to mix several components in a single stage, and allows controlling the structure and composition of the final solid mixture at molecular level [96]. In addition, sol-gel method gives a homogeneous mixture of binary oxides with enhanced efficiency for catalytic reaction. The nominal $Ce_{0.5}Zr_{0.5}O_2$, $Ce_{0.5}Zr_{0.2}Mn_{0.3}O_2$ and $Ce_{0.5}Mn_{0.5}O_2$ samples were prepared by citric acid sol–gel [45] method. The nitrates were mixed according to the ratio of Ce:Mn:Zr. Citric acid was added as the complexing agent with a 1.3:1 ratio of citric acid to metal ions including Ce^{3+}, Zr^{4+}, and Mn^{2+}. Then an appropriate amount of polyglycol was added. The blended solution was sufficiently mixed in a magnetic stirrer and heated at 80 °C till the formation of a transparent gel. The resulting gel was dried at 110 °C to receive the brown powders. The present powders were subjected to decomposition at 300 °C for 1 h and calcination at 700 °C for 3 h under static air in a muffle furnace. Nanostructured MnO_2 was also prepared by using citric acid, in which solution of manganese acetate with citric acid was adjusted to pH = 6 by adding ammonia. This was stirred at 80 °C to get dried gel which was finally calcined [97]. Other types of manganese oxides were also prepared by sol-gel using fumaric acid, PVA etc [98-100].

Mixed manganese oxides such as Cu-Mn, Mg-Mn were prepared by this method [42,101]. Nanosized lithium manganese oxide powder with spinel structure has been synthesized by using an aqueous solution of metal nitrates containing polyvinyl alcohol [102]. The role of PVA and the calcinations conditions for the formation of $LiMn_2O_4$ have been studied. PVA has only one hydroxyl group attached every second carbon atom in the carbon backbone of a long chain molecule. The role of PVA is to cover the cations so that precipitation of the cations can be prevented. In addition, the nitrate ions in solution act as an oxidizing agent for the decomposition of PVA [103,104].

2.5.3 Hydrothermal route

The synthesis of manganese oxide nanostructures has attracted a great deal of interest due to the fact that the physical properties of these materials can be modified when they have a nanometer dimension. Among various synthetic approaches established for MnO_x nanomaterials, hydrothermal synthesis represents the most common route and offers advantages such as mild conditions, simple manipulations and good possibilities for scale-up [105-108]. It is known that different polymorphs of MnO_2 nanomaterials can be successfully synthesized by tuning the experimental parameters of hydrothermal reaction system [109-111]. Consequently, understanding the nucleation and crystallization mechanisms of MnO_2 under hydrothermal conditions is very important for improved control of size, crystallinity, stoichiometry and dimensional anisotropy. However, it is a challenging task under hydrothermal conditions, there might be numerous chemical and physical processes occurring simultaneously and competing.

Nanorods of β-MnO_2 were prepared by hydrothermal treatment of aqueous solution of manganese nitrate [37]. The manganese nitrate solution was loaded into a Teflon-lined stainless steel autoclave and heated at 190 °C for 6 h. A dark brown powder formed was

washed, centrifuged and dried in air at 70 °C for 12 h. Y. Zhu and others have synthesized different kinds of polymorphs of MnO_2 [38]. In typical synthesis of α- MnO_2 nanorods, the mixture of $MnSO_4$ and $KMnO_4$ stirred well and transferred into a Teflon-lined stainless steel autoclave and heated at 160 °C for 12 h. The product was collected, washed and dried at 80 °C. Similarly the β-MnO_2 nanorods were obtained from the reaction of $KMnO_4$ and $MnSO_4$ at 160 °C for 12 h. For the preparation of γ-MnO_2 nanorods, the $MnSO_4$ and $(NH_4)_2S_2O_8$ were well mixed and hydrothermally treated at 90 °C for 12 h. the δ-MnO_2 nanorods were obtained by the chemical oxidation of $MnSO_4$ and $KMnO_4$ which were hydrothermally heated at 240 °C for 24 h [38]. Whereas, the D. K. Walanda et al. also prepared polymorphs of MnO_2 with different approach by this method [112]. The β-MnO_2 nanorods were also prepared via redox reaction of $MnSO_4$ and $(NH_4)_2S_2O_8$ under hydrothermal condition [113,114]. Moreover, single-crystalline β-MnO_2 nanotubes were successfully prepared by this method through oxidizing $MnSO_4$ with $NaClO_3$ in the presence of poly vinyl pyrrolidone [115]. The ε-MnO_2 3D hierarchical nanostructures were synthesized by transferring the homogeneous mixture of $MnCl_2$ and $NaClO_4$ in to a Teflon-lined stainless steel autoclave and heated at 140-180 °C for 24 h. The black solid obtained was washed, centrifuged and dried at 60 °C for 16 h [116]. Orchid-like Cr doped MnO_2 nanostructures were prepared by this method by using $MnSO_4$, $KClO_3$ and $Cr_2(SO_4)_3$ [117].

Single-crystalline α-Mn_2O_3 nanorods as well as single-crystalline Mn_3O_4 particles were prepared through simple and facile preparation method of ammonium-hydrothermal treatment of MnO_2 [118]. One dimensional Mn_2O_3 nanostructures were fabricated via facile hydrothermal treatment using nitrilotriacetate and manganese acetate [119]. The hydrothermal cleavage-decomposition mechanism was used to synthesized single crystal

Mn_2O_3 nanorods using $KMnO_4$ as Mn source and cetyltrimethylammonium bromide (CTAB) as reducing agent [120,121].

Various noble metal supported on MnO_x were synthesized. The synthesis involves first the preparation of MnO_x supported by hydrothermal process and further the noble metals were supported by an incipient wetness impregnation method [122,123].

2.5.4 Precursor route

The precursor method is highly used specially for the nanomaterial synthesis. The advantage of using precursor technique is that the materials are formed with high degree of purity and homogeneity and also requires lower temperature for formation of metal oxides, the calcination temperature could control the crystalline manganese oxide phases. Various types of organic moieties were used as a precursor which can bind to the metal ion forming the metal precursor. Lu et al. prepared mesoporous amorphous MnO_2 and mesoporous Mn_2O_3 compose of nano-crystals by selective calcinations of oxalate precursor [124]. MnO_x nanocrystals of high catalytic activity were synthesized by Mn oxalate precipitation, synthesis involve the precipitation of Mn oxalate from Mn nitrate solution using oxalic acid as precipitating agent. The obtained precipitate was filtered, washed and dried and subsequently transformed into manganese oxide using temperature programmed oxidation. Alternatively, the as-prepared Mn-oxalate was transformed into well-crystalline Mn_3O_4 by temperature programmed decomposition [73]. The hopcalite-type catalysts for H_2 and CO oxidation were prepared. The oxides were prepared by using metal nitrates as precursors: $Cu(NO_3)_2{\cdot}3H_2O$ and $Mn(NO_3)_2{\cdot}4H_2O$. The salts at a molar ratio of $Cu(NO_3)_2$:$Mn(NO_3)_2$ = 1:2 were solved in distilled water, the solution was evaporated to dryness and the nitrates decomposed at 250 °C. The solid material was then

calcined to get final oxide [125]. Various other forms of MnO_x are also prepared by this method using different precursors [126,127].

The samarium-manganese oxide was prepared by the citrate method. The solution of manganese nitrate, samarium oxide and citric acid was slowly evaporated to form a dense gel. The precursor formed was heated in air to final calcinations temperature to form final oxide material [128]. Various transition and noble metal doped/supported MnOx were synthesized by this route [129-131].

2.5.5 Impregnation method

The impregnation method is most simple and widely used preparation method for the preparation of active metal supported on oxide support [132-136]. These materials were developed specially for catalytic applications. The manganese oxides can be used as a support as well as an active species which is supported on some inert support [137,138] such as silica and alumina. Cerium cation incorporated manganese oxide OMS-2 were prepared by impregnation method, the synthesis involve the addition of OMS-2 to the cerium nitrate solution in methanol. The mixture was stirred for 24 h followed by drying at 120 °C for 8 h and calcined at 400 °C in air [139].

J. S. Park et al. prepared PdO_x/MnO_2 by this method [140]. The dried oxide was dispersed in a aqueous solution of $PdCl_2$ and the mixture was stirred followed by evaporation. The resultant solid was dried at 80 °C for 24 h and reduced in He flow at 300 °C for 3 h.

The PdO_x-MnO_x supported on inert support were prepared by wetness impregnation method [141-142]. A typical synthesis involves addition of alumina powder to the aqueous solution of manganese nitrate. Excess water was removed. Aliquots of this catalyst was

used to prepare the bimetallic catalysts. Palladium nitrate solution was employed for this, the procedure was same as above. Finally the dried impregnates were calcined at 400 °C for 4 h in air [32]. The Ag-Mn, Ag-Co and Ag-Ce composite oxide supported on alumina were also prepared by this method. The alumina powder was taken in appropriate metal ion solution, the samples were dried at 120 °C and calcined in air at 500 °C [143]. MnO_x-Pt and MnO_x-Pd supported on alumina was also prepared by this method which is used for catalytic applications [144].

2.5.6 Reflux and thermal decomposition method

Reflux method is highly used for the preparation of manganese oxide materials. This method is basically employed for the synthesis of manganese oxide octahedral molecular sieves (OMS-2). A representative synthesis of OMS-2 involves the addition of $KMnO_4$ solution to a mixture of manganese sulphate and nitric acid in a flask fitted with a reflux condenser. The dark brown slurry was reflux for 24 h, then filtered and washed with deionized water several times and dried at 120 °C overnight. This gave K-OMS-2. Further, H-K-OMS-2 was prepared by mixing the K-OMS-2 with nitric acid and the slurry was stirred at 80 °C for 6 h. The product was filtered, washed and dried at 120 °C for 12 h and then calcined at 280 °C for 6 h [34,35,145-147]. These material are porous in nature and show high catalytic activity in oxidation reactions. Manganese oxide octahedral molecular sieves (OMS-2) were synthesized using $MnSO_4$ and $KMnO_4$ as precursors by a reflux method under acidic conditions. CuO/OMS-2 catalysts were prepared by an impregnation method and tested for CO oxidation [148].

Noble and transition metal doped MnO_x materials were also prepared by this method [149-153]. Ag-MnO_x catalysts were synthesized by adding the nitric acid and manganese sulphate solution to the aqueous solution of $KMnO_4$ and appropriate amount of silver

nitrate. The resulting black precipitate was stirred and refluxed at 100 °C for 48 h. The solid was filtered, washed, dried and calcined to get a final product [153].

The β-MnO_2 nanorods were successfully prepared by a simple refluxing route using manganese sulphate, sodium persulphate and sodium hydroxide [154]. The electrolytic manganese dioxide were also prepared by reflux method [155].

The thermal decomposition is a simple method for the preparation of nanomaterials. The α-Mn_2O_3 nanocrystals were prepared by direct thermal decomposition of $MnCO_3$ powder in a static air. The controlled calcination of $MnCO_3$ powder was carried out at 700 °C for 5 h. Fabrication of chain-like Mn_2O_3 nanostructures was carried out by thermal decomposition of manganese phthalate coordination polymers [33,156]. The uniform-sized MnO nanospheres and nanorods were fabricated by the thermal decomposition of Mn-surfactant complexes [157].

Various types of supported MnO_x materials were also prepared by this method [158-160]. The noble metal such as gold was deposited on α-Mn_2O_3 support in which the nanostructured α-Mn_2O_3 was prepared by the direct thermal decomposition of $MnCO_3$ powder in static air, further the different amounts of gold were deposited by deposition-precipitation using urea as the precipitating agent [48,161].

2.5.7 Other methods of synthesis

The synthesis of manganese oxide is important, since Mn can go in different oxidation state forming different types of MnO_x. The preparation method is also crucial in preparing catalytic materials because it directly affects the activity of the catalyst. There are also several other routes which are reported for the preparation of manganese oxides besides the above mention methods.

Chang et al. reported preparation of gold supported on MnO_2-TiO_2 by deposition-precipitation method. The synthesis involves first the preparation of MnO_2-TiO_2 which is prepared by incipient wetness impregnation method. The aqueous solution of chloroauric acid was added to the solution containing support, NH_4OH was added. The precipitate was then filtered, washed, dried and calcined to obtain supported gold catalysts [44,47].

J. Cao and others reported a new method for the preparation of double-shelled Mn_2O_3 hollow spheres [162]. First, there is preparation of $MnCO_3$ microspheres using $MnSO_4$, ethanol and HCO_3. Then these microspheres were added to water and stirred, to this $KMnO_4$ solution was added and stirred. Further, HCl was added to this acid treated product. The mixture was washed and calcined. A new and facile route was developed to prepare the single-crystalline Mn_2O_3 with cuboctahedral, truncated-octahedral and octahedral shape via a solvothermal approach [163]. Uniform Mn_2O_3 octahedral nanoparticles were also synthesized by a mediated *N,N*-dimethylformamide (DMF) solvothermal route [164]. The Mn_2O_3 octahedra were formed through oriented aggregation of primary nanocrystals. Meanwhile, poly(vinyl-pyrrolidone) (PVP) was applied as a surfactant to facilitate the oriented aggregation of small Mn_2O_3 nanoparticles into octahedral crystallites.

Single crystal α-Mn_2O_3 nanowires were prepared through a simple one-pot molten salt route [165]. $NaNO_3$ and NaF were mixed together, the mixture was put into the crucible and heated to 420 °C to form solution, manganese sulphate was added into this solution. After being kept at 420 °C for 20 min, the mixture was cooled, washed with water, centrifuged and dried at 60 °C for 12 h.

Different polymorphs of MnO_2 were fabricated by using sonochemistry method. The α-MnO_2 prepared by the application of ultrasound radiation on a solution consists of Mn

acetate followed by mild drying [166]. Another method uses the solution of potassium bromate and manganese sulphate, and by altering the proportions of reagents leads to the formation of different phases [167].

$LaMnO_3$ and $LaCoO_3$ were prepared by dissolving separately La_2O_3, Mn or Co metal in Conc. HNO_3, solutions were heated to dryness. The residues were dried, mixed and finally fired 600-700 °C for 6-10 h [8]. the same oxides were by other method from their oxalates using ceramic technique [8]. the oxalates were mixed using acetone in an agate mortar and pestle. the dried mixture was decomposed at 600 °C, the obtained oxide mixture were pelletized and further calcined at 1100 °C.

The $La_{1-x}Ca_xMnO_3$ perovskites were prepared by mechanochemical and ceramic method [168]. In the mechanochemical synthesis of $La_{1-x}Ca_xMnO_3$, a mechanically preactivated mixture containing appropriate proportions of the La_2O_3, CaO, and MnO_2 oxides was calcined at 900 or 1100 °C for 4 h. Ceramic synthesis was carried out by calcination of mixtures of the starting oxides at 1100 °C for 100 h.

The mixed MnO_x-CeO_2 binary oxide catalysts were prepared by co-precipitation using Mn acetate and Ce nitrate and involving the surfactant cetyltrimethyl-ammonium bromide (CTAB). Pd/MnO_x-CeO_2 catalysts were prepared by adding the Pd nitrate salt which was simultaneously precipitated with Mn acetate and Ce nitrate during the preparation process [169]. Nano-sized manganese oxide particles were prepared by low-pressure spray pyrolysis using a new type of liquid aerosol generator called as FEAG process [170]. The precursor particles with micron size, hollow and thin wall structures turned to nano-sized manganese oxide particles after post treatment at temperatures of 700 and 800 °C.

Cryptomelane solids were prepared by solid-state reaction between Mn^{7+} and Mn^{2+} species in a high-energy ball milling with stainless steel balls and jar [171,172]. In a

typical experiment, $KMnO_4$ and $Mn(CH_3COO)_2{\cdot}4H_2O$ were mixed homogeneously and then milled for 1 h. The resulting black solid was kept for 4 h in a capped bottle at 80 °C. The obtained product was thoroughly washed with water until neutrality, dried at 80 °C overnight and finally calcined at 450 °C for 2 h [173]. The FeCo-MnO nanocomposites were prepared by ball milling the mixtures of Fe, Co and Mn, where MnO was obtained from the oxidation of Mn after or during the milling process [174].

A series of manganese-cerium oxide composites were prepared by the solution combustion technique using urea as a fuel. The solution containing salts of Mn and Ce along with urea was kept in the furnace at 500 °C, the solution got ignited and burnt with flame, solid product was recovered after completion of the combustion process [175].

α-MnO_2 and β-MnO_2 single crystal nanowires were prepared through simple soft chemical process. Synthesis involves the dispersion of γ–MnO_2 in water and transferred to autoclave and kept at 140-200 °C for 72 days, the product was filtered, washed and dried at 60 °C [176]. Suib et al. prepared amorphous MnO_2 by reduction method which involves the reduction of $KMnO_4$ by oxalic acid [177]. Whereas Yagi et al. prepared amorphous MnO_2 by reduction of $KMnO_4$ by formic acid and H_2O_2, the precipitate was washed and dried [178]. An activated MnO_2 was synthesized by rheological phase reaction method from Mn benzoate and $KMnO_4$. The rheological phase reaction occurred at 60-70 °C. A black micropowder with high dispersity and good fluidity was obtained [179]. The Ag–OMS-2 nanorods were synthesized by a simple solid-state reaction of $AgMnO_4$ with manganese acetate. The nanorods had a diameter of about 8 nm and lengths of 50–150 nm with the co-existence of micropores and mesopores [180].

Mn_3O_4 and Mn_2O_3 nanocrystals were synthesized by using mesoporous silica (SBA-15) as a nanoreactor. The starting materials used were Mn (II) acetylacetonate and Mn (III)

acetylacetonate. The precursor obtained was washed and finally calcined [181]. Isolated Mn_2O_3 nanotubes/fiber were fabricated at large scale via liquid-phase catalysis method. Ferric nitrate acts as catalyst, nano-Mn_2O_3 with different microstructures including nanotubes, nanofibers and nanoparticles could be selectively synthesized [182]. In other case nanocrystalline spherical α-Mn_2O_3 particles were prepared by mechanochemical reduction of $KMnO_4$ with NH_4Cl. All milling experiments were performed in high energy planetary mill in air atmosphere [183]. A novel route was used to prepare the ultrafine powder of MnO_2, by solid state reaction of $KMnO_4$ with manganese acetate or manganese chloride at room temperature, the powder was washed and dried in vacuum [184].

2.6. Catalytic CO oxidation over manganese based catalysts

To achieve CO elimination, it is necessary to catalyze its oxidation. One of the roles of the catalyst is to concentrate the pollutant at its surface, which allows the oxidation reaction to proceed at a sufficient rate. Since the beginning of the 20^{th} century, some oxides such as hopcalite have been known to oxidize CO at ambient temperature. Hopcalite is a binary amorphous Mn–Cu oxide, the texture of which can be stabilized by addition of CaO, Al_2O_3, or bentonite clay.

The development of catalytic converters in the 1970s in the United States and in the 1990s in Europe highlighted the exceptional activity of noble metals for CO oxidation [185–187] and the specific role of oxides with a high oxygen storage capacity (OSC) to allow the metal to continue to work in cycled conditions [185]. However, due to the increasing price of noble metals and to remarkable progresses in oxide syntheses, catalytic oxidation of CO over other oxide catalysts has recently gained interest. CO oxidation can be considered as an interesting probe reaction for oxide surface characterization.

Manganese oxides (MnO_x) were widely used as a catalyst for CO oxidation reaction for last several years. Manganese oxides in association with other transition-metal elements are very active for CO oxidation. These catalysts are eco-friendly and have no detrimental properties.

Liang et al. studied the effect of phase structures on the activities of the MnO_2 nanorods for CO oxidation reaction. The activities of the catalysts decrease in the order of α- $\approx$ δ- > γ- > β-MnO_2. The catalytic activity for CO oxidation was dominated by the crystal phase and channel structure of the MnO_2 nanorods [38]. The complete CO conversion over the MnO_x nanocrystals has been reported recently [73]. This catalyst gets deactivated with time on stream, but the activity can be recovered by heating in oxygen. An important clue in assessing the superior CO oxidation activity of MnO_x is its nanocrystalline structure with particle size below 3 nm. Different structures of MnO_x were tested for low temperature CO oxidation reaction by K. Ramesh et al. [41]. The catalytic reactivity followed the trend of $MnO \leq MnO_2 \leq Mn_2O_3$. The kinetic study of CO oxidation was done in combination with temperature programmed oxidation and reduction. Ivanova and co-workers have shown that the complete CO conversion can be achieved at 100 °C over manganese dioxide which is obtained from fluorine-containing electrolytes [188]. Mn_2O_3 nanoparticles and nanowires [164,165] were prepared by different methods, they exhibit excellent catalytic performance on the catalytic oxidation of CO.

The mixed manganese oxide in the form of hopcalite, $CuMn_2O_4$, is used as a catalyst for the oxidation of CO at ambient temperature. G.J. Hutchings et al. had prepared copper manganese oxide for ambient temperature CO oxidation. The effect of a range of preparation variables were investigated in details [82,85,189]. They also prepared Co promoted hopcalites, which shows higher activity for CO oxidation at ambient temperature [82,]. Also the influence of preparation method on catalytic activity of sol-gel

derived Cu-Mn oxides for CO oxidation was investigated [42]. Hopcalites found to to deactivate for CO oxidation reaction in few minutes under moist condition. Hahn et al. compared activity of a hopcalite-type catalyst for H_2 and CO oxidation with that of single-phase oxides CuO, Mn_2O_3 and $CuMn_2O_4$ (spinel) and a mixture of 1:1 CuO and Mn_2O_3 in order to elucidate the effects that are responsible for the high catalytic activity of the former [125]. Cu-Mn oxides supported on Mg-F_2 and Al_2O_3 was studied for CO oxidation and proved to be an interesting support for Cu-Mn oxides [14].

Octahedral molecular sieves (OMS-2) of manganese oxides are cryptomelane-type manganese oxides, with a porous structure (0.46 nm) arising from edge sharing of 2×2 [MnO_6] octahedral chains to form one-dimensional tunnel structures [190]. Mn species in the OMS-2 material have mixed-valent Mn^{4+}, Mn^{3+} and some Mn^{2+} sites. Divalent and trivalent transition metal ions incorporated into OMS-2 have been developed as promising catalysts for oxidation reactions [146-150]. Transition metal (Cu, Co, Ni and Zn)-modified cryptomelane-type manganese dioxide nanomaterials were synthesized and tested for CO oxidation [173]. All the solids were active in the preferential oxidation of CO in the presence of hydrogen (PROX), being the modified with copper the most active promoting the redox properties of the material, or facilitating the CO chemisorption process during the reaction. One-dimensional titanium–cryptomelane manganese oxide nanomaterials were tested for CO oxidation. These materials showed high catalytic activities toward CO oxidation at ambient temperature. The surface area, the morphology and the titanium content of titanium– cryptomelane catalysts greatly affected their catalytic activities toward CO oxidation [147].

Recently Luo et al. reported activity of CuO/OMS-2 catalyst for CO oxidation and compared with the CuO/MnO_x catalyst [148]. Cu/OMS-2 catalysts exhibit high CO oxidation activities and the lowest temperature for 90% conversion of CO is 55 °C. The

interaction between the highly dispersed CuO and OMS-2 support generates active sites for CO oxidation. CO oxidation may follow the Mars-van-Krevelen mechanism with Cu^{2+}–O^{2-}–Mn^{4+}↔Cu^{+}–□–Mn^{3+} + O_2 redox couple.

The CO oxidation reaction was studied on Ag–OMS-2 nanorods [180]. These nanorods showed quite high catalytic performance for CO oxidation with 100% CO conversion at 90 °C, mainly because of the significantly enhanced oxygen activation and CO adsorption with the presence of Ag+ in the tunnels. In other case, the Ag/OMS-2 catalysts gave full conversion at 120 °C [191]. In the long time stability test 100% CO conversion can maintain for 250 h at 120 °C with about 90% selectivity. The reason for the deactivation of this catalyst is that the fine-dispersed silver species are agglomerated to form Ag_2O and parts of OMS-2 are reduced to Mn_2O_3, accompanied with a structure reordering. For low-temperature CO oxidation, Suib et al. [151] found that Co-, Ag- and Cu-OMS-2 with the cryptomelane structure showed higher activity catalysts as compared to known Hopcalite-like Cu–Mn mixed oxides and other base metal supported catalysts, and the average oxidation numbers of manganese species and the species and position of the doped in these OMS-2 catalysts had proved to dominate their activities. Rongrong et al. also suggested that Ag doped OMS-2 catalysts showed excellent catalytic activity for CO oxidation and activity increases after Ag doping [153].

The catalysts based on supported gold nanoparticles have attracted tremendous recent attention owing to their unique catalytic properties for various redox reactions, in particular, for CO oxidation under ambient conditions. It is generally accepted that gold dispersed on reducible oxides is more active and stable than that supported on non-reducible oxides [192]. Various types of manganese oxides supported gold catalysts were prepared and tested for low temperature CO oxidation reaction [46,90]. They exhibit superior activity for CO oxidation reaction. A comparative study on ceria and manganese

oxide supported gold catalysts for the oxidation of CO at low temperature was investigated [44]. The redox efficiency of CeO_2 and MnO_2 is responsible for high CO conversion at room temperature. Au/CeO_2 demonstrates higher catalytic activity than Au/MnO_2. The co-existence of metallic and oxidized gold species on Au/CeO_2 seems to be the main reason for the higher activity. Chang et al. reported CO oxidation activity over Au/MnO_2-TiO_2 catalysts [47]. The higher activity of these catalysts could be attributed to the synergistic effect of gold particle size, optimum combination of metallic and electron-deficient gold species, as well as to strong Au-support interactions [193]. Nanostructured α-Mn_2O_3 used as support for anchoring gold nanoparticles, which exhibited high activities for low-temperature CO oxidation in presence or absence of excess H_2 [48]. The superior activities of Au/α-Mn_2O_3 was attributed to its unique redox properties and the facile formation of activated oxygen species on the surface and the superior performance of O_2-pretreated Au/α-Mn_2O_3 catalyst is due to the creation of a specific oxygen-enriched interface leading to an enhanced metal-support synergy [161].

Park et al. examined PdO_x/MnO_2 as a catalyst for CO oxidation, and showed higher catalytic activity compared to PdO_x/Mn_2O_3. The support supplies oxygen to Pd, where the oxidation occurs with adsorbed CO and the ability of the support to provide oxygen improves the performance of the catalyst. Hence, the readiness of MnO_2 to be reduced with maintaining a higher oxidation state showed higher CO oxidation activity than Mn_2O_3 as support for PdO_x [140]. When Pd was supported on MnO_x-CeO_2 catalyst, its activity for CO oxidation is greatly enhanced, due to the acceleration of gas-phase oxygen activation and transferring via spillover [169]. The gas-phase oxygen activated by Pd can directly react with the adsorbed CO to form CO_2.

Effect of crystal phases of MnO_2 was studied for CO oxidation reaction. MnO_2 is an effective catalyst in CO oxidation, and its activity depends on the crystal phase of MnO_2.

α-MnO_2 exhibits a higher activity than β-MnO_2, because the α-MnO_2 nanowires has a "noncompact" structure and can be reduced more easily than the β-MnO_2 nanorods. Introducing Ag onto MnO_2 produced a strong Ag–MnO_2 interaction. The catalytic activity clearly correlates with this interaction, which is determined by crystal phase and surface structure [122]. Ag-Mn, Ag-Co and Ag-Ce composite oxides supported on Al_2O_3 catalysts were used for CO oxidation, these catalysts showed higher activity for this reaction. There is a cooperative action in binary oxide catalysts [143].

CuO–CeO_2 catalysts doped with transition metal oxides (ZnO, MnO_2 and Fe_2O_3) were prepared by co-precipitation method for the selective CO oxidation. The doping of ZnO remarkably improved the catalytic activity, while Fe_2O_3 or MnO_2 deteriorated the catalytic properties [194].

(Ni, Co, Mn)Al_x intermetallides were synthesized and used for CO oxidation. These catalysts are shown to possess high activity and their development is considered to be a promising direction in the catalysis of deep oxidation processes [195].

The kinetics of oxidation-reduction reaction between CO and NO over perovskite catalysts $LaMnO_3$ and $LaCoO_3$ prepared by ceramic and wet methods has been studied in the temperature range 200-800 °C. The rate-controlling step in the catalytic reduction of NO by CO is presumably the active site reduction process [8].

$LaMn_{1-X}Co_XO_3$ perovskites were used for CO oxidation reaction. A significant rise in CO oxidation was observed by B-site substitution of Co^{3+} in $LaMnO_3$, where as $LaMnO_3$ shows least activity. $LaCoO_3$ is oxygen deficient giving rise to Co^{2+} ions for the charge neutrality, it favours easy release of lattice oxygen to CO [24]. $La_{1-X}Ca_XMnO_{3+\delta}$ perovskites were also tested for CO oxidation reaction, the leading role in CO oxidation on perovskites is played by the weakly bound surface forms of oxygen [168]. Perovskite type

oxides $La_{1-X}Ce_XMnO_3$ were also tested for CO oxidation reaction [c2-89]. The introduction of Ce in the perovskite lattice results in enhanced catalytic activity. It was suggested that the number of cation/anion vacancies directly related to the catalytic activity by facilitating the CO adsorption.

Gurav et al. studied the kinetics of CO oxidation over $Zn_{1-X}Cu_XMn_2O_4$ spinels in the temperature range 100-400 °C. Higher activity of intermediate compositions is due to the cooperative effect of two different A-site metal ions and crystallographic phase transition [23]. The catalytic oxidation of CO over nanocrystallite $Cu_xMn_{1-X}Fe_2O_4$ powders was studied. The maximum CO conversion was observed for $Cu_{0.5}Mn_{0.5}Fe_2O_4$. The high catalytic activity of $Cu_{0.5}Mn_{0.5}Fe_2O_4$ can be attributed to the changes of the valence state of catalytically active components of the ferrite powders [196]. Nonstoichiometric nickel-manganese spinel oxides are found to be highly active for CO oxidation, some conversion being observed at room temperature [158]. A detailed mechanism was proposed wherein CO reacts with coordinatively unsaturated cations to give carbonyl complexes which in turn react with surface oxygen activated on anionic vacancies.

Mn/CeO_2 catalysts were prepared by thermal decomposition method and catalytic activities for CO oxidation were investigated [160]. Only a small amount of Mn is needed to form active sites for CO oxidation, and the excess Mn oxide form bulk MnO_2 particles which may cover a part of active Mn oxide species resulting in the decrease of the catalytic activity. The catalytic activity also depends on the calcination temperature.

2.7 The mechanism for CO oxidation reaction over manganese oxides

Various types of reaction mechanisms were proposed for CO oxidation reaction over manganese oxide catalysts. CO oxidation over metals is believed to follow a competitive Langmuir-Hinshelwood mechanism where CO and O_2 adsorb on the same site. However,

there were also reports suggesting Eley-Rideal mechanism, in which, gas phase CO directly reacts with adsorbed oxygen. Various steps occurring during catalytic CO oxidation reaction are given in scheme 1.

$$O_2 \longrightarrow 2O_{ads} \quad (1)$$

$$CO_{gas} \longrightarrow CO_{ads} \quad (2)$$

$$CO_{ads} + O_{ads} \longrightarrow CO_{2\ ads} \quad (3)$$

$$CO_{2\ ads} \longrightarrow CO_{2\ gas} \quad (4)$$

Scheme 1. Sequential elementary steps occurring during the CO oxidation

A different kind of mechanism was given by Liang et al. over the MnO_2 nanorods. CO chemisorption, the Mn-O bond strength of the MnO_2 oxides, and transformation of intermediate oxides Mn_2O_3 and Mn_3O_4 into MnO_2 can significantly influence the catalytic performance of the MnO_2 nanorods. Larger the amount of CO adsorption, lesser is the strength of the Mn-O bond thus easier transformation of intermediate oxides Mn_2O_3 and Mn_3O_4 into MnO_2 which are consistent with the higher catalytic activities of the MnO_2 nanorods for CO oxidation [38]. The detailed mechanism by Liang et al. for carbon monoxide oxidation is given in scheme 2.

$$CO_{ads} + 2MnO_2 \longrightarrow CO_2 + Mn_2O_3 \quad (1)$$

$$CO_{ads} + MnO_2 + Mn_2O_3 \longrightarrow CO_2 + Mn_3O_4 \quad (2)$$

$$2Mn_3O_4 + O_{2\ air} \longrightarrow 2MnO_2 + 2Mn_2O_3 \quad (3)$$

$$2Mn_2O_3 + O_{2\ air} \longrightarrow 4MnO_2 \quad (4)$$

Scheme 2. Mechanism for CO oxidation reaction over MnO_2 nanorods.

Among the various mechanisms which are proposed for CO oxidation, the Mars-van-Krevelen type of mechanism is widely accepted for CO oxidation reaction over manganese oxide catalysts [41,173,197] implying that lattice oxygen incorporation occurs during CO oxidation and that the reduced surface of the manganese oxide is rejuvenated by taking up oxygen from the feed gas mixture. Scheme 3 shows the Mars-van-Krevelen mechanism over manganese oxides.

First there is adsorption of CO over the surface and then it takes oxygen from lattice.

$$C{-}O_{gas} \longrightarrow C{-}O_{ads} \quad (1)$$

$$Mn{-}O + C{-}O_{ads} \longrightarrow Mn{-}O\cdots\cdots C{-}O_{ads} \quad (2)$$

$$Mn{-}O\cdots\cdots C{-}O_{ads} \longrightarrow Mn{-}[\,]_{\text{oxygen vacancy}} + CO_{2\,ads} \quad (3)$$

$$Mn{-}[\,]_{\text{oxygen vacancy}} + \tfrac{1}{2}\,O_{2\,gas} \longrightarrow Mn{-}O \quad (4)$$

$$CO_{2\,ads} \longrightarrow CO_{2\,gas} \quad (5)$$

Scheme 3. Mars-van-Krevelen mechanism for CO oxidation reaction over manganese oxide catalysts.

2.8 Influence of moisture on CO oxidation reaction over the catalysts

For the past several decades, the oxidation of carbon monoxide (CO) has become important in numerous applications, such as air/gas purification, life-support respirators, exhaust pollution reduction for automobiles/factories etc. These results in a pressing need for CO oxidation catalysis; and many catalyst systems (noble metals, metal oxides, and composites) have been studied for high CO conversion at various temperatures and

environments. Among them, metal oxide catalysts with low production costs and high CO oxidation activity proved to be the most attractive.

Most CO oxidation applications involve moist environments with rapid flow rates, therefore highly moisture tolerant catalysts are necessary. Noble metal catalysts are known to be less susceptible to water and have been successfully applied in motor vehicles, but high production costs hinder their wider applications. Most of the inexpensive and highly active metal oxide catalysts, such as Co_3O_4, on the other hand are rapidly deactivated with trace amounts of moisture (3-10 ppm moisture level) from the feed gas. The super dry conditions created by passing the feed gas through molecular sieve traps at dry ice temperature (-77 °C) is required to avoid water deactivation. This pretreatment, however, is not applicable for most applications.

Last several years the effect of moisture on the activity of various catalysts has been investigated. It has been shown that gold-based catalyst is substantially more active for CO oxidation resulting in high activity and its catalytic activity can be enhanced by moisture [198-205]. Mullins et al. reported the CO oxidation and role of moisture on an atomic oxygen covered Au(111) surface. The role of adsorbed water was studied by using isotopically labeled water. Evidence is present that shows activated water or OH groups formed from water can directly participate in oxidizing CO on an atomic oxygen covered Au(111) surface [198]. The mechanism is shown in scheme 4.

$$CO_{gas} \longrightarrow CO_{ads} \quad (1)$$

$$H_2O_{gas} \longrightarrow H_2O_{ads} \quad (2)$$

$$H_2O_{ads} \longrightarrow OH_{ads} + H_{ads} \quad (3)$$

$$CO_{ads} + OH_{ads} \longrightarrow HOCO_{ads} \quad (4)$$

$$HOCO_{ads} \longrightarrow CO_{2gas} + H_{ads} \quad (5)$$

$$2H_{ads} \longrightarrow H_{2\ gas} \quad (6)$$

Scheme 4. Mechanism for CO oxidation reaction in presence of moisture.

In further studies, Mullins and others showed direct involvement and promoting role of water in CO oxidation on oxygen-covered Au(111) at low temperatures and they also proved that water promotes CO oxidation on Au(111) by directly reacting with adsorbed oxygen atoms to form OH groups, followed by OH reacting with CO to form CO_2 on the surface [199]. Thus enhancing the production of CO_2 on the surface of Au(111).

Haruta et al. studied the effect of moisture in reactant gas for low temperature CO oxidation over Au supported on TiO_2, Al_2O_3 and SiO_2 support [200]. Moisture enhances the catalytic activities and the effect of moisture depends on the type of metal oxide support. The oxygen may be activated by moisture, the support surface serves as a moisture reservoir. This activated oxygen will rapidly react with CO adsorbed on gold to form an intermediate, which is immediately transformed into CO_2. The moisture play two roles, one is decomposition of the carbonate species accumulated during the reaction at the perimeter interface between Au particles and oxide support and other is the activation of oxygen [200,201]. In other study, Costello et al. prepared Au supported on different oxide supports and effect of moisture was studied for CO oxidation. The catalytic activity under moisture was found to differ depending on the support material [202]. The effect of water vapour was tested on the activity of Au/MnO_x and Au/FeO_x catalysts. From the results it may be concluded that water seemed to be innocuous to the catalytic activity over these catalysts because it can provide hydroxyl group, which is necessary for the reaction to takes place [203]. Date and Haruta investigated the effect of moisture on CO oxidation over Au/TiO_2. The activity is mainly affected by the amount of moisture adsorbed on the

catalyst. Moisture enhances the reaction by more than 10 times up to 200 ppm H_2O, while further increase in moisture suppresses the reaction [204]. Where as in other case, effect of adsorbed water on CO oxidation on a series of $Au/TiO_2(110)$ catalysts was studied. The adsorption of water induces desorption of predeposited molecularly chemisorbed O_2. Thus, adsorbed water slightly inhibits CO oxidation on atomic oxygen precovered $Au/TiO_2(110)$ catalyst [205].

The oxidation of CO was also studied on Pt based catalysts [206-208]. Ebbesen et al. reported the effect of water on activity of Pt/Al_2O_3. The moisture influences the metal particle potential as well as the CO molecule directly [206]. Furthermore, the rate of CO oxidation changes significantly when carried out in water as compared to gas phase. Due to the hydration of adsorbed CO molecule, the CO bond weakened significantly, which facilitates its oxidation. Whereas in case of bimetallic catalysts $PtAu/CeO_2$, the water vapour in the feed stream provokes a significant decrease in CO conversion. The reason may be due to the blockage of active sites by water vapour [207]. $Pt–Mg/Al_2O_3$ catalysts are more influenced by moisture than Pt/Al_2O_3 catalysts in CO oxidation reaction. Here, due to Mg there is a presence of basic site which reacts with moisture and increases OH^- concentration on the surface. Accordingly, $Pt–Mg/Al_2O_3$ catalysts are more affected by moisture than Pt/Al_2O_3 catalysts because of the increase of OH^- concentration on the surface [208].

Low temperature CO oxidation was carried out on hydrous and anhydrous PdO to study the effect of surface water species. Hydrous PdO showed complete conversion at room temperature due to the presence of hydroxyl group, anhydrous PdO do not exhibit significant activity even at 100 °C. Thus presence of hydroxyl groups is required for low temperature CO oxidation [21]. Enhanced activity was observed over Ir/TiO_2 catalyst for CO oxidation reaction. The water was adsorbed onto the exposed Ir surface as well as onto

TiO_2. The exposed Ir surface could resist the reoxidation by the water adsorption, as the adsorbed water depressed the interaction between activated oxygen and the active Ir metal surface [209].

Kramer and others studied the activity of $Cu_{20}Mn_{80}O_x$ and $Pt_1Cu_{20}Mn_{79}O_x$ catalysts under moist condition and found that these catalysts get deactivated for CO oxidation after a few minutes in moist air [42]. Even the presence of noble metal did not improve its moisture resistance. Suib et al. investigated the catalytic performance of copper manganese oxide catalysts at ambient temperature synthesized using the redox method under moist conditions [210]. These catalysts resist water poisoning for 10 min whereas commercial Hopcalite is known to deactivate rapidly under moisture. Further, the catalytic activities of water-poisoned CuMnOx catalysts were fully restored by treating them in a stream of helium at 180 °C for 2 h. The hydrophobic polymer coated $CuMnO_x$ and Co_3O_4 showed better activity in moisture than the uncoated $CuMnO_x$ and Co_3O_4 catalysts [211]. The hydrophobic polymer might form a porous layer on the surface of the catalyst with a selective permeability of CO, O_2, and CO_2 but not to water molecules which results in better activity. An interesting study was done by Shen et al. for low temperature CO oxidation reaction over Co_3O_4 nanorods without the presence of any noble metal. Tricobalt tetraoxide nanorods not only catalyse CO oxidation at temperatures as low as –77 °C but also remain stable in a moist stream of normal feed gas [212].

2.9 Effect of partial pressure oxygen on CO oxidation reaction

The amount of oxygen present in the feed gas highly influences the CO oxidation reaction over different catalysts. Oxygen rich catalyst surface are generally found to show higher activity [198]. The rate of CO conversion found to increase in the presence of

excess oxygen in the feed mixture. Well-defined Pt-nanoparticles with an average diameter of 1 nm supported on a series of zeolite Y samples containing different monovalent (H^+, Na^+, K^+, Rb^+, and Cs^+) and divalent (Mg^{2+}, Ca^{2+}, Sr^{2+}, and Ba^{2+}) cations have been used as model systems to investigate the effect of promotor elements in the oxidation of CO in excess oxygen [213].

The platinum metals Pt, Rh, Ir, and Pd are known to be efficient catalysts for the CO oxidation reaction as long as the oxygen excess in the gas feed is moderate. Ruthenium is a very poor catalyst in CO oxidation [214,215]. However, when the CO oxidation reaction proceeds under high pressure with excess oxygen, Ru turns out to be much more efficient than the other platinum-group metals [216-218]. It was speculated that under such conditions Ru(0001) is covered with a chemisorbed O overlayer, whereas the other platinum-metal surfaces might be deactivated by the onset of metal oxidation. However, a pronounced enhancement of the CO conversion rate by more than two orders of magnitude with respect to a surface covered with a complete (1×1)O monolayer was reported for "oxygen-rich" Ru(0001) surfaces which contained an oxygen amount equivalent to at least 3 ML (monolayers) [219].

The activity of a 5-wt% Cu/CeO_{2-X} catalyst during preferential CO oxidation in hydrogen-rich gas mixtures was studied in a microchannel reactor [220]. An increase of the O_2 concentration from a 1.2 to 3 fold excess reduced the CO concentration to 10 ppm in a broad temperature interval of 50 °C at weight hour space velocity (WHSV) up to 275,000 $cm^3\ g^{-1}\ h^{-1}$. The preferential CO oxidation could be carried out at higher flow rates and at higher selectivities in the microchannel reactor compared to a fixed-bed flow reactor.

The preferential oxidation of CO on Ru/Al_2O_3 and Pt/Al_2O_3 in simulated reformer gas was investigated over a wide range of CO partial pressures and O_2 excess [221]. The CO oxidation rate increases with almost first order with increasing O_2 partial pressure under these conditions up to 3 kPa O_2 pressure. A further increase in the O_2 pressure from 3 to 5 kPa over Ru/Al_2O_3 had very little effect on the reaction rate. This result is in excellent agreement with data obtained on single-crystal Ru(0001) surfaces in the absence of H_2 [222]. The selectivity was slightly affected by the varying O_2 partial pressure up to 3 kPa, and in the range of 45–50%, but decreased abruptly to 15% at higher O_2 partial pressures (3–5 kPa) for Ru/Al_2O_3. For Pt/Al_2O_3, it was slightly lower, but the overall dependence on the oxygen partial pressure range investigated (up to 2 kPa) was comparable.

CHAPTER 3

PREPARATION AND INSTRUMENTAL TECHNIQUES

PREPARATION AND INSTRUMENTAL TECHNIQUES

Introduction

The successful industrial heterogeneous catalysts should possess high catalytic activity for the desired reaction, high selectivity for the intended product and acceptable commercial life. The characterization of catalytic materials is a very important step in the process of catalyst development, which gives insight into the relation between physical and chemical properties of the catalyst and its activity. If the structure and composition of the catalyst can be correlated with its activity and selectivity, the working phenomenon of the catalyst can be understood.

In this work, the catalysts were prepared by co-precipitation method and impregnation method. All the prepard catalysts were characterized by various physico-chemical methods such as X-ray diffractometry, TG-DTA, FTIR spectroscopy, BET surface area measurements, SEM, TEM, electrical resistivity, magnetic susceptibility etc.

The theory and experimental procedure of various characterization techniques used for the present study are briefly described in the following section.

3.1 Preparation of Catalysts

3.1.1 Preparation of doped MnO_2 catalysts

$Mn_{1-X}Ni_XO_2$ [where X = 0, 0.05, 0.10, 0.15, 0.20]

$Mn_{1-X}Ce_XO_2$ [where X = 0, 0.05, 0.10, 0.15, 0.20]

$Mn_{1-X}Pd_XO_2$ [where X = 0, 0.02, 0.05, 0.08]

$Mn_{1-X}Rh_XO_2$ [where X = 0, 0.02, 0.05, 0.10]

$Mn_{1-(X+Y)}Cu_XPd_YO_2$ [where X=0 Y=0, X=0.10 Y=0, X =0.08 Y=0.02 and X=0.05 Y=0.05]

$Mn_{1-X}Ag_XO_2$ [where X = 0, 0.02, 0.05, 0.10, 0.15, 0.20]

Nano-sized Ni, Ce, Pd, Rh and Cu-Pd doped MnO_2 catalysts were prepared by dextrose assisted co-precipitation method. All the chemicals used were of analytical grade. Stoichiometric amounts of manganese acetate and respective metal salts were dissolved in distilled water (in case of Pd doped MnO_2, palladium chloride was dissolved with few ml of concentrated nitric acid and heated with stirring to dissolve completely). These solutions were added to 2% dextrose solution at 100 °C with stirring, dextrose solution was added to avoid the agglomeration. The precipitation was carried out by adding drop by drop solution of sodium hydroxide (10%) to the above solution under vigorous stirring. Subsequently the suspension of precipitated metal hydroxide mixture (at pH = 9) was subjected to oxidation by drop wise addition of 30% H_2O_2 solution with stirring in order to adjust the appropriate oxidation state of metal ions. The precipitate was then digested on a water bath for three hours. The resulting precipitate was filtered off, washed with distilled water and ethanol, and dried in air at 150 °C for 6 h. Finally the dried precipitate was homogenized well in mortar and calcined in air at 400 °C for 10 h.

Nano-sized Ag doped MnO_2 catalysts were prepared by precipitation and drying method. Stoichiometric amount of manganese acetate and silver nitrate were dissolved in distilled water at room temperature in separate beaker. Both this solutions were added to 200 ml distilled water at 100 °C with stirring. Liquid ammonia solution was added till pH = 9. Subsequently, the suspension was subjected to oxidation by dropwise addition of 30%

H_2O_2 solution with constant stirring in order to adjust the appropriate oxidation state of metal ions. The suspension was then stirred continuously at 100 °C till dryness. The resulting product was dried at 150 °C for 6 h and homogenized well in mortar before calcination at 400 °C for 10 h in air.

3.1.2 Preparation of doped Mn_2O_3 catalysts

$Mn_{2-X}Ni_XO_3$ [where X = 0, 0.05, 0.10, 0.15, 0.20]

$Mn_{2-X}Ce_XO_3$ [where X = 0, 0.05, 0.10, 0.15, 0.20]

$Mn_{2-X}Pd_XO_3$ [where X = 0, 0.02, 0.05, 0.08]

$Mn_{2-X}Ag_XO_3$ [where X = 0, 0.05, 0.10, 0.15, 0.20]

Nano-sized Ni, Ce and Pd doped Mn_2O_3 catalysts were prepared by dextrose assisted co-precipitation technique. The metal salts of A.R. grade were taken in stoichiometric proportions and dissolved in distilled water (palladium chloride (AR) was taken in separate beaker to this little distilled water and few ml of concentrated nitric acid was added and heated with stirring to dissolve completely). These solutions were added to 2% dextrose solution at 100 °C with stirring, which will avoid the agglomeration and particles will remain suspended. The precipitation was carried out by adding drop by drop solution of sodium hydroxide (10%) to the above solution under vigorous stirring. Subsequently the suspension of precipitated metal hydroxide mixture (at pH = 9) was subjected to oxidation by drop wise addition of 30% H_2O_2 solution with constant stirring to adjust the oxidation state of metal ions. The precipitate was then digested on a water bath for 3 h. Further the precipitate was filtered washed with water and ethanol and dried in air at 150

°C for 6 h. Finally the dried precipitate was homogenized well in pestle mortar and calcined in air at 700 °C for 5 h.

Nano-sized Ag doped Mn_2O_3 catalysts of composition $Mn_{2-X}Ag_XO_3$ (where X = 0, 0.05, 0.10, 0.15 and 0.20) were prepared by starch assisted co-precipitation method. All the chemicals used were of analytical grade. Calculated amount of manganese acetate and silver nitrate were dissolved in distilled water. Both these solutions were added to 2% starch solution at 100 °C with stirring. Liquid ammonia was added dropwise with stirring till pH = 9. Subsequently, the suspension was subjected to oxidation by dropwise addition of 30% H_2O_2 solution with constant stirring in order to adjust the oxidation state of metal ions. The suspension was then stirred continuously at 100 °C till dryness. The resulting product was dried at 150 °C for 6 h. Finally the dried precipitate was homogenized well in pestle mortar and calcined in air at 700 °C for 5 h.

3.1.3 Preparation of supported catalysts

Pd / MnO_2 (2.4, 5.9 and 9.3 wt% Pd)

Pd Cu / MnO_2 (2.4 wt% Pd 5.7 wt% Cu and 5.9 wt% Pd 3.5wt% Cu)

Rh / MnO_2 (3.5, 5.7 and 11.2 wt% Rh)

Pd / Mn_2O_3 (3.3 and 5.3 wt% Pd)

The supported catalysts were prepared by an impregnation method. The pure MnO_2/Mn_2O_3 powder prepared by the above methods was mixed with an aqueous solution of metal ions to be supported under vigorous stirring. Sodium hydroxide (10%) solution was added drop by drop with stirring to precipitate metal hydroxide. The suspension was

then filtered and dried in air. The obtained sample was homogenized well in mortar and dried at 200 °C for 5 h.

3.2 Instrumental techniques

3.2.1 X-ray diffraction (XRD)

The powder diffraction is the most important technique used for the characterization of all crystalline materials. It furnishes vital information regarding the phase purity, structure type, isomorphous substitution, degree of crystallinity and estimation of particle size as well as unit cell parameters [223]. The XRD method involves the interaction between the incident monochromatized X-rays (like Cu Kα or Mo Kα source) with the atoms of a periodic lattice. X-rays scattered by atoms in an ordered lattice interfere constructively in directions given by Bragg's law:

$$n\lambda = 2d\sin\theta,\ n = 1,2,3\ldots \qquad (1)$$

Where λ is the wavelength of the X-rays, d is the distance between the pairs of adjacent lattice planes, θ is the angle between the incoming X-rays and the normal to the reflecting lattice plane and n is the integer called order of the reflection.

Bragg peaks are measured by observing the intensity of the scattered radiation as a function of scattering angle 2θ. The angles of maximum intensity enable one to calculate the spacings between the lattice planes and allow furthermore for phase identification. The width of diffraction peaks carries information on the dimensions of the reflecting planes. Diffraction lines from the perfect crystals are very narrow where as the diffraction lines for poorly crystalline and amorphous materials are broad.

Conventionally, XRD has several limitations. A key disadvantage of XRD is that it is highly applicable to crystalline materials. Moreover, it is time-consuming and requires a large quantity of sample. Fortunately, synchrotron-based XRD is useful to circumvent these limitations. They offer exceptional resolution, even on very small samples containing only a few grains of a particular mineral.

Powder X-ray diffraction (XRD) patterns of all catalysts reported in this thesis were obtained on a RIGAKU Ultima IV diffractometer using Cu $K\alpha$ radiation (λ = 1.5418 nm). Samples were scanned within the 2θ range of 10-80° with a step size of 0.02.

3.2.2 Thermal analysis (TG/DTA)

Thermal analysis is a group of techniques in which a physical property of substance and/or its reaction products is measured as a function of temperature whilst the substance is subjected to a controlled temperature program [224]. In thermogravimetric analysis the mass of a sample in a controlled atmosphere is recorded continuously as a function of temperature or time as the temperature of the sample is increased (usually linearly with time). A plot of mass or mass percent as a function of time is called a thermogram, or a thermal decomposition curve. Differential thermal analysis is a technique in which the difference in temperature between a substance and a reference material is measured as a function of temperature while the substance and reference material are subjected to a controlled temperature program. Usually, the temperature program involves heating the sample and reference material in such a way that the temperature of the sample T_s increases linearly with time. The difference in temperature ΔT between the sample temperature and the reference temperature T_r ($\Delta T = T_r - T_s$) is then monitored and plotted against sample temperature to give a differential thermogram.

Thermal analysis ie, thermogravimetry and differential thermal analysis for calcined oxides were carried out on a NETZCH STA 409 PC TG/DSC-DTA instrument. The analyses were carried out in air with flow of 100 ml min^{-1}. All the samples were heated from ambient to 1100 °C at a heating rate of 10 K min^{-1}. The sample and reference crucibles use were of recrystallized alumina.

3.2.3 Fourier transform–infrared (FT–IR) spectroscopy

Infrared spectroscopy (IR) can be considered as the first and the most important of the modern spectroscopic techniques that has found general acceptance in catalysis. The technique is used to identify phases that are present in the catalyst or its precursor stages, the adsorbed species, adsorption sites and the way in which the adsorbed species are chemisorbed on the surface of the catalyst. Infrared spectroscopy is the most common form of vibrational spectroscopy and it depends on the excitation of vibrations in molecules or in solid lattices by the absorption of photons, which occurs if a dipole moment changes during the vibration. The intensity of the infrared band is proportional to the change in dipole moment.

Fourier transform–infrared (FT–IR) spectroscopy has proved valuable for the characterization of transition-metal oxides. Vibrational spectra of prepared manganese oxides were analyzed using FT–IR spectroscopy as complementary techniques in the wavenumber ranging 400–1500 cm^{-1} to investigate internal and external modes of manganese oxides lattices. Effect of incorporation of various dopants in the lattice of manganese oxide has been studied. Doped manganese oxides spectra were compared with that of pristine manganese oxide.

Fourier transform–infrared (FT–IR) analyses of the prepared catalysts were undertaken in the range 400-1500 cm^{-1} with SHIMADZU IR prestige-21 spectrophotometer. The sample was grind thoroughly with KBr powder. Then it was mounted on the sample holder, this sample holder was placed in the instrument and the spectra were recorded.

3.2.4 Electrical conductivity

For electrical conductivity measurements, doped manganese oxide samples in the form of pallet of 0.5 cm radius and 0.15 cm thickness were used. Pallets were prepared by compressing 0.4 g of sample with hydraulic press at 5 ton of pressure and sintered. Pallets were heated at 150 °C for 2 h in an oven prior to measurements. The conductivity set up was calibrated using NaCl crystal. Electrical conductivity from room temperature to 400 °C of all the samples was measured in conductivity unit cell by two probe method in air. Log σ v/s 1/Tx1000 plots were plotted for all the samples.

3.2.5 Magnetic susceptibility

The magnetic susceptibility of all the doped manganese oxide samples at room temperature was determined by Gouy method. The gram susceptibility (χ_g) and magnetic moment (μ_{eff}) values were found out at ambient temperature.

The magnetic field employed was 8600 gauss. A tube filled up to a certain height with the magnetic sample is suspended from an arm of a sensitive balance such that the bottom part of the sample is in a strong magnetic field and the top part is in a zero field. The sample is placed in the jaws of an electromagnet and the difference in weight was measured without magnetic field and with magnetic field by using the analytical balance at

room temperature [225]. The $Hg[Co(NCS)_4]$ is used as a the standard material, the gram susceptibility (χ_g) value of this is 16.44 X 10^{-6}.

The molar susceptibility (χ_M) is calculated by multiplying χ_g with the molecular weight of the compound.

The magnetic properties of the materials are often conveniently expressed in terms of the magnetic moment (μ). This parameter is directly related to the number of unpaired electrons present. The value of μ can be calculated by equation

$$\mu = 2.84 \sqrt{\chi_M \times T} \qquad (5)$$

3.2.6 UV-Visible absorbance/diffuse reflectance spectroscopy

Diffuse reflectance spectroscopy (DRS) is a technique based on the reflection of light in the ultraviolet (UV), visible (VIS) and near-infrared (NIR) region by a powdered sample. In a DRS spectrum, the ratio of the light scattered from an "infinitely thick" closely packed sample layer and the scattered light from an infinitely thick layer of an ideal non-absorbing (white) reference sample is measured as a function of the wavelength λ. The scattered radiation, emanating from the sample, is collected in an integration sphere and detected.

DRS is particularly suitable for studying the speciation of supported transition metal ions (TMI), because it measures both their d-d transitions and charge transfer bands. The obtained information is directly chemical since the outer shell electrons are probed. DRS is a powerful technique to identify and characterize the metal ion coordination. It's a non destructive technique that uses the interaction of light, absorption and scattering, to

produce a characteristic reflectance spectrum, providing information about the structure and composition of the medium. It also provides the information regarding the band gap of the materials, especially the semiconducting metal oxides.

The diffuse reflectance spectra of dry powders were recorded using a Shimadzu UV-2450 UV–Visible spectrometer equipped with a diffuse reflectance accessory in the wavelength range of 800–200 nm. $BaSO_4$ was used as a reference. The band gap energies of the catalysts was estimated from the differential plots obtained from the UV-visible reflectance spectra.

3.2.7 X-ray photoelectron spectroscopy (XPS)

The X-ray photoelectron spectroscopy (XPS) is based on the photoelectric effect, which involves the bombardment of a sample surface with X-rays and the measurement of the concomitant photoemitted electrons. The photoemitted electrons have discrete kinetic energies that are characteristic of the emitting atoms and their bonding states. The kinetic energy, Ek, of these photoelectrons is determined by the energy of the X-ray radiation, hν, and the electron binding energy, Eb, as given by:

$$Ek = h\nu - Eb \qquad (6)$$

The experimentally measured energies of the photoelectrons are given by:

$$Ek = h\nu - Eb - Ew \qquad (7)$$

Where, Ew is the work function of the spectrometer.

The binding energies of the peaks are characteristic of each element. The peak areas can be used (with appropriate sensitivity factors) to determine the composition of the

materials surface. The shape of each peak and the binding energy can be slightly altered by the chemical state of the emitting atom, which provide chemical bonding information as well. XPS and the related Auger electron spectroscopy (AES) can provide elemental analysis for essentially the entire periodic table. Because the electrons whose energies are analyzed arise from a depth of no greater than about 5 nm, the technique is surface-sensitive.

X-ray photoelectron spectra of the present study were acquired on a VG Microtech Multilab ESCA 3000 spectrometer using a non-monochromatized MgKa X-ray source ($h\gamma$ = 1253.6 eV) at room temperature. Base pressure in the analysis chamber was maintained at 3-6 x 10^{-10} Torr range. The energy resolution of the spectrometer was determined from the full width at half maximum of metallic gold and the value obtained is better than 0.8 eV for MgKα radiation and 1.1 eV for AlK α radiation respectively, at a pass energy of 20 eV. The error in the BE values [226] reported is ± 0.1 eV.

3.2.8 BET surface area

The most common method of measuring surface area of catalytic materials is that based on the theory developed by Brunauer, Emmett and Teller in 1938 considering the multilayer adsorption. The isotherm points are transformed with the linear version of BET equation (2).

$$P/V_{ads}\,(P_0-P) = 1/V_mC + [(C-1)/V_mC] \times (P/P_0) \qquad (2)$$

where P = adsorption equilibrium pressure, P_0 = standard vapour pressure of the adsorbent, V_{ads} = volume at STP occupied by molecules adsorbed at pressure P, V_m = volume of adsorbate required for a monolayer coverage, C = constant related to heat of

adsorption. A plot of P/V ads (P_0-P) Vs (P/P_0) will yield a straight line usually in the range $0.05 \leq P/P_0 \leq 0.35$. The slope (s) and intercept (i) of the BET plot are

$$S = (C-1)/V_mC \text{ and } i = 1/ V_mC \qquad (3)$$

Solving these equations permits the calculation of Vm. Then the specific surface area of the catalyst can be calculated as,

$$\text{Specific surface area } (m^2/g) = [(V_mNa)/22414 \times Wt] \times A_m \qquad (4)$$

Where, A_m = mean cross sectional area occupied by adsorbate molecule (16.2 A^2 for N_2), Wt = weight of the catalyst sample, Na = Avogadro number, V_m = monolayer volume in ml at STP.

The BET surface area, SBET, of the catalysts was measured by nitrogen adsorption-desorption method at liquid nitrogen temperature using a SMART SORB–91 surface area analyzer. About 400 mg of sample was regenerated at 200 °C for 2 h prior to the adsorption experiments.

3.2.9 Scanning electron microscopy (SEM)

Scanning electron microscopy is an easy technique to study the texture, topography and surface features of powders or solid pieces. SEM scans over a sample surface with a probe of electrons (5-50 eV) and detects the yield of either secondary or back-scattered electrons as a function of the position of the primary beam. The parts of the surface facing the detector appear brighter than parts of the surface with their surface normal pointing away

from the detector. The interaction between the electron beam and the sample produces different types of signals providing detailed information about the surface structure and morphology of the sample. Magnification of 20-50,000 is possible with a resolution of about 5 nm. Crystallite shape, size and size distributions are easily obtained for particles larger than 5 nm.

The surface morphology was determined with JSM-5800LV scanning electron microscope and JEOL JSM-6360LV scanning electron microscope (SEM) instrument operating at 20 kV.

3.2.10 Transmission electron microscopy (TEM)

Transmission electron microscopy (TEM) is a microscopy technique whereby a beam of electrons is transmitted through an ultra thin specimen, interacting with the specimen as it passes through. An image is formed from the interaction of the electrons transmitted through the specimen; the image is magnified and focused onto an imaging device, such as a fluorescent screen, on a layer of photographic film, or to be detected by a sensor such as a CCD camera.

TEMs are capable of imaging at a significantly higher resolution than light microscopes, owing to the small de Broglie wavelength of electrons. This enables the instrument's user to examine fine detail—even as small as a single column of atoms, which is tens of thousands times smaller than the smallest resolvable object in a light microscope. TEM forms a major analysis method in a range of scientific fields, in both physical and biological sciences. TEMs find application in cancer research, virology, materials science as well as pollution and semiconductor research.

At smaller magnifications TEM image contrast is due to absorption of electrons in the material, due to the thickness and composition of the material. At higher magnifications complex wave interactions modulate the intensity of the image, requiring expert analysis of observed images. Alternate modes of use allow for the TEM to observe modulations in chemical identity, crystal orientation, electronic structure and sample induced electron phase shift as well as the regular absorption based imaging.

Transmission Electron Microscope (TEM) images were recorded on a PHILIPS CM 200 electron microscope operating with an accelerating voltage of 200 KV and providing a resolution of 2.4 A^{o}.

3.2.11 Temperature programmed desorption

TPD is a technique for studying the kinetics of adsorbates on solid surfaces. The data are collected under well-controlled flow or vacuum conditions. After analysis, it yields kinetic parameters as a function of adsorbate surface coverage. An evolved gas analyzer such as quadruple mass spectrometer is tuned to monitor one or more mass fragments simultaneously that can be correlated to the desorbing species with respect to sample temperature. The desorption temperature, the shape of the desorption peak, and how these changes are related to initial surface coverage and heating rate are analyzed to provide information about the binding character of the adsorbate/substrate system.

When an acid is neutralized by reaction with a base, the heat of neutralization is evolved. The higher the heat of neutralization, stronger is the acid strength and so it can be used to characterize acid-strength. This principle can be used to characterize the acid sites present on a solid acid by TPD of probe molecules like ammonia and pyridine. This is a

popular method for the determination of acidity of solid acids as well as acid strength because it is an easy and reproducible method. Ammonia is used frequently as a probe molecule because of its small molecular size, stability and strong basic strength [227]. First the sample is contacted with a base (NH_3 or pyridine) to neutralize the acidic sites present. Then the temperature is raised at a constant rate and the amount of desorbed base is monitored and recorded. In short, TPD consists of heating a sample at a constant rate and measuring the quantity of material desorbed at each temperature. TPD data provide a partially averaged value for acid strength. It is a simple and rapid method to characterize acidity. NH_3-TPD is one of the most often used methods [34]. In principle, the concentration of sites having similar acid strength and the average heat of adsorption or activation energy of NH_3 desorption can be determined using the TPD method. Often the temperature of maximum desorption rate, i.e., the temperature of a TPD peak (Tmax), is used as a rough measure of the acid strength of the sorption sites. Among the limitations of this method is that it can distinguish sites by sorption strength only, but not Lewis and Bronsted type-sites. Moreover, desorption may proceed simultaneously from sites of different types resulting in composite curve consisting of overlapping TPD peaks. In a NH_3-TPD spectrum for solid acids, generally two peaks are observed, one at low temperature (LT) corresponding to NH_3 desorbing from the weaker acidic sites (also observed for nonacidic silicates) and another one at higher temperature (HT) corresponding with the stronger acidic sites. The area under these peaks gives information about the amount of these strong acid sites whereas the peak-maximum-temperature (Tmax) gives information about its acid-strength.

The temperature programmed desorption experiments were carried out with a Micromeritics Autochem 2910 catalyst characterization system, equipped with a TCD detector.

3.3 Catalytic activity measurement

3.3.1 Set-up for CO oxidation activity measurement

The catalytic tests for CO oxidation by O_2 were performed at atmospheric pressure in a continuous flow, fixed bed glass reactor. The catalyst powder of 0.9 g was supported between glass wool plugs in a glass reactor which was placed in an electric furnace. The reaction temperature was measured by inserting a thermo-couple in the middle of the catalyst bed. The catalytic activity was determined using a feed gas composition of 5% CO and 5% O_2 in nitrogen. All these three gases were first mixed in a mixing bulb. The individual gas flow rates were controlled using flow meters and precision needle valves, previously calibrated for each specific gas. Prior to the CO oxidation reaction the catalyst was activated by passing O_2 at 100 ^{o}C for 30 min. The mixture of gases was then allowed to pass over the catalyst at a rate of 5000 ml h^{-1}. The CO was prepared in the laboratory by standard procedure and further purified by passing through alkali and molecular sieve traps. O_2, N_2 and H_2 gases were used from pure commercial cylinders.

The feed gases and the products were analyzed employing an online Gas Chromatograph, H_2 was used as a carrier gas. The NEUCON Gas Chromatograph equiped with both thermal conductivity and flame ionization detector was used for the analysis of reaction gases and reaction products. The separation of various components was achieved on molecular sieve 13X column and porapak Q column was used for reference.

The diagram showing the reaction set-up for the catalytic CO oxidation reaction is given in Fig. 3.1

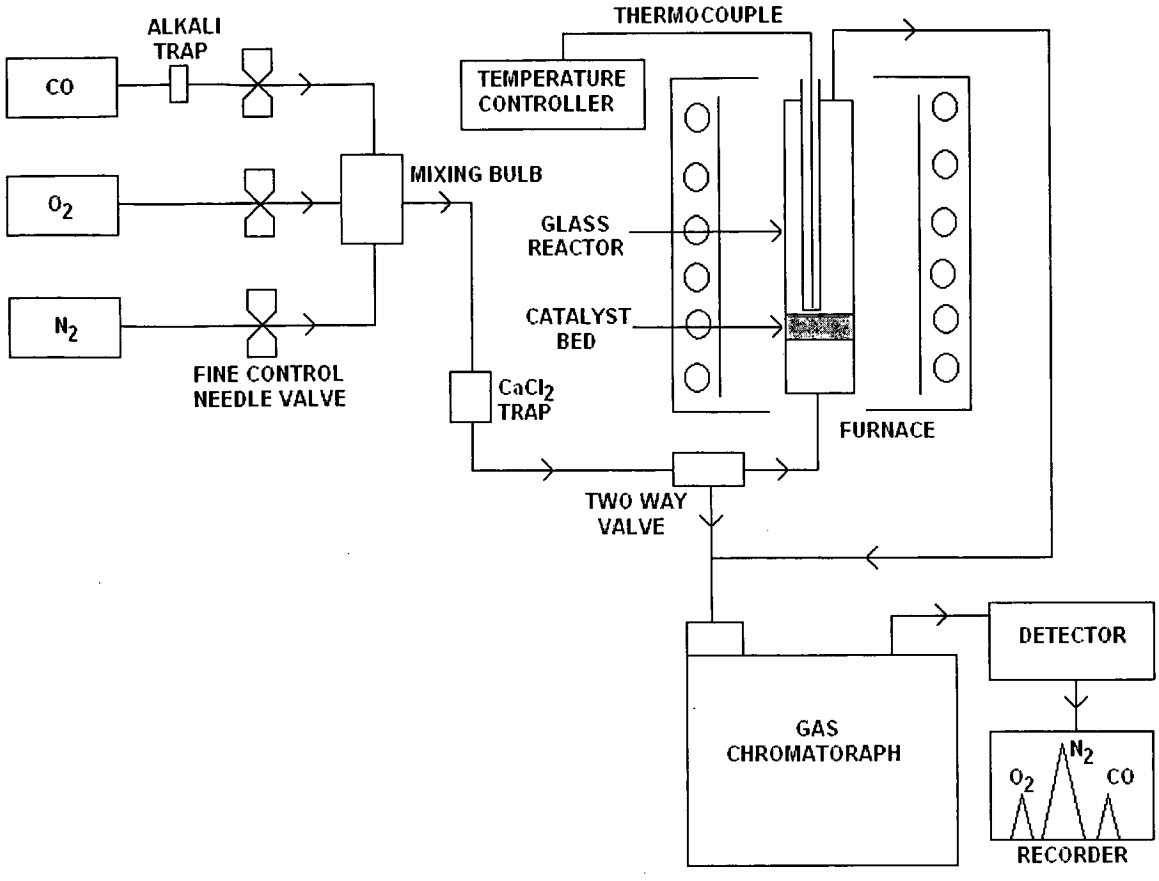

Fig. 3.1 The reaction set-up for the catalytic CO oxidation reaction.

CHAPTER 4

SOLID STATE AND SPECTROSCOPIC STUDIES

4.1 X-ray diffraction

The X-ray diffraction is an important technique used for the phase identification of the prepared metal oxide samples and determination of their crystal structure.

4.1.1 MnO_2 doped samples

Fig. 4.1 shows the XRD patterns of MnO_2, $Mn_{0.95}Ni_{0.05}O_2$ and $Mn_{0.80}Ni_{0.20}O_2$. The diffraction peaks in Fig 4.1a could be indexed to MnO_2 phase with tetragonal system which agrees well with the values reported in ICDD card No: 44-0141.

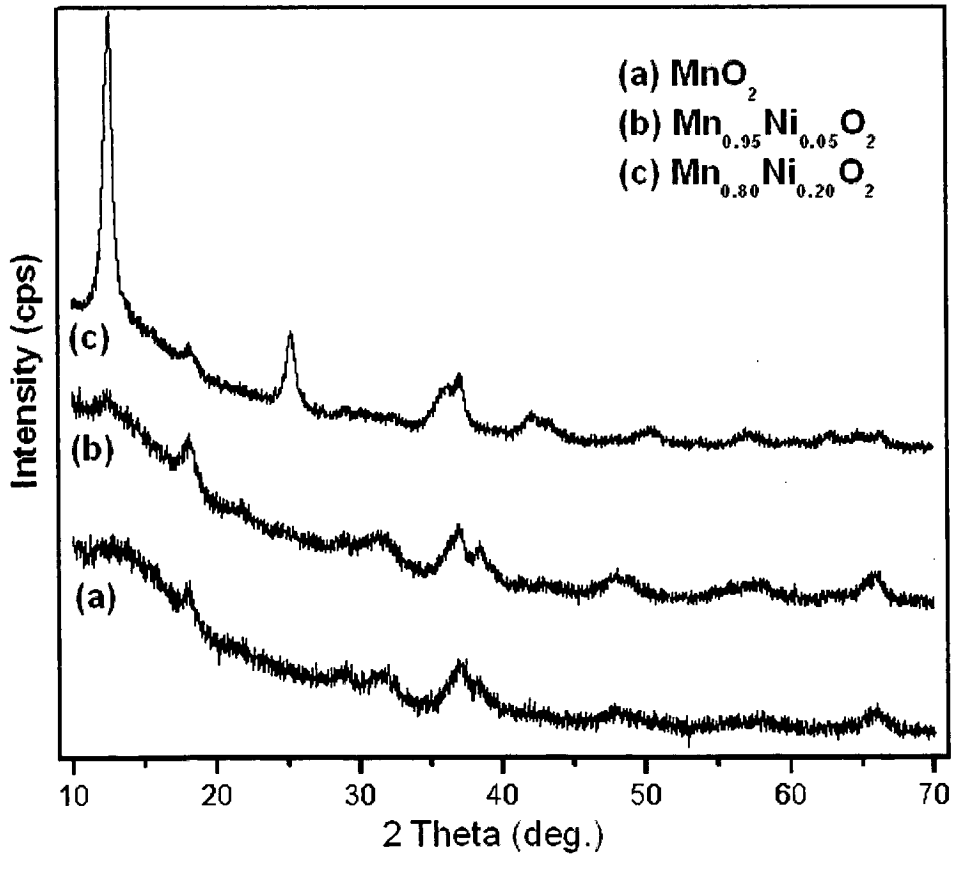

Fig. 4.1 XRD patterns for (a) MnO_2, (b) $Mn_{0.95}Ni_{0.05}O_2$ and (c) $Mn_{0.80}Ni_{0.20}O_2$.

$Mn_{0.95}Ni_{0.05}O_2$ shows almost similar pattern like MnO_2 but with increase in Ni content shows structural changes. Fig. 4.1c for $Mn_{0.80}Ni_{0.20}O_2$ shows structural change in MnO_2 and the diffraction peaks agrees well with values reported in ICDD card No: 72-1982 for MnO_2 with tetragonal system.

Fig.4.2 shows the XRD pattern for MnO_2 and $Mn_{0.92}Pd_{0.08}O_2$. The peaks were assigned for MnO_2 at the 2θ angles of 37.34° (131), 38.42° (230), 42.3° (300), 56.22° (160) and 65.04° (421) shown in Fig. 4.2a, all the reflections of the XRD pattern can be readily indexed to the pure pyrolusite which agrees well with the values reported in the literature.

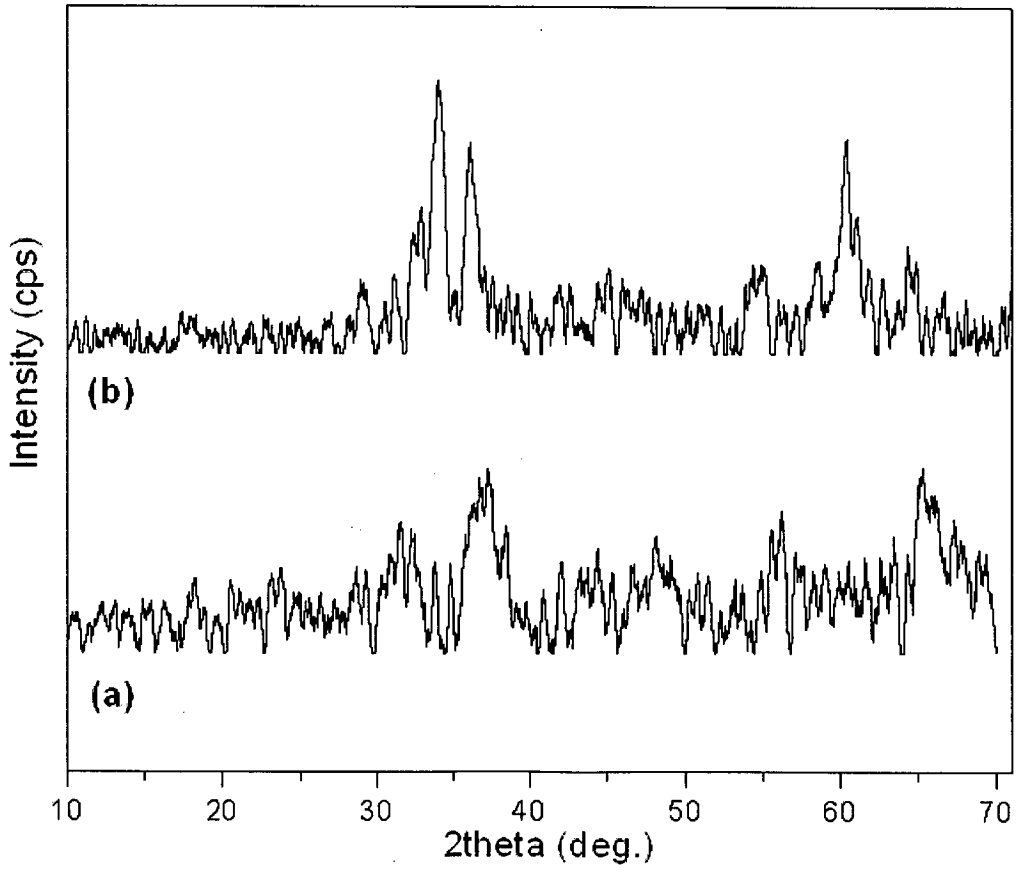

Fig. 4.2 XRD pattern of (a) MnO_2 and (b) $Mn_{0.92}Pd_{0.08}O_2$.

Whereas the XRD phase identification of $Mn_{0.92}Pd_{0.08}O_2$, revealed characteristic signals at 2θ values of 34.04° (130), 36.04° (021), 55.03° (221) and 60.34° (231) which is shown in Fig. 4.2b and these reflections correspond to the ramsdellite structure. It was observed

that after incorporation of palladium in the lattice of MnO_2, the phase changes from pyrolusite to ramsdellite. No characteristic peaks for palladium or palladium oxide were observed in the XRD pattern.

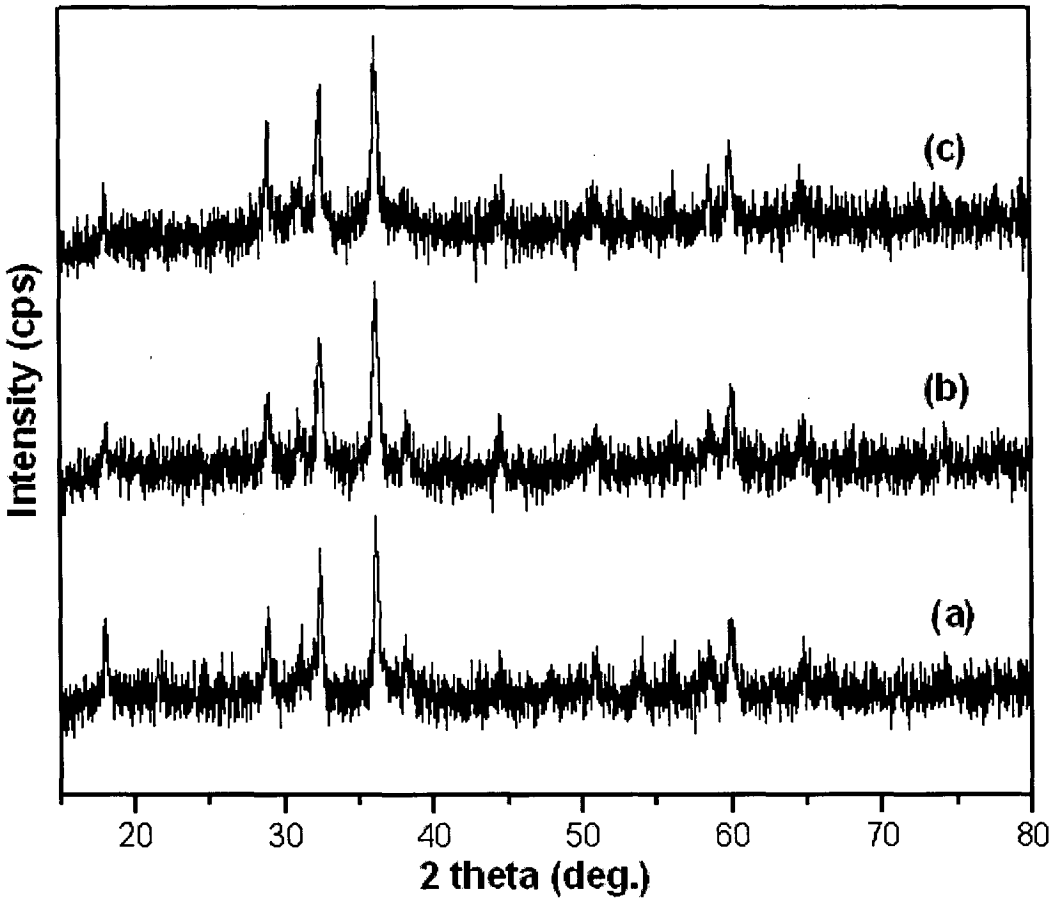

Fig. 4.3 XRD pattern of (a) MnO_2, (b) $Mn_{0.95}Ag_{0.05}O_2$ and (c) $Mn_{0.90}Ag_{0.10}O_2$.

The XRD patterns for silver doped MnO_2 samples are shown in Fig. 4.3. The XRD pattern of the calcined MnO_2 (Fig.4.3a) shows well defined diffraction features characteristics of nanocrystalline MnO_2, indexed to the tetragonal phase. After doping of Ag, an almost identical pattern was obtained for Ag doped MnO_2 samples as that of pristine MnO_2 indicating the well maintenance of the crystal structure of the nanocrystalline MnO_2 catalyst. Fig. 4.3b and c shows the XRD patterns for $Mn_{0.95}Ag_{0.05}O_2$ and $Mn_{0.90}Ag_{0.10}O_2$ catalysts. No distinct Ag reflections are visible in the XRD patterns of any sample indicating that Ag is well incorporated in MnO_2.

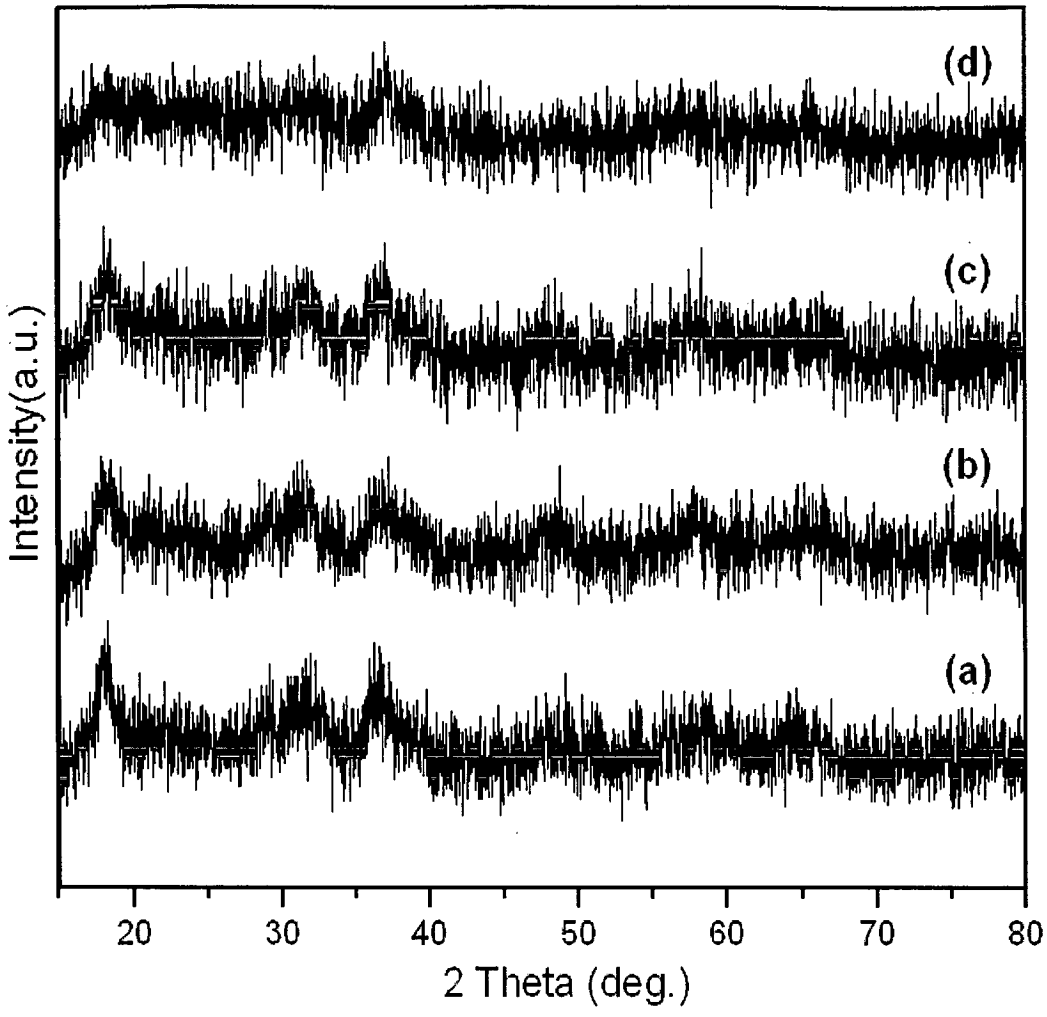

Fig. 4.4 XRD patterns for (a) MnO_2, (b) $Mn_{0.92}Rh_{0.02}O_2$, (c) $Mn_{0.95}Rh_{0.05}O_2$ and (d) $Mn_{0.90}Rh_{0.10}O_2$.

The XRD patterns for rhodium doped MnO_2 are illustrated in Fig. 4.4. All the samples showed diffraction features characteristic of MnO_2. These catalysts are poorly crystalline materials and broadening of peaks indicates that these materials are highly nanocrystalline. No extra peaks were visible for rhodium, indicating that rhodium is well incorporated in the MnO_2 lattice.

The XRD patterns of Cu-Pd doped MnO_2 (Fig. 4.5) showed diffraction features characteristic of nanocrystalline MnO_2, indexed to the tetragonal phase (ICDD card 44-0141). Fig. 4.5b and c displays the diffraction patterns for $Mn_{0.90}Cu_{0.10}O_2$ and

$Mn_{0.90}Cu_{0.08}Pd_{0.02}O_2$, which shows similar characteristic features of nanocrystalline MnO_2 indicating that Cu and Pd are well dispersed in MnO_2 matrix.

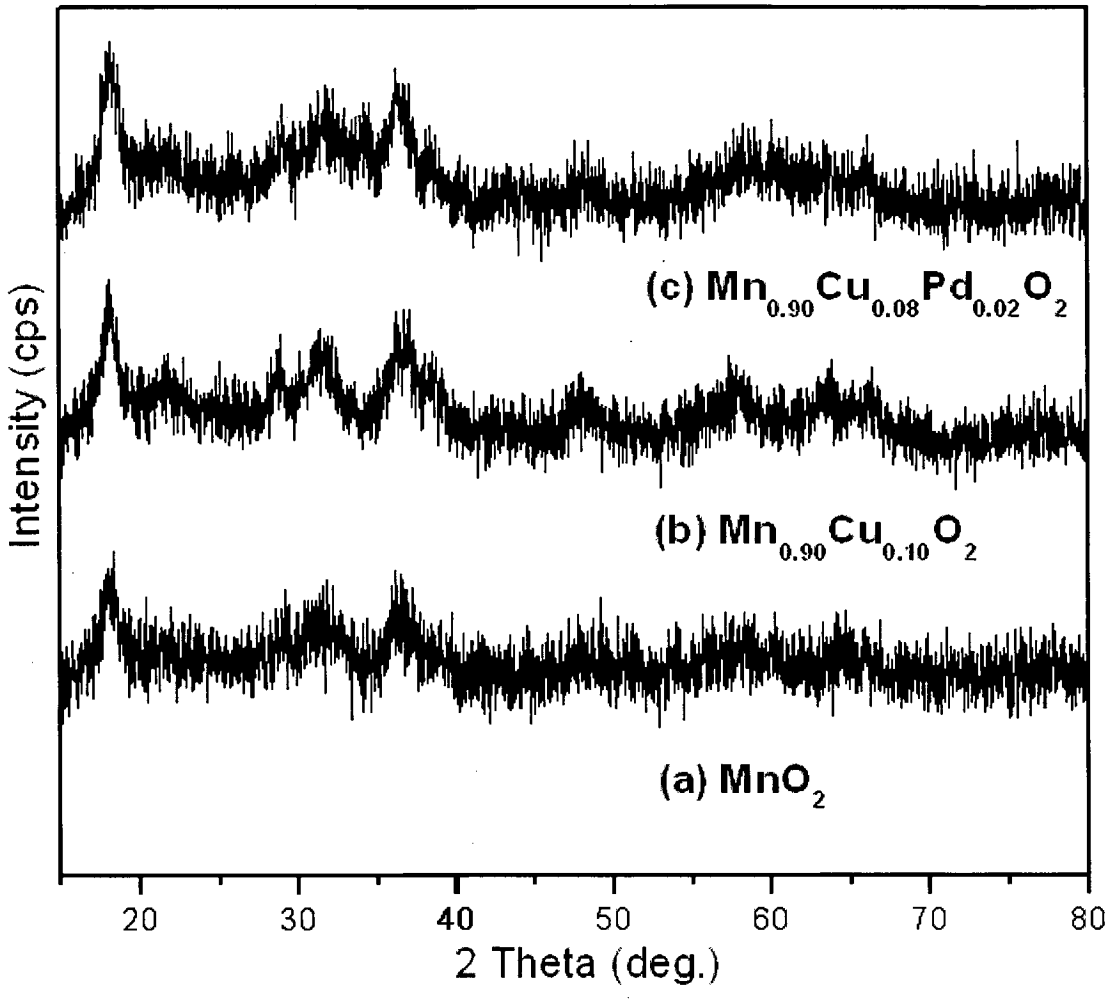

Fig.4.5 XRD patterns of (a) MnO_2, (b) $Mn_{0.90}Cu_{0.10}O_2$ and (c) $Mn_{0.90}Cu_{0.08}Pd_{0.02}O_2$

4.1.2 Doped Mn_2O_3 catalysts

The XRD patterns for Ni doped Mn_2O_3 catalysts are shown in Fig. 4.6. The pure Mn_2O_3 showed the formation of cubic system of Mn_2O_3 which agrees well with the reported data (ICDD card No: 01-1061). After incorporation of nickel in to the lattice of Mn_2O_3, a change in the phase of Mn_2O_3 was observed due to the incorporation of Ni ions into the lattice of Mn_2O_3.

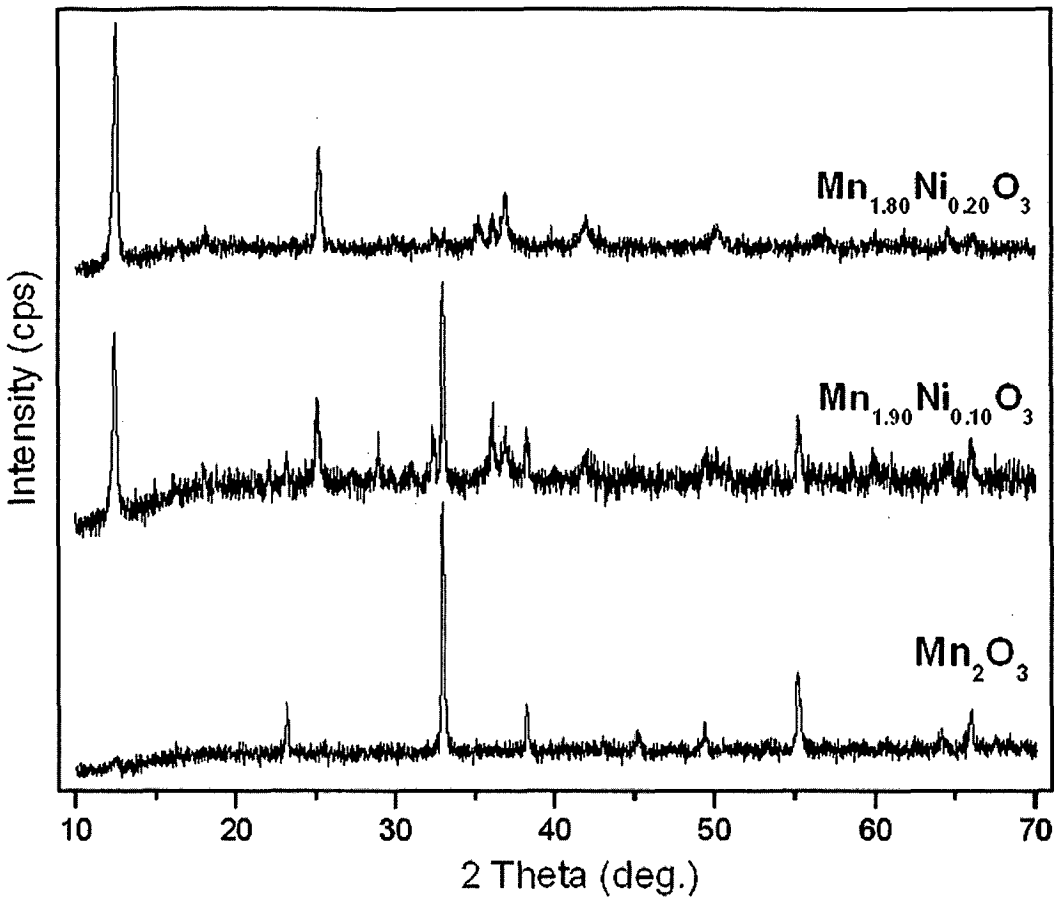

Fig.4.6 XRD patterns of (a) Mn_2O_3, (b) $Mn_{1.90}Ni_{0.10}O_3$ and (c) $Mn_{1.80}Ni_{0.20}O_3$.

The Fig. 4.7 illustrates the diffraction patterns for palladium doped Mn_2O_3 samples. The diffraction peaks in Fig. 4.7a could be indexed to Mn_2O_3 phase with cubic system which agrees well with the values reported in ICDD card No: 01-1061. Where as the XRD patterns of doped samples $Mn_{1.95}Pd_{0.05}O_3$ and $Mn_{1.92}Pd_{0.08}O_3$ (Fig. 4.7 b and c) can be indexed to tetragonal system of Mn_2O_3 which agrees well with values reported in ICDD card No: 06-0540. Thus after incorporation of Pd in Mn_2O_3 a change in phase of Mn_2O_3 was observed.

From the diffraction patterns it can also seen that the samples are nanocrystalline in nature. No peaks for palladium were observed indicating that palladium is well incorporated in the Mn_2O_3 lattice.

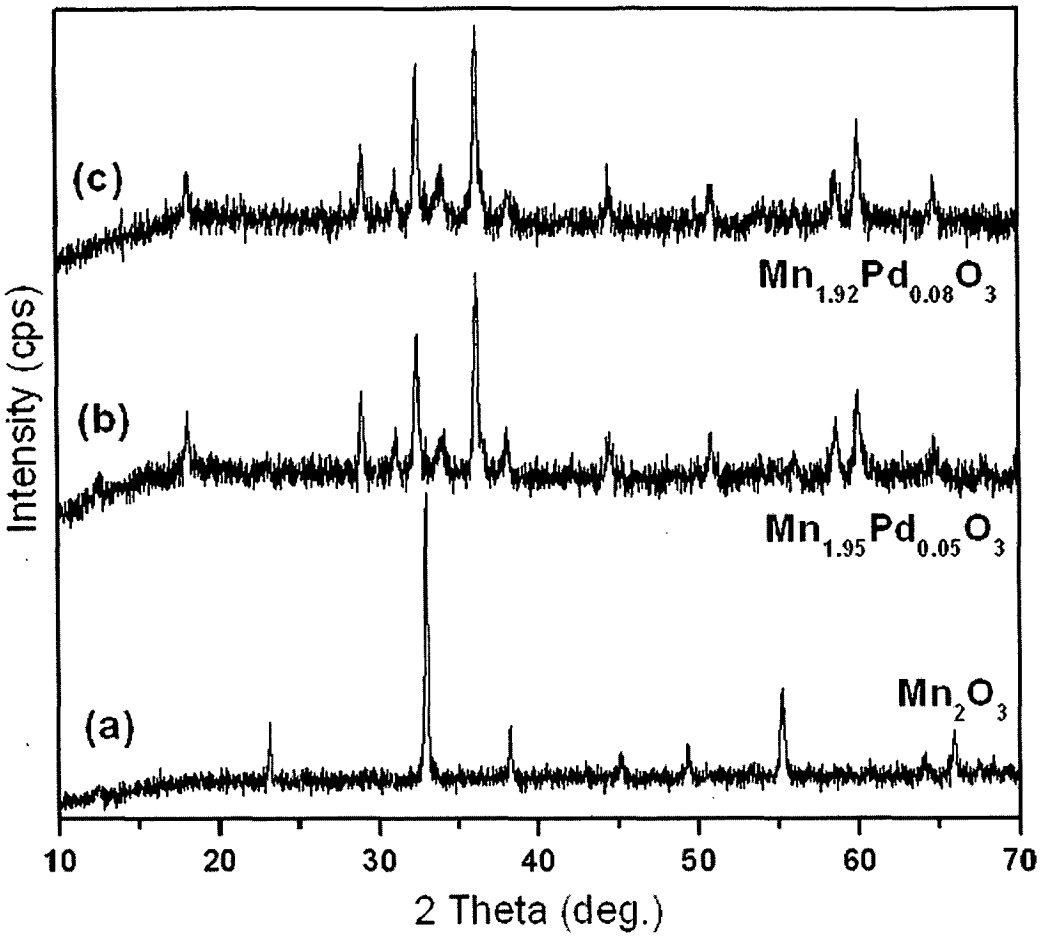

Fig.4.7 XRD patterns of (a) Mn_2O_3, (b) $Mn_{1.95}Pd_{0.05}O_3$ and (c) $Mn_{1.92}Pd_{0.08}O_3$.

The XRD patterns for Ag doped Mn_2O_3 catalysts are illustrated in Fig. 4.8. All the samples show diffraction peaks characteristic of cubic phase of Mn_2O_3, which are consistent with the reported values (ICDD card No: 01-1061). From this pattern it can be seen that the product has high crystallinity.

The extra peaks can be seen at 2θ values of 28.95° (202), 32.35° (221) and 36.16° (203) in the samples $Mn_{1.90}Ag_{0.10}O_3$ and $Mn_{1.80}Ag_{0.20}O_3$ (Fig.4.8 c and d). These extra peaks corresponds to high intensity peaks of Mn_2O_3 in tetragonal system (ICDD card No: 06-0540) which indicates that there is also a formation of tetragonal phase of Mn_2O_3 as an impurity.

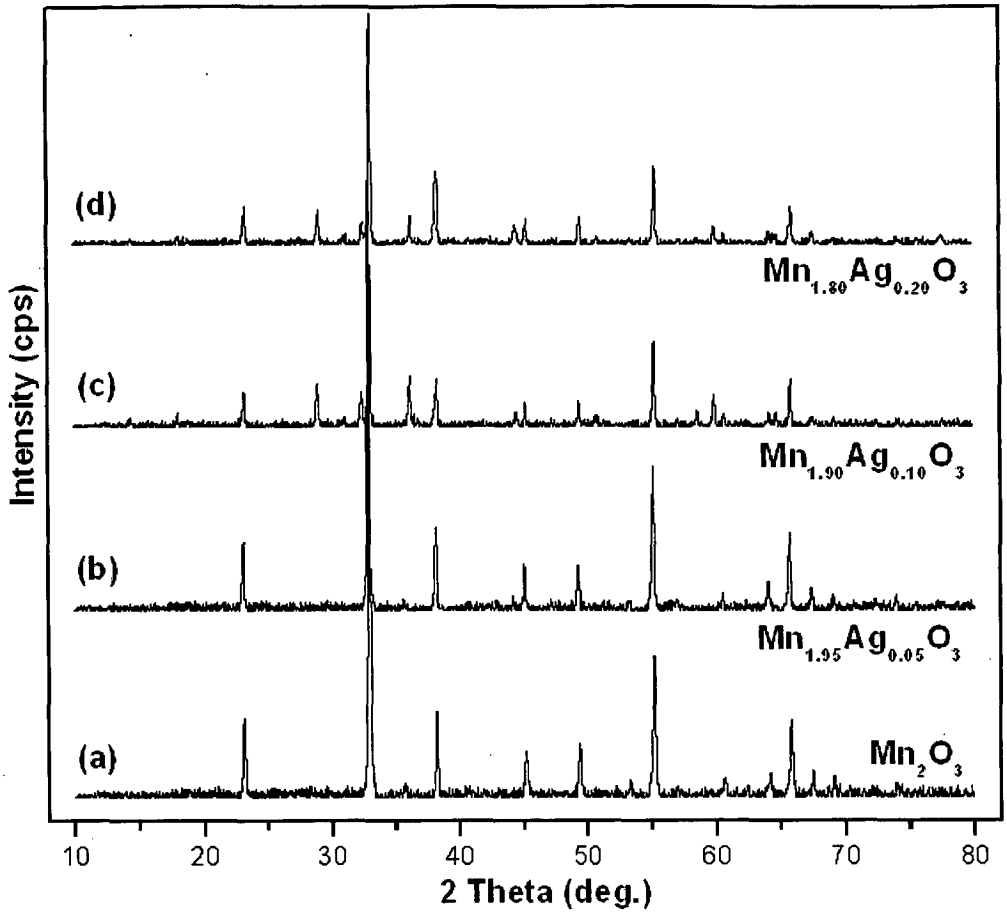

Fig.4.8 XRD patterns of (a) Mn_2O_3, (b) $Mn_{1.95}Ag_{0.05}O_3$, (c) $Mn_{1.90}Ag_{0.10}O_3$ and (d) $Mn_{1.80}Ag_{0.20}O_3$.

4.1.3 Supported manganese oxide catalysts

Fig. 4.9 shows the XRD patterns of palladium supported Mn_2O_3 catalysts along with pristine Mn_2O_3. Both 3.3 wt% Pd/Mn_2O_3 and 5.3 wt% Pd/Mn_2O_3 catalysts showed similar diffraction features as that of pristine Mn_2O_3, which agrees well with the values reported in literature data (ICDD card No: 01-1061). No extra reflections can be seen for palladium, which shows that palladium is highly dispersed on Mn_2O_3 support. All the diffraction features can be index to a cubic phase of Mn_2O_3.

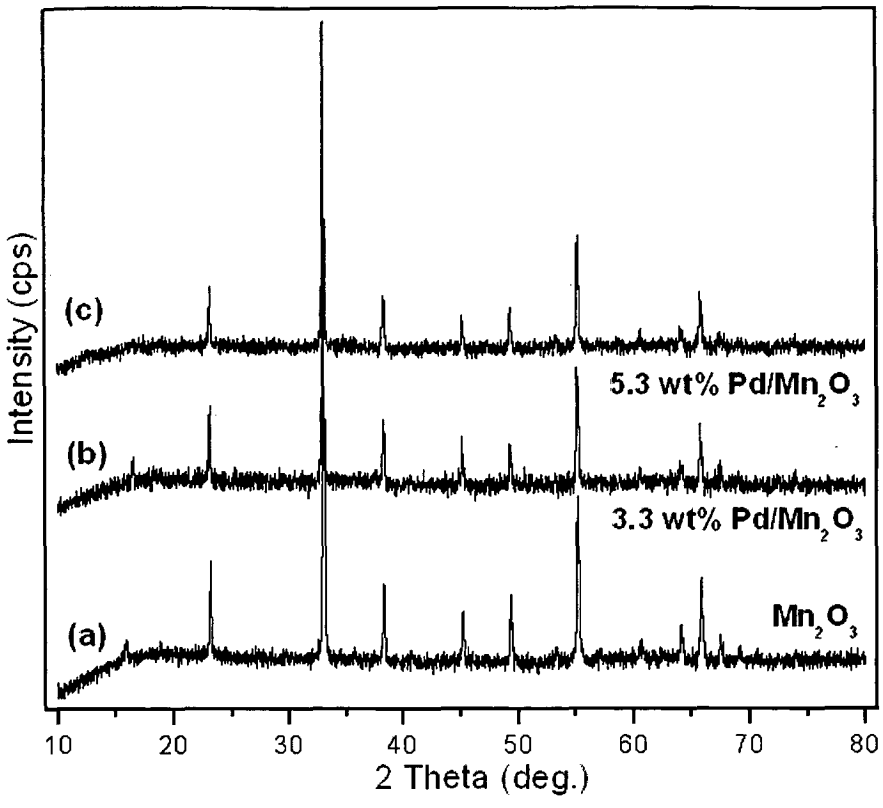

Fig.4.9 XRD patterns of (a) Mn_2O_3, (b) 3.3 wt% Pd/Mn_2O_3 and (c) 5.3 wt% Pd/Mn_2O_3.

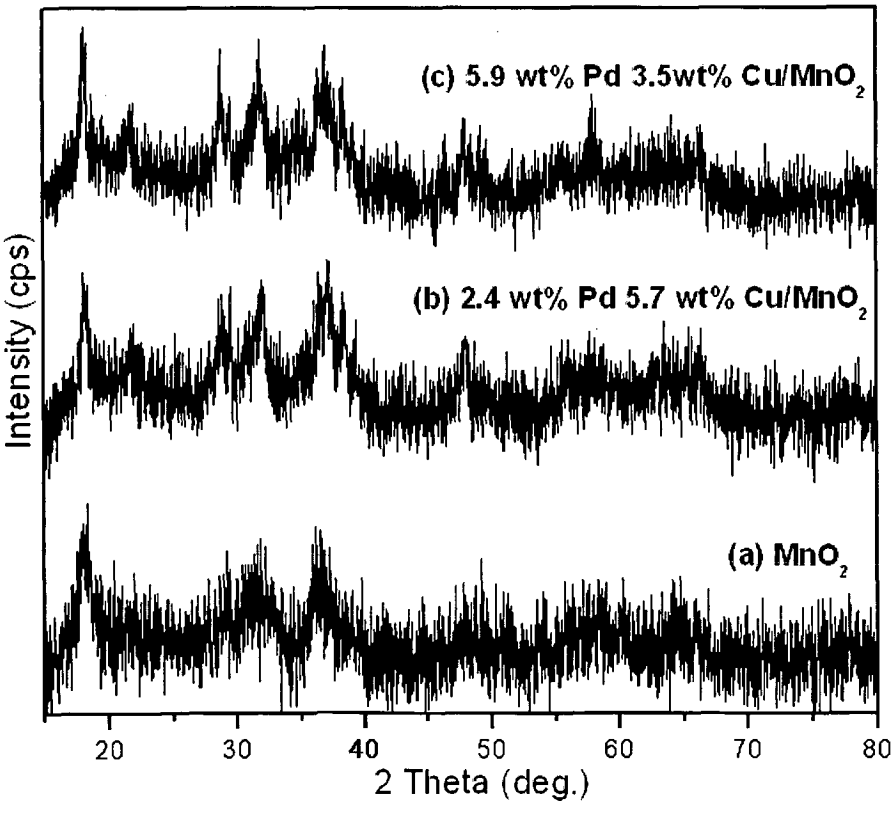

Fig.4.10 XRD patterns of (a) MnO_2, (b) 2.4 wt% Pd 5.7 wt% Cu/MnO_2 and (c) 5.9 wt% Pd 3.5 wt% Cu/MnO_2.

The XRD patterns for Cu-Pd supported MnO_2 are shown in Fig. 4.10. The pure MnO_2 shows diffraction features, characteristic of tetragonal MnO_2, which agrees well with reported literature data ICDD card 44-0141. The Cu Pd supported samples also showed identical patterns as that of MnO_2. No new reflections can be seen for Cu or Pd indicating that these metal ions are highly dispersed in MnO_2. The peaks are very broad signifying that these materials are poorly crystalline and the particles are nano-sized.

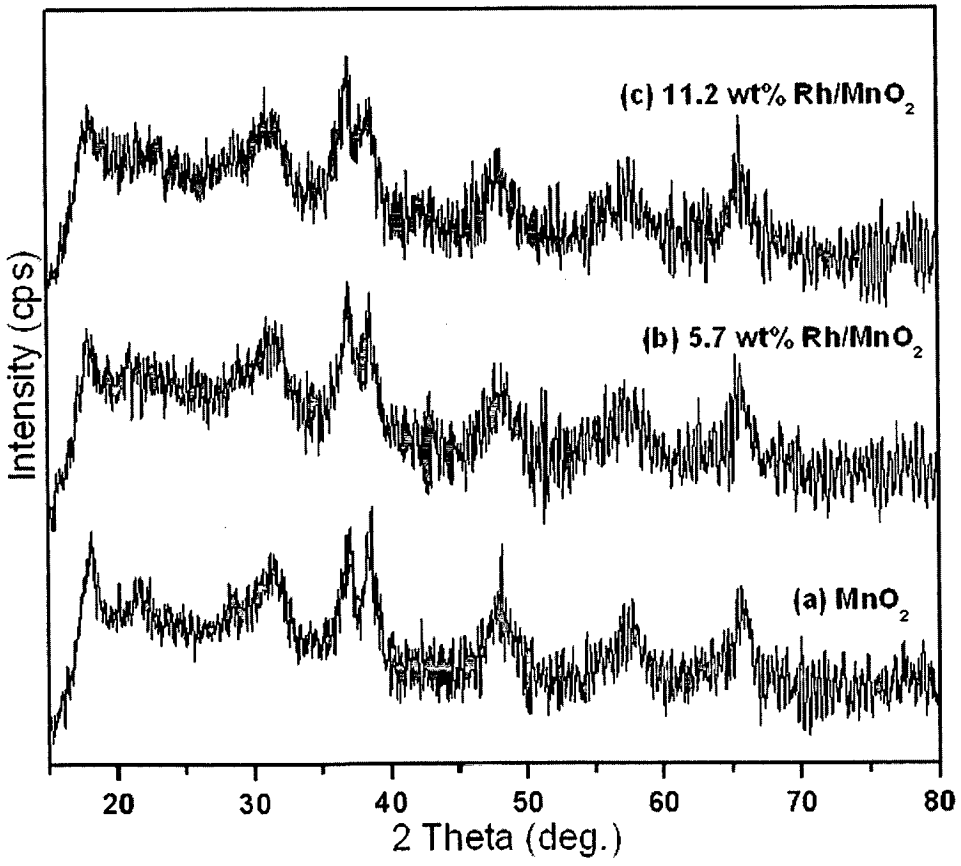

Fig.4.11 XRD patterns of (a) MnO_2, (b) 5.7 wt% Rh/MnO_2 and (c) 11.2 wt% Rh/MnO_2.

The rhodium and palladium supported MnO_2 catalysts shows diffraction patterns similar to pristine MnO_2 (Fig 4.11 and 4.12). The intensities and widths of the diffraction peaks were greatly lowered and widened signifying the poor crystallinity of these catalysts. Fig. 4.11 shows XRD patterns of (b) 5.7 wt% Rh/MnO_2 and (c) 11.2 wt% Rh/MnO_2 and Fig. 4.12 shows XRD patterns of (b) 2.4 wt% Pd/MnO_2, (c) 5.9 wt%

Pd/$MnO_2$and (d) 9.3 wt% Pd/MnO_2. In both the cases no extra reflections can be seen for Rh or Pd and the peaks are also broad and lowered which made it difficult to discern.

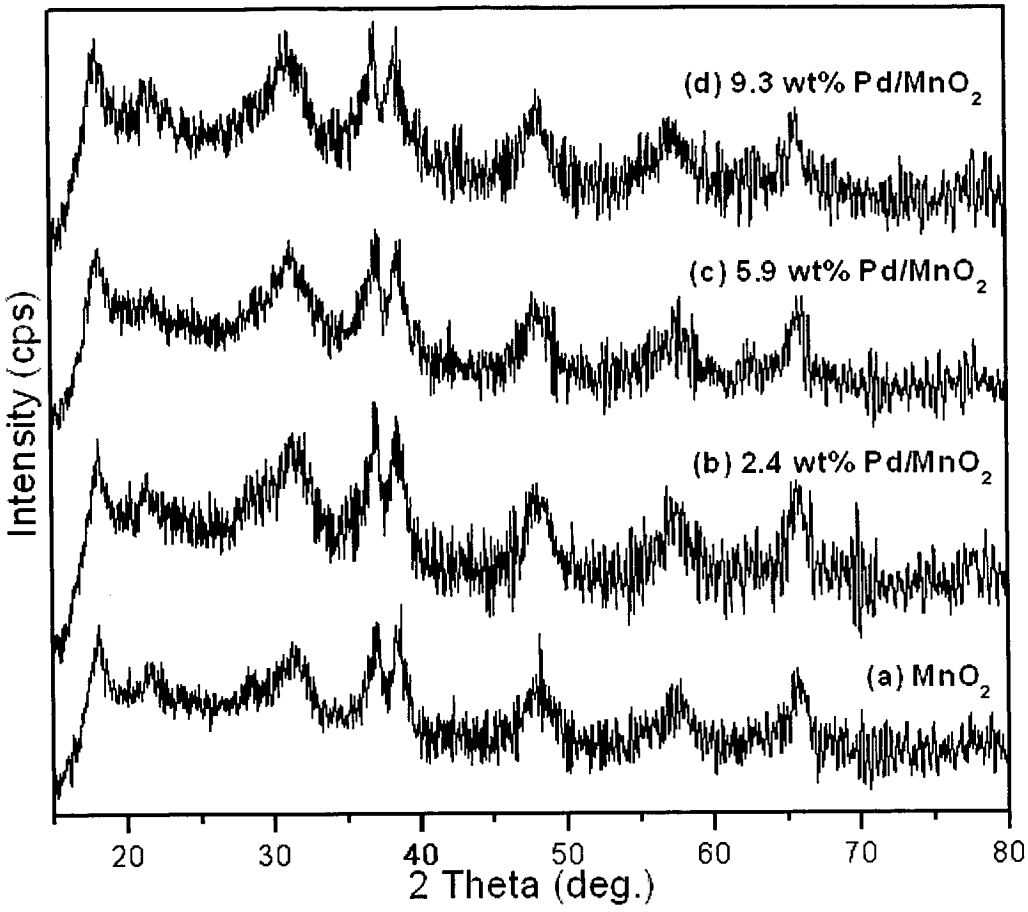

Fig.4.12 XRD patterns of (a) MnO_2, (b) 2.4 wt% Pd/MnO_2, (c) 5.9 wt% Pd/MnO_2 and (d) 9.3 wt% Pd/MnO_2.

4.2 Thermal analysis (TG/DTA)

Thermal analysis is a technique in which the physical properties of substance can be monitored with respect to temperature. It is very much useful to find out the decomposition temperature of the precursor and has other various applications. Thermal analysis (TG/DTA) has been employed to study the phase change in manganese oxides with increasing temperature and to observe the effect of dopants on thermal stability.

Fig. 4.13a displays the thermal analysis (TG/DTA) plot for pure MnO_2. Two major weight losses can be seen with corresponding endothermic peaks in DTA curve. The first weight loss in the temperature range of 580-670 °C is due to the loss of oxygen and conversion of MnO_2 to Mn_2O_3 phase [37]. The second weight loss at 950-1000 °C corresponds to decomposition of Mn_2O_3 phase to Mn_3O_4 [127] with loss of oxygen. This also confirms that the prepared manganese oxide samples which are calcined at 400 °C are forming MnO_2 phase.

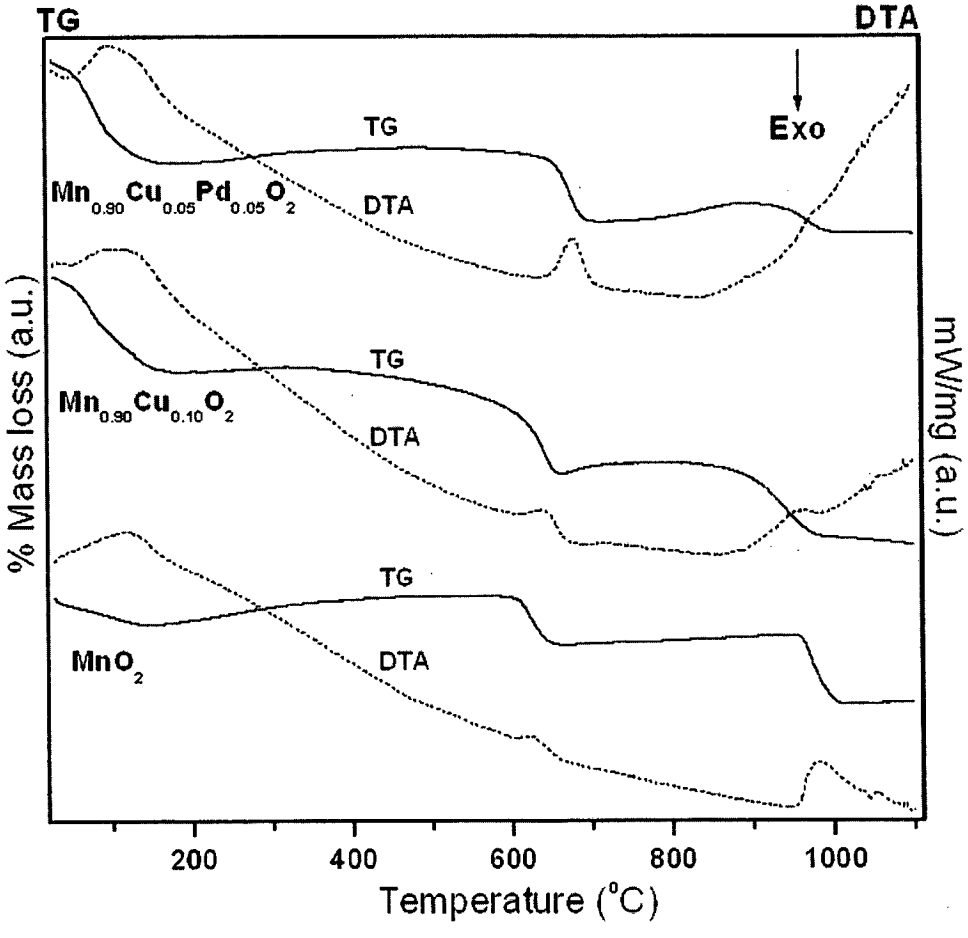

Fig. 4.13 Thermal analysis (TG/DTA) pattern for MnO_2, $Mn_{0.90}Cu_{0.10}O_2$ and $Mn_{0.90}Cu_{0.05}Pd_{0.05}O_2$.

Similar behavior is shown by Cu-Pd doped MnO_2 samples (Fig. 4.13b and c). In case of $Mn_{0.90}Cu_{0.10}O_2$ (Fig. 4.13b), the material converts to Mn_2O_3 phase in the temperature range 590-700 °C which shows increase of the thermal stability after incorporation of Cu in

lattice of MnO_2. After incorporation of Cu-Pd, as in $Mn_{0.90}Cu_{0.05}Pd_{0.05}O_2$ sample (Fig. 4.13c) the conversion to Mn_2O_3 phase was observed at 630-720 °C, which showed further increase in thermal stability [228]. Thus introduction of small amount of Cu and Pd into the crystal lattice of MnO_2 results in a remarkable increase of the thermal stability, preventing release of oxygen and reduction of Mn ions.

The TG/DTA pattern for $Mn_{0.95}Ni_{0.05}O_2$ is shown in Fig. 4.14. Thermal study shows initial weight loss below 200 °C due to loss of adsorbed water [101]. The weight loss in 600–690 °C regions with an endothermic peak is due to the loss of oxygen and this weight loss is generally considered to be due to the conversion of MnO_2 to Mn_2O_3 phase [131]. Further weight loss in the temperature range 920–1000 °C with an small endotherm is considered due to the conversion of Mn_2O_3 to Mn_3O_4 phase [127].

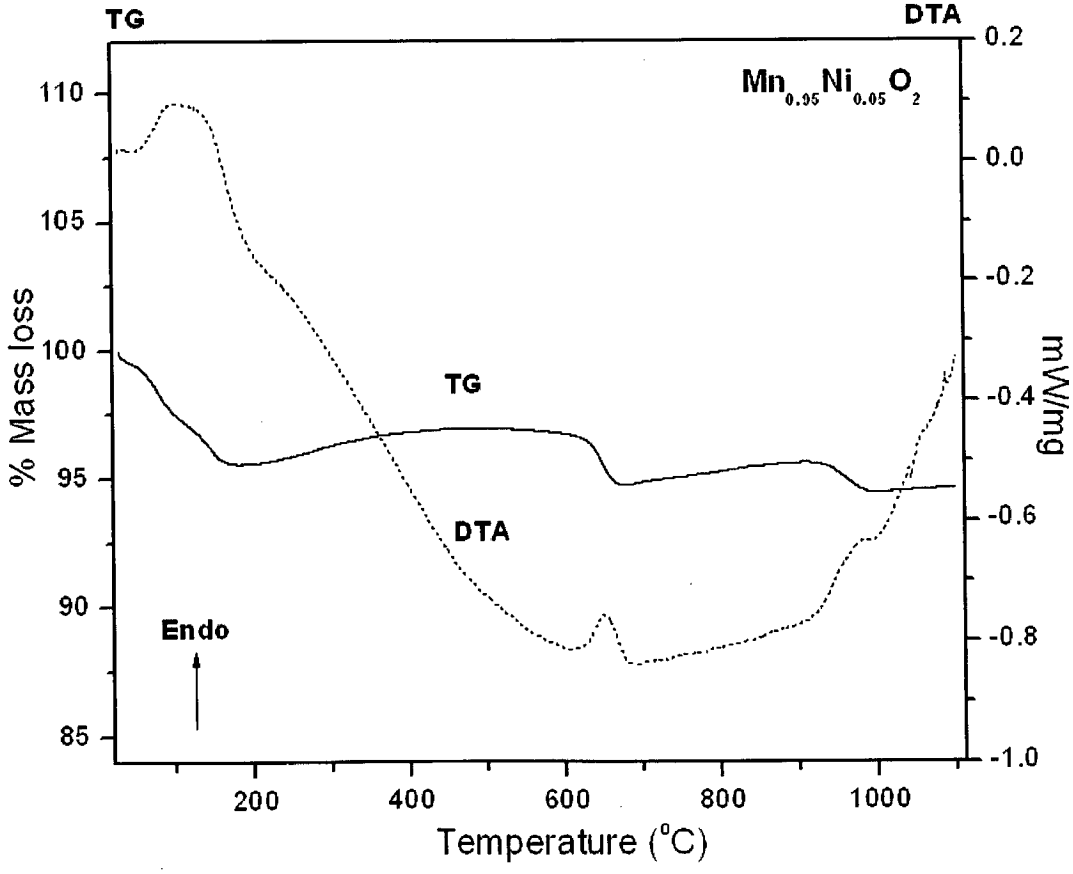

Fig. 4.14 Thermal analysis (TG/DTA) pattern for $Mn_{0.95}Ni_{0.05}O_2$.

Similar behaviour has been exhibited by other Ni doped samples. It is seen that MnO_2 phase is thermally stable up to temperature of around 530 °C, above this temperature it changes to Mn_2O_3 phase. Thus manganese oxide shows change in phase with respect to increasing temperature.

Fig. 4.15 illustrates the TG/DTA pattern for $Mn_{0.92}Pd_{0.08}O_2$. It shows similar behavior like MnO_2. The conversion of MnO_2 phase to Mn_2O_3 phase was seen in range 630-730 °C with an endothermic peak which further change to Mn_3O_4 phase in range 890-1000 °C. Similar type of behavior was shown by other Pd doped samples.

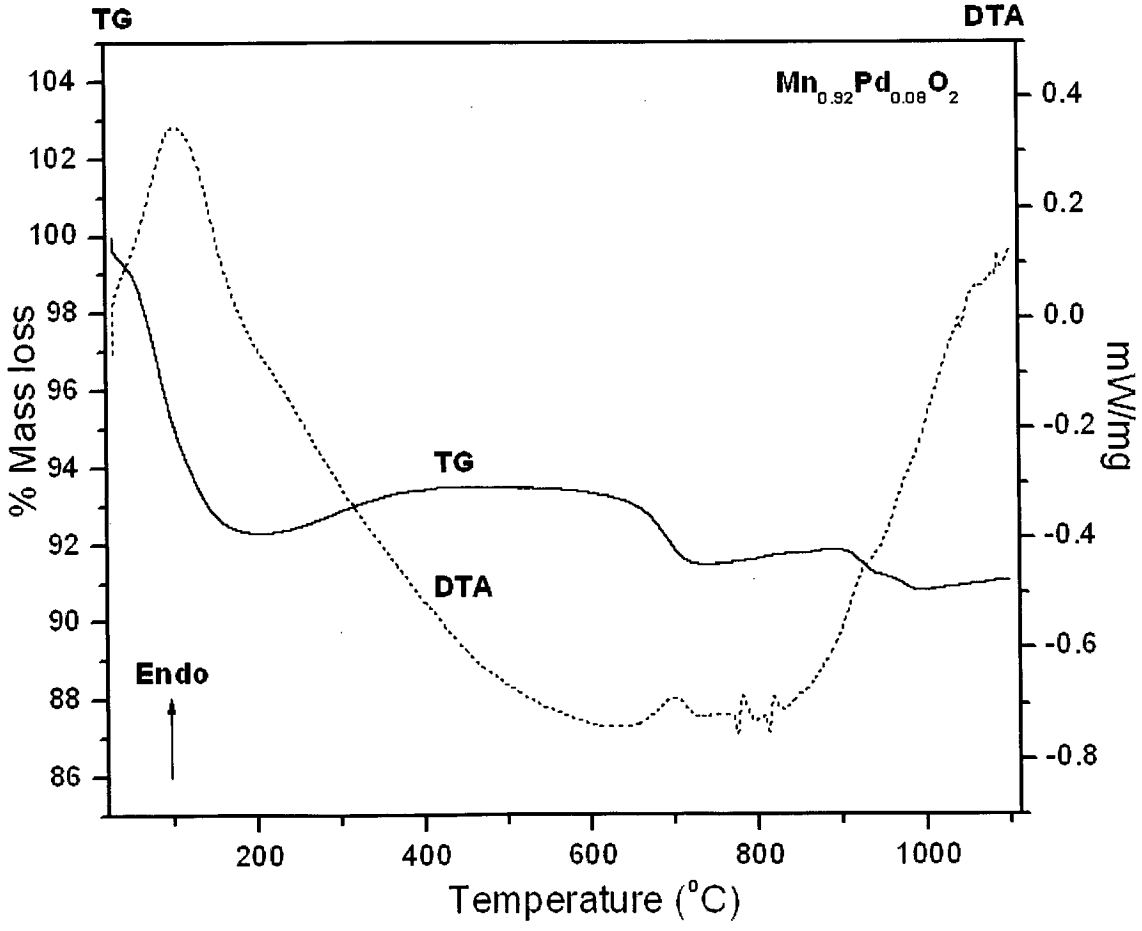

Fig. 4.15. Thermal analysis (TG/DTA) pattern for $Mn_{0.92}Pd_{0.08}O_2$.

Fig. 4.16 shows TG/DTA patterns for Rh doped MnO_2 catalysts. All the samples showed similar patterns. The conversion of MnO_2 to Mn_2O_3 phase was observed with

corresponding endothermic peak in the temperature range 600-720 °C which is due to the loss of oxygen, further Mn_2O_3 phase converts to Mn_3O_4 phase in the temperature range 930-1020 °C.

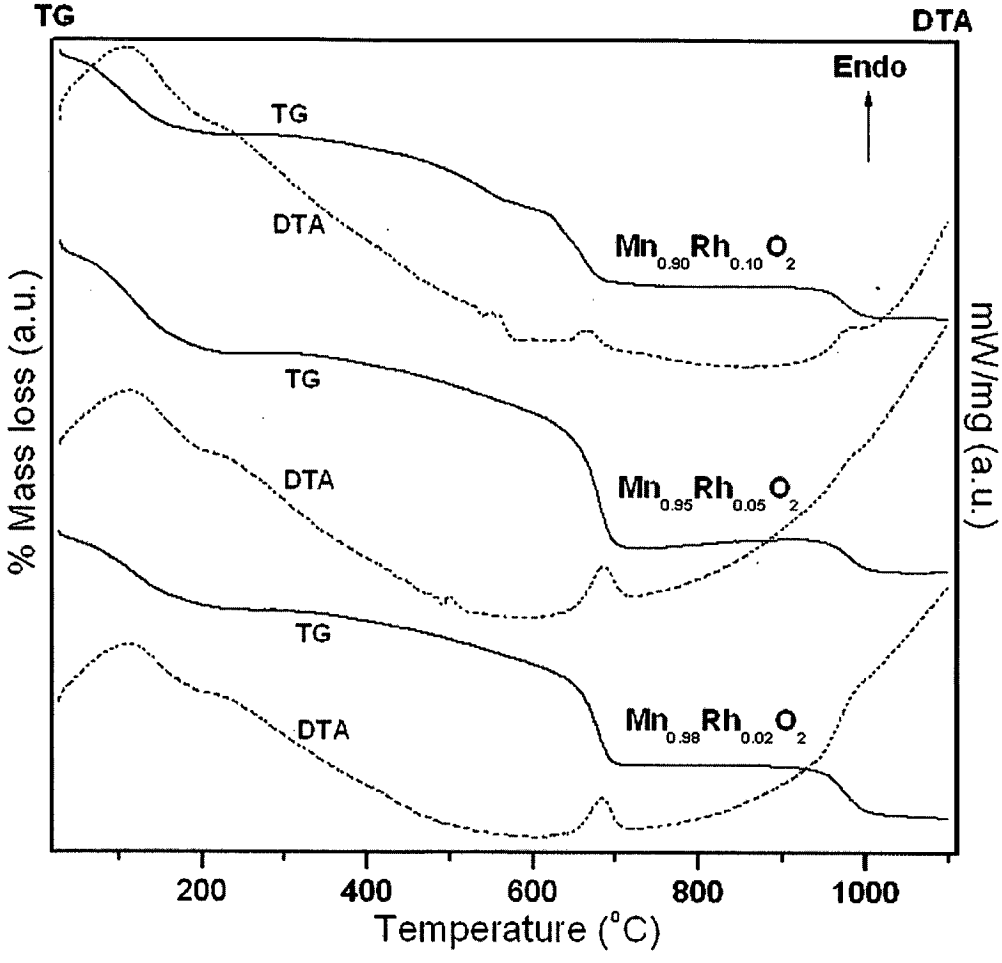

Fig. 4.16 Thermal analysis (TG/DTA) pattern for $Mn_{0.98}Rh_{0.02}O_2$, $Mn_{0.95}Rh_{0.05}O_2$ and $Mn_{0.90}Rh_{0.10}O_2$.

In case of Ag doped MnO_2 catalysts the TG/DTA patterns for $Mn_{0.98}Ag_{0.02}O_2$ and $Mn_{0.85}Ag_{0.15}O_2$ are shown in Fig. 4.17. In case of $Mn_{0.98}Ag_{0.02}O_2$, the decomposition to Mn_2O_3 phase was seen in the range around 530-640 °C with the loss of oxygen along with corresponding endotherm in DTA. Mn_2O_3 phase further converts to Mn_3O_4 phase in 950-1020 °C with an endothermic peak [127]. $Mn_{0.85}Ag_{0.15}O_2$ catalyst converts to Mn_2O_3 in the temperature range of 660-740 °C and further to Mn_3O_4 in the range around 940-1020 °C.

Conversion of MnO_2 to Mn_2O_3 phase was observed at higher temperature in case of $Mn_{0.85}Ag_{0.15}O_2$ catalyst as compared to $Mn_{0.98}Ag_{0.02}O_2$, which shows increase of thermal stability towards decomposition [228]. Thus introducing small amount of Ag in the crystal lattice of MnO_2 shows increase in thermal stability preventing oxygen release.

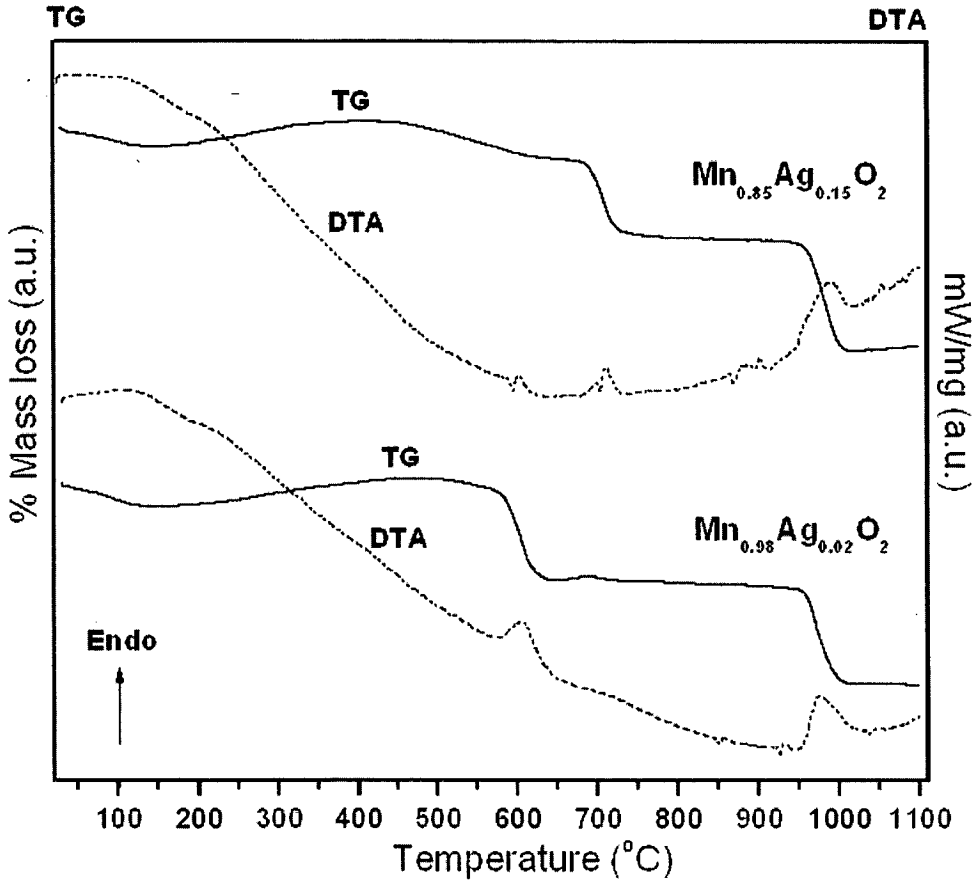

Fig. 4.17 Thermal analysis (TG/DTA) pattern for $Mn_{0.98}Ag_{0.02}O_2$ and $Mn_{0.85}Ag_{0.15}O_2$.

Fig. 4.18 shows the thermal analysis study of Ag doped Mn_2O_3 catalysts along with pure Mn_2O_3. The Mn_2O_3 shows only one major weight loss as can be seen in the temperature range 960-1020 °C along with the corresponding endothermic peak, this weight loss is due to the phase transformation to Mn_3O_4 [33]. All the Ag doped catalysts also showed similar pattern. From this data it can also confirmed that the phase formed is pure Mn_2O_3, no other phase of manganese oxide is seen. Thus it shows that after calcining the manganese oxide samples at 700 °C, there is a formation of Mn_2O_3 phase.

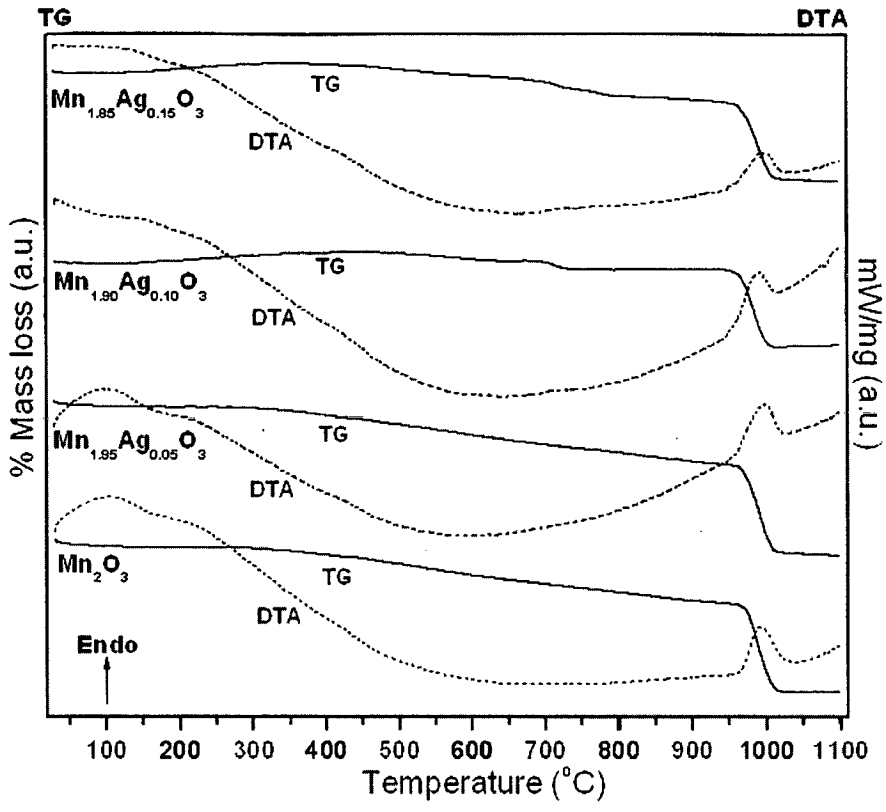

Fig. 4.18 Thermal analysis (TG/DTA) pattern for Mn_2O_3, $Mn_{1.95}Ag_{0.05}O_3$, $Mn_{1.90}Ag_{0.10}O_3$ and $Mn_{1.85}Ag_{0.15}O_3$.

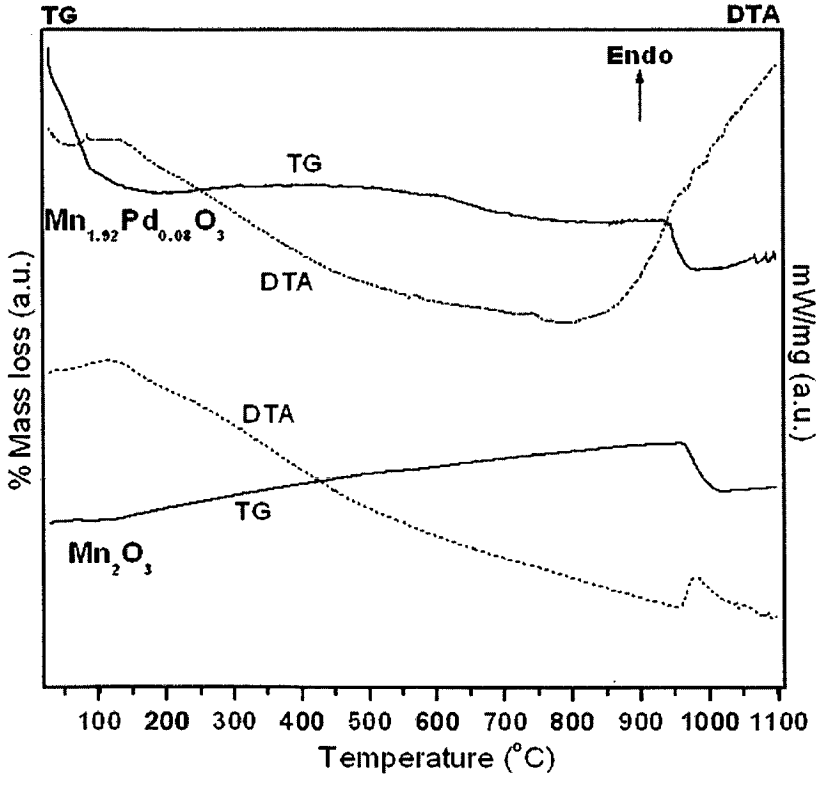

Fig. 4.19 Thermal analysis (TG/DTA) pattern for Mn_2O_3 and $Mn_{1.92}Pd_{0.08}O_3$.

The thermal analysis data for Pd doped Mn_2O_3 is shown in Fig. 4.19. Thermal study of Mn_2O_3 shows the major weight loss in 960-1020 °C region (Fig. 4.19) with an endothermic peak, this weight loss is due to the loss of oxygen and conversion of the phase from Mn_2O_3 to Mn_3O_4 [33]. In case of $Mn_{0.92}Pd_{0.08}O_3$ the material converts to Mn_3O_4 in the temperature range 935-980 °C which is at lower temperature as compared to Mn_2O_3 catalyst as seen in Fig. 4.19. This illustrates the poor stability of Pd doped samples, a decrease of thermal stability is observed with the introduction of small fraction of Palladium into the crystal lattice of Mn_2O_3 [228].

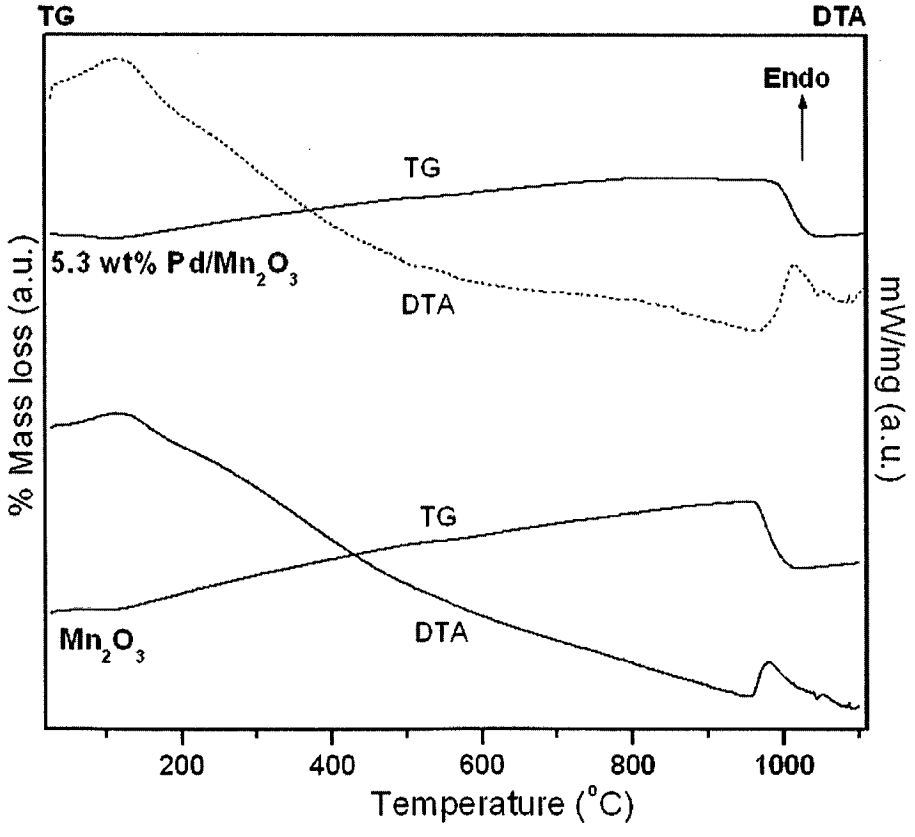

Fig. 4.20 Thermal analysis (TG/DTA) pattern for Mn_2O_3 and 5.3 wt% Pd/Mn_2O_3.

The Fig. 4.20 illustrates the TG/DTA pattern for Pd/Mn_2O_3 sample. In case of 5.3 wt% Pd/Mn_2O_3 sample, the phase transformation of Mn_2O_3 to Mn_3O_4 is observed in the region 970-1030 °C (Fig. 4.20) with an endothermic peak which is more or less similar to pristine Mn_2O_3. The TG/DTA results also indicate that the prepared samples are of pure Mn_2O_3

phase [127], since no weight loss is seen in the region 550-650 °C which generally corresponds to the transformation of MnO_2 to Mn_2O_3 phase.

The TG/DTA study for rhodium supported catalysts shows some interesting behavior as illustrated in Fig. 4.21. All the rhodium supported MnO_2 catalysts showed two major weight losses with corresponding endothermic peaks which are similar to that of MnO_2. The phase transformation of MnO_2 to Mn_2O_3 was found to be shifting towards higher temperature with increasing Rh loadings as can be seen in Fig. 4.21. After incorporation of Rh over MnO_2, increase in thermal stability was observed for the conversion of MnO_2 to Mn_2O_3 phase. The thermal stability may be observed due to the interactions of supported Rh with MnO_2 support [228].

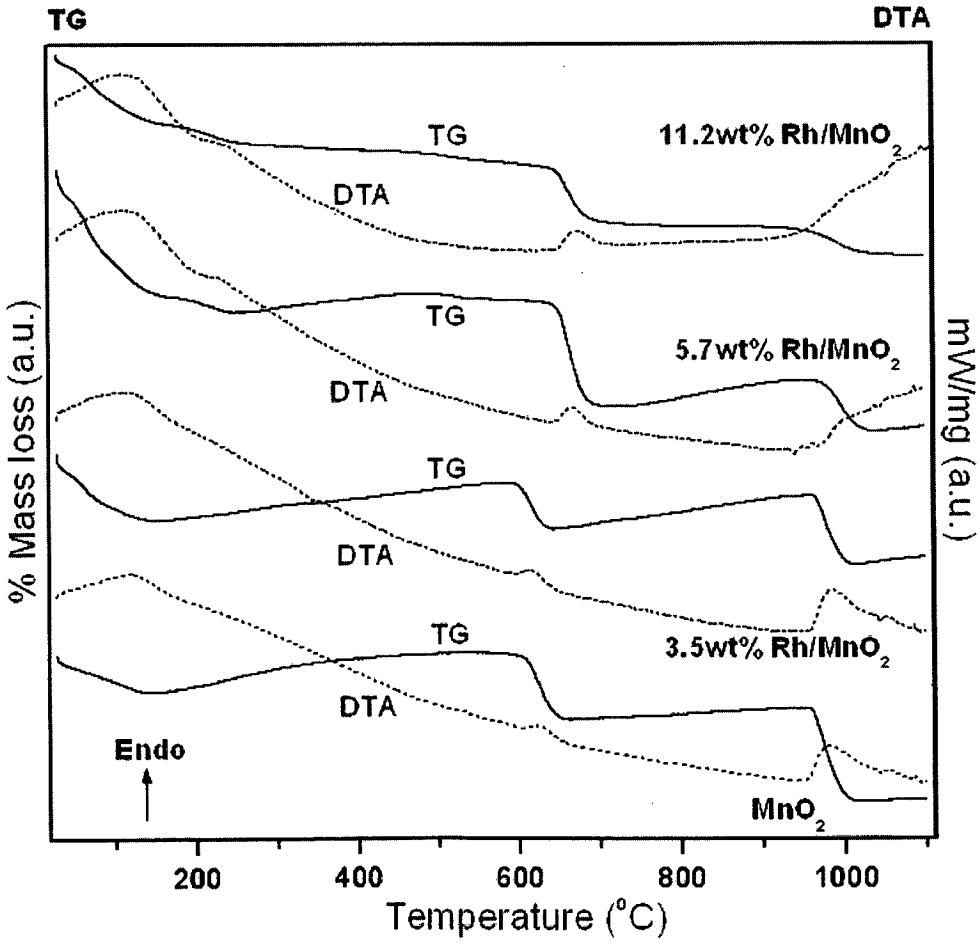

Fig. 4.21 Thermal analysis (TG/DTA) pattern for MnO_2, 3.5 wt% Rh/MnO_2, 5.7 wt% Rh/MnO_2 and 11.2 wt% Rh/MnO_2.

Thus, from TG/DTA pattern one can get information about the different phases of manganese oxides. Since manganese oxides can have variable oxidation states, they can form different oxides. MnO_2 phase is stable up to a temperature of around 550 °C [131,37], above that temperature it converts to Mn_2O_3 phase [127]. Mn_2O_3 phase is stable up to a temperature of 1000 °C and it transforms to Mn_3O_4 with increase in temperature [33]. Mn_3O_4 phase further converts to MnO at temperature above 700 °C [33]. From this data one can get information about the calcination temperature to obtain particular phase of manganese oxide. Also one can confirm the formation of particular phase. Also the effect of dopants can be observed which shows some thermal stability towards phase transformation temperature. The information regarding the presence of impurity can also be obtained with this data.

4.3 FTIR spectroscopy

The FTIR spectra of the prepared samples were recorded. The IR spectra give characteristic metal-oxygen vibrations which are important for the structural characterization of the metal oxides. Manganese oxides show characteristic modes of vibrations which is useful for the characterization of their different phases. Incorporation of dopants into the lattice of manganese oxide shows some structural modifications which can be studied by monitoring the IR spectra.

The FTIR spectra of undoped MnO_2 along with $Mn_{0.95}Ni_{0.05}O_2$ and $Mn_{0.85}Ni_{0.15}O_2$ are presented in Fig. 4.22. The MnO_2 shows IR bands at 520 and 608 cm^{-1} [229]. The IR band observed at 575 cm^{-1} is due to Mn–O vibration and at 435 and 455 cm^{-1} are due to O–Mn–O vibrations [230]. All these bands are characteristic of MnO_2 and are also prominent in

Ni doped samples. The intensity of bands at 520 and 455 cm^{-1} to some extent increases in Ni doped MnO_2 samples, which may be due to the overlap of Ni–O vibrations [231].

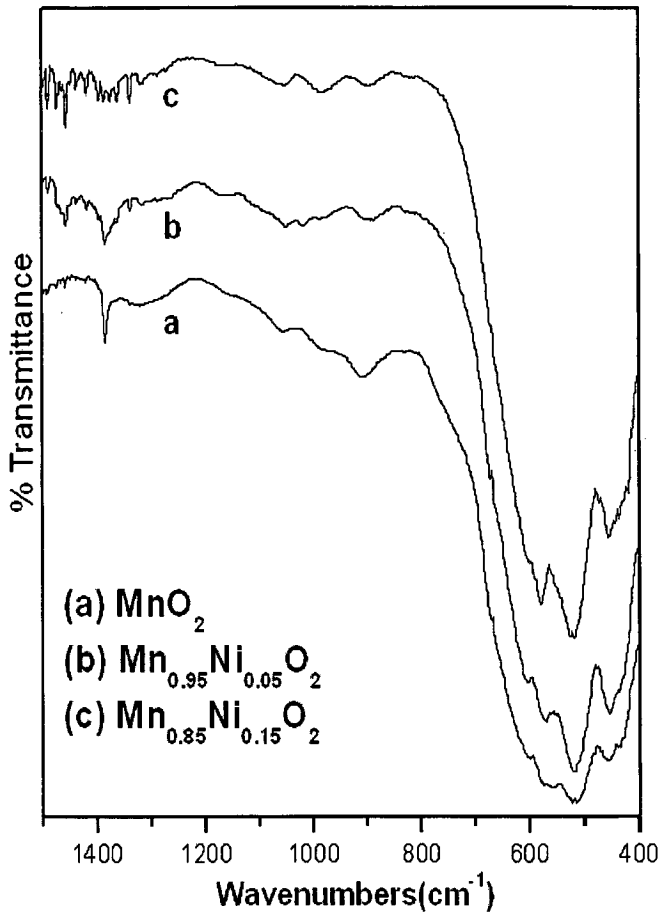

Fig. 4.22 Shows the FTIR spectra of Ni doped MnO_2 series.

Fig. 4.23 shows the FTIR spectra of MnO_2 (a), $Mn_{0.95}Pd_{0.05}O_2$ (b) and $Mn_{0.92}Pd_{0.08}O_2$ (c) samples. The samples were characterized by IR spectra in the region 1500–400 cm^{-1}. At ~ 910, 605 and 520 cm^{-1} characteristic vibration modes are seen of MnO_2 [229], these vibrations are also prominent in Pd doped samples. In case of doped samples the bands were found to shift towards higher frequency to a small extent, this is due to the incorporation of Pd in MnO_2 lattice. IR bands at ~ 570, 455 and 435 cm^{-1} corresponding to Mn–O and O–Mn–O vibrations [230] are prominent in MnO_2, but whose intensity was found to be decreasing in $Mn_{0.95}Pd_{0.05}O_2$ and $Mn_{0.92}Pd_{0.08}O_2$ indicating the effect of Pd doping. A small band at ~ 665 cm^{-1} starts appearing with increasing concentration of Pd in

MnO_2, but in pristine MnO_2 this peak is not seen, also the intensity of peak at ~ 605 cm^{-1} goes on increasing with Pd content both this peaks are the characteristic vibrations of PdO [232].

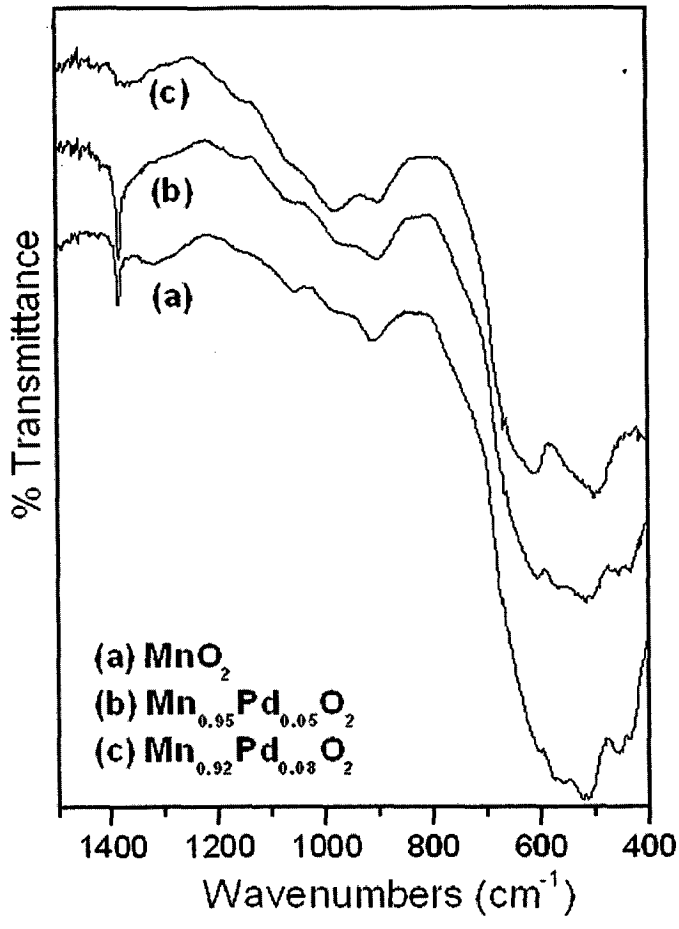

Fig. 4.23 Shows the FTIR spectra of Pd doped MnO_2 series.

The FTIR spectra for Ag doped MnO_2 samples are shown in Fig 4.24. IR spectra for undoped MnO_2 along with $Mn_{0.95}Ag_{0.05}O_2$, $Mn_{0.90}Ag_{0.10}O_2$ and $Mn_{0.85}Ag_{0.15}O_2$ are presented. The MnO_2 shows characteristic broad bands at ~528 and 630 cm^{-1}, these bands are attributed to the antisymmetry stretching mode of MnO_6 octahedra [230,97]. These bands are also prominent in Ag doped MnO_2 catalysts indicating that MnO_2 phase is stable after doping. It is observed that with increase in Ag concentration in MnO_2 the intensity of these bands shifted towards higher frequency values which can be seen at ~506 and 612 cm^{-1} due to the incorporation of Ag in MnO_2 lattice.

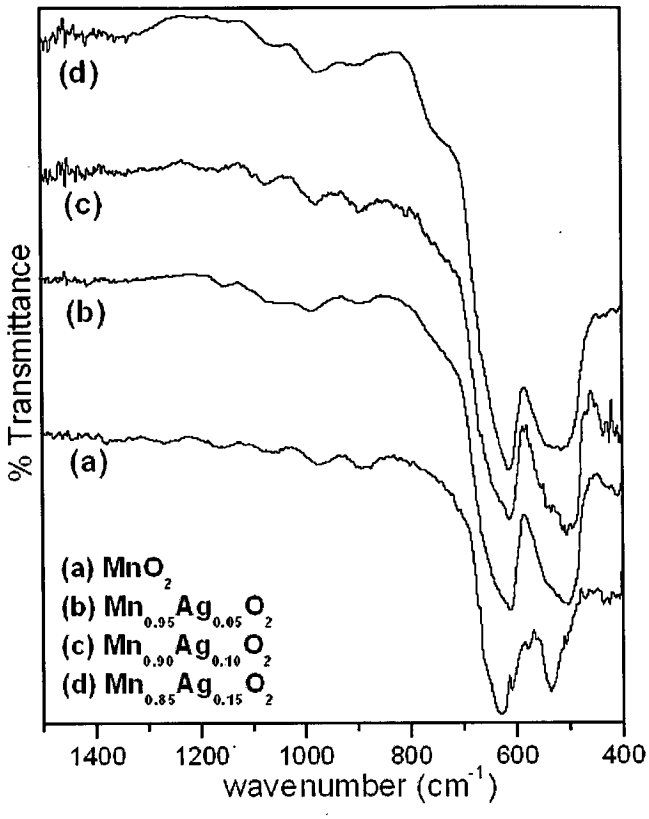

Fig. 4.24 Illustrates the FTIR spectra of Ag doped MnO_2 series.

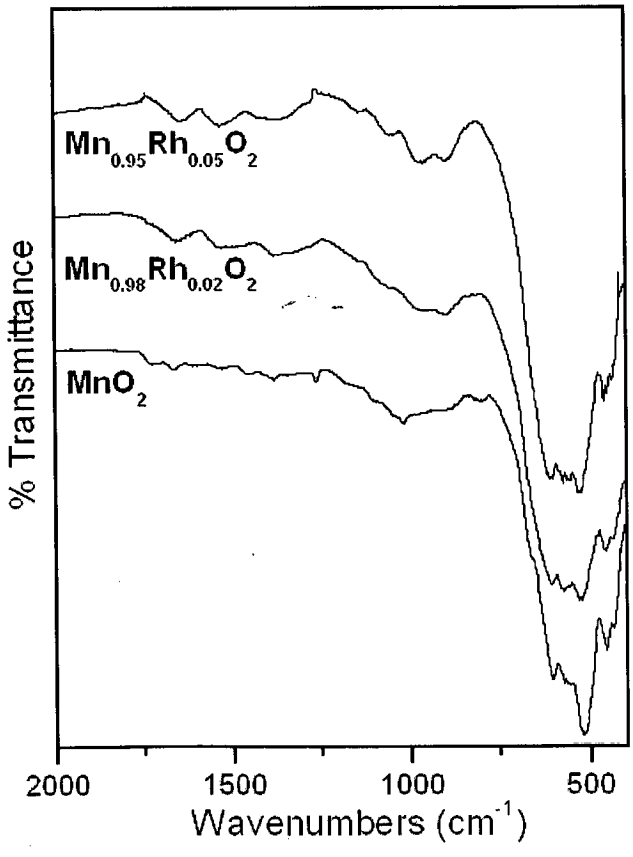

Fig. 4.25 Illustrates the FTIR spectra of doped Rh doped MnO_2 series.

The characteristic IR vibrations of Rh doped MnO_2 catalysts are presented in Fig. 4.25. The figure shows the FTIR spectra of MnO_2, $Mn_{0.98}Rh_{0.02}O_2$ and $Mn_{0.95}Rh_{0.05}O_2$ catalysts. The MnO_2 shows the prominent bands at 520 and 607 cm^{-1}, which are characteristic vibrations of manganese dioxide [74,229]. These bands are also seen in Rh doped samples which show the structural features of MnO_2. The bands at 455 and 435 cm^{-1} corresponding to O–Mn–O vibrations of MnO_2 and at 574 cm^{-1} is due to Mn–O vibration of MnO_2, these IR bands are also prominent in Rh doped samples.

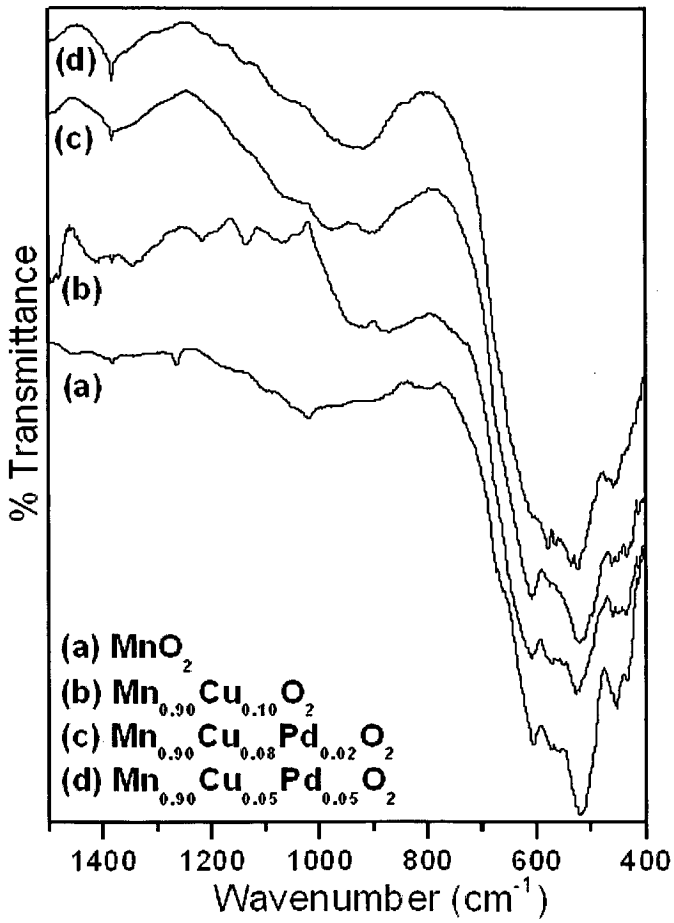

Fig. 4.26 Illustrates the FTIR spectra of CuPd doped MnO_2 series.

The Fig. 4.26 shows the IR spectra of CuPd doped MnO_2 catalysts. Several vibrational modes which are characteristic of MnO_2 are observed. Two strong bands are observed at 520 and 608 cm^{-1} in MnO_2 [229]. These bands are also seen in CuPd doped samples, but their intensity was found to be decreasing with increase of CuPd concentration in MnO_2.

The IR band at around 575 cm^{-1} is due to Mn–O vibration [230] of MnO_2 and is seen in all the samples. The bands at 454 and 435 cm^{-1} are seen in MnO_2 which correspond to O–Mn–O vibrations of MnO_2, their intensity was found to be decreasing in doped samples and almost disappears in $Mn_{0.90}Cu_{0.05}Pd_{0.05}O_2$.

The FTIR spectra for Ni-Mn_2O_3 series is shown in Fig. 4.27. The peaks at ~ 665 and 575 cm^{-1} attributed to Mn–O stretching vibration of Mn_2O_3 [233] which are also prominent in Ni doped samples, peak at ~ 528 cm^{-1} attributed to Mn–O bending vibration of Mn_2O_3 [100]. The peaks at ~ 945 and 970 cm^{-1} were seen in Mn_2O_3 sample but whose intensity was found to be decreasing with Ni doping. Two peaks at ~ 880 and 418 cm^{-1} starts appearing with increasing concentration of Ni which are absent in the pristine Mn_2O_3 sample.

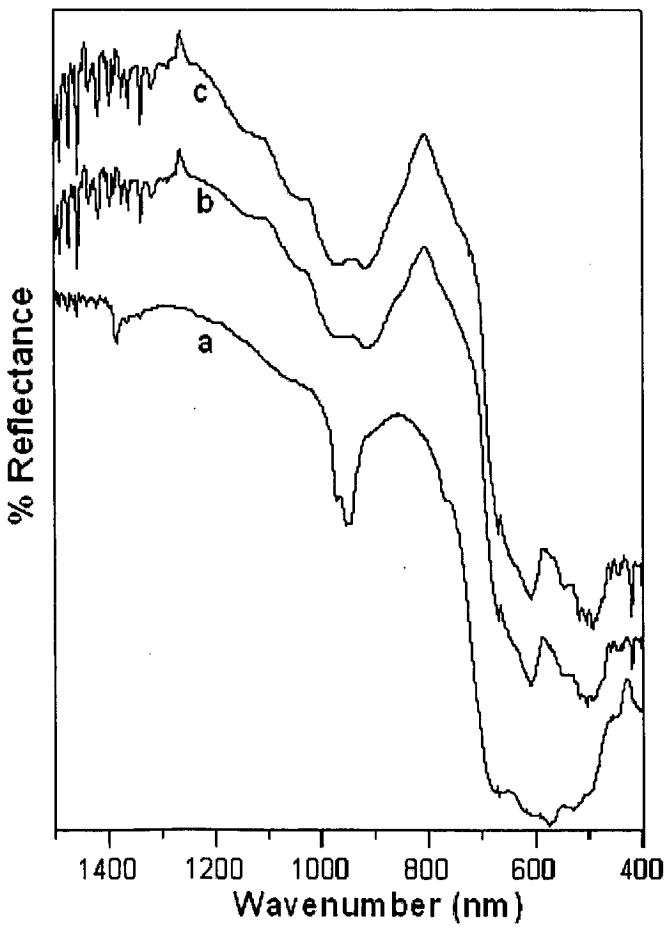

Fig. 4.27 Shows the FTIR spectra of Ni doped Mn_2O_3 series.

The Fig. 4.28 shows the FTIR spectra of Ce doped Mn_2O_3 catalysts. The band at ~ 665 cm^{-1} is attributed to Mn–O stretching vibration of Mn_2O_3 [233] which is also prominent in Ce doped Mn_2O_3 samples, band at ~ 528 cm^{-1} is attributed to Mn–O bending vibration of Mn_2O_3 [100]. The vibrations at ~ 950 and 970 cm^{-1} are seen in Mn_2O_3 sample but their intensity was found to be decreasing with cerium doping. The bands at ~ 910, 605 and 420 cm^{-1} starts appearing with increasing concentration of Ce which are absent in pure Mn_2O_3 sample.

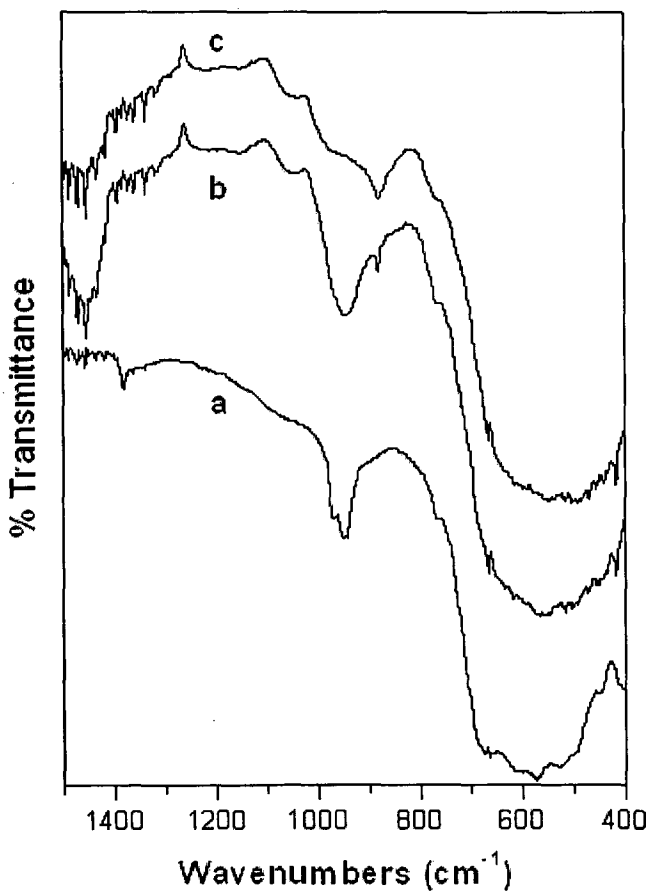

Fig. 4.28 Shows the FTIR spectra of Ce doped Mn_2O_3 series.

The FTIR spectra of Ag doped Mn_2O_3 catalysts are shown in Fig. 4.29. Several vibration modes can be seen at 673, 608, 574, 530, 453 cm^{-1} which are characteristic of Mn_2O_3 material [74]. The bands at around 673 and 574 cm^{-1} [100] are attributed to Mn–O stretching vibrations of Mn_2O_3 and the one at 530 cm^{-1} is due to Mn–O bending vibrations

of Mn_2O_3. All the vibrations are also seen in Ag doped Mn_2O_3 samples indicating that the crystal structure of Mn_2O_3 is retained after doping. These bands are found to be shifted in frequency to some extent which is due to the effect of Ag doping in the lattice structure of Mn_2O_3.

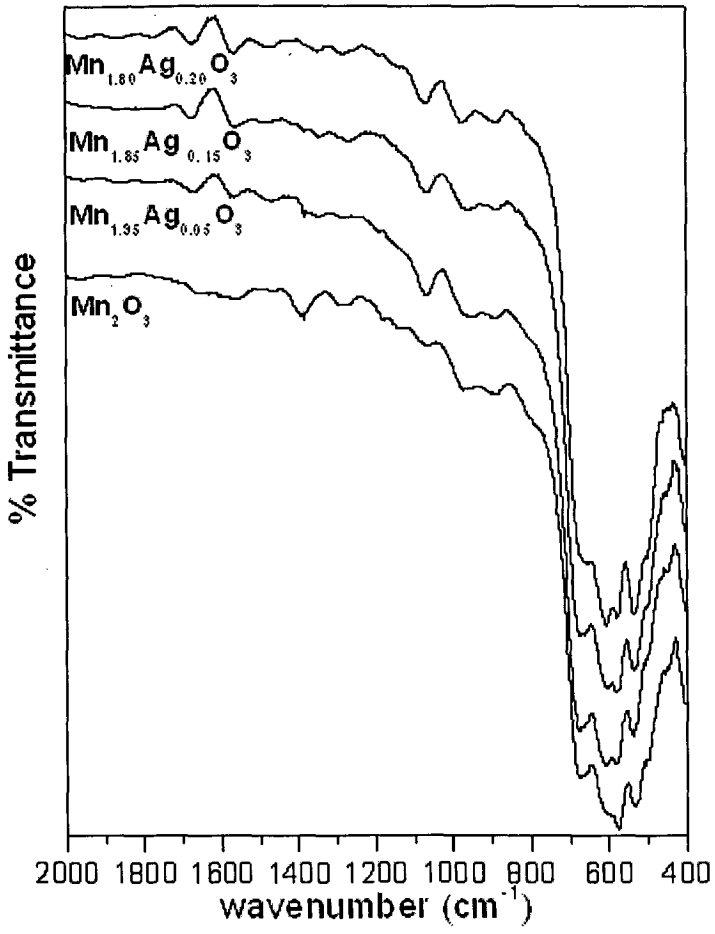

Fig. 4.29 Shows the FTIR spectra of Ag doped Mn_2O_3 series.

4.4 Electrical resistivity measurements

Temperature variation of electrical resistivity from room temperature to 400 °C of all the doped samples was measured in conductivity unit cell by two probe method in air. Samples in the form of pallet of 0.5 cm radius and 0.15 cm thickness were used. Pallets were prepared by compressing 0.4 g of sample with hydraulic press at 5 ton of pressure,

and sintered at 400 °C for 72 h. Pallets were heated at 150 °C for 2 h in an oven prior to measurements and kept in desiccator.

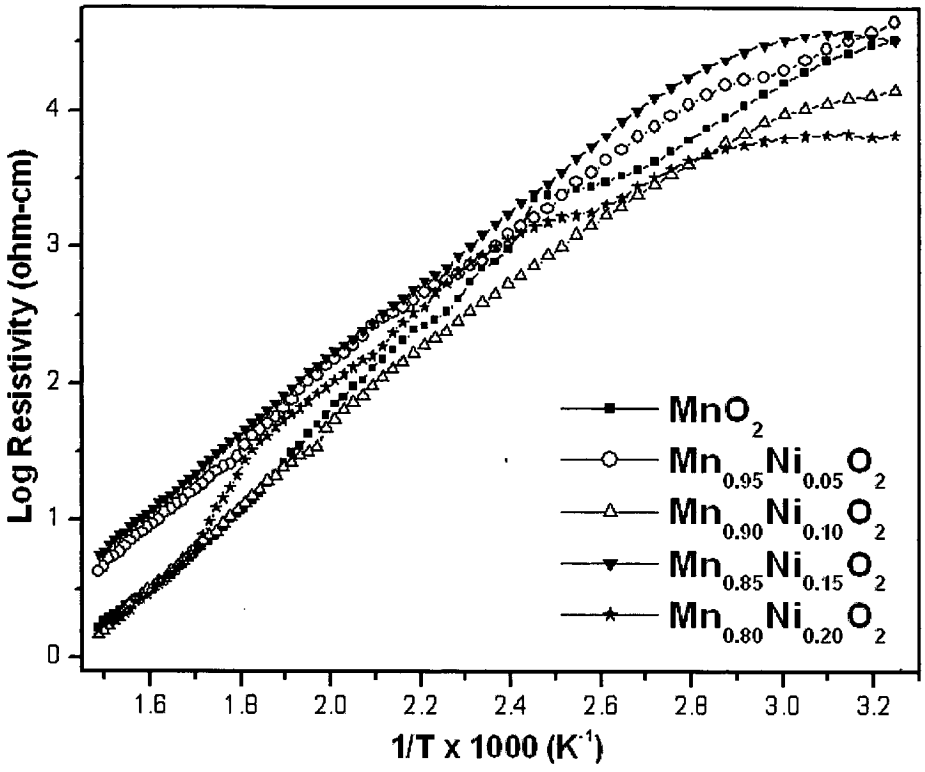

Fig. 4.30 Electrical resistivity plot for Ni-MnO_2 series.

From Fig. 4.30 it can be seen that the conductance of all the samples increases with increasing temperature and exhibits semiconducting behavior [234]. Pristine MnO_2 was found to be a good semiconductor, and after doping with the Ni it retains the same behavior. It should be noted that Ni doped MnO_2 remain unchanged at 400 °C, which is confirmed by TG/DTA studies.

Similar is the case with cerium doped manganese dioxide catalysts and the plot of electrical resistivity of the same is shown in Fig. 4.31. From the figure it is seen that the electrical resistivity of all samples decreased with increase of temperature indicating semiconducting nature of these materials [228]. Moreover, it is also observed that the Ce doped MnO_2 samples showed higher resistance compared to pure MnO_2.

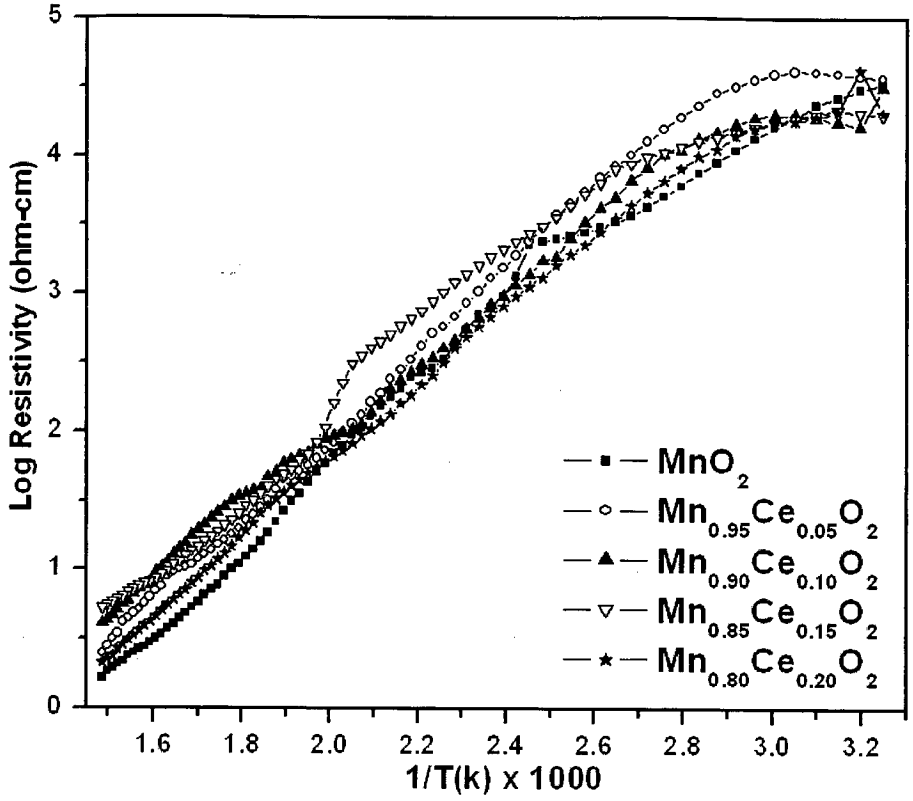

Fig. 4.31 Electrical resistivity plot for Ce-MnO_2 series.

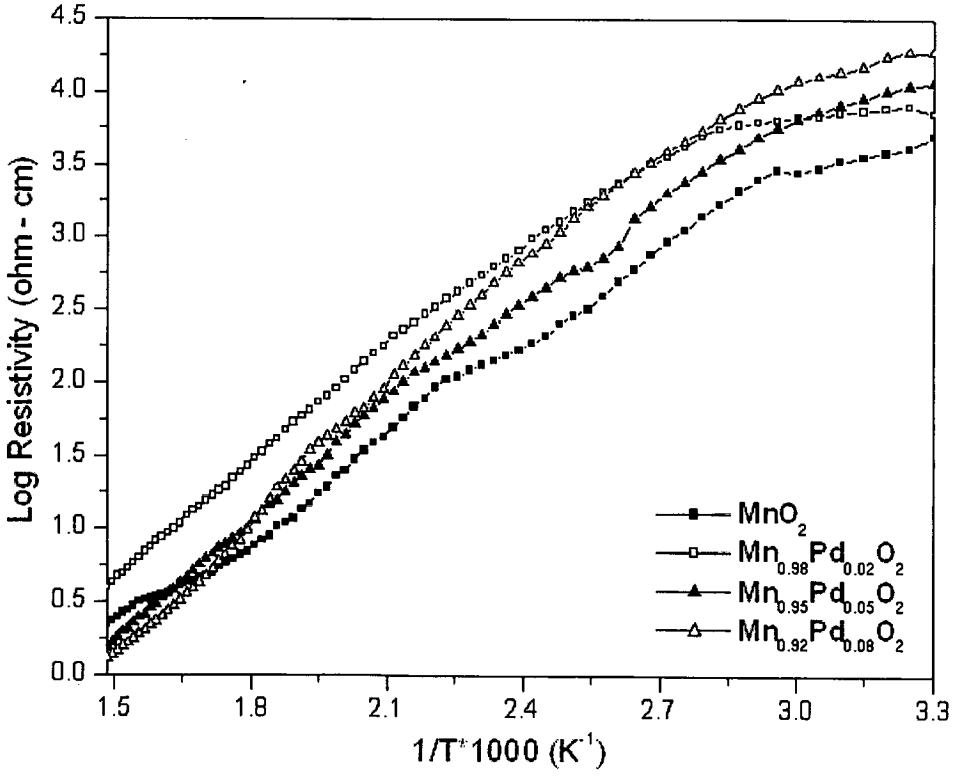

Fig. 4.32 Electrical resistivity plot for Pd-MnO_2 series.

The plot of resistivity versus temperature for palladium doped MnO_2 samples is presented in Fig. 4.32. The Electrical resistivity (ρ) for the Pd doped MnO_2 catalysts at various temperatures was measured using two probe method in temperature range from room temperature to 400 °C. The electrical conductivity goes on increasing with increase in temperature. Thus indicating that the samples are semiconducting in nature [116]. The undoped MnO_2 shows lesser resistivity as compared to Pd doped MnO_2, it can be considered from figure that with increasing Pd content resistivity of samples increase to a slight extent.

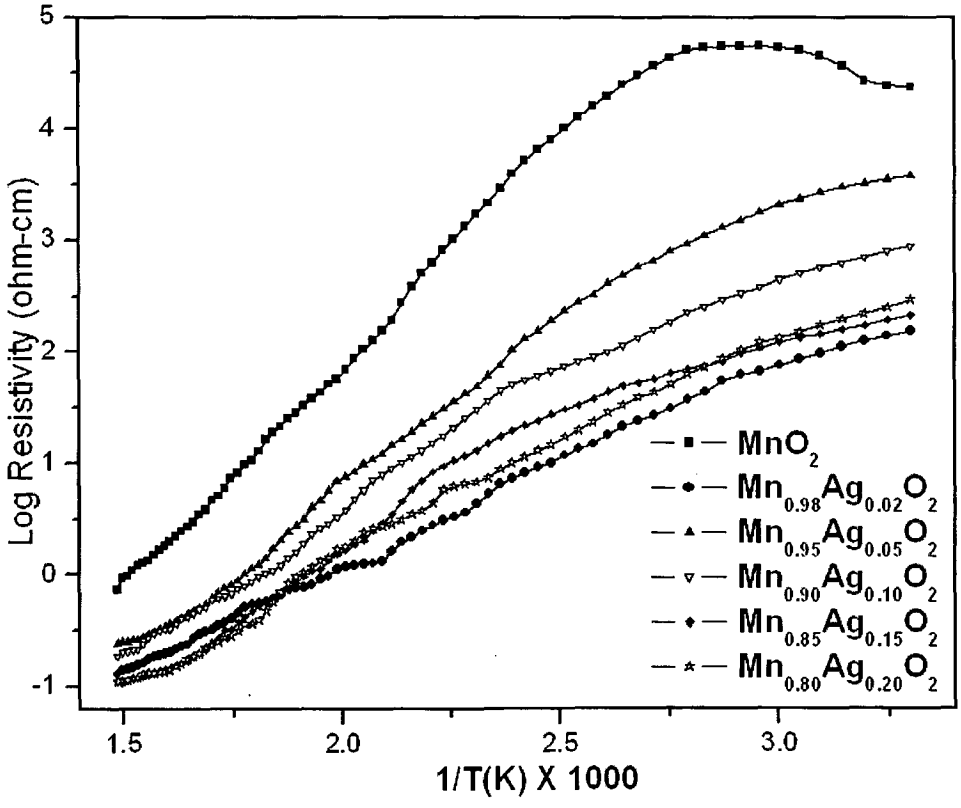

Fig. 4.33 Electrical resistivity plot for Ag-MnO_2 series.

The Electrical resistivity (ρ) for different Ag doped MnO_2 catalysts in temperature range from room temperature to 400 °C and the plot of resistivity versus temperature is presented in Fig. 4.33. The electrical conductivity goes on increasing with increase in temperature. Thus indicating that these samples are semiconducting in nature [116]. The

undoped MnO_2 shows higher resistivity as compared to Ag doped MnO_2, and with increasing Ag concentration in MnO_2 electrical conductivity goes on increasing. As Ag is good electrical conductor, due to the presence of silver into the lattice structure of MnO_2 there is enhancement in the conduction of electrons. Thus showing better conductivity after incorporation of Ag.

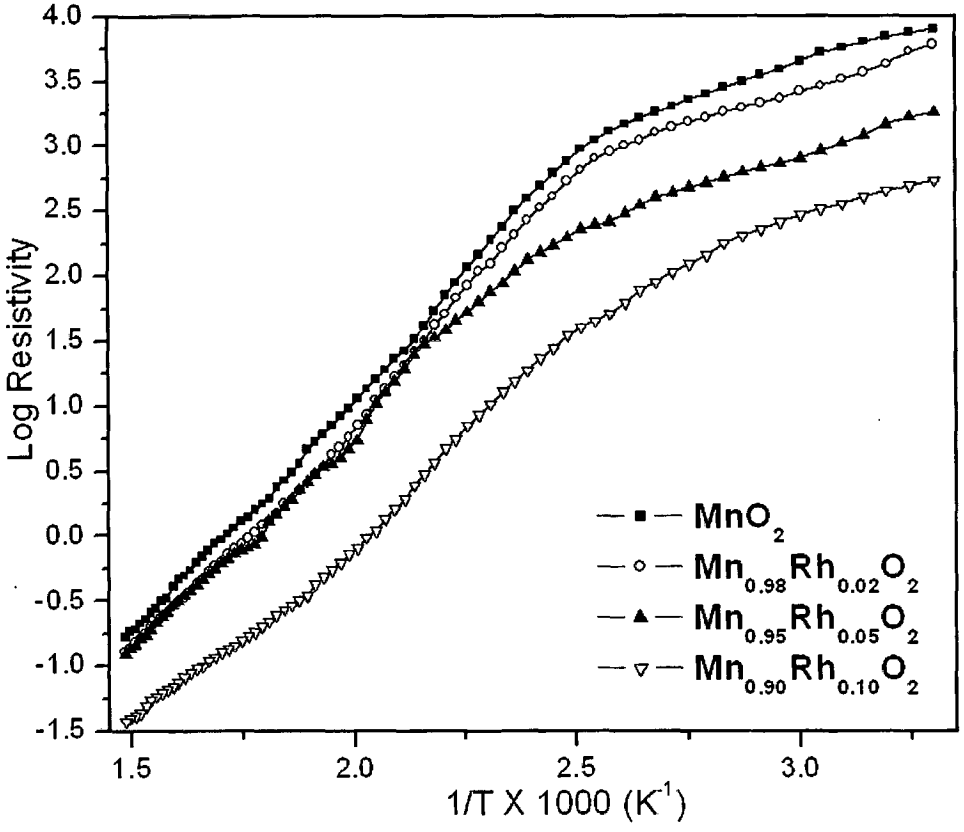

Fig. 4.34 Electrical resistivity plot for Rh-MnO_2 series.

Fig. 4.34 depicts the plot of log resistivity verses temperature for rhodium doped manganese dioxide series. The conductance of all the samples increased with increasing temperature and exhibits semiconducting behavior [229]. The figure also shows that pure MnO_2 shows more resistance as compared to Rh doped MnO_2 samples. The amounts of rhodium have especially significant impacts on the conductivity of MnO_2. In other words, the conductivity was correlated with the doping amount of rhodium. With increasing concentration of rhodium in MnO_2 a decrease in resistivity has been observed.

Incorporation of rhodium into the lattice of MnO_2 helps in fast movement of conducting electrons, thus increasing the conductivity.

The Fig. 4.35 shows the electrical resistivity verses temperature plot over Ni doped Mn_2O_3 catalysts. The Mn_2O_3 material is a good semiconducting material, with increasing temperature the resistivity of Mn_2O_3 goes on decreasing. After doping with Ni, the resistivity trend is similar to that of undoped Mn_2O_3. Thus the semiconducting behavior of Mn_2O_3 retains even after doping.

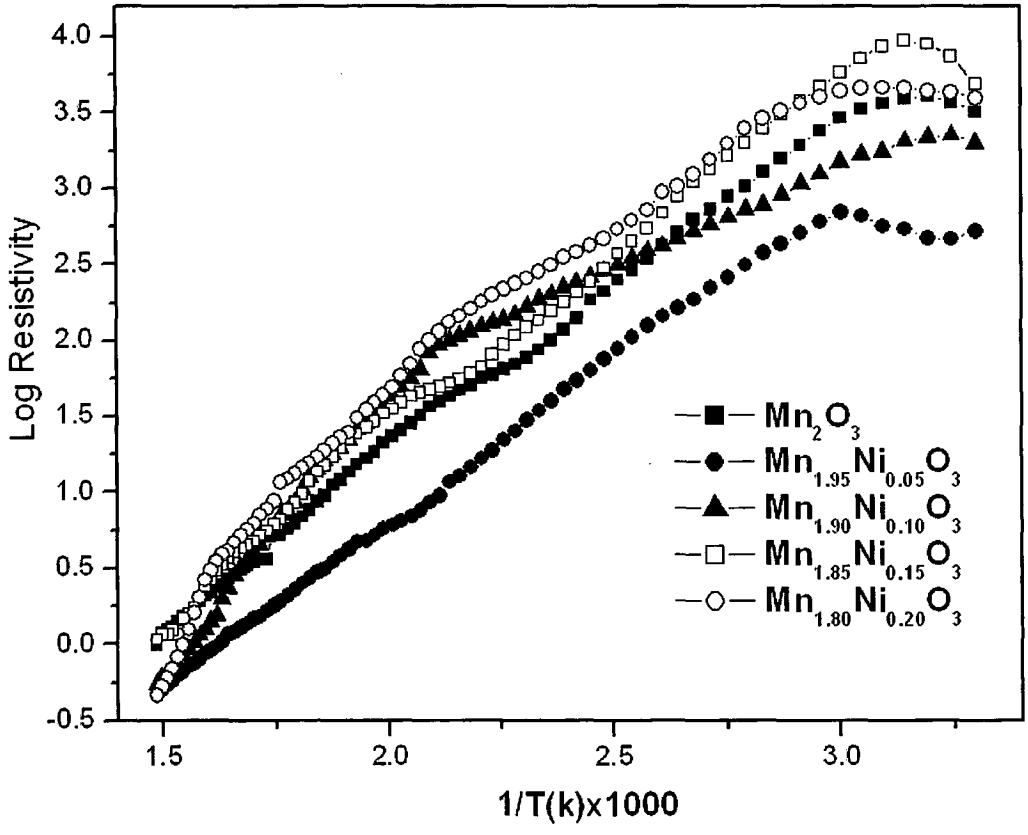

Fig. 4.35 Electrical resistivity plot for Ni-Mn_2O_3 series.

The Fig. 4.36 shows the plot of electrical resistivity verses temperature for Ag doped Mn_2O_3 catalysts in the temperature range from ambient to 400 °C. The dc electrical conductivity is found to be strongly dependent on temperature. It can be seen that conductance of both the pure Mn_2O_3 and Ag doped Mn_2O_3 increases with increasing temperature, and exhibits semiconductor behavior.

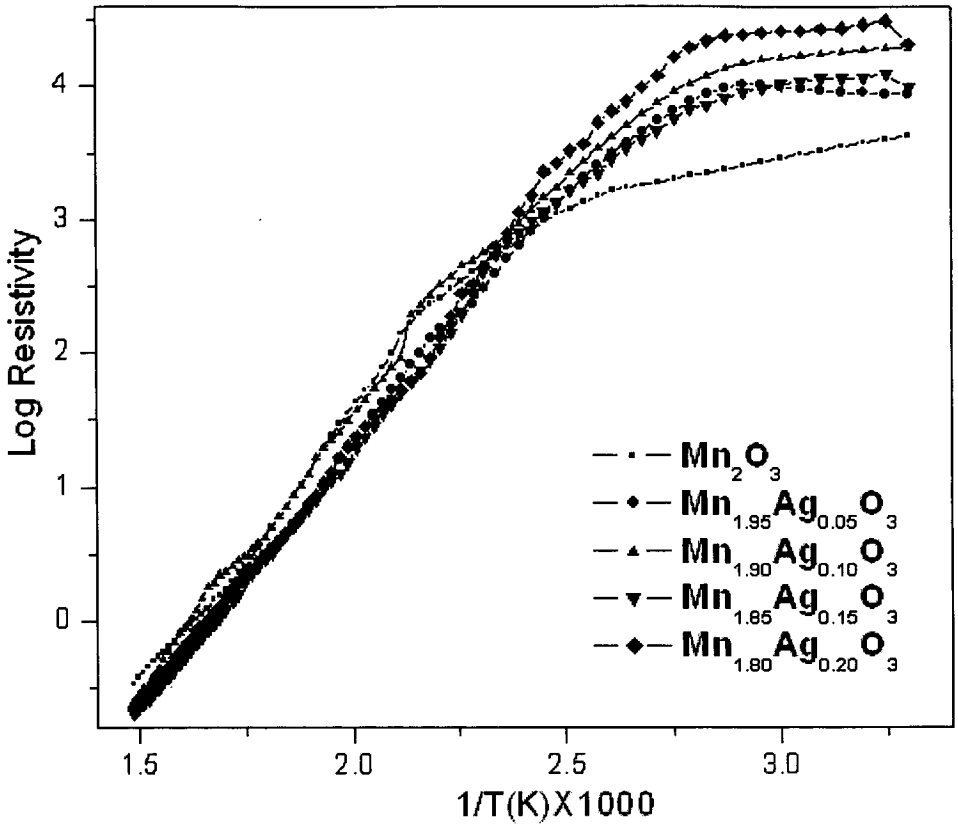

Fig. 4.36 Electrical resistivity plot for Ag-Mn_2O_3 series.

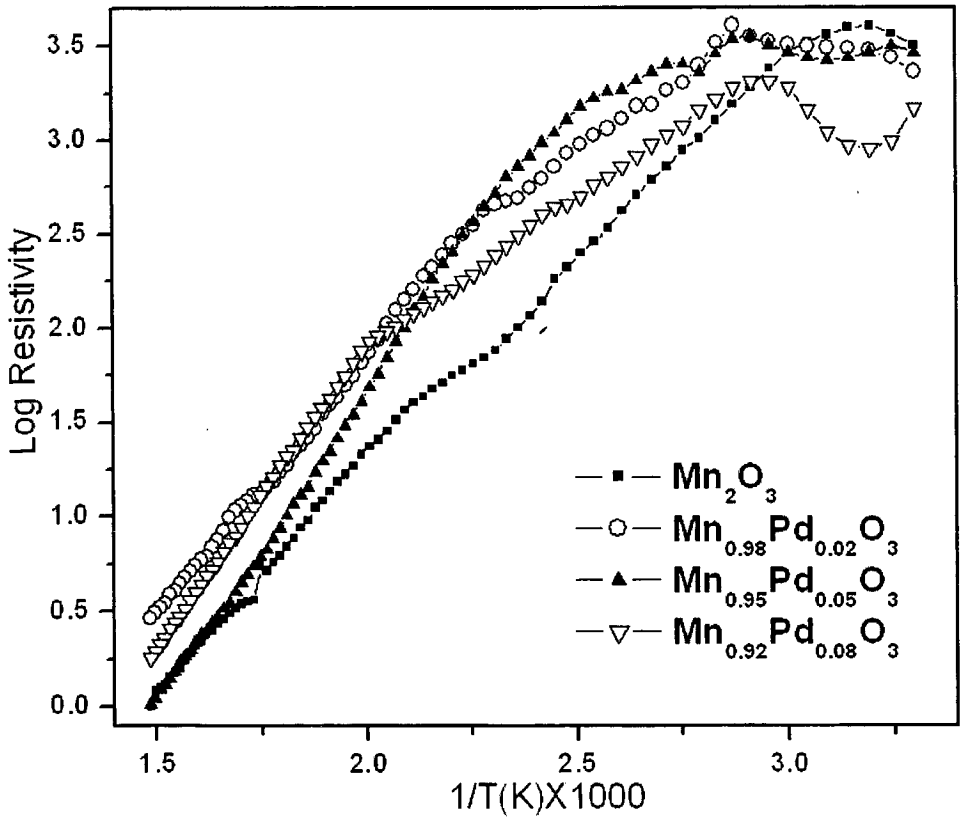

Fig. 4.37 Electrical resistivity plot for Pd-Mn_2O_3 series.

The electrical resistivity plot for Pd doped Mn_2O_3 series is shown in Fig. 4.37. All the samples showed similar trend as that of pristine Mn_2O_3. The resistivity decreases with increasing temperature as expected, presenting the semiconducting behavior of these samples. Initially there is little decrease in conductivity up to a temperature of 100 °C. This little decrease may be due to the presence of moisture on surface.

The activation energy for electrical conduction in polycrystalline materials generally involves the combination of the energy required to raise the carriers from the dominant levels to their corresponding transport bands and the energy required to create the carriers in the dominant levels [235]. The low activation energy predicts that the small polaron conduction dominates in the studied temperature range.

4.5 Magnetic Susceptibility

The magnetic susceptibility of the different compounds was determined by Guoy balance at room temperature, using field strength of 8600 gauss.

Magnetic moment value of the doped MnO_2 samples is almost above 3 B.M. This confirmed that the Mn^{4+} ion in MnO_2 has three unpaired electrons (paramagnetic properties) [236]. But significant deviation from the paramagnetic regime to the ferromagnetic behavior was reported at lower temperature that is below 100 K [116,228]. The pristine MnO_2 showed higher values of magnetic susceptibility and magnetic moment as compared to the doped MnO_2 catalysts, with increasing concentration of dopants the magnetic susceptibility and magnetic moment values was found to decrease due to the influence of dopants in the lattice structure of MnO_2.

In case of Mn_2O_3 catalyst, the magnetic moment value was found to be above 4 B.M. indicating that Mn was present in 3+ oxidation state having four unpaired electrons. The undoped Mn_2O_3 showed higher values of magnetic susceptibility and magnetic moment values than doped Mn_2O_3. With increasing concentration of dopants these values were found to be decreasing due to the influence of dopants in Mn_2O_3 lattice.

The observed gram susceptibility values and magnetic moment values at room temperature are presented in Table 4.1.

Table 4.1 The gram susceptibility (X_g) and magnetic moment (μ_{eff}) values of all the samples.

Ni-MnO_2 series

Sample	X_g	μ_{eff} (B.M.)
MnO_2	4.9161×10^{-5}	3.2051
$Mn_{0.95}Ni_{0.05}O_2$	5.8351×10^{-5}	3.4955
$Mn_{0.90}Ni_{0.10}O_2$	5.3707×10^{-5}	3.3572
$Mn_{0.85}Ni_{0.15}O_2$	4.1056×10^{-5}	3.2921
$Mn_{0.80}Ni_{0.20}O_2$	3.5307×10^{-5}	2.7278

Ce-MnO_2 series

Sample	X_g	μ_{eff} (B.M.)
MnO_2	4.9161×10^{-5}	3.2051
$Mn_{0.95}Ce_{0.05}O_2$	4.6774×10^{-5}	3.2019
$Mn_{0.90}Ce_{0.10}O_2$	4.3958×10^{-5}	3.1757
$Mn_{0.85}Ce_{0.15}O_2$	3.8156×10^{-5}	3.0240
$Mn_{0.80}Ce_{0.20}O_2$	2.9594×10^{-5}	2.7194

Pd-MnO_2 series

Sample	X_g	μ_{eff} B.M.)
MnO_2	$4.9161x10^{-5}$	3.2051
$Mn_{0.98}Pd_{0.02}O_2$	$4.4210x10^{-5}$	3.0571
$Mn_{0.95}Pd_{0.05}O_2$	$4.0238x10^{-5}$	2.9422
$Mn_{0.98}Pd_{0.08}O_2$	$3.9226x10^{-5}$	2.9300

Ag-MnO_2 series

Sample	X_g	μ_{eff} (B.M.)
MnO_2	$6.0845x10^{-5}$	3.5656
$Mn_{0.95}Ag_{0.05}O_2$	$5.4207x10^{-5}$	3.4163
$Mn_{0.90}Ag_{0.10}O_2$	$4.8841x10^{-5}$	3.2904
$Mn_{0.85}Ag_{0.15}O_2$	$4.4178x10^{-5}$	3.1740
$Mn_{0.80}Ag_{0.20}O_2$	$4.3123x10^{-5}$	3.1792

Rh-MnO_2 series

Sample	X_g	μ_{eff} (B.M.)
MnO_2	$6.7350x10^{-5}$	3.7514
$Mn_{0.98}Rh_{0.02}O_2$	$6.6860x10^{-5}$	3.7585
$Mn_{0.95}Rh_{0.05}O_2$	$6.4202x10^{-5}$	3.7128
$Mn_{0.90}Rh_{0.10}O_2$	$4.8296x10^{-5}$	3.2632

Ni- Mn_2O_3 series

Sample	X_g	μ_{eff} (B.M.)
Mn_2O_3	$6.6303x10^{-5}$	5.0140
$Mn_{1.95}Ni_{0.05}O_3$	$4.8611x10^{-5}$	4.2598
$Mn_{1.90}Ni_{0.10}O_3$	$4.7202x10^{-5}$	4.1629
$Mn_{1.80}Ni_{0.15}O_3$	$4.3567x10^{-5}$	3.9658
$Mn_{1.80}Ni_{0.20}O_3$	$3.9535x10^{-5}$	3.7455

Ce-Mn_2O_3 series

Sample	X_g	μ_{eff} (B.M.)
Mn_2O_3	$6.6303x10^{-5}$	5.0140
$Mn_{1.95}Ce_{0.05}O_3$	$4.8399x10^{-5}$	4.3059
$Mn_{1.90}Ce_{0.10}O_3$	$4.6053x10^{-5}$	4.2201
$Mn_{1.80}Ce_{0.15}O_3$	$4.3138x10^{-5}$	4.1035
$Mn_{1.80}Ce_{0.20}O_3$	$3.8291x10^{-5}$	3.8841

Pd-Mn_2O_3 series

Sample	X_g	μ_{eff} (B.M.)
Mn_2O_3	$6.9669x10^{-5}$	5.1416
$Mn_{1.98}Pd_{0.02}O_3$	$6.2251x10^{-5}$	4.8591
$Mn_{1.95}Pd_{0.05}O_3$	$5.2759x10^{-5}$	4.4718
$Mn_{1.92}Pd_{0.08}O_3$	$6.3657x10^{-5}$	4.9096

Ag-Mn_2O_3 series

Sample	X_g	μ_{eff} (B.M.)
Mn_2O_3	$6.6912x10^{-5}$	5.0380
$Mn_{0.95}Ag_{0.05}O_3$	$6.8204x10^{-5}$	5.1278
$Mn_{0.90}Ag_{0.10}O_3$	$6.2116x10^{-5}$	4.9270
$Mn_{0.85}Ag_{0.15}O_3$	$5.9660x10^{-5}$	4.8761
$Mn_{0.80}Ag_{0.20}O_3$	$5.0704x10^{-5}$	4.5326

4.6 UV-Visible diffuse reflectance spectroscopy (DRS)

The diffuse reflectance spectra (DRS) for all the samples were recorded in the range 400 to 800 nm wavelength range and the % reflectance was measured against the wavelength. The plots of absorbance against the wavelength were plotted. Using the wavelength values, the band gaps of all the samples were calculated [237] using the equation (1) given below:

$$Eg = 1239.8/\lambda \quad (1)$$

Where Eg is the band gap of the sample in eV and λ is the corresponding wavelength in nm.

Table 4.2 The bang gap values of the samples.

Sample	Band gap (eV)
Ni-MnO_2 series	
MnO_2	2.17
$Mn_{0.95}Ni_{0.05}O_2$	2.10
$Mn_{0.90}Ni_{0.10}O_2$	2.08
$Mn_{0.85}Ni_{0.15}O_2$	2.08
$Mn_{0.80}Ni_{0.20}O_2$	2.08
Ce-MnO_2 series	
MnO_2	2.17
$Mn_{0.95}Ce_{0.05}O_2$	2.27
$Mn_{0.90}Ce_{0.10}O_2$	2.40
$Mn_{0.85}Ce_{0.15}O_2$	2.47
$Mn_{0.80}Ce_{0.20}O_2$	2.45
Pd-MnO_2 series	
MnO_2	2.17
$Mn_{0.98}Pd_{0.02}O_2$	2.27
$Mn_{0.95}Pd_{0.05}O_2$	2.29
$Mn_{0.98}Pd_{0.08}O_2$	2.25
CuPd-MnO_2 series	
MnO_2	2.17
$Mn_{0.90}Cu_{0.10}O_2$	2.23
$Mn_{0.90}Cu_{0.08}Pd_{0.02}O_2$	2.21
$Mn_{0.90}Cu_{0.05}Pd_{0.05}O_2$	2.21

Ni-Mn_2O_3 series	
Mn_2O_3	2.06
$Mn_{1.95}Ni_{0.05}O_3$	2.06
$Mn_{1.90}Ni_{0.10}O_3$	2.13
$Mn_{1.80}Ni_{0.15}O_3$	2.13
$Mn_{1.80}Ni_{0.20}O_3$	2

Ce-Mn_2O_3 series	
Mn_2O_3	2.06
$Mn_{0.95}Ce_{0.05}O_3$	2.31
$Mn_{0.90}Ce_{0.10}O_3$	2.29
$Mn_{0.85}Ce_{0.15}O_3$	2.31
$Mn_{0.80}Ce_{0.20}O_3$	2.41

The band gap calculated by this method depends strongly on various parameters such as the thickness of coating, scattering coefficient, refractive index and average crossing parameters. Therefore the obtained values of band gap for these samples may not be the expected values.

The pristine MnO_2 shows the band gap around 2.17 eV, all the doped MnO_2 samples show band gap in the same range. The undoped Mn_2O_3 catalyst shows band gap of 2.06 eV. The nickel doped Mn_2O_3 shows band gap in the same range, whereas the cerium doped samples shows little higher band gap. The representative absorbance verses wavelength plots for Ni doped MnO_2 and Ni doped Mn_2O_3 are shown in Fig. 4.38 and 4.39 respectively.

The UV-visible spectra for Ag-doped MnO_2 nanoflowers show that incorporation of Ag into MnO_2 leads to a red shift in the optical response and a concomitant reduction of the band gap energy [238]. The optical band gap *Eg* of the nanoflowers obtained by wet chemical and photochemical routes is estimated to be 2.51 and 2.56 eV, respectively.

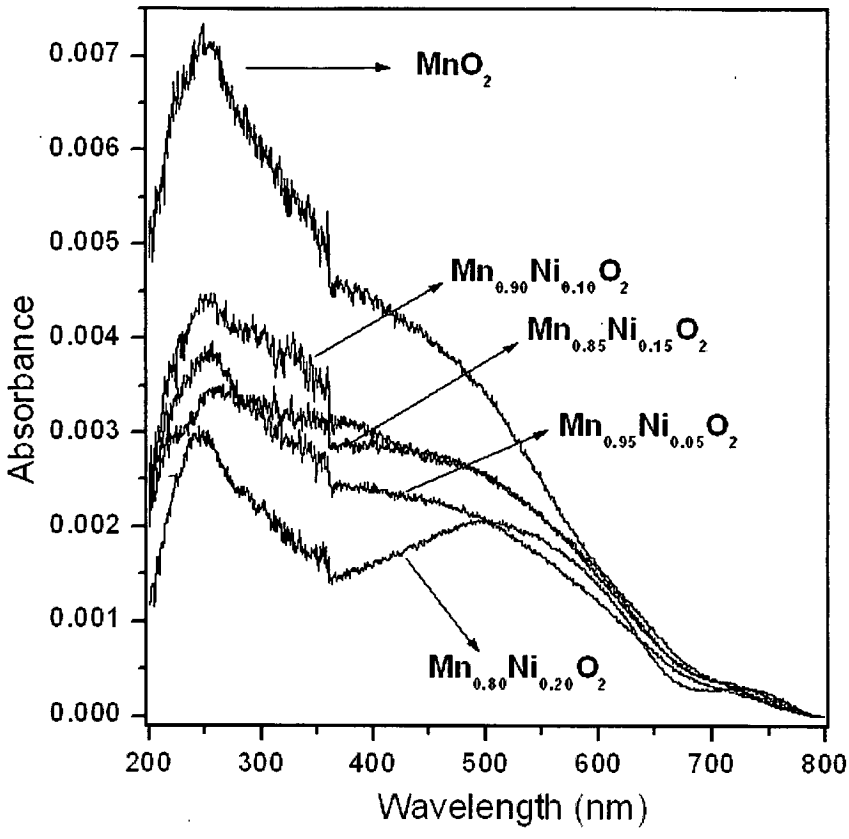

Fig. 4.38 The UV-Visible absorbance against wavelength plot of Ni doped MnO_2.

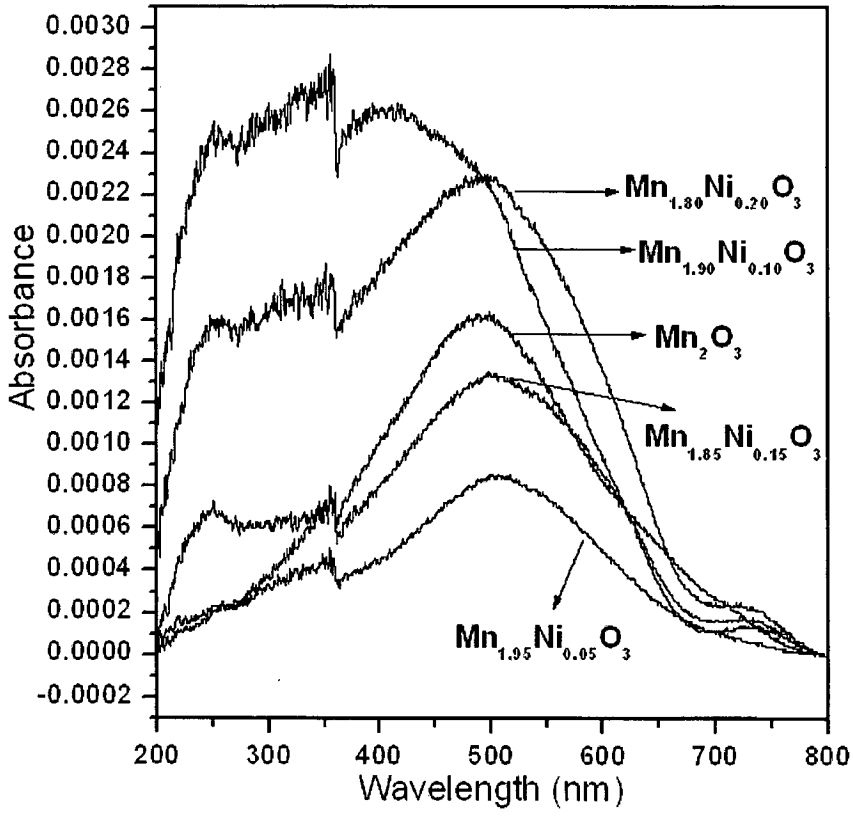

Fig. 4.39 The UV-Visible absorbance against wavelength plot of Ni doped Mn_2O_3.

The optical absorption of the MnO_2 in the visible light range originates mainly from d-d transitions of Mn ions. Mn 3d energy level splits into higher (e_g) and lower (t_{2g}) energy levels due to the ligand field of MnO_6 octahedra. The band gap energy corresponds to the energy difference between Mn 3d t_{2g} and e_g states. Mn 3d t_{2g} and e_g states serve as the "valence band" and the "conduction band" of the semiconductor, respectively.

4.7 X-ray photoelectron spectroscopy (XPS)

The XPS characterization was performed to investigate the chemical state of manganese oxide. The XPS spectra of Mn 2p and O 1s were obtained. For all samples, two main peaks due to Mn $2p_{3/2}$ and Mn $2p_{1/2}$ were observed from 639 eV to 660 eV. It was reported that $2p_{3/2}$ binding energy of Mn(0) and Mn(IV)O_2 was 639.0 eV and 642.1 eV, respectively [239,240]. Therefore, it is not easy to discern the oxidation state of manganese species without peak deconvolution because there is only 3.1 eV energy difference between Mn(0) and Mn(IV). The peak position of $2p_{3/2}$ for MnOx catalysts can exclude the possibility that there exist manganese species whose oxidation state is 0 or 2+. Therefore the deconvolution of $Mn_{3/2}$ was conducted based on the assumption that there are only Mn(III) and Mn(IV) species [77]. The presence of satellite peak was also considered in the peak deconvolution. This satellite structure, noticeable on the higher binding energy side of the Mn 2p core-line in the XPS spectrum of the manganese compounds, originates from the charge transfer between outer electron shell of ligand and an unfilled 3d shell of manganese during creation of core-hole in the photo-electron process [241].

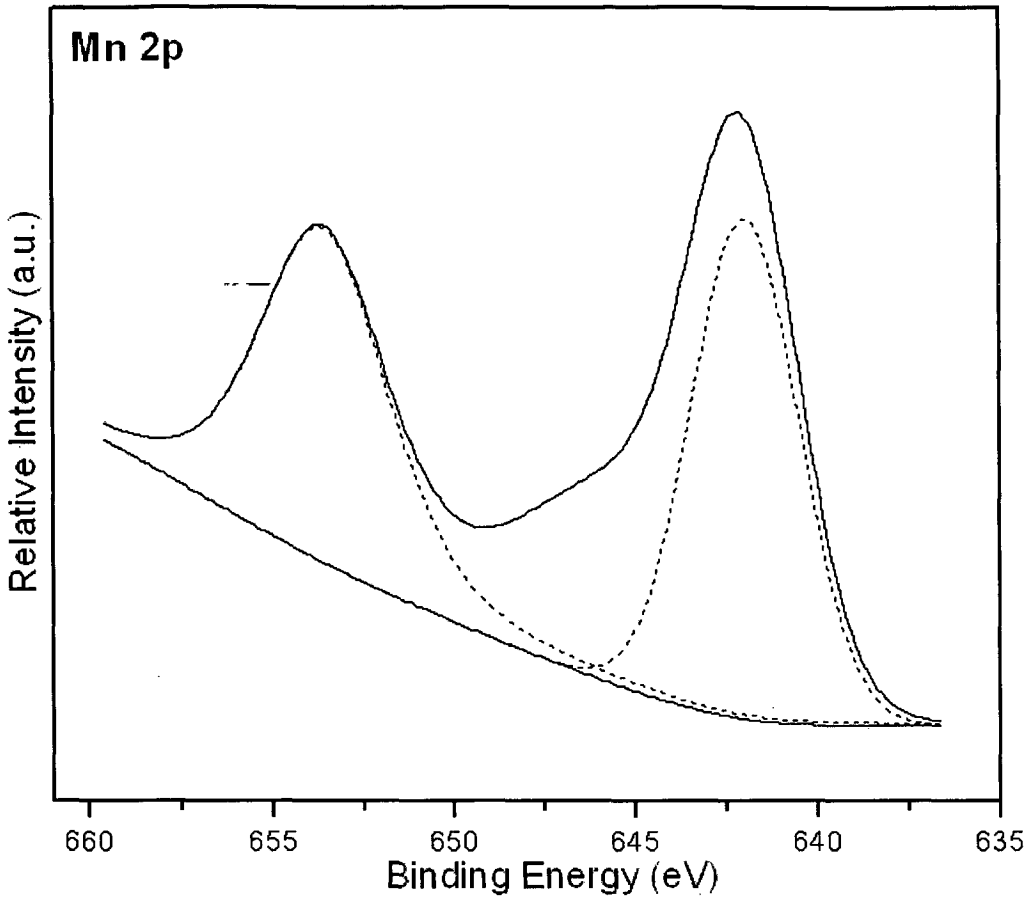

Fig. 4.40 The Mn 2p XPS spectra of pristine MnO_2.

The Fig. 4.40 shows the Mn $2p_{3/2}$ and $2p_{1/2}$ spectra of undoped MnO_2. The Mn $2p_{3/2}$ peak located at 642 eV and Mn $2p_{1/2}$ peak observed at 653.6 eV respectively, indicating that the oxidation state of manganese is Mn(IV) which agrees well with that reported for MnO_2 [38,124]. The O 1s XPS spectra of undoped MnO_2 is shown in Fig. 4.41, two surface oxygen species could be clearly observed. The binding energy of 529.8 eV was characteristic of the lattice oxygen and the binding energy of 532.8 eV might be assigned to the defect oxide or the surface oxygen ions with low coordination situation [38,124]. According to the literature the peak at 531.2 eV is assigned to the oxygen of the surface hydroxyls [242] abd the peak at 533.2 eV is considered as the oxygen of free water.

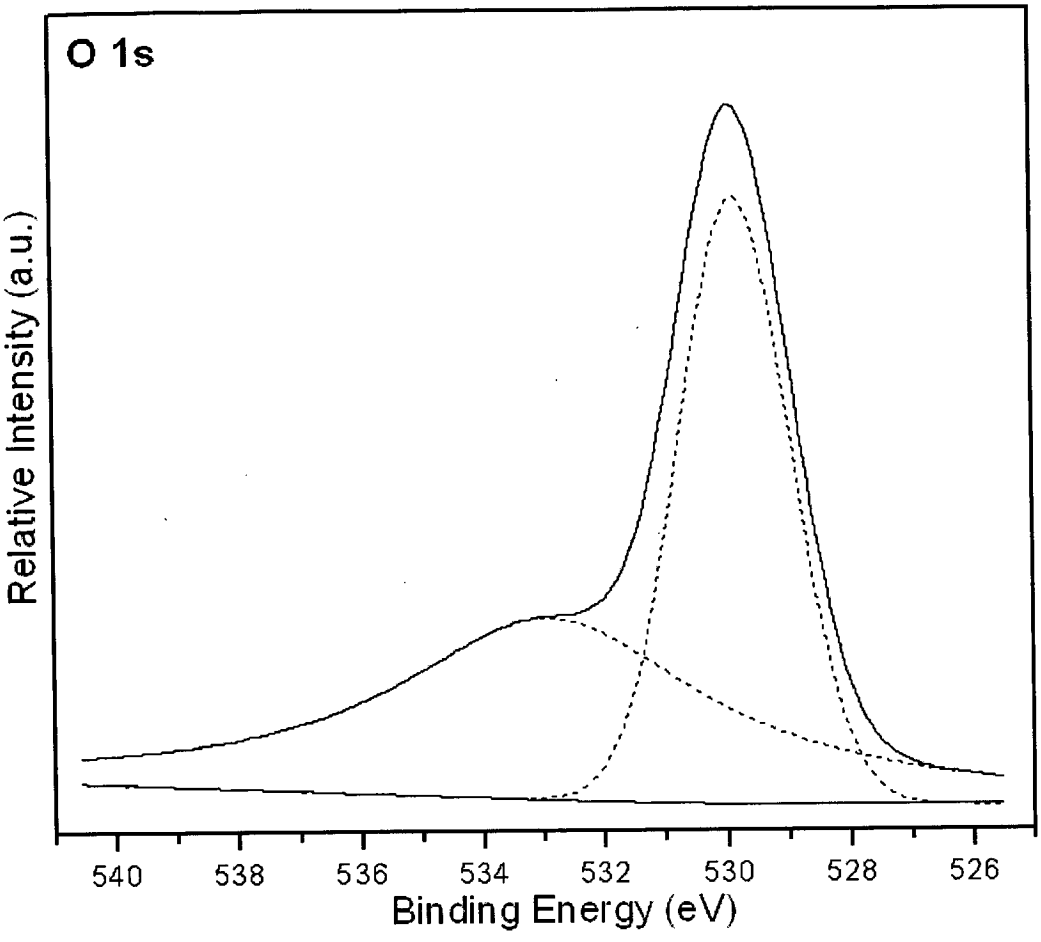

Fig. 4.41 The O 1s XPS spectra of pristine MnO_2.

CHAPTER 5

CATALYTIC STUDIES

CATALYTIC STUDIES

Introduction

Carbon monoxide (CO) is one of the main toxic gaseous pollutants which is generally produced and released from the combustion process of fossil fuels. Catalytic oxidation of carbon monoxide to carbon dioxide at a reasonably low temperature has been of considerable interest due to its significance in many industrial applications such as indoor and outdoor air cleaning, CO gas sensors, CO_2 lasers, fuel cells, automotive exhaust treatment as well as to meet stringent environmental regulations.

5.1 BET Surface area

The BET surface area for all the prepared catalysts has been determined using nitrogen physisorption at liquid nitrogen temperature. Results are summarized in the table 5.1. The MnO_2 series showed higher surface area than Mn_2O_3 and supported series. Moreover, among all doped MnO_2 series the Rh doped showed highest surface area this was found to be increasing with increasing Rh loadings. Whereas the Ag doped MnO_2 series showed lowest surface area and surface area decreases with Ag loadings. The lowest surface area is shown by Mn_2O_3 series and among all Mn_2O_3 series, Ag doped Mn_2O_3 series showed very low surface area.

Although the MnO_2 and Mn_2O_3 series were prepared by similar co-precipitation method, MnO_2 series showed higher surface area than Mn_2O_3. This may be because the calcination temperature is much higher in case of Mn_2O_3 preparation. The surface area of the catalysts mainly depends on the method of preparation of catalysts and the catalysts

with higher surface area gives much better activity. The preparation of catalysts thus becomes an important step.

The supported samples were prepared by wet impregnation method. Pd supported MnO_2 and Rh supported MnO_2 catalysts showed higher surface among all supported samples. The Table 5.1 shows the BET surface area of all the samples.

Table 5.1 The BET surface area of all the prepared samples.

MnO_2 series

Sample	Surface area (m^2g^{-1})
Ni-MnO_2 series	
MnO_2	52
$Mn_{0.95}Ni_{0.05}O_2$	46
$Mn_{0.90}Ni_{0.10}O_2$	42
$Mn_{0.85}Ni_{0.15}O_2$	39
$Mn_{0.80}Ni_{0.20}O_2$	32
Ce-MnO_2 series	
MnO_2	52
$Mn_{0.95}Ce_{0.05}O_2$	63
$Mn_{0.90}Ce_{0.10}O_2$	60
$Mn_{0.85}Ce_{0.15}O_2$	59
$Mn_{0.80}Ce_{0.20}O_2$	56
Pd-MnO_2 series	
MnO_2	52
$Mn_{0.98}Pd_{0.02}O_2$	55
$Mn_{0.95}Pd_{0.05}O_2$	48
$Mn_{0.98}Pd_{0.08}O_2$	45
Ag-MnO_2 series	
MnO_2	24

$Mn_{0.98}Ag_{0.02}O_2$	26
$Mn_{0.95}Ag_{0.05}O_2$	23
$Mn_{0.90}Ag_{0.10}O_2$	24
$Mn_{0.85}Ag_{0.15}O_2$	12
$Mn_{0.80}Ag_{0.20}O_2$	10

Rh-MnO_2 series

MnO_2	62
$Mn_{0.98}Rh_{0.02}O_2$	65
$Mn_{0.95}Rh_{0.05}O_2$	74
$Mn_{0.90}Rh_{0.10}O_2$	92

CuPd-MnO_2 series

MnO_2	62
$Mn_{0.90}Cu_{0.10}O_2$	52
$Mn_{0.90}Cu_{0.08}Pd_{0.02}O_2$	63
$Mn_{0.90}Cu_{0.05}Pd_{0.05}O_2$	68

Mn_2O_3 series

Sample	**Surface area (m^2g^{-1})**

Ni-Mn_2O_3 series

Mn_2O_3	5.5
$Mn_{1.95}Ni_{0.05}O_3$	3.2
$Mn_{1.90}Ni_{0.10}O_3$	8.9
$Mn_{1.80}Ni_{0.15}O_3$	4.4
$Mn_{1.80}Ni_{0.20}O_3$	5.7

Ce-Mn_2O_3 series

Mn_2O_3	5.5
$Mn_{1.95}Ce_{0.05}O_3$	10
$Mn_{1.90}Ce_{0.10}O_3$	20.7
$Mn_{1.80}Ce_{0.15}O_3$	7.3

$Mn_{1.80}Ce_{0.20}O_3$	19.9

Pd-Mn_2O_3 series

Mn_2O_3	5.5
$Mn_{1.98}Pd_{0.02}O_3$	3.4
$Mn_{1.95}Pd_{0.05}O_3$	12.4
$Mn_{1.92}Pd_{0.08}O_3$	14.7

Ag-Mn_2O_3 series

Mn_2O_3	6.6
$Mn_{0.95}Ag_{0.05}O_3$	1.7
$Mn_{0.90}Ag_{0.10}O_3$	2.1
$Mn_{0.85}Ag_{0.15}O_3$	1.7
$Mn_{0.80}Ag_{0.20}O_3$	1.5

Supported sample

Sample	**Surface area (m^2g^{-1})**
Pd/Mn_2O_3	
3.3wt% Pd/Mn_2O_3	13
5.3wt% Pd/Mn_2O_3	10
Rh/MnO_2	
3.5wt% Rh/MnO_2	52
5.7wt% Rh/MnO_2	59
11.2wt% Rh/MnO_2	58
Pd/MnO_2	
2.4wt% Pd/MnO_2	66
5.9wt% Pd/MnO_2	65
9.3wt% Pd/MnO_2	60
$CuPd/MnO_2$	

5.7wt% Cu 2.4wt% Pd/MnO_2	20
3.5wt% Cu5.9wt% Pd/MnO_2	19

5.2 Scanning electron microscopy (SEM)

The SEM technique was employed to study the surface morphology and the particle nature of the calcined catalysts.

The SEM images of $Mn_{0.95}Ni_{0.05}O_2$ and $Mn_{0.95}Ce_{0.05}O_2$ calcined at 400 °C are shown in Fig.5.1a and b. From these images it is clear that the particles are nano-sized and in the range of ~25–40 nm. Particles are found to be almost spherical in shape and agglomerated in appearance to some extent. All this indicates that preparation method highly influences the particle nature of the samples.

Preparation of catalysts by co-precipitation technique in dextrose solution may highly influence the particle size; also not much agglomeration of particles is seen. During the preparation due to the addition of dextrose solution the precipitated mixture does not gets easily settled, it remains suspended in the solution due to this particles remain separated resulting in small sized, spherical nano particles.

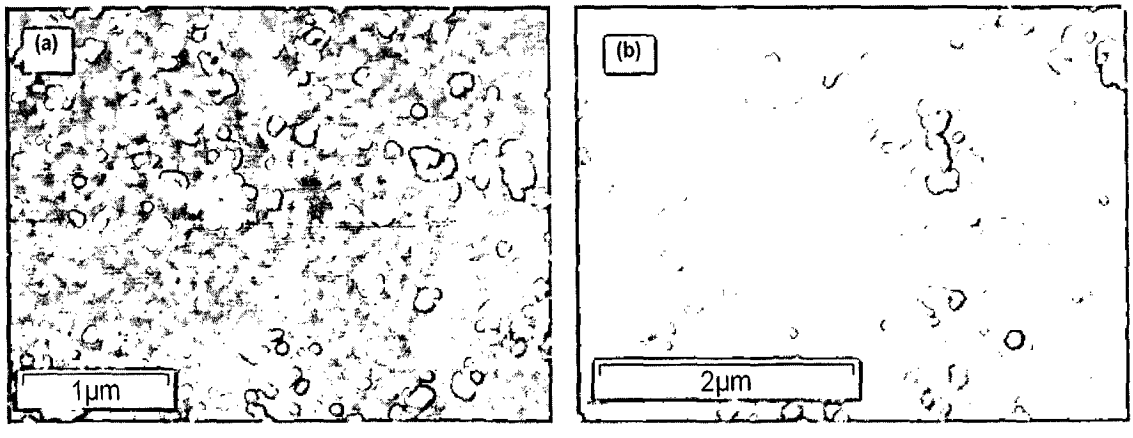

Fig. 5.1 SEM images (a) $Mn_{0.95}Ni_{0.05}O_2$ & (b) $Mn_{0.95}Ce_{0.05}O_2$.

In case of $Mn_{0.98}Pd_{0.02}O_2$ and $Mn_{0.92}Pd_{0.08}O_2$ (Fig. 5.2a and b) both catalysts shows spherical shape morphology. The particles are uniform and seemed to be nano-sized. The average particle size is approximately found to be in the range 20-40 nm. From these images it is clear that the particles are agglomerated.

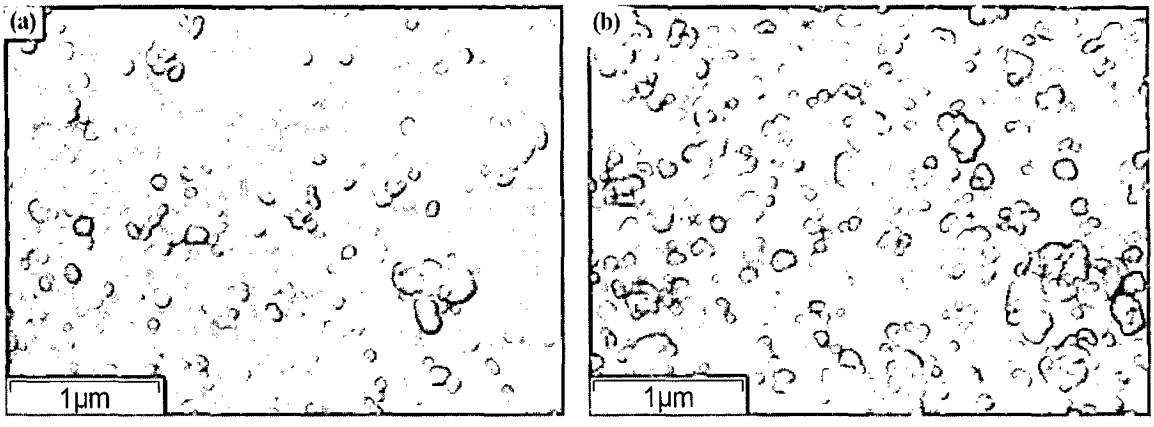

Fig. 5.2 SEM images of (a) $Mn_{0.98}Pd_{0.02}O_2$, (b) $Mn_{0.92}Pd_{0.08}O_2$.

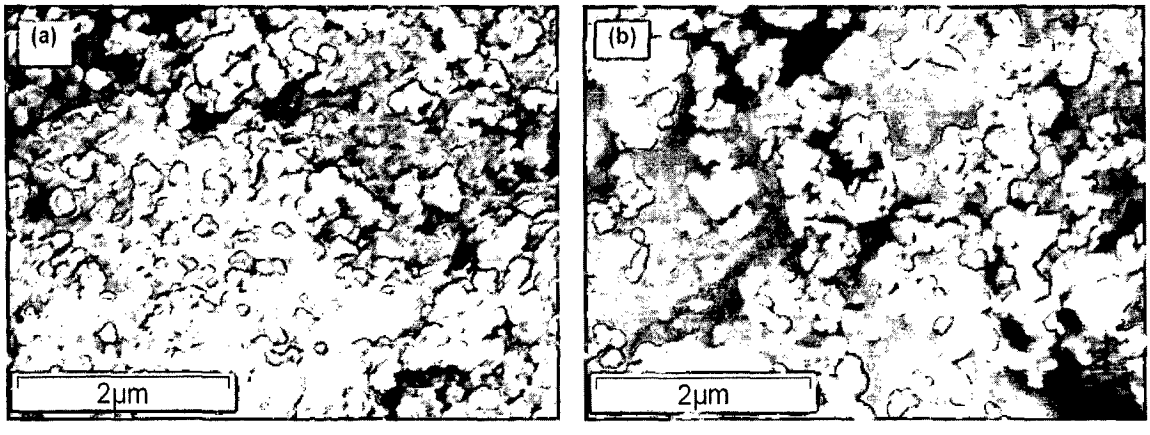

Fig. 5.3 SEM images of (a) $Mn_{0.95}Ag_{0.05}O_2$, (b) $Mn_{0.90}Rh_{0.10}O_2$.

The SEM image of $Mn_{0.95}Ag_{0.05}O_2$ catalyst is illustrated in Fig. 5.3a, the image shows the aggregates of nano particles. The particles are roughly spherical in appearance and the particle size was approximately below 40 nm. Fig. 5.3b also shows the SEM image of $Mn_{0.90}Rh_{0.10}O_2$ catalyst, the particles are nano-sized and agglomerated in appearance.

The SEM images of $Mn_{0.90}Cu_{0.08}Pd_{0.02}O_2$ and $Mn_{0.90}Cu_{0.05}Pd_{0.05}O_2$ are shown in Fig. 5.4a and b, indicating that all the products have almost identical morphology. The particles

are highly agglomerated in both the cases. The particle nature found to be somewhat spherically elongated and the average particle size is roughly found to be below 50 nm.

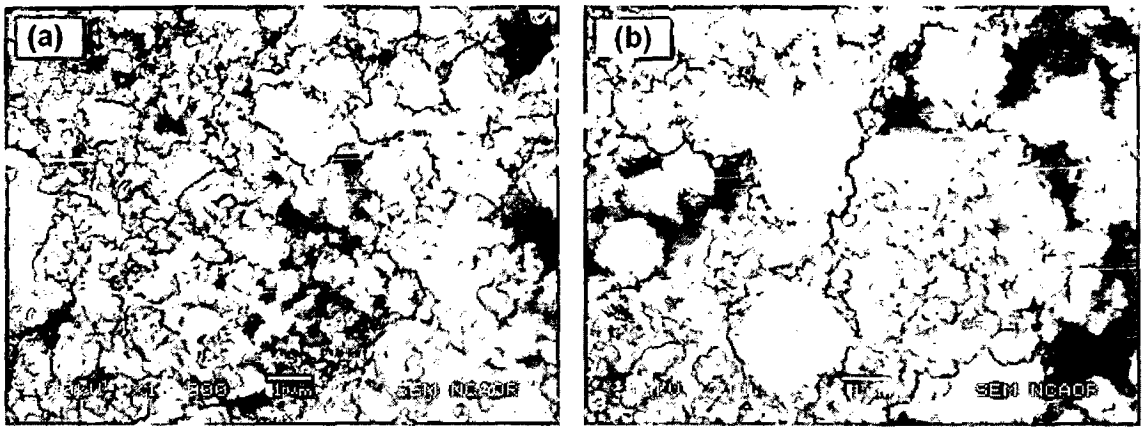

Fig. 5.4 SEM images of (a) $Mn_{0.90}Cu_{0.08}Pd_{0.02}O_2$, (b) $Mn_{0.90}Cu_{0.05}Pd_{0.05}O_2$.

The SEM images for pure Mn_2O_3 and doped Mn_2O_3 catalysts are illustrated in Fig. 5.5. The pristine Mn_2O_3 (Fig. 5.5a) shows almost spherical morphology. The particles were in the range of 50–100 nm diameters. The preparation method influences the particle nature of the materials. The particle size was found to be higher as compared to MnO_2 samples and the BET surface area of doped Mn_2O_3 samples was also found to be very less due to higher sintering temperature. Fig. 5.5b is for $Mn_{1.95}Ni_{0.05}O_3$ catalyst, this catalyst shows rod-like morphology with length of rods upto 200 nm. The morphology was found to be different than that of pure Mn_2O_3 catalyst.

The cerium doped Mn_2O_3 catalyst shows morphology similar to that of pristine Mn_2O_3. The particles were found to be spherical in shape and agglomerated in appearance to some extent. The particle size seemed to be less than pristine Mn_2O_3 with the average particle size in the range of approximately less then 80 nm. Fig. 5.5c shows the representative image of $Mn_{1.80}Ce_{0.20}O_3$ catalyst.

The SEM image of $Mn_{1.92}Pd_{0.08}O_3$ catalyst shows agglomerated clusters of spherical nano-particles as shown in Fig 5.5d. The size of the particle was found to be in the range

60–100 nm. Moreover, the morphology is almost similar to the pristine Mn_2O_3 catalyst. The BET surface area was found to be very less which may be due to the agglomeration of particles. Thus the particle nature mainly depends on the method of preparation of the catalyst. The nano-sized particles with high surface area are more preferable for catalytic reactions.

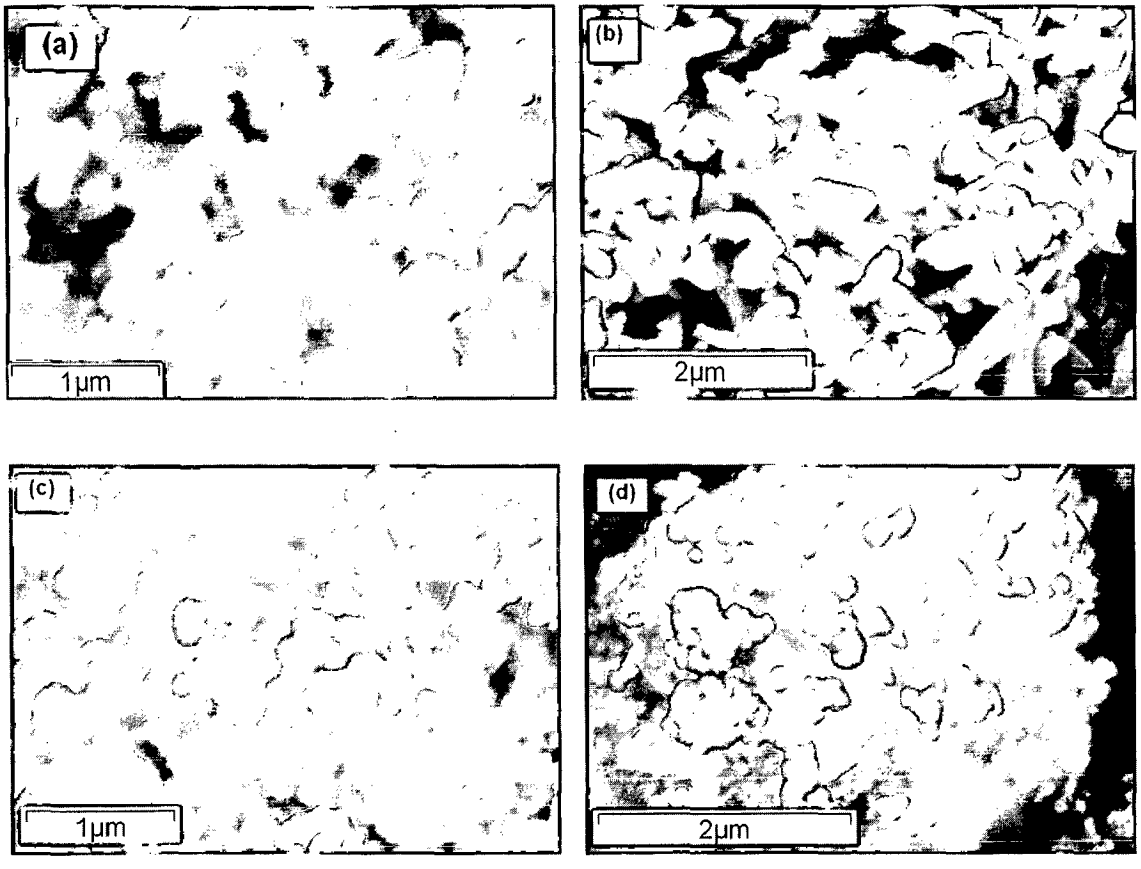

Fig. 5.5 SEM images of (a) Mn_2O_3 and (b) $Mn_{1.95}Ni_{0.05}O_3$, (c) $Mn_{1.80}Ce_{0.20}O_3$ and (d) $Mn_{1.92}Pd_{0.08}O_3$.

The SEM micrographic images of supported samples are shown in Fig. 5.6. The supported samples were prepared by impregnation method. The Fig. 5.6a shows SEM image of 3.3 wt% Pd/Mn_2O_3 catalyst, from figure it is clear that the particles are unevenly distributed. The particles are agglomerated and are almost spherical in shape with size approximately range 60-100 nm. The preparation method highly influences the particle size of the catalysts, supported Mn_2O_3 sample showed the morphology which is different

than that of doped Mn_2O_3 sample. Fig. 5.6b illustrates the representative SEM image of Cu-Pd/MnO_2 catalyst. Particles are found to be nano-sized and agglomerated in appearance. The average particle size is less than 50 nm and the particles shows more or less spherical morphology.

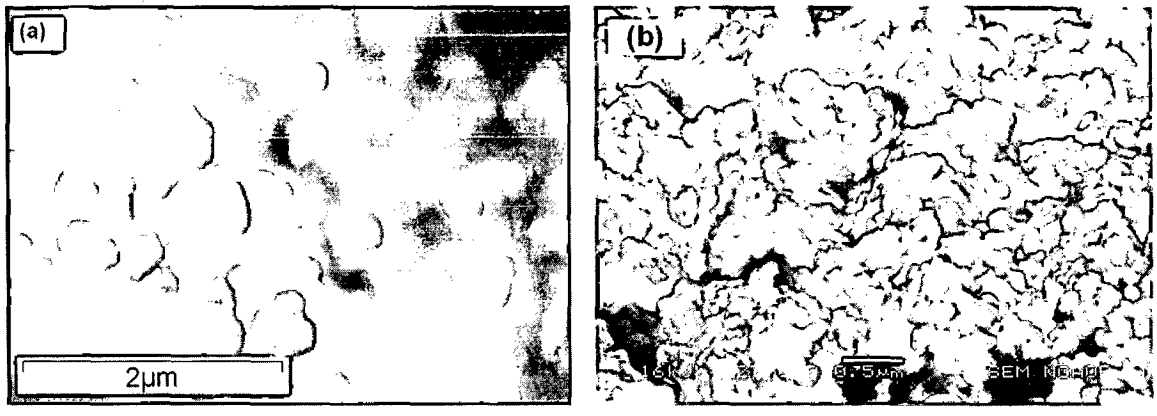

Fig. 5.6 SEM images of (a) 3.3 wt% Pd/Mn_2O_3 and (b) 3.5 wt% Cu 5.9 wt% Pd/MnO_2.

5.3 Transmission electron microscopy (TEM)

The representative TEM images of MnO_2, $Mn_{0.95}Ag_{0.05}O_2$ and $Mn_{0.90}Cu_{0.05}Pd_{0.05}O_2$ catalysts are shown in Fig. 5.7a, b, c and d. From the figure it is clear that the particles are nanosized and in the range 25-40 nm, the particles are agglomerated in appearance and spherical in nature. Inset in the figure shows electron diffraction patterns, Fig. 5.7a shows that rings are made of discrete spots signifying crystalline nature of nanosized MnO_2. But in contrast, Ag doped MnO_2 catalysts (Fig. 5.7c) exhibited clear continuous ring patterns demonstrating that Ag doped catalysts are polycrystalline in nature. Incorporation of Ag thus causes changes in the degree of crystallinity.

Fig. 5.7d represents the TEM image of $Mn_{0.90}Cu_{0.05}Pd_{0.05}O_2$ catalyst. The image shows that the Cu-Pd doped catalysts have nano-rod like morphology with length of around 40 nm and thickness of 10 nm. The broad and diffuse lines in X-ray diffraction pattern also

indicated that particles are nano-sized. These particles seemed to be agglomerated in appearance.

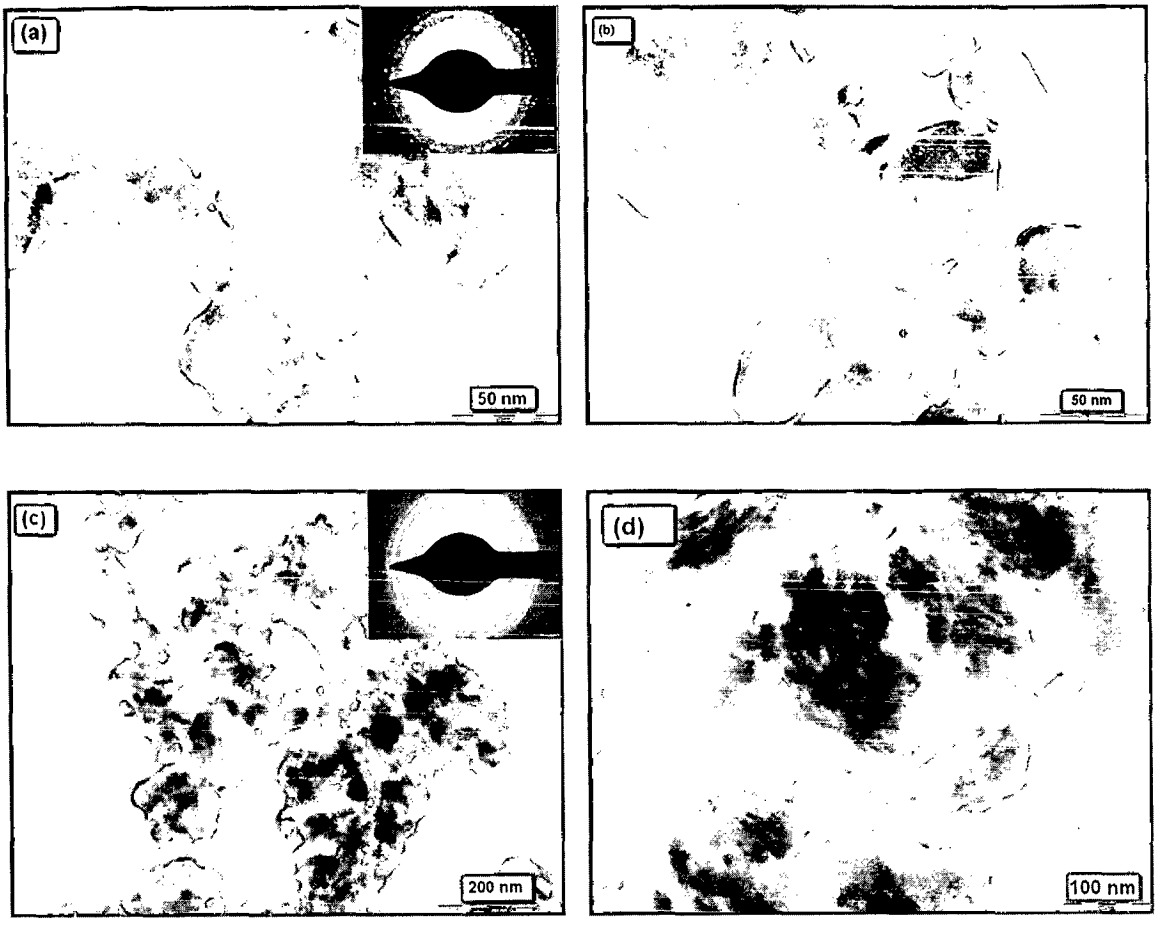

Fig. 5.7 TEM images of (a) (b) MnO_2, (c) $Mn_{0.95}Ag_{0.05}O_2$ and (d) $Mn_{0.90}Cu_{0.05}Pd_{0.05}O_2$.

The TEM micrographs for supported samples are shown in Fig 5.8 along with electron diffraction patterns. The 3.5 wt% Rh/MnO_2 catalyst showed elongated rod-like morphology (Fig. 5.8a). This rods are around 40-50 nm in length with thickness less than 10 nm. The electron diffraction pattern shows clear continuous ring patterns indicating that the sample is polycrystalline in nature. These results are further supported by X-ray diffraction which shows nanocrystalline nature of these samples.

The TEM image of 3.5 wt% Cu 5.9 wt% Pd/MnO_2 catalyst is shown in Fig. 5.8b. The TEM image shows that Cu-Pd supported MnO_2 catalyst particles were aggregated and

nano-sized. The morphology of these samples seemed to be different as compare to that of Cu-Pd doped MnO_2 samples. The electron diffraction pattern of the selected area shows that the 3.5 wt% Cu 5.9 wt% Pd/MnO_2 exhibited continuous ring patterns demonstrating that these samples are polycrystalline in nature.

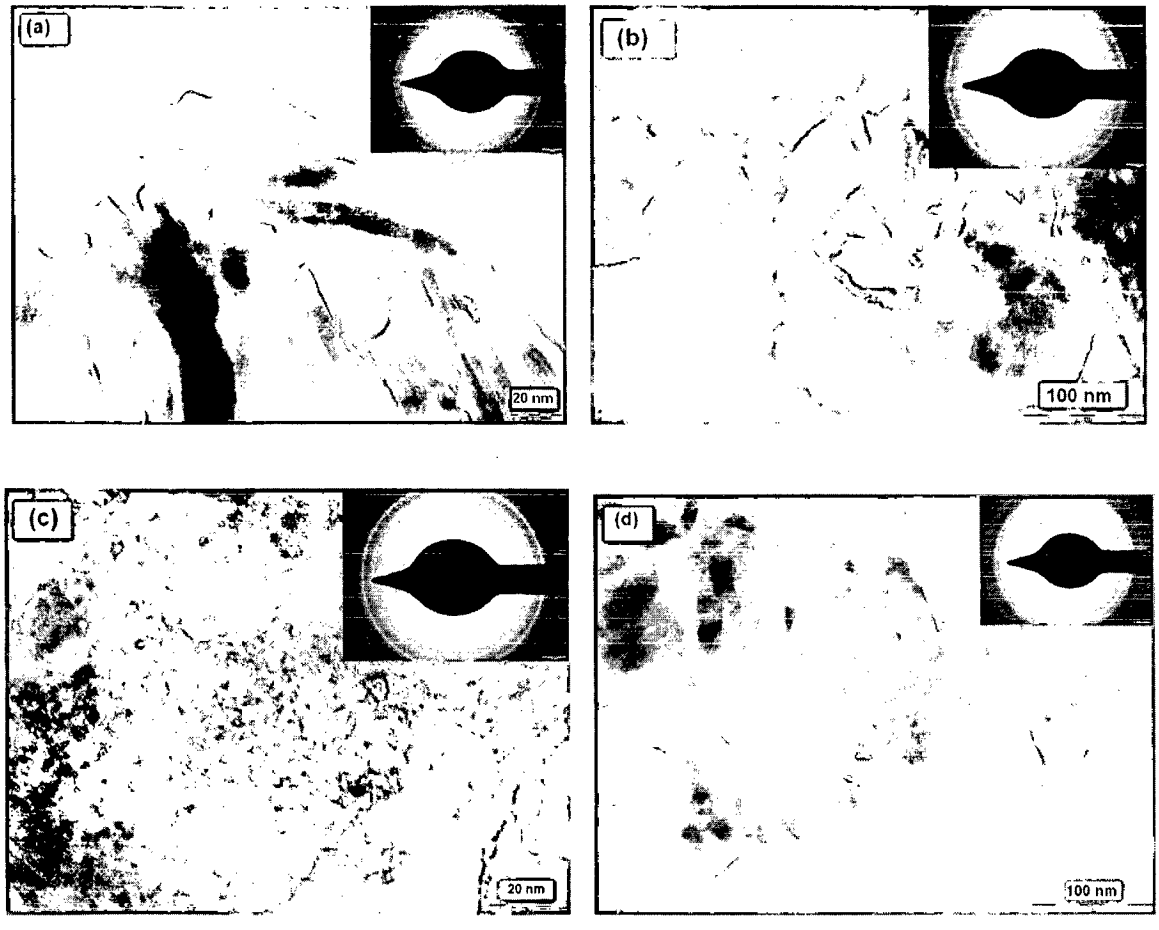

Fig. 5.8 TEM images of (a) 3.5 wt% Rh/MnO_2, (b) 3.5 wt% Cu 5.9 wt% Pd/MnO_2, (c) 9.3 wt% Pd/MnO_2 and (d) 5.3wt% Pd/Mn_2O_3.

Fig. 5.8c shows TEM image and electron diffraction pattern of the 9.3 wt% Pd/MnO_2 catalyst. From the TEM image it is evident that the particles are nano-sized with particle size less than 10 nm. The particles are spherical in shape and agglomerated in appearance. The electron diffraction shows the continuous rings patterns indicating polycrystalline nature of this sample.

The TEM image of 5.3 wt% Pd/Mn_2O_3 catalyst is shown in Fig. 5.8d. From this image it is clear that the particles are nano-sized and the average particle size is around 50 nm. Particles are found to be almost elongated-like spherical in appearance. Inset in the Fig. 5.8d show electron diffraction pattern, 5.3 wt% Pd/Mn_2O_3 catalysts exhibited clear continuous ring patterns demonstrating the polycrystalline nature. All this indicates that the preparation method highly influences the particle nature of the samples.

5.4 Temperature programmed desorption of NH_3 (NH_3-TPD)

Temperature programmed desorption (TPD) profiles of ammonia over MnO_2 and $Mn_{0.95}Ag_{0.05}O_2$ catalysts are shown in Fig. 5.9. NH_3-TPD was performed to explore the adsorption sites over these catalysts, basically presence of acidic sites is needed on the surface of the catalysts for adsorption of CO molecules. TPD of ammonia is conventionally employed to monitor the acidity of the solid surface.

Fig. 5.9a shows TPD spectra of MnO_2. The spectra shows one weak desorption peak observed at around 200 °C, one high intensity peak at 643 °C and one medium intensity peak at 537 °C which corresponds to weak, strong and moderate adsorption sites in MnO_2. The intensity and peak area of the NH_3 desorption peak is a measure of amount of NH_3 adsorbed. The desorption profile of $Mn_{0.95}Ag_{0.05}O_2$ catalyst shows one higher intensity peak at 604 °C and one new intermediate broad peak at 230 °C which was weak intensity peak in MnO_2 as can be seen in Fig. 5.9b. The high intensity desorption peak of $Mn_{0.95}Ag_{0.05}O_2$ found to be shifted towards low temperature region at around 40 °C, its peak height is more and also the area under this peak is more as compared to high intensity desorption peak of MnO_2. The peak at 537 °C which was shown by MnO_2 gets partially merged with high intensity peak in $Mn_{0.95}Ag_{0.05}O_2$, this peak also becomes broader and is

shifted towards lower temperature. The weak intensity peak of MnO_2 which was seen at 200 °C was found to be shifted towards higher temperature by around 30 °C in $Mn_{0.95}Ag_{0.05}O_2$, its peak height is more and it is a broad peak.

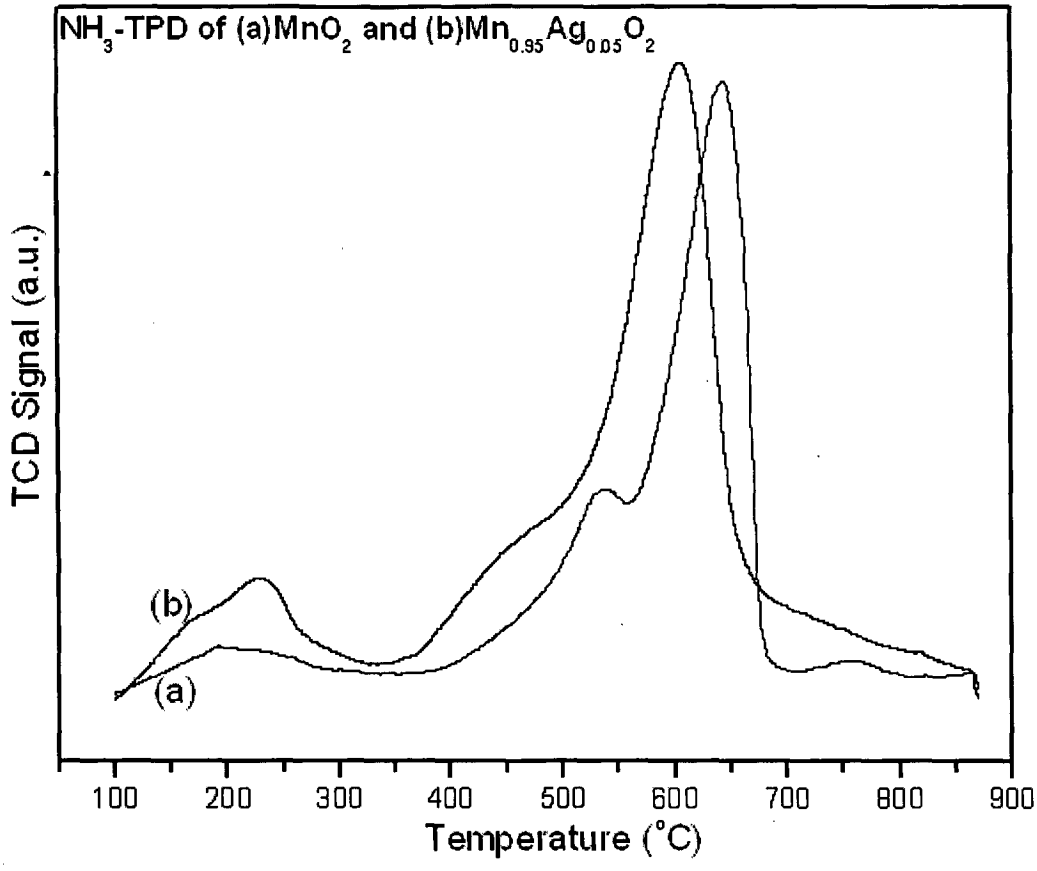

Fig. 5.9 NH_3-TPD (Temperature programmed desorption) profile for (a) MnO_2 and (b) $Mn_{0.95}Ag_{0.05}O_2$.

Thus incorporation of Ag in MnO_2 results in shifting high intensity peak to lower temperature also increasing its peak area, besides this there is appearance of broad peak at lower temperature. This change occurs mainly due to doping of Ag in MnO_2 which shows improved adsorption behavior and indicates the presence of strong Acidic sites which is important for CO oxidation reaction. All this factors indicates that incorporation of Ag in MnO_2 enhances the adsorption capabilities of MnO_2.

5.5 Catalytic activity over various catalysts

The general introduction about this reaction is given in chapter 2. The catalytic oxidation of CO was carried out over all the prepared catalysts. The laboratory created exhaust gas composition was 5% CO and 5% O_2 in nitrogen.

5.5.1 CO oxidation over doped MnO_2 catalysts

Fig. 5.10 shows the catalytic performance for CO oxidation over Ni doped MnO_2 catalysts. MnO_2 shows good activity and 100% CO conversion is achieved at around 200 ^oC. Ni doped catalysts showed lower activity than MnO_2 as can be seen from Fig. 5.10 and activity decreases with increase in Ni content in MnO_2. Incorporation of Ni in lattice of MnO_2 changes the atomic spacing of the manganese oxide and decreases the adsorption ability of MnO_2 [243]. Also surface area results showed decrease of surface area with increasing Ni in MnO_2. This decreases the active sites which are responsible for the adsorption of CO resulting in lower activity.

Similar is the case with cerium doped MnO_2. Ce doped catalysts showed poor catalytic activity and with increase of cerium concentration the activity decreases. The results are shown in Fig. 5.11. Pure cerium oxide was prepared by same method and tested for CO oxidation for comparative study with doped samples. This pure CeO_2 showed very poor activity as compared to MnO_2 catalyst, it showed around 50% conversion at 400 ^oC as can be seen in figure which shows very poor activity. Thus cerium incorporation in MnO_2 decreases the catalytic property of MnO_2 for CO oxidation reaction. There may be increase in activation energy for CO adsorption.

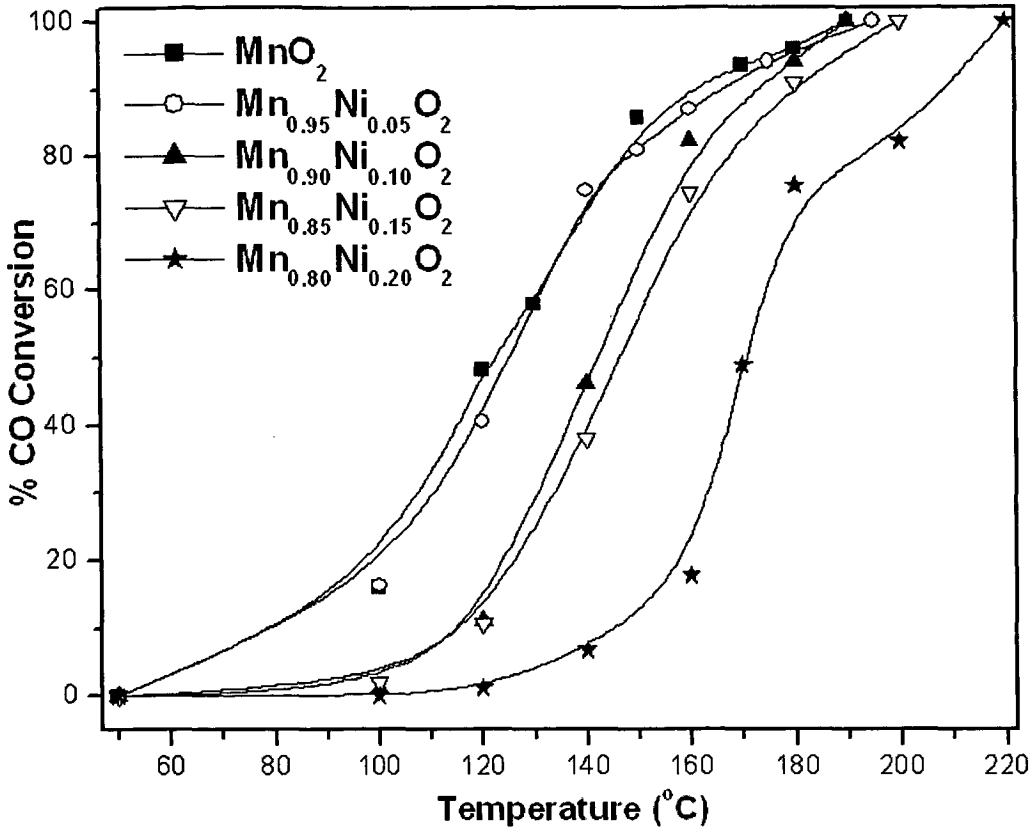

Fig. 5.10 CO conversion against Temperature over Ni-MnO_2 series.

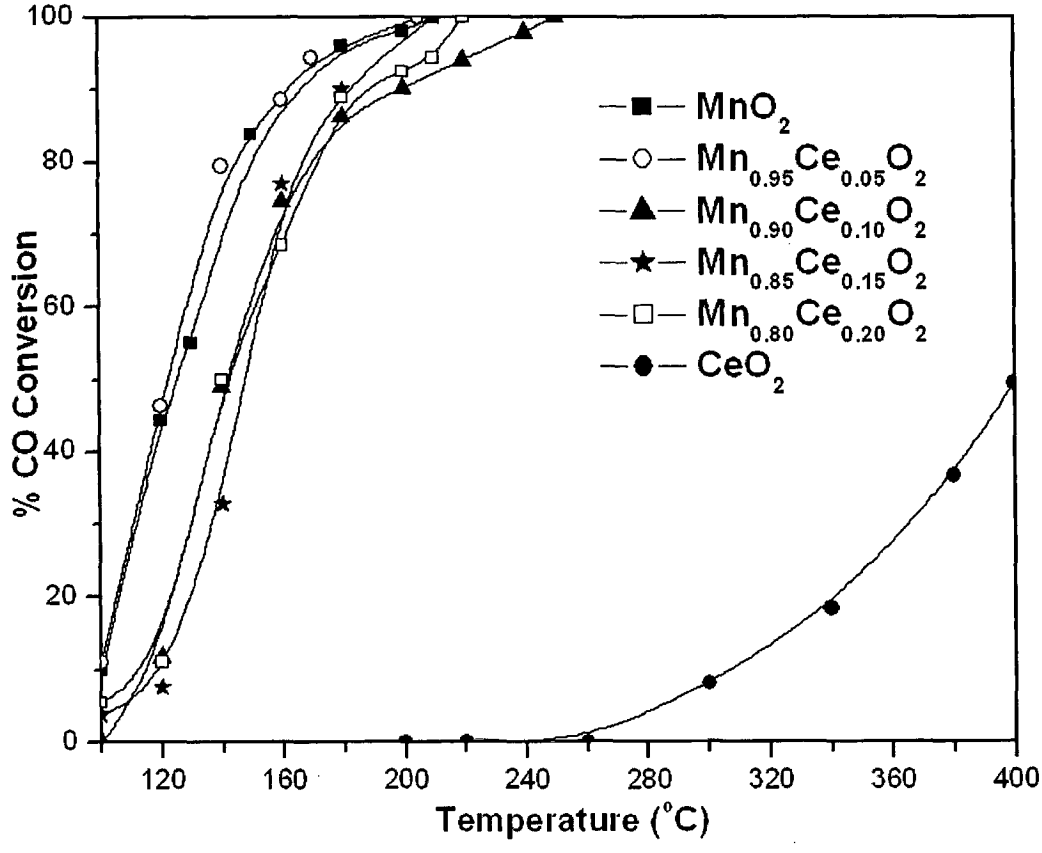

Fig. 5.11 CO conversion against Temperature over Ce-MnO_2 series.

Fig. 5.12 shows the catalytic performance for CO oxidation of the as prepared MnO_2 and Pd doped MnO_2 catalysts. From this figure it is clear that the catalysts show a high activity for CO oxidation with incorporation of Pd. It is clear from the figure that the light–off temperature (T_{50}) of Pd doped MnO_2 catalysts are at much lower temperature than that of MnO_2 catalyst. MnO_2 showed light off temperature (T_{50}) at 130°C, whereas $Mn_{0.92}Pd_{0.08}O_2$ gave at 69°C. This shows the difference of nearly 60°C. The gradual increase of Pd content to 8%, the active sites may be increasing accordingly. The 100% CO conversion on MnO_2 obtained at 200 °C, $Mn_{0.98}Pd_{0.02}O_2$ and $Mn_{0.95}Pd_{0.05}O_2$ showed T_{100} at 110 °C and 115 °C respectively. The $Mn_{0.92}Pd_{0.08}O_2$ gave total conversion at around 90 °C which is to a great extent much lower as compared to MnO_2, indicating that Pd doped MnO_2 is an excellent catalyst for CO oxidation reaction.

Generally CO oxidation on transition metal oxides follows a mechanism proposed by Mars–Van Krevelen [197], implying that the lattice oxygen incorporation occurs during CO oxidation and that the reduced surface of the metal oxide is rejuvenated by taking up oxygen from the feed mixture [244]. On the other hand, it is well known that the reactivity for the structure sensitive reaction depends on the particle size, surface morphology and crystal plane of the catalyst [122]. Thus surface structure of the catalyst also influences catalytic performance.

Maximum CO conversion over metal oxide catalyst greatly depends on the method of preparation. The preparation method mainly determines the surface area, and the higher surface area generally corresponds to higher oxidation activity. Inspite of $Mn_{0.92}Pd_{0.08}O_2$ having lower surface area it showed highest activity because Pd–MnO_2 interaction might result in more favorable surface active sites which give higher CO conversion at low temperature. This may be the main reason for higher catalytic activity.

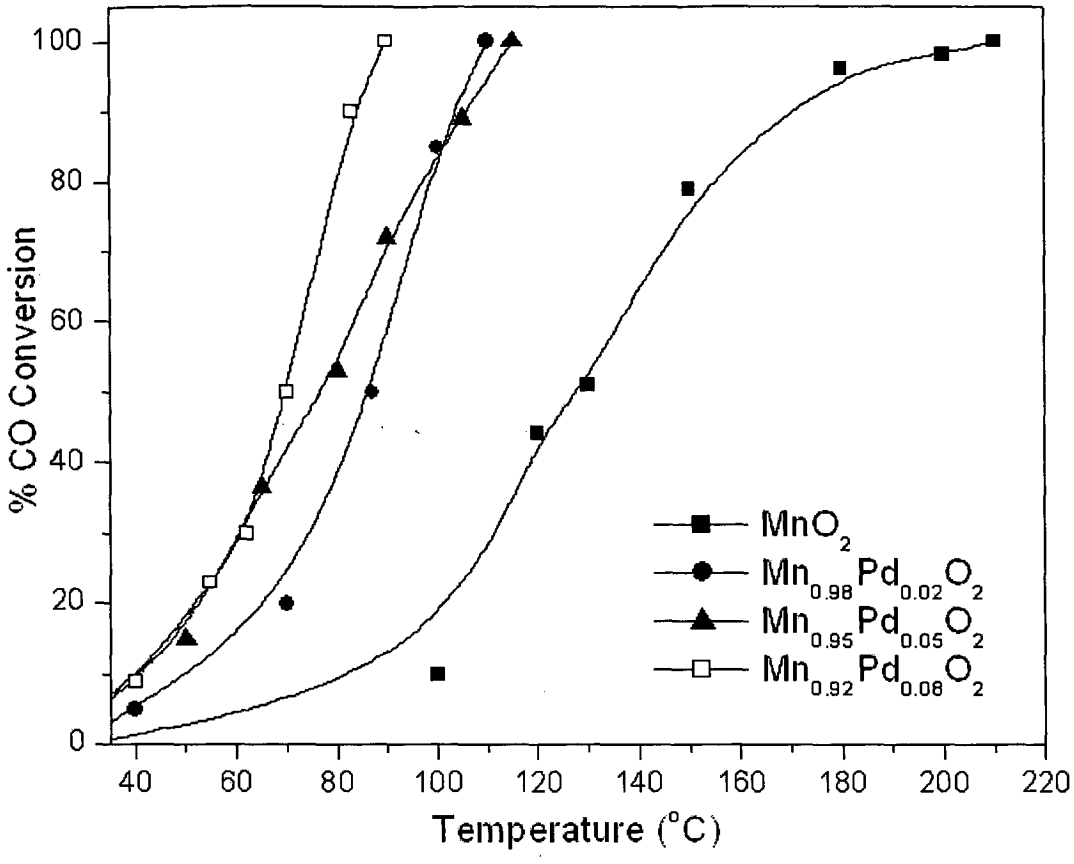

Fig. 5.12 CO conversion against Temperature over Pd-MnO_2 series.

Fig. 5.13 displays the temperature dependence of the CO oxidation over silver doped manganese dioxide catalysts. It is clear that the activity of the Ag doped MnO_2 catalysts are much higher than that for the pure MnO_2 catalysts. The incorporation of Ag greatly improved the catalytic activity for CO oxidation. The T_{50} and T_{100} (light-off temperature of 50% and 100% CO conversion respectively) values over Ag doped MnO_2 catalysts were obviously lower than that of pure MnO_2. The pure MnO_2 shows complete CO oxidation at 180 °C where as Ag doped MnO_2 catalysts show complete conversion below 125 °C. Moreover one can see that complete oxidation of CO could be attained at temperature 80 °C over $Mn_{0.95}Ag_{0.05}O_2$ catalyst. Even the Ag doped OMS-2 catalysts shows lower activity and shows complete CO oxidation above 100 °C [151,153]. The data in Fig. 5.13 also indicates that the oxidation activity per catalysts increased monotonously

with Ag doping, but for higher Ag doped samples the catalytic activity was found to be decreasing.

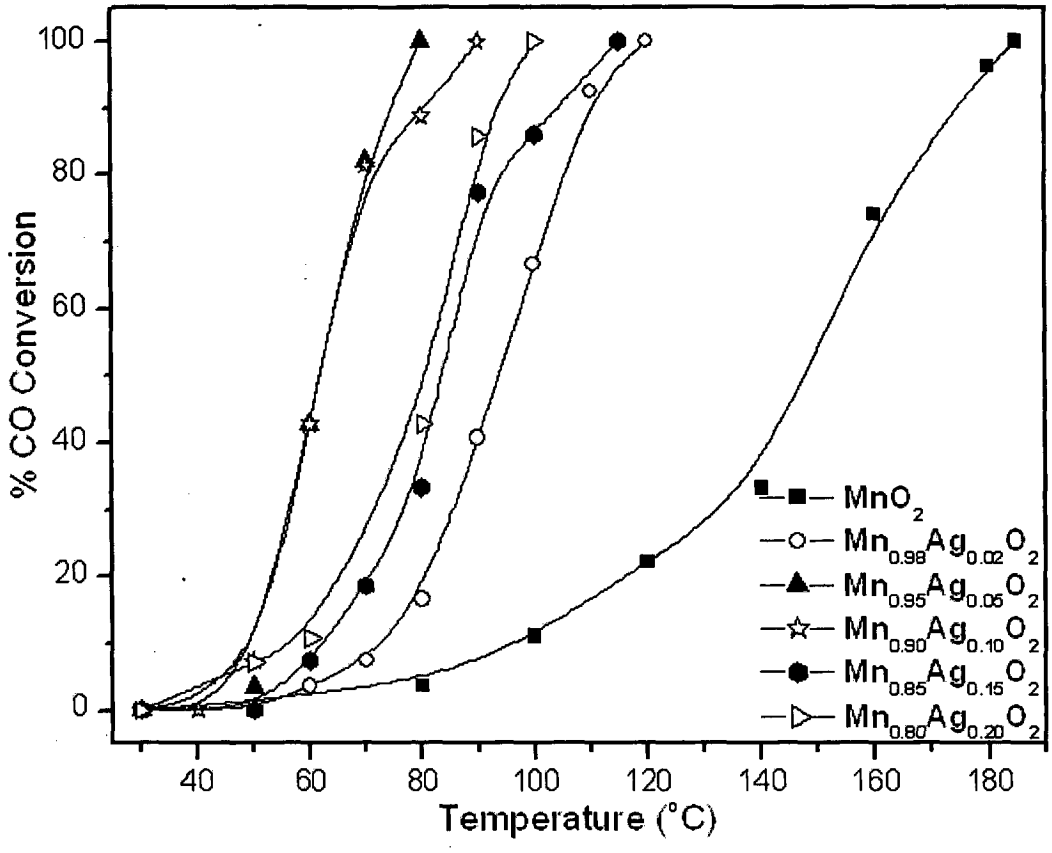

Fig. 5.13 CO conversion against Temperature over Ag-MnO_2 series.

Catalyst preparation is an important factor relating to the activity of catalyst. The preparation method mainly determines surface area and high surface area generally corresponds to more exposed active sites. Although these catalysts are of low surface area they show high catalytic activity for CO oxidation mainly due to more exposed active sites per unit area, hence results indicate that the catalytic activities of Ag doped MnO_2 are not significantly correlated with the BET surface areas. With gradual increase of Ag content to 10%, the active sites increase correspondingly, which results in the promotion of oxidation activity, while further increase of Ag content to 20%, excess Ag species may forms bulk AgO, leading to the less profound interaction between MnO_2 and Ag which causes decrease of CO oxidation activity.

As it is evidenced from TPD studies that there are strong adsorption sites on surface of Ag doped catalyst which are responsible for CO adsorption. As an electron donor, when CO molecule adsorbs on the surface of Ag, the C=O bond is activated by the back donation electrons from the filled d orbitals of Ag to CO $2\pi^*$ antibonding molecular orbitals. In addition incorporation of Ag produces a strong Ag–MnO_2 interaction [122] which also promotes CO adsorption. XRD and TEM studies suggest that Ag is highly incorporated in MnO_2 and probably interact strongly with MnO_2.

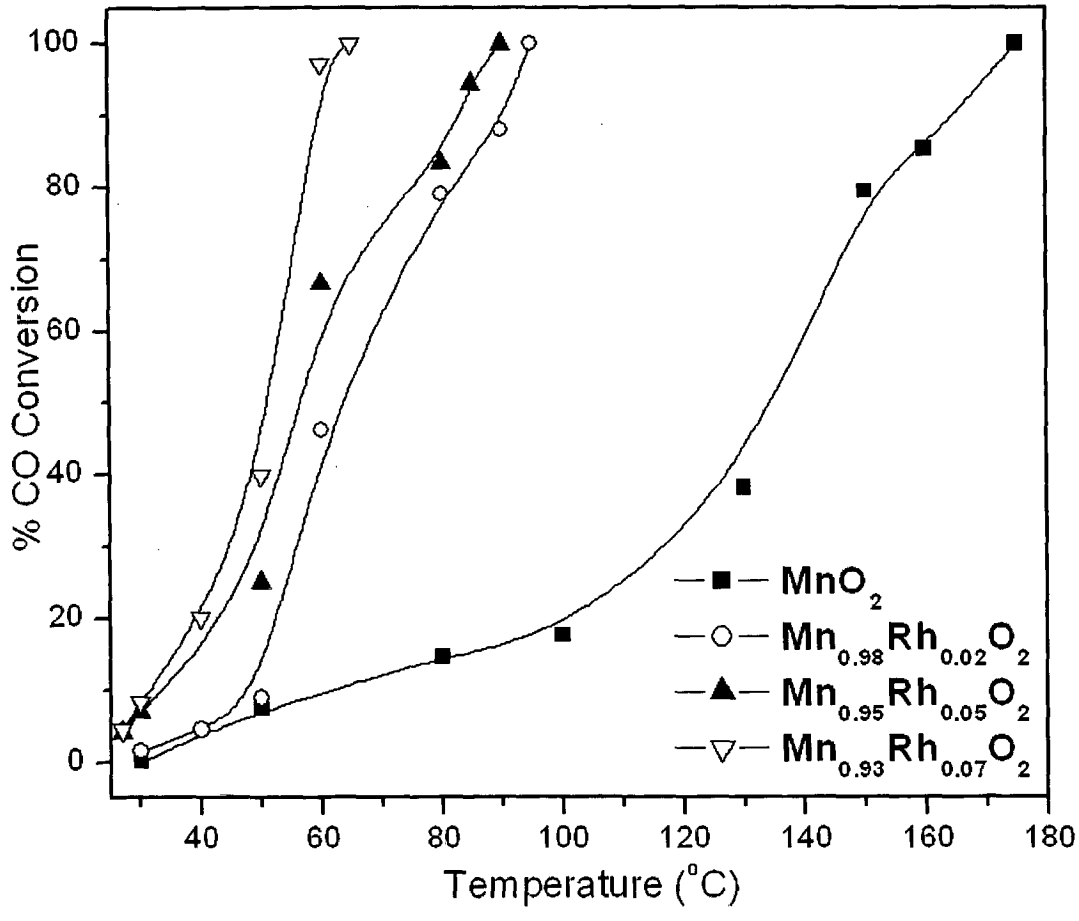

Fig. 5.14 CO conversion activity against Temperature over Rh-MnO_2 series.

Results of the oxidation of CO over the rhodium doped manganese dioxide catalysts against temperature are shown in Fig. 5.14. All the Rh doped catalysts are highly active for CO oxidation reaction at lower temperature as compared to pristine MnO_2. The data in Fig. 5.14 also indicate that the oxidation activity per catalyst increased monotonously with

increasing Rh concentration for the present samples, with T_{50} decreasing with increasing Rh loadings.

The preparation of catalysts and their calcination temperature also becomes the important factor for higher catalytic activity of the catalysts. XRD and TEM data illustrate that these catalysts are nano-crystalline in nature, the particles shows nano-rod like morphology. The BET surface area is also found to be very high as compare to other doped catalysts. All these factors highly influences the activity of these catalysts, the higher activity is mainly due to more exposed surface active sites which are mainly due to the presence of highly active rhodium incorporated in MnO_2 lattice.

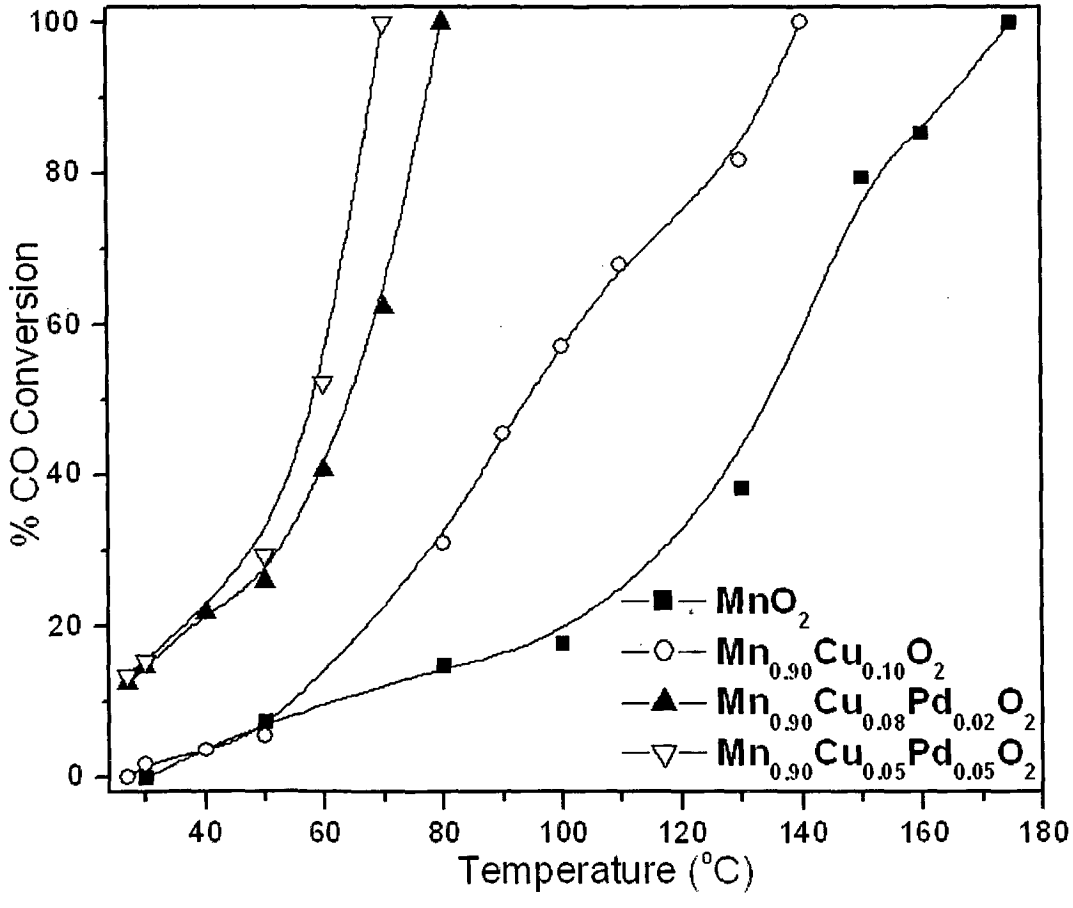

Fig. 5.15 CO conversion against Temperature over CuPd-MnO_2 series.

Fig. 5.15 displays the temperature dependence of the CO conversions for various Cu-Pd doped manganese dioxide catalysts. From the figure it is clear that the Cu-Pd doped

catalysts showed high activity for CO oxidation as compared to pure MnO_2 which gives complete conversion at around 180 °C. These catalysts showed activity even at room temperature. Incorporation of Cu-Pd in MnO_2 greatly improved the catalytic behavior of MnO_2, drastic decrease in total CO conversion temperature was observed and it showed conversion even at room temperature. In case Cu-Pd doped MnO_2, complete CO conversion was achieved at around 80 °C over $Mn_{0.90}Cu_{0.05}Pd_{0.05}O_2$ catalysts. The data in Fig. 5.15 also indicates that the oxidation activity increases monotonously with Cu-Pd loading with T_{50} decreasing with increase Pd loading. Addition of Cu-Pd facilitates the adsorption of CO as well as O_2 mainly due to more exposed surface active sites which may result due to interactions between Cu-Pd and MnO_2 showing enhanced activity. Catalyst preparation is an important factor relating to the activity of catalyst. The preparation method mainly determines the surface area and high surface area generally corresponds to more exposed active sites.

5.5.2 CO oxidation over doped Mn_2O_3 catalysts

Temperature dependence of the CO conversion for various Ni doped Mn_2O_3 illustrated in Fig. 5.16. Undoped Mn_2O_3 gave complete conversion of CO at a much higher temperature of around 400 °C. There is decrease in total CO conversion temperature in Ni doped Mn_2O_3 catalysts indicating that nickel doped catalysts showed better activity. The T_{50} and T_{100} (light-off temperature of 50% and 100% CO conversion respectively) values over Ni doped Mn_2O_3 catalysts were obviously lower than that of pure Mn_2O_3. Moreover, one can see that complete conversion can be achieved at a temperature around 300 °C over Ni doped Mn_2O_3 which is 100 °C less as compared to pure Mn_2O_3.

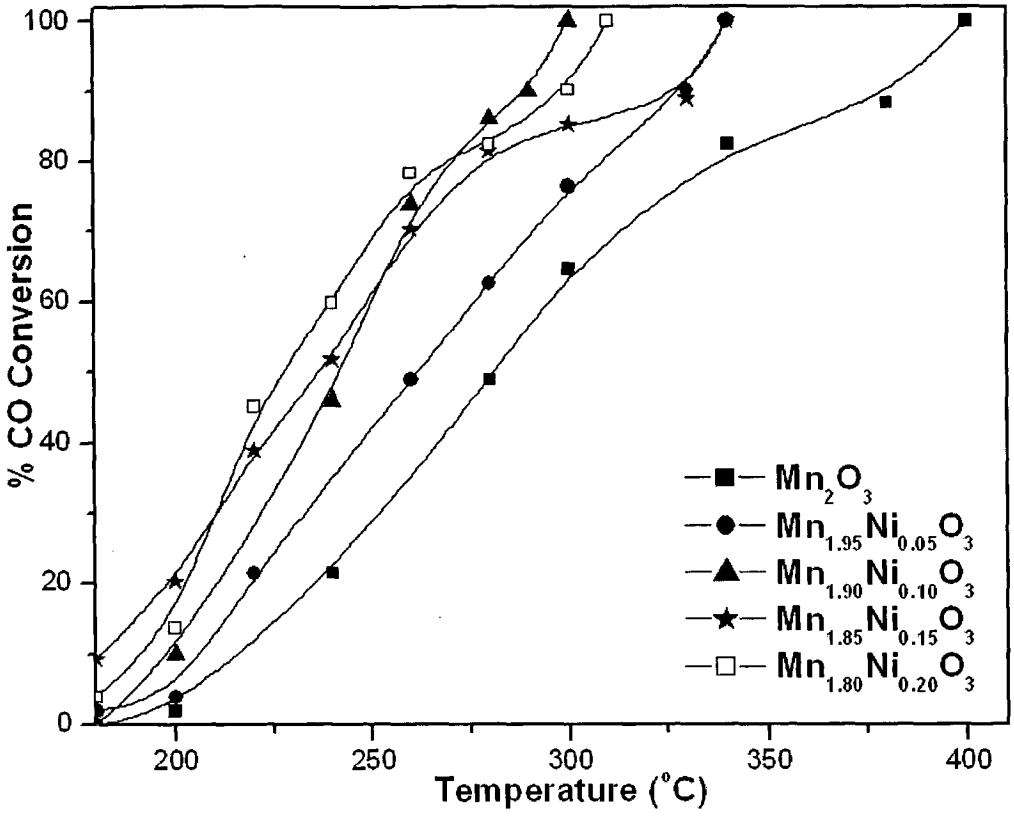

Fig. 5.16 CO conversion against Temperature over Ni-Mn_2O_3 series.

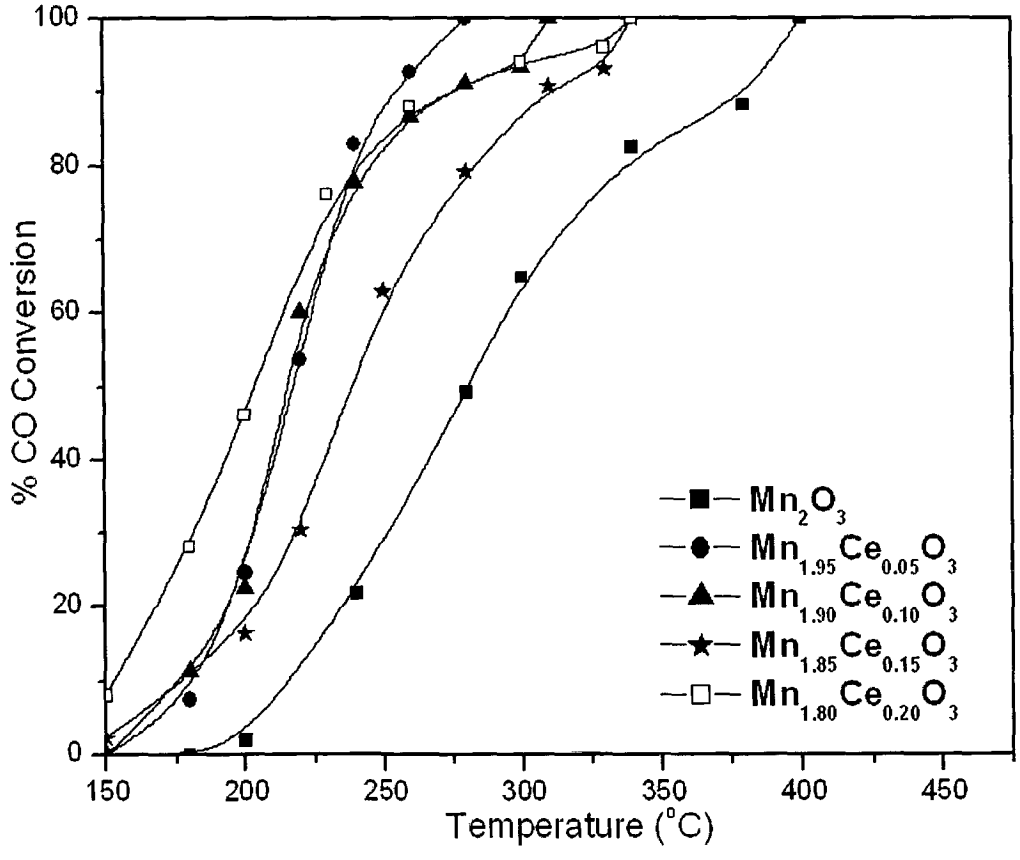

Fig. 5.17 CO conversion against Temperature over Ce-Mn_2O_3 series.

Similar is the case with the cerium doped Mn_2O_3 catalysts. Fig. 5.17 shows the CO oxidation activity against temperature over different catalysts. The complete conversion of CO could be achieved at lower temperature over ceriun doped catalysts compare to pristine Mn_2O_3 catalyst which shows synergistic effect of doping. The Ce doped gave conversion at around 280 °C which is around 120 °C less compare to pristine Mn_2O_3. From the BET surface area measurement studies it is evident that the surface areas of these catalysts are much lower. Hence the surface active sites will be less available for the adsorption of reactant and therefore higher activation energy is required for the reaction.

Fig. 5.18 displays the temperature dependence of the CO conversions for various Pd doped Mn_2O_3 catalysts. From the figure it is clear that Pd doped Mn_2O_3 catalysts show high activity for CO oxidation as compared to pure Mn_2O_3 catalyst which shows the synergistic effect of doping. In case of Pd doped Mn_2O_3 complete conversion was obtained at around 180 °C, whereas pristine Mn_2O_3 gave complete conversion at 400 °C which is at a much higher temperature compare to doped catalysts. Introduction of Pd in Mn_2O_3 greatly improved the catalytic behavior of Mn_2O_3, drastic decrease in total CO conversion temperature is observed. The data in Fig. 5.18 also indicates that the oxidation activity per catalyst increase monotonously with Pd loading with T_{50} decreasing with increased Pd loading. Another important occurrence is the smooth light-off behavior of doped catalysts, in contrast to that of pristine Mn_2O_3. It is clear that the light–off temperature (T_{50}) of Pd doped Mn_2O_3 catalysts are at a much lower temperature than that of Mn_2O_3 catalyst. Addition of Pd in Mn_2O_3 facilitates the adsorption of CO as well O_2 which in turn shows higher activity.

Generally CO oxidation on manganese oxides follows a mechanism proposed by Mars-Van Krevelen [197] implying that lattice oxygen incorporation occurs during CO oxidation and that the reduced surface of the manganese oxide is rejuvenated by taking up

oxygen from the feed mixture. CO is adsorbed on the surface as bidentate carbonate, the adsorbed CO extracts surface oxygen atom to form CO_2 and surface oxygen vacancy. The oxygen vacancy is filled by gas phase O_2, weakening the bond in O_2 molecule. This adsorbed O_2 species, which is believed to be present possibly as O_2^- ion radical, may react readily with a neighboring CO molecule adsorbed as bidentate carbonate, forming CO_2 again and recovering back the catalysts surface. Presence of Pd greatly improved this activity by increasing active sites.

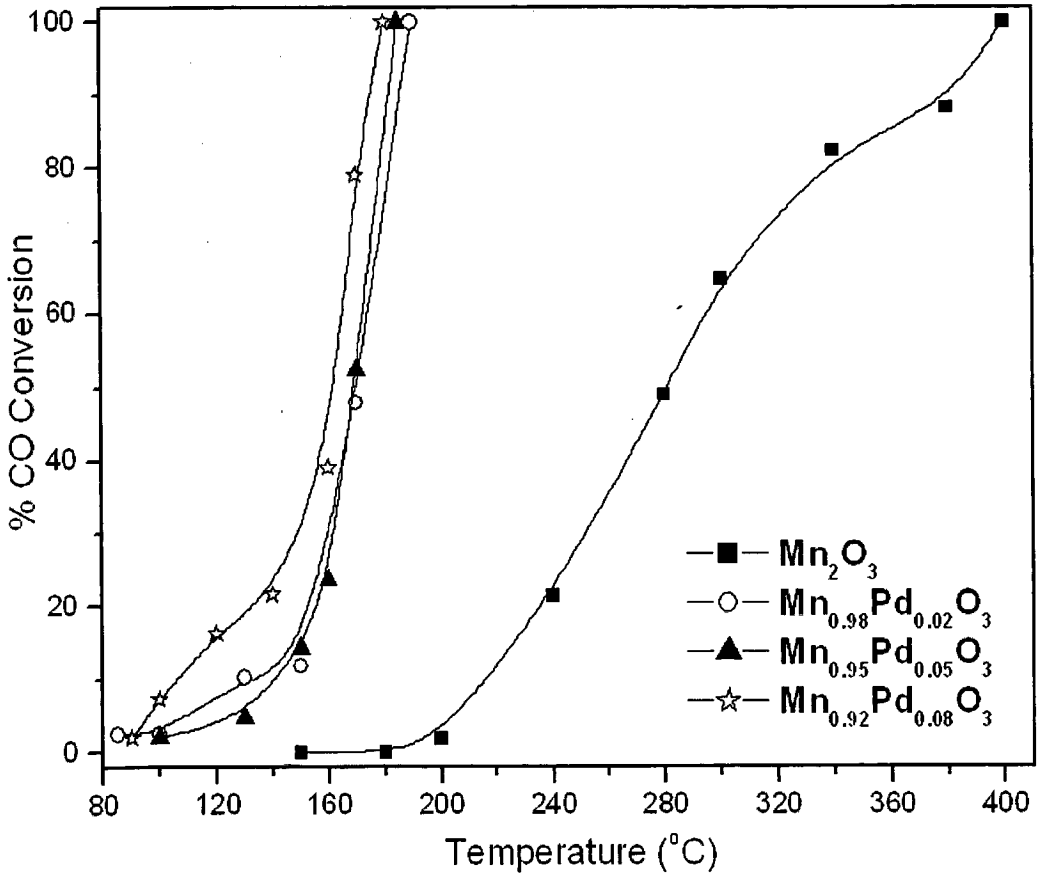

Fig. 5.18 CO conversion against Temperature over Pd-Mn_2O_3 series.

The catalytic activity of silver doped Mn_2O_3 catalysts for CO conversion reaction given in Fig. 5.19. The Ag doped Mn_2O_3 catalysts showed good activity as compared to undoped Mn_2O_3. The Mn_2O_3 showed complete conversion of CO at a temperature of 310 °C whereas the silver doped catalysts show the conversion below 260 °C. Nevertheless, one

can see that the complete conversion of CO could be reached at a temperature of 220 °C which is approximately 100 °C lower than pristine Mn_2O_3. The BET surface area of silver doped Mn_2O_3 was found to be very less as can be seen in the BET data. Inspite of lower surface area these catalysts showed good activity. The higher activity may be due to the presence of Ag species.

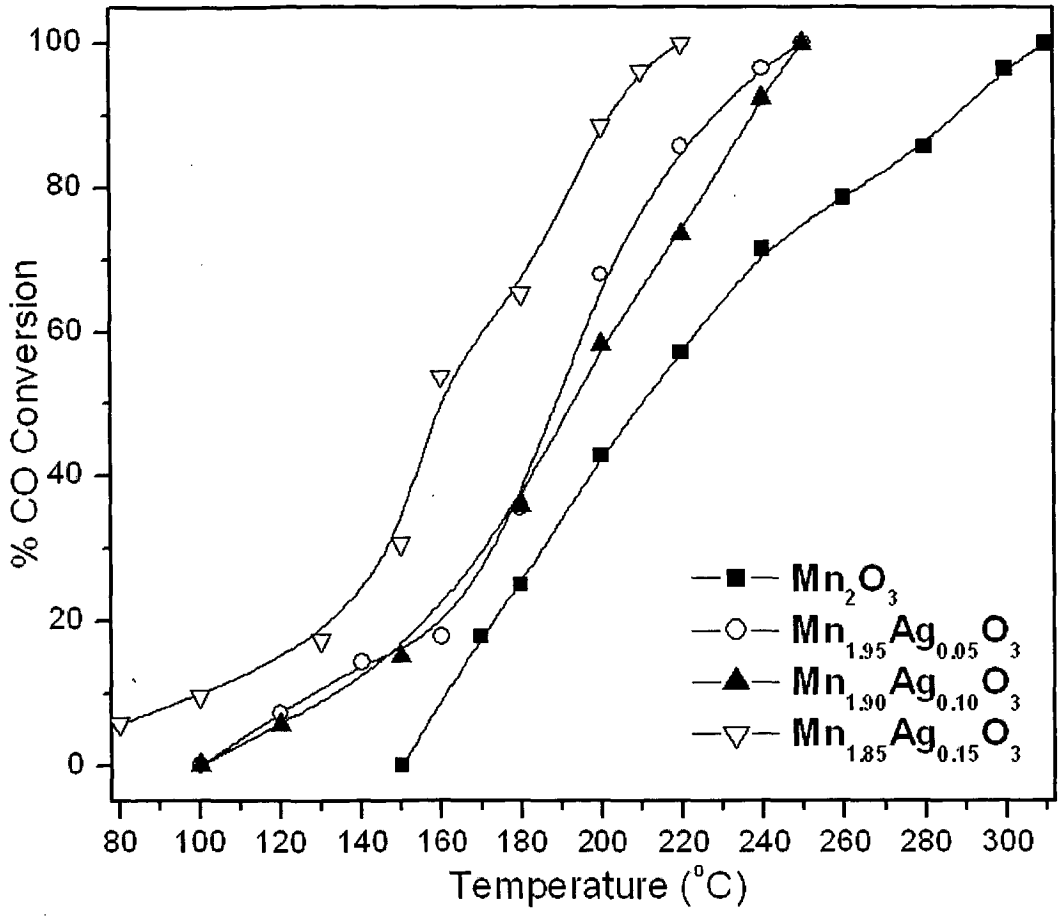

Fig. 5.19 CO conversion against Temperature over Ag-Mn_2O_3 series.

5.5.3 CO oxidation over supported catalysts

The outlet CO concentrations over different palladium supported Mn_2O_3 catalysts as a function of catalyst temperature are shown in Fig. 5.20. As the reactor temperature increased, the CO concentration decreased. The complete conversion of CO was obtained

at a temperature of 110 °C over 3.3 wt% Pd/Mn_2O_3 catalyst, 5.3 wt% Pd/Mn_2O_3 catalysts gave total conversion at 90 °C and both showed the activity at room temperature. The pristine Mn_2O_3 gave complete conversion at 400 °C which is at a much higher temperature compared to supported catalysts. The data in Fig. 5.20 also indicates that the oxidation activity increases with Pd loading with T_{50} decreasing with increase in Pd loading.

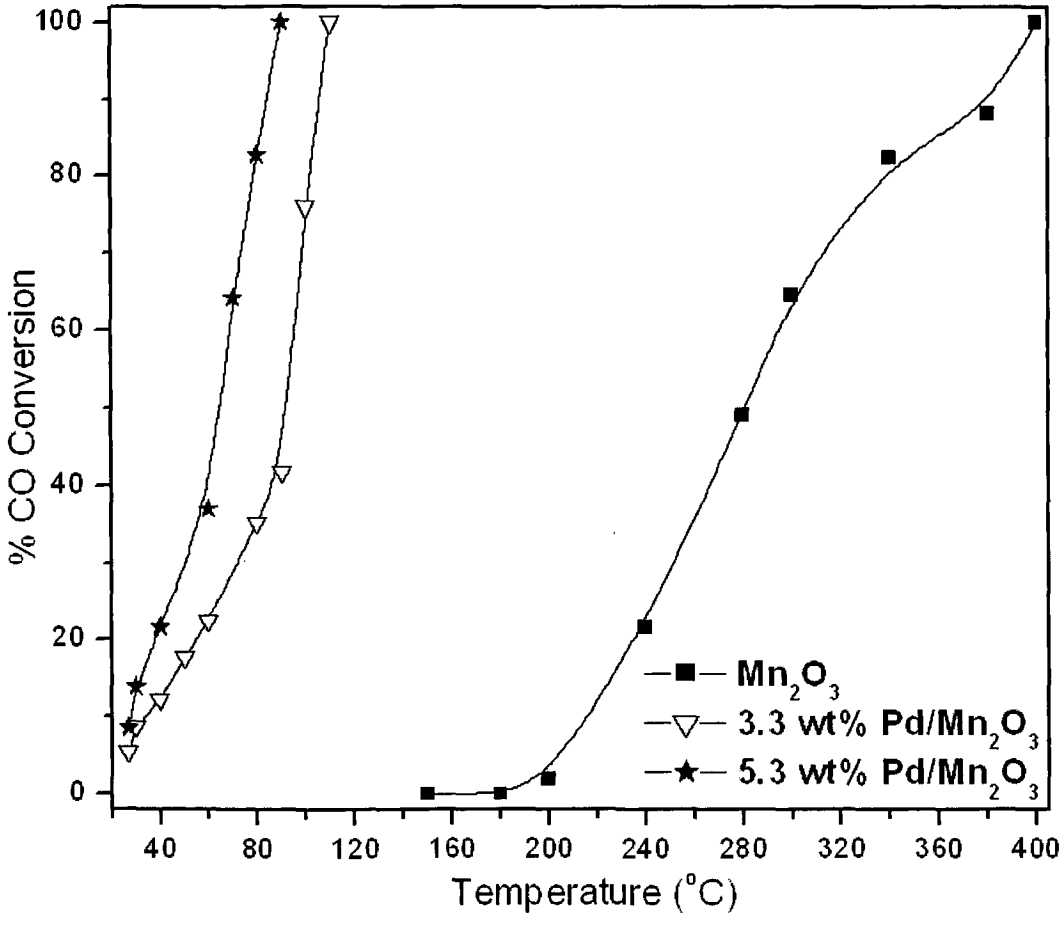

Fig. 5.20 CO conversion against Temperature over Pd supported Mn_2O_3 series.

The pristine Mn_2O_3 shows very poor activity, the surface area of Mn_2O_3 is 5.5 m^2g^{-1} which is very low and the surface area of Pd supported samples is almost double than that of pure Mn_2O_3. However, if the catalytic activity for CO oxidation is considered one can see that the surface area is still comparatively less for Pd supported samples. The drastic decrease in total CO conversion temperature was observed over Pd supported Mn_2O_3 catalysts, complete conversion can be achieved at a temperature less than 100 °C over Pd

supported Mn_2O_3 which is 300 °C less compared to pure Mn_2O_3. The higher activity is mainly due to more exposed surface active sites which may result due to the Pd-Mn_2O_3 interactions [122]. The active oxygen on Pd is consumed mainly in the oxidation of CO, and Mn serves as an oxygen carrier [245]. Moreover, interaction favors the oxygen spillover from Mn to Pd and improves catalytic activity.

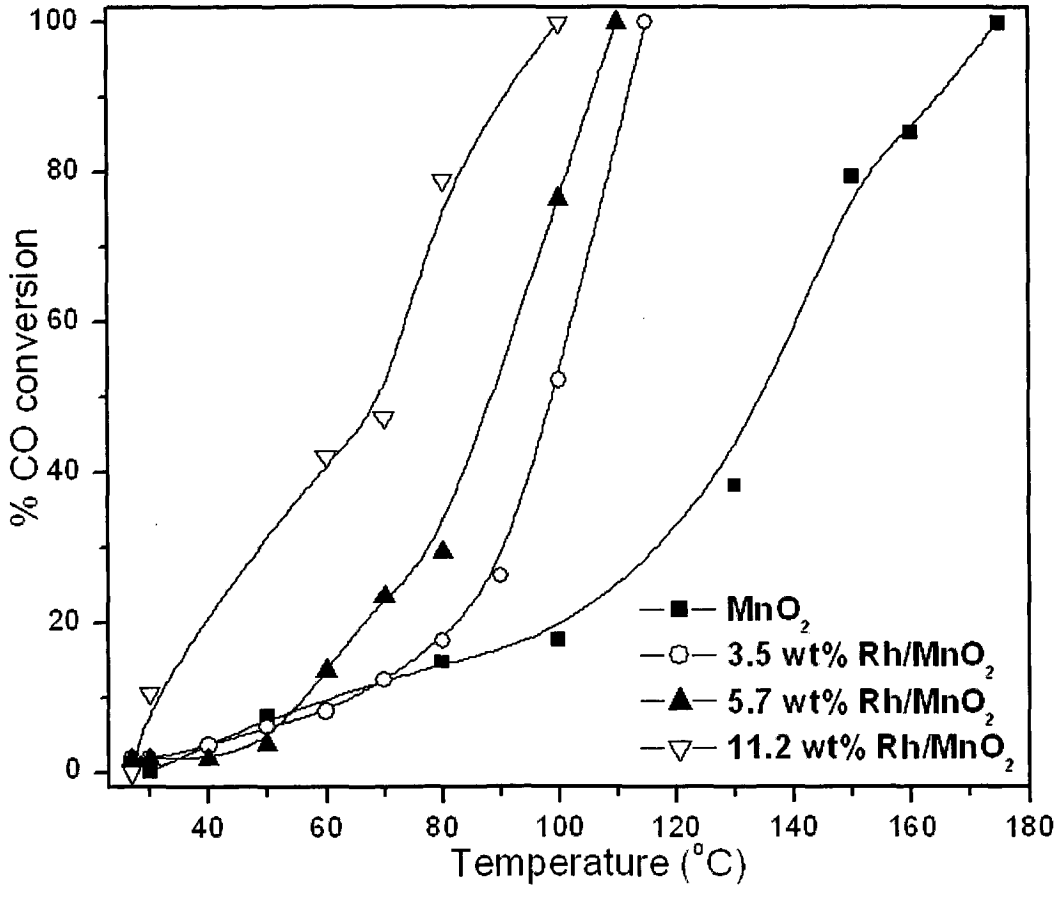

Fig. 5.21 CO conversion against Temperature over Rh supported MnO_2 series.

The CO oxidation curves over the rhodium supported on MnO_2 series of catalysts are shown in Fig. 5.21. Curves are depicted as percentage CO conversion versus reaction temperature. The activity results have shown that the Rh/MnO_2 catalysts are more active than the pristine MnO_2. With increasing Rh loadings the CO oxidation activity was found to be increasing as can be seen from figure. The 11.2 wt% Rh/MnO_2 show complete conversion of CO at 100 °C, which is the most active among all. The surface area of all Rh

supported catalysts was found to be almost in the same range, but with increasing concentration of rhodium activity increases. Thus the activity depends on the amount of Rh loadings. The CO oxidation activity of Rh supported MnO_2 catalysts was found to be lower as compared to the activity of Rh doped MnO_2 catalysts. The surface area of Rh doped samples was higher and increases with increasing Rh loading than Rh supported sample, there may be a possibility of the formation of bulk Rh_2O_3 species which may lead to less profound interaction between Rh and MnO_2.

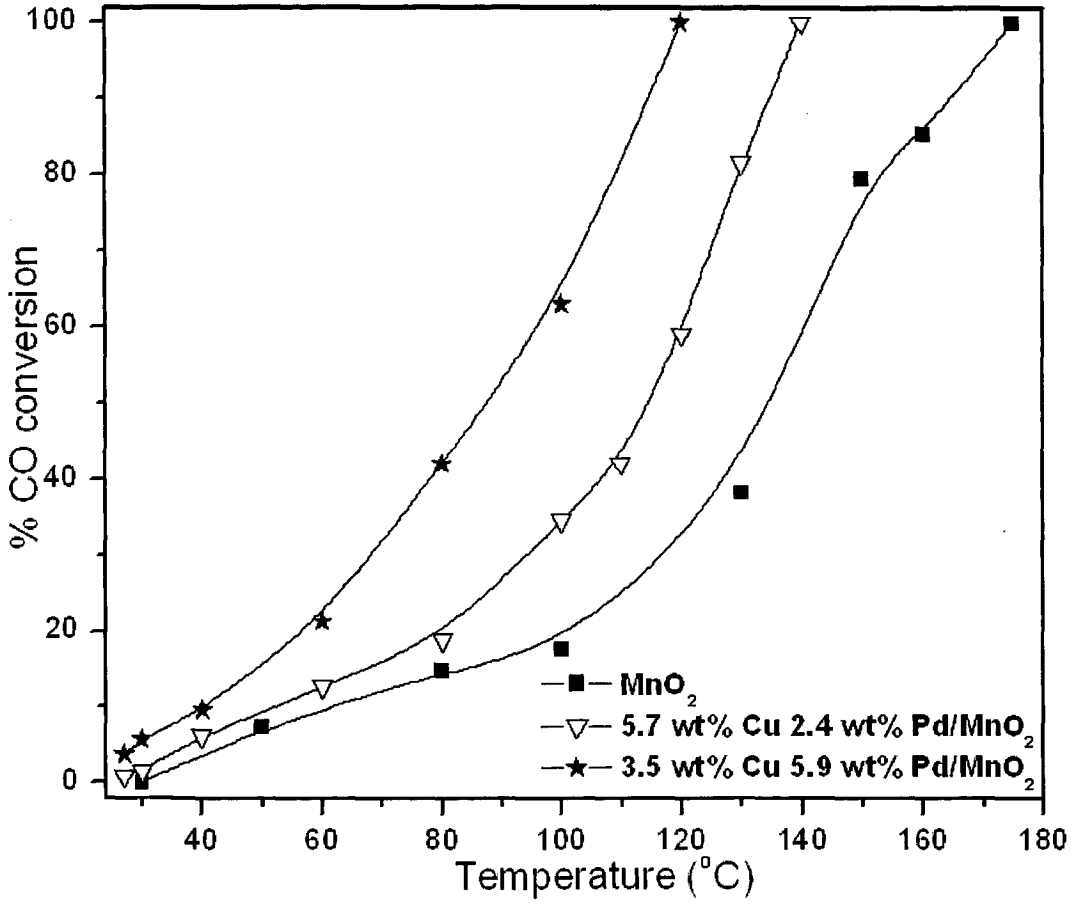

Fig. 5.22 CO conversion against Temperature over Cu-Pd supported MnO_2 series.

Fig. 5.22 shows the catalytic performance for CO oxidation of the Cu-Pd supported MnO_2 catalysts, as well as pure MnO_2 catalyst for comparison. From the figure it is clear that the Cu-Pd supported MnO_2 catalysts showed high activity for CO oxidation as compared to pure MnO_2 which gives complete conversion at around 180 °C. Incorporation

of Cu-Pd in MnO_2 improved the catalytic behavior of MnO_2. 3.5 wt% Cu 5.9 wt% Pd/MnO_2 catalyst gave complete conversion at 120 °C, which is relatively lower than pure MnO_2, and showed difference of around 60 °C. Compared to other supported catalysts which are mentioned above, the CO oxidation activity of these Cu-Pd MnO_2 supported catalysts seems to be lower. Surface area may be one of the reasons for the same, as the surface area of other supported MnO_2 catalysts is much higher than Cu-Pd MnO_2 supported catalysts. Moreover, the catalytic activities of Cu-Pd doped MnO_2 catalysts are higher than Cu-Pd supported MnO_2 and their surface area was also higher.

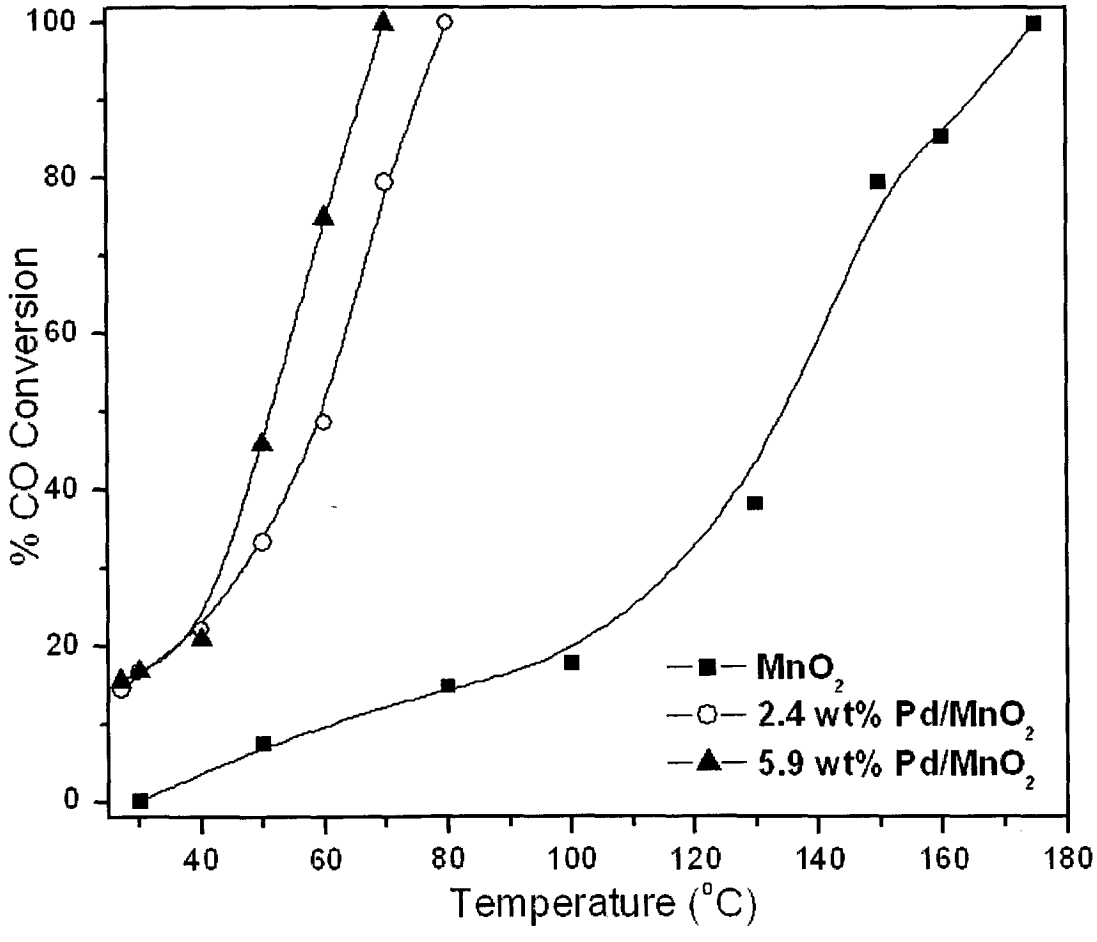

Fig. 5.23 CO conversion against Temperature over Pd supported MnO_2 series.

Fig. 5.23 shows the CO oxidation activity over Pd supported MnO_2 samples. In the present study the CO oxidation ability of Pd supported manganese dioxide was evaluated and compared with other supported catalysts. Pd supported samples showed very good

activity as can be seen in Fig. 5.23, both the samples showed room temperature CO conversion. The activity of these catalysts found to be much higher compared to pristine MnO_2. Even the activity of Rh supported samples was also found to be lower for CO oxidation reaction. A synergistic effect has been observed for CO oxidation as palladium metal and manganese support oxide were combined [47,48].

5.6 Influence of partial pressure oxygen

20% O_2 and 40% O_2

The normal laboratory prepared feed gas composition was 5% CO, 5% O_2 in nitrogen, but for the study of the effect of excess oxygen, we increased the concentration of oxygen in the feed gas. Effect of excess oxygen was studied with oxygen concentration 20% (5% CO, 20% O_2 in nitrogen) and 40% (5% CO, 40% O_2 balance in nitrogen). This study was done to determine the role of excess oxygen in CO oxidation reaction over these catalysts. This excess oxygen study was done on some of the prepared series

Fig. 5.24 illustrates the effect of excess oxygen, both 20% and 40% O_2 on Ag doped MnO_2 series. No decrease in activity for CO conversion was observed under the influence of 20% O_2, but instead it showed slight increase in activity. Also in case of 40% O_2 slight increase in activity was observed than that of 20% O_2. From the above figures it is clear that influence of excess oxygen favours catalysts for CO oxidation reaction and showed improved activity. Thus the possibility of blocking of active sites for CO adsorption over the surface due to excess oxygen is not encountered. The total CO oxidation temperature is also lowered by around 10 ^{o}C, thus higher oxygen in feed gas supports the CO oxidation activity of the catalysts.

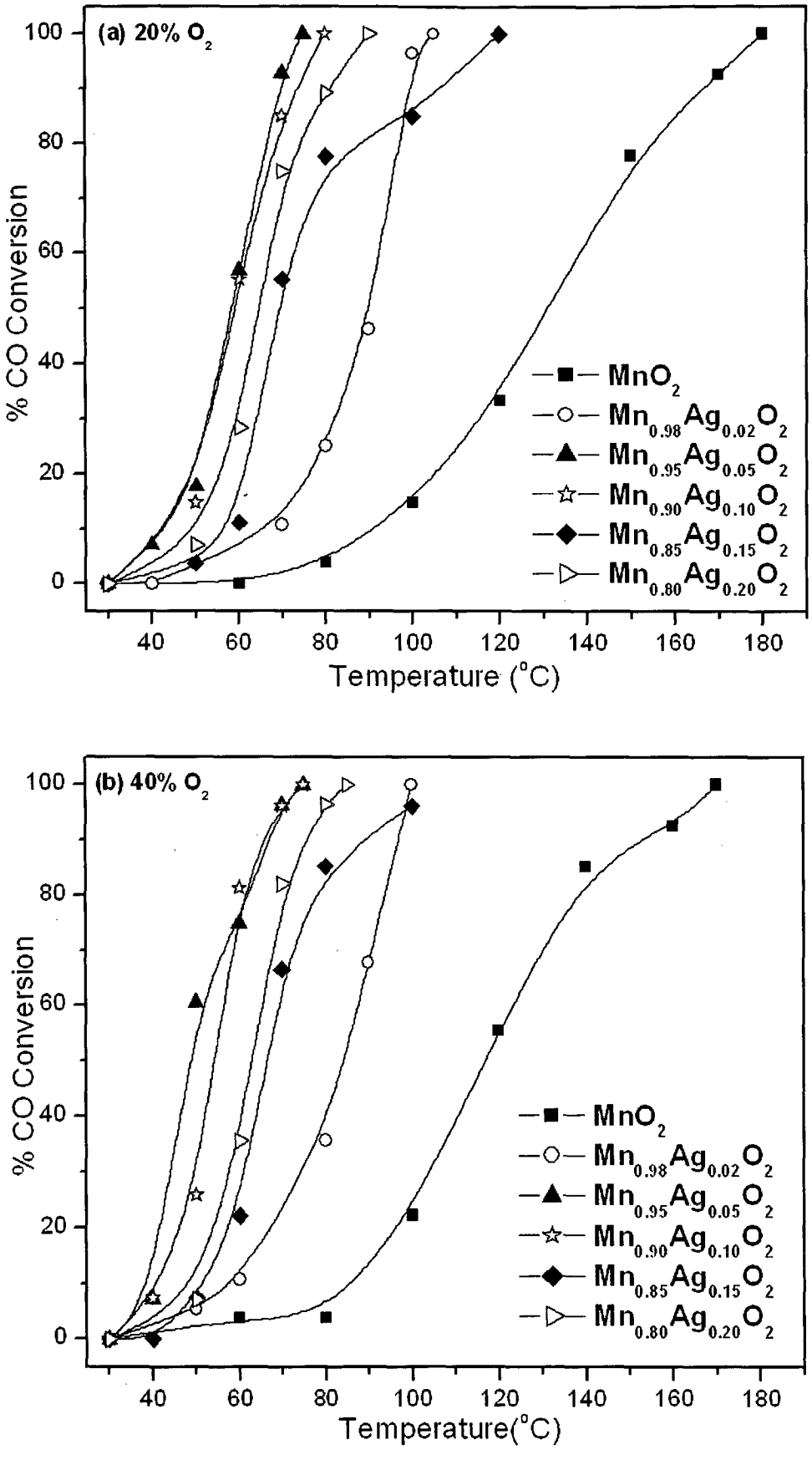

Fig. 5.24 Excess oxygen study over Ag-MnO_2 series, (a) 20% O_2 and (b) 40% O_2.

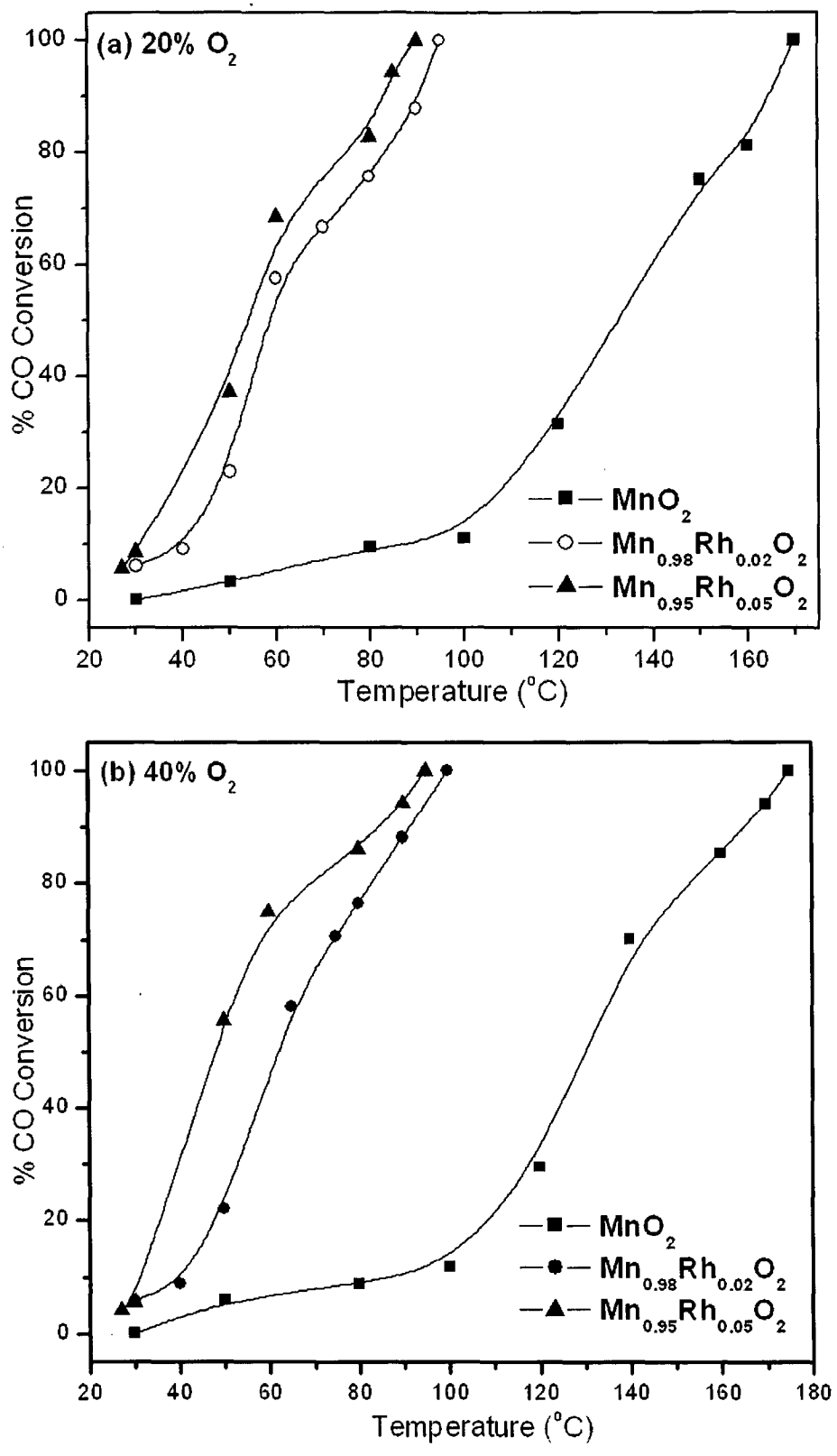

Fig. 5.25 Excess oxygen study over Rh-MnO_2 series, (a) 20% O_2 and (b) 40% O_2.

Rhodium doped MnO_2 catalysts also showed good activity in presence of excess oxygen in the feed gas mixture, the results are shown in Fig. 5.25. The $Mn_{0.98}Rh_{0.02}O_2$ and

$Mn_{0.95}Rh_{0.05}O_2$ catalysts showed good activity at lower temperature, they also showed similar activity in presence of higher oxygen. Under both the conditions they showed good activity without any deactivation process.

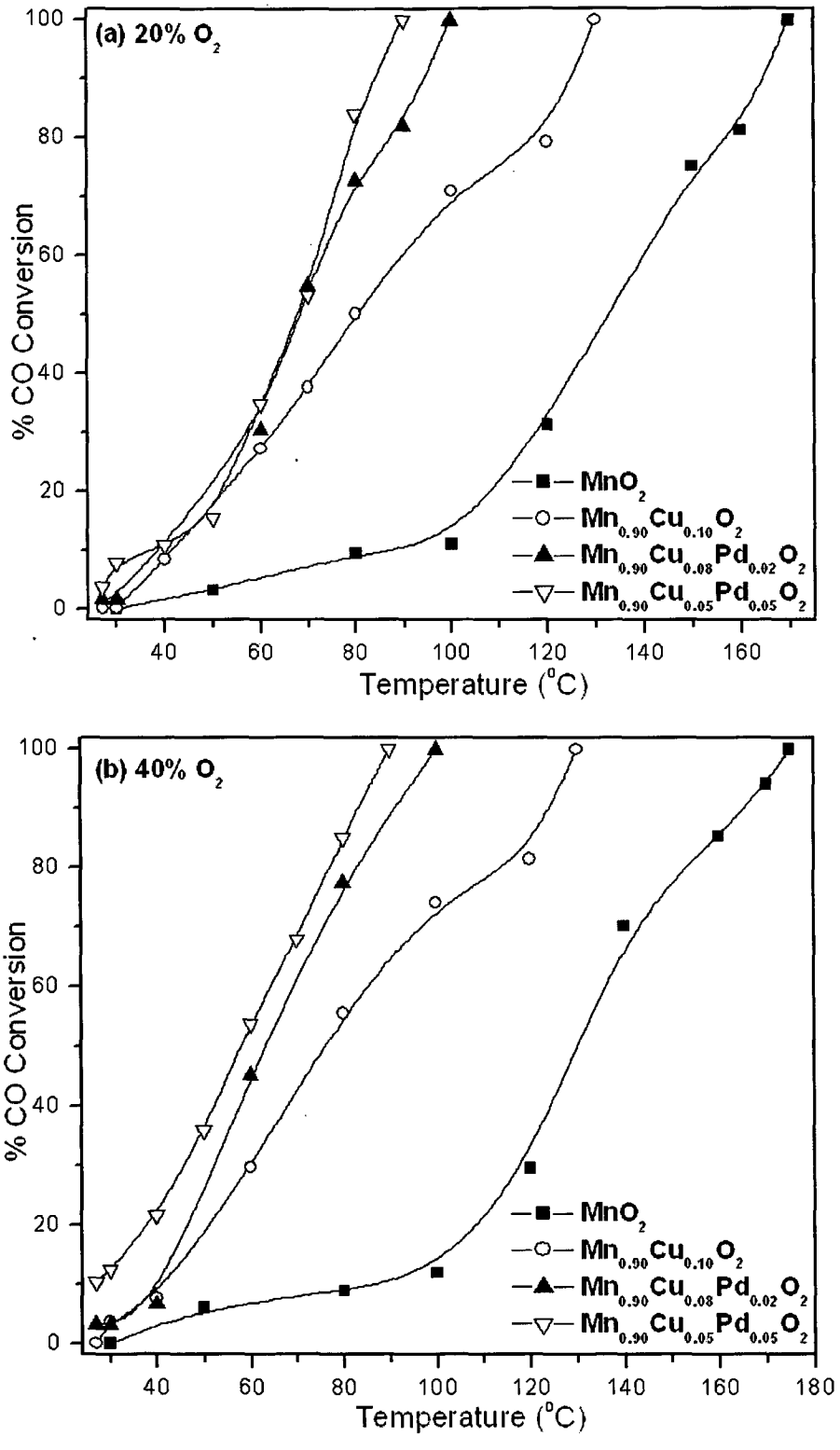

Fig. 5.26 Excess oxygen study over CuPd-MnO_2 series, (a) 20% O_2 and (b) 40% O_2.

Fig. 5.26 shows the catalytic activity of Cu-Pd doped MnO_2 catalysts under the influence of excess oxygen. Presence of more amount of oxygen in the feed gas does not affect the catalytic CO oxidation reaction over these catalysts. It can be seen that in presence of excess oxygen, the catalysts works well, and even showed improved activity.

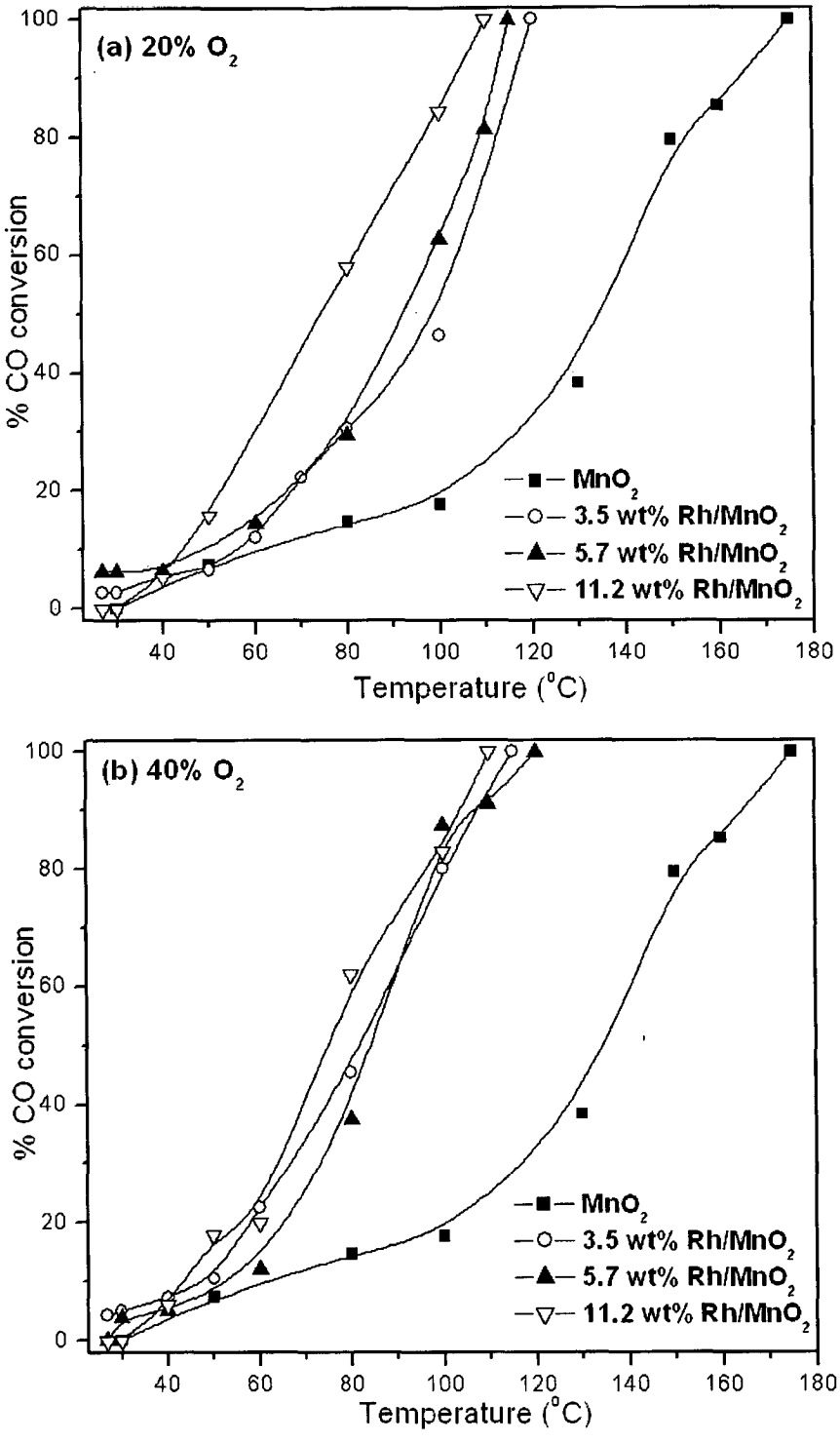

Fig. 5.27 Excess oxygen study on Rh supported MnO_2 series, (a) 20% O_2 and (b) 40% O_2.

Excess oxygen studies were also carried out on some of the supported catalysts. The Fig. 5.27 shows the results for Rh supported MnO_2 catalysts. From figure it is observed that 3.5 wt% Rh/MnO_2 and 5.7 wt% Rh/MnO_2 shows almost the same behavior, 11.2 wt% Rh/MnO_2 shows little bit of change in the CO oxidation curve. Moreover, one can see that total conversion temperature remains almost similar in both the condition.

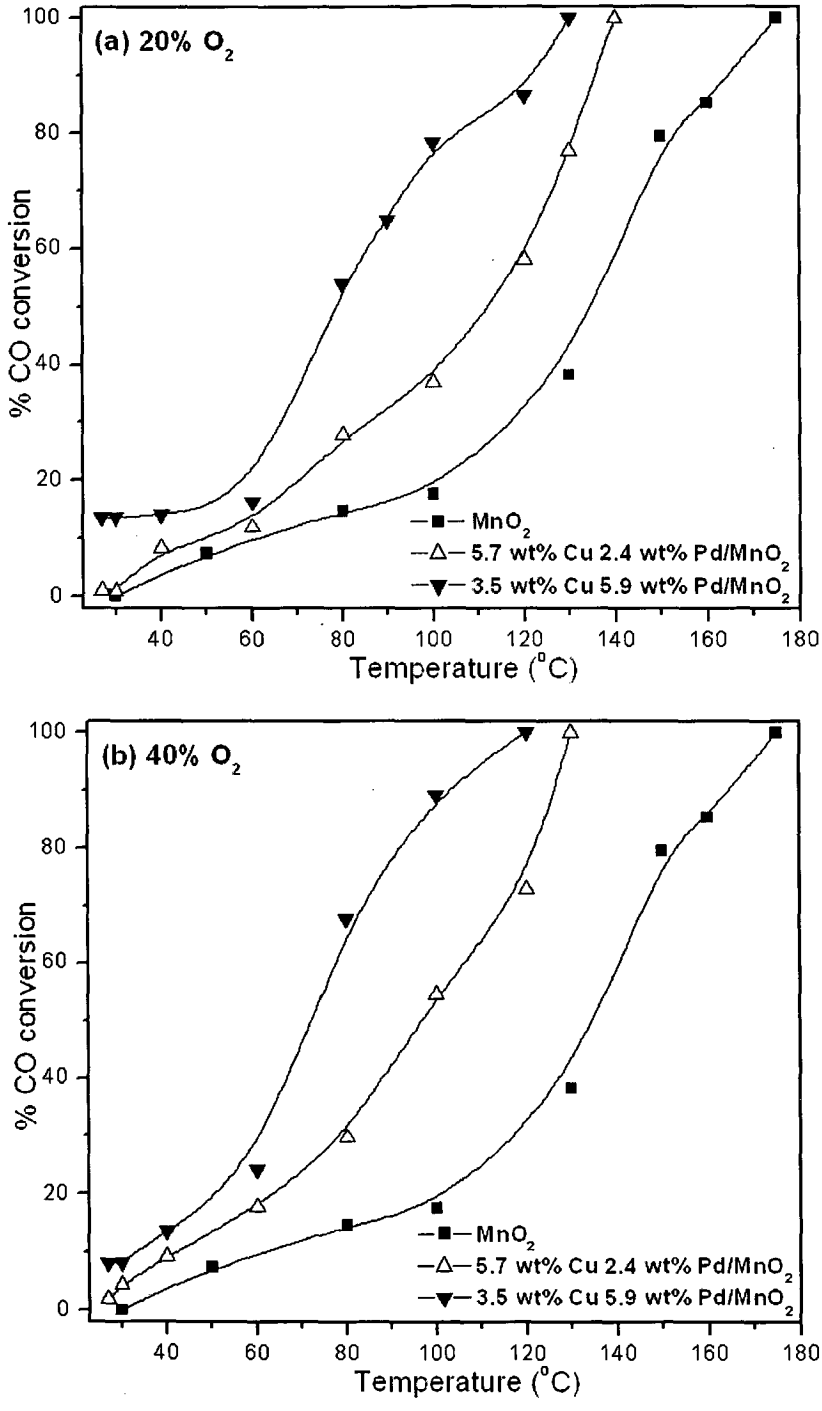

Fig. 5.28 Excess oxygen study over $CuPd/MnO_2$ series, (a) 20% O_2 and (b) 40% O_2.

Fig. 5.28 depicts the influence of excess oxygen over CuPd supported MnO_2 series. The catalytic performance of these catalysts was found to be same as that of 5% O_2 in the feed. No deactivation is accounted but rather it showed improved behavior.

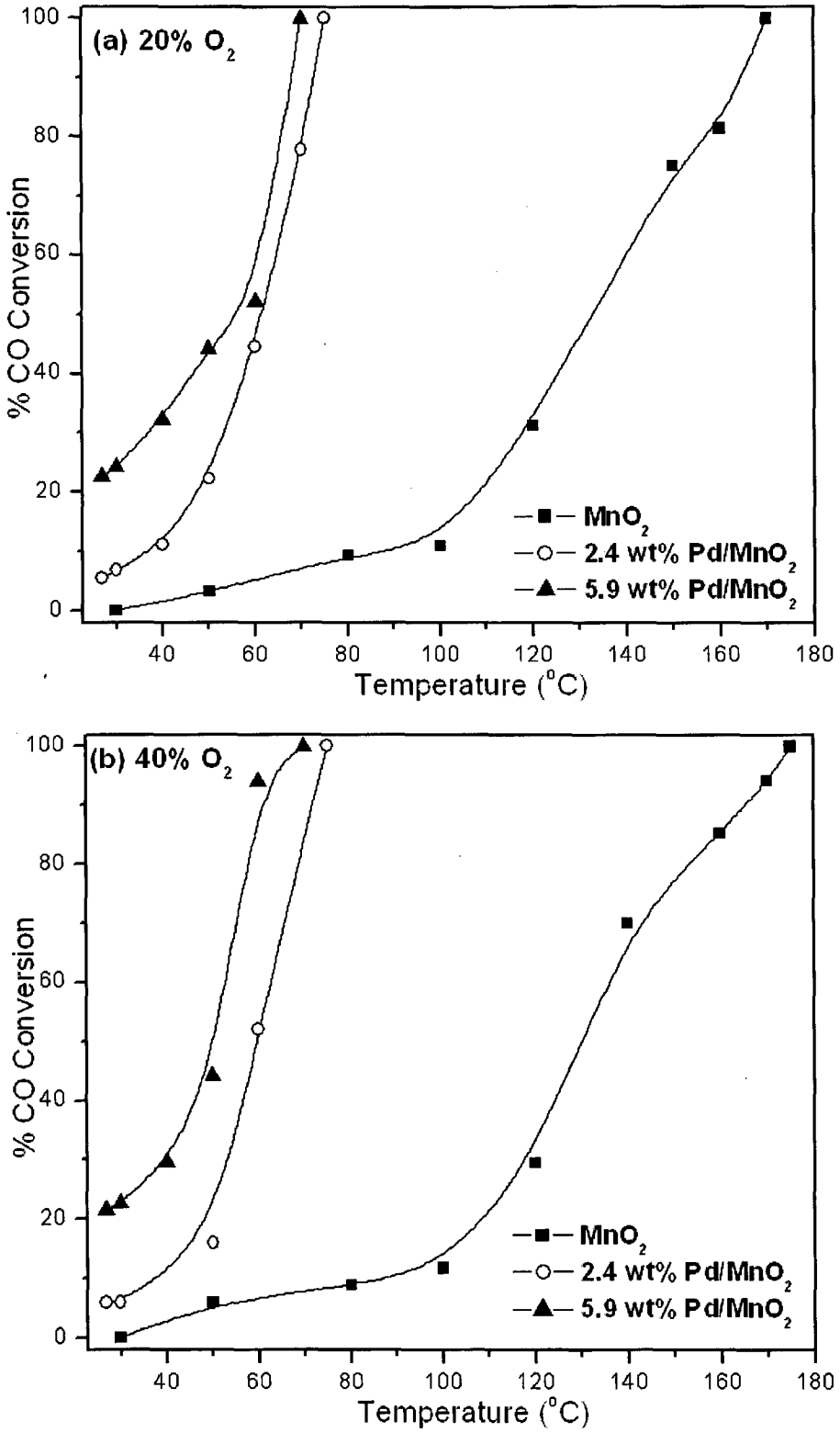

Fig. 5.29 Excess oxygen study on Pd supported MnO_2 series, (a) 20% O_2 and (b) 40% O_2.

The influence of excess oxygen over Pd supported MnO_2 catalysts is shown in Fig. 5.29 These catalysts also showed a good activity under the influence of excess oxygen. Moreover, in both the conditions (20% and 40% O_2 partial pressure) catalysts found to be stable for CO oxidation reaction.

5.7 Stability study (Time on stream studies)

Time on stream experiments were carried out on the catalysts for oxidation reaction of CO continuously for longer period by maintaining the catalysts at a fixed temperature to evaluate the stability of catalysts. The experimental conditions were the same as that for CO activity test with feed gas composition 5% CO and 5% O_2 in nitrogen and with the flow rate of 5000 ml h^{-1}.

Activity alone is not the only criterion that must be fulfilled for a suitable catalyst for CO oxidation. Long term stability is also a crucial feature, the catalysts must be stable for longer period with good efficiency which will make it cost effective. Two main factors may contribute to the deactivation of catalyst surface in CO oxidation reaction, first is the growth of particle size induced by the exothermic nature of the reaction and secondly due to the accumulation of carbonates blocking the active sites.

Some of the selected catalysts from the all different series have been tested for time on stream studies experiment.

The activities of the catalysts MnO_2 and $Mn_{0.92}Pd_{0.08}O_2$ were tested for CO oxidation continuously for 10 h by maintaining the temperature of the catalyst near to its 50% CO conversion temperature (T_{50}).

MnO_2 catalyst was maintained at a fixed temperature of 130 °C to check the activity. Around 52% CO conversion was observed in 1 h. After 10 h nearly 60% CO conversion was observed, indicating increase in activity with time. Fig. 5.30 depicts the results of the activity test. No decrease in activity of the catalyst was accounted during this period, signifying that MnO_2 catalyst is a good catalyst for CO conversion.

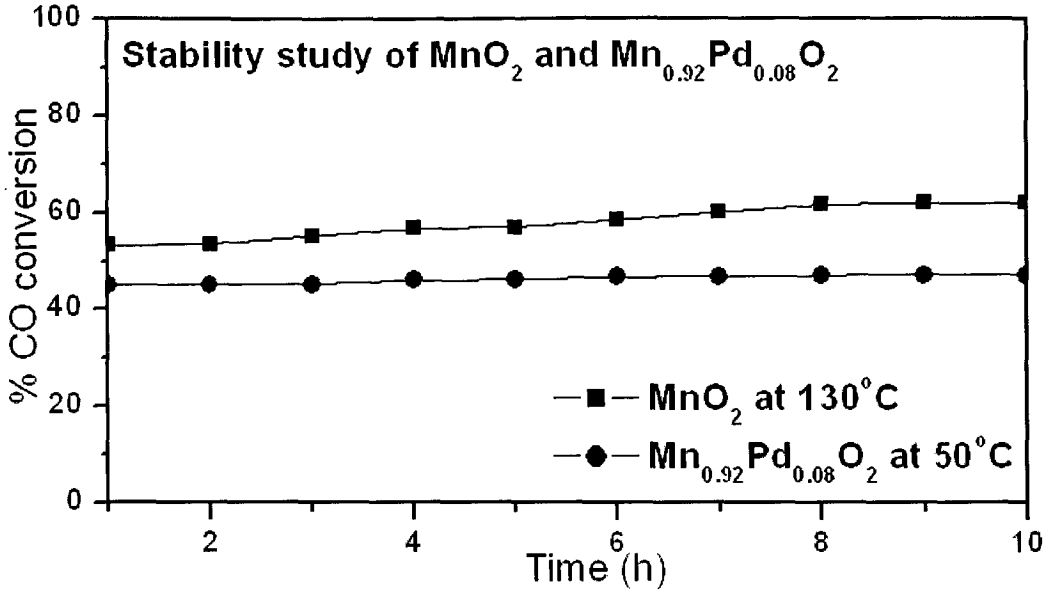

Fig. 5.30 Stability study of MnO_2 and $Mn_{0.92}Pd_{0.08}O_2$ at temperature 130 °C and 50 °C.

The activity of $Mn_{0.92}Pd_{0.08}O_2$ was also tested for 10 h continuously. This test was performed to ascertain whether the activity of the catalyst retains with increasing reaction time or not. The catalyst was kept at a fixed temperature of 50 °C. With increase in the reaction time, the CO conversion remains almost constant with a slight increase. Fig. 5.30 shows the results of activity test. It is reported that palladium oxide powder shows high activity for CO oxidation even at room temperature [246], but its activity decreases with increasing temperature. But when MnO_2 was doped with Pd, a strong interaction occurs between Pd and MnO_2 which results in high catalytic activity. Even catalyst like Ag doped OMS-2 shows very low activity at 100 °C and its activity goes on decreasing with increasing time [151].

Time on stream studies were carried out on MnO_2 and $Mn_{0.95}Ag_{0.05}O_2$ catalysts for oxidation of CO continuously for 12 h. MnO_2 catalyst was maintained at 130 °C, from Fig. 5.31 it is clear that the catalyst is stable for CO oxidation for longer period and also an increase in activity was observed. The $Mn_{0.95}Ag_{0.05}O_2$ catalyst was maintained at 60 °C, it also shows good stability and increase in activity. Initially it showed around 42% conversion which reaches to 55% after 12 h. Comparatively, the Ag doped OMS-2 catalyst showed low activity at 100 °C and whose activity declines with increase in reaction time [151].

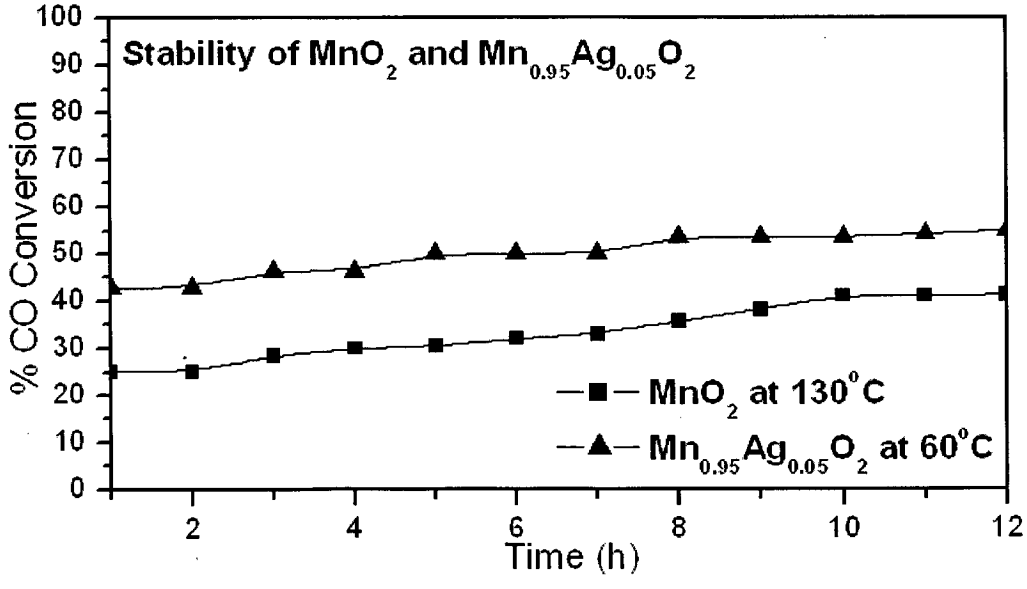

Fig. 5.31 Stability study of MnO_2 and $Mn_{0.95}Ag_{0.05}O_2$ at temperature 130 °C and 60 °C.

Thus the results of stability test shows that MnO_2 and Ag doped MnO_2 catalysts are highly stable for CO oxidation reaction. The basic building block for most of the manganese oxide is the MnO_6 octahedra [40], they are generally porous material and often crystallizes as microporous tunnel structures. This tunnel structure is necessary for high CO oxidation activity [151] and incorporation of Ag ions and their mobility may also play important role in CO oxidation.

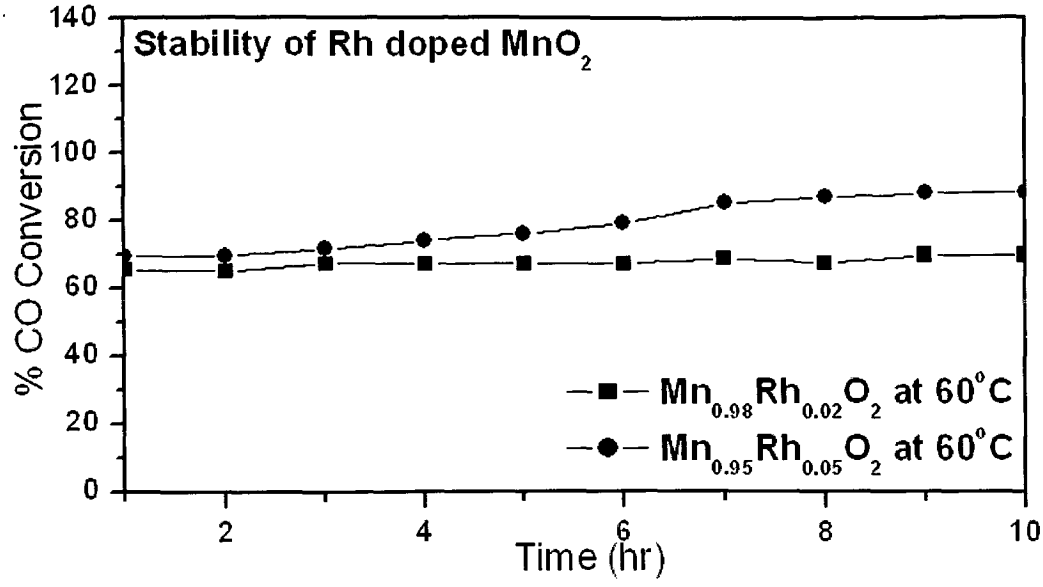

Fig. 5.32 Stability study of Rh doped MnO_2 catalysts.

Fig. 5.32 shows the time on stream studies for Rhodium doped MnO_2 catalysts to study the activity for longer period of time. These catalysts were kept at fixed temperature of 60 °C, they showed good activity for longer period of time and no deactivation is observed in the long run. The $Mn_{0.95}Rh_{0.05}O_2$ catalyst showed increase in activity with time, the increase in activity with time crop up may be due to the activation of surface active sites which are responsible for CO adsorption resulting in more CO conversion.

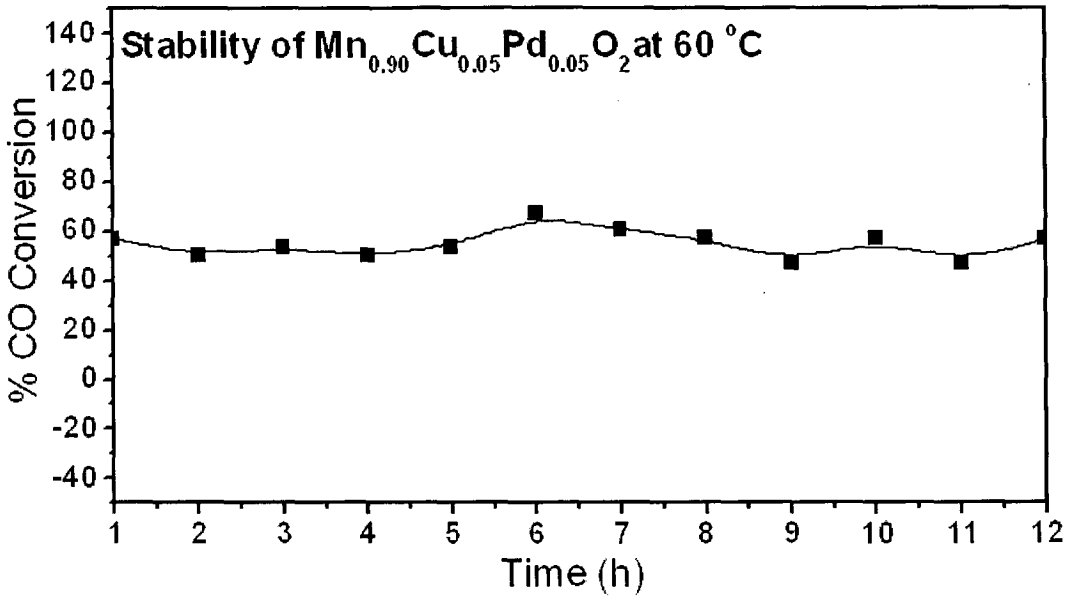

Fig. 5.33 Stability study of $Mn_{0.95}Cu_{0.05}Pd_{0.05}O_2$ at fixed temperature 60 °C.

$Mn_{0.90}Cu_{0.05}Pd_{0.05}O_2$ catalyst was maintained at a fixed temperature of 60 °C. After 1 h, the CO conversion was around 56% which remained almost stable up to 12 h, indicating good stability with time as seen in Fig. 5.33. No decline in activity was accounted during this period signifying good stability of this catalyst.

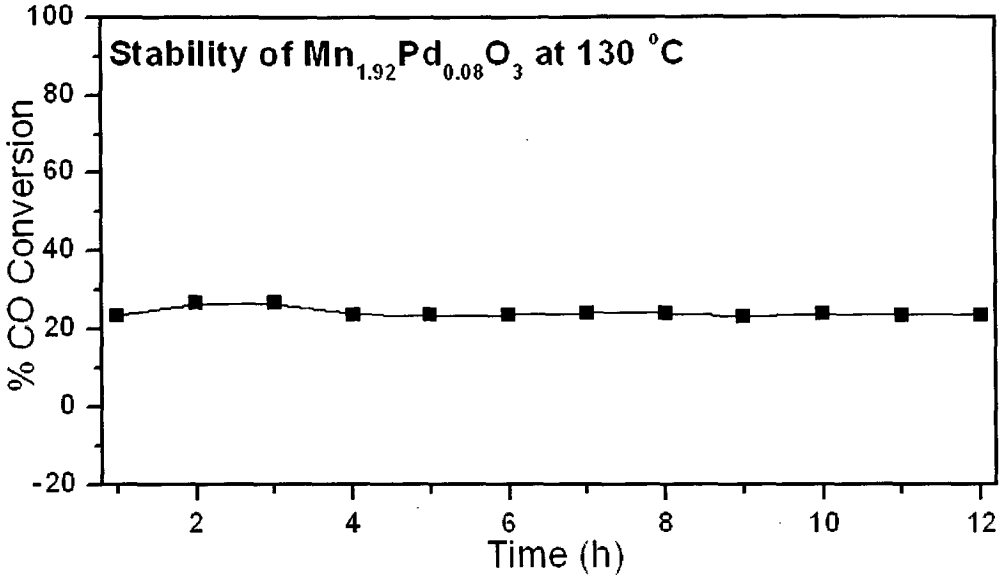

Fig. 5.34 Stability study of $Mn_{1.92}Pd_{0.08}O_3$ at fixed temperature 130 °C.

Fig. 5.34 shows the time on stream studies for $Mn_{1.92}Pd_{0.08}O_3$. This catalyst was maintained at a fixed temperature of 130 °C. After 1h, the CO conversion was around 23%, initially it showed a slight raise in the activity. With increasing time the activity of this catalyst remained almost stable for up to 12 h, indicating good stability with time. Thus the doped Mn_2O_3 catalysts also showed good stability for CO oxidation reaction for longer period.

The time on stream studies were also carried on some of the selected supported catalysts. The time on stream studies were performed for these catalysts to determine whether they retain their activity for longer period of time.

Fig. 5.35 shows the time on stream studies for 5.3 wt% Pd/Mn_2O_3 catalyst. This catalyst was kept at a fixed temperature of 60 °C. Around 20% CO conversion was shown after 1 h

which remained steady with increase in reaction time. No decline in activity was accounted during this period signifying good stability of these catalysts.

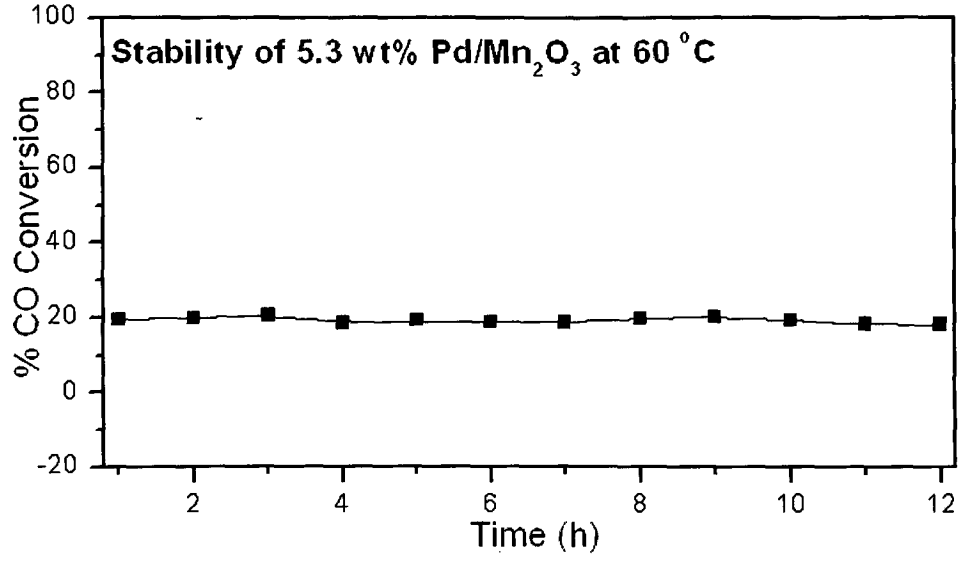

Fig. 5.35 Stability study of 5.3 wt% Pd/Mn_2O_3 at fixed temperature 60 °C.

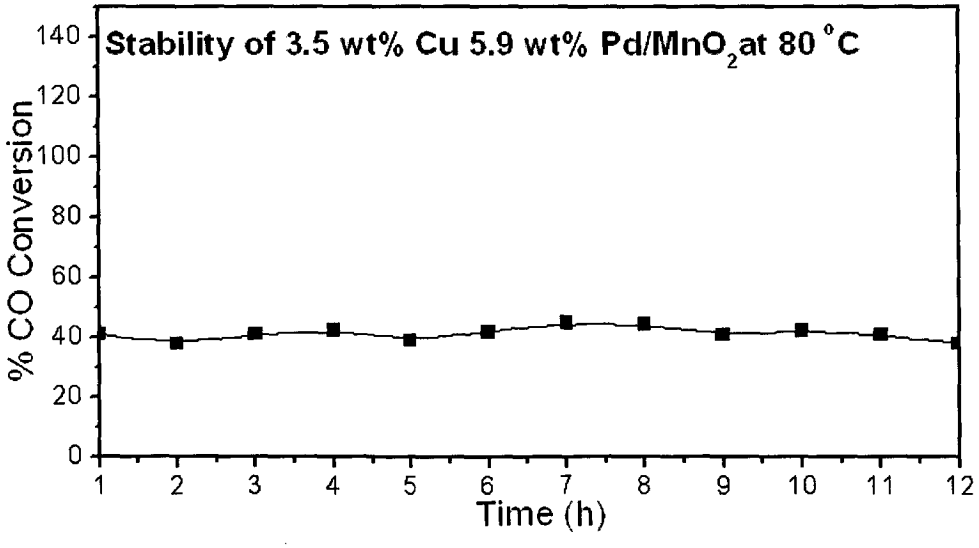

Fig. 5.36 Stability study of 3.5 wt% Cu 5.9 wt% Pd/MnO_2 at fixed temperature 80 °C.

The stability of 3.5 wt% Cu 5.9 wt% Pd/MnO_2 catalyst was also tested, this catalyst was kept at fixed temperature of 80 °C. The Fig. 5.36 depicts the time on stream studies of 3.5 wt% Cu 5.9 wt% Pd/MnO_2. Around 40% CO conversion was shown after 1 h which remained steady with increase in reaction time. No decline in activity was accounted during this period signifying good stability of this catalyst.

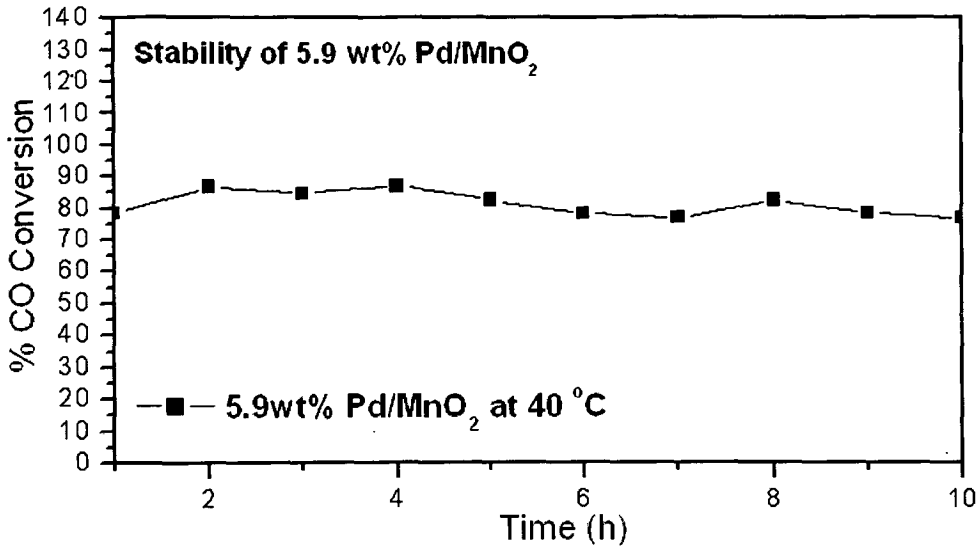

Fig. 5.37 Stability study of 5.9 wt% Pd/MnO_2 catalysts.

The time on stream study for palladium supported MnO_2 catalysts is shown in Fig. 5.37. The 5.9 wt% Pd/MnO_2 catalyst was kept at fixed temperature of 40 °C. This catalyst showed around 80% CO conversion after 1h, and further increase in reaction time the activity found to be stable and reaches around 78% after 10 h.

5.8 Influence of moisture on catalytic activity

The influence of moisture on catalytic activity was studied to determine whether the addition of a few moles of water vapor along with feed gases enhances or suppresses the reaction. The prepared catalysts will be of immense importance if it gives good activity in presence of moisture. The activity was studied in the presence of high and low moisture content. The experimental conditions were the same as that for CO oxidation activity with feed gas composition 5% CO and 5% O_2 in nitrogen and with the flow rate of 5000 ml h^{-1}.

The activity of catalyst in the presence of low moisture content was tested by allowing the mixture of feed gases to pass through water trap (maintained at room temperature) before passing through the catalyst bed. At room temperature the number of water

molecules passing along with feed gases was around $1.6730x10^{21}$ molecules h^{-1}. Also the activity of the catalyst was tested with high moisture content by allowing the mixture of feed gases to pass through water trap (maintained at 50 °C temperature) before passing through the catalyst. At 50 °C the number of water molecules passing along with feed gases was around $8.3117x10^{21}$ molecules h^{-1}. In both the cases time on stream experiments were performed by keeping catalysts at fixed temperature.

The activities of MnO_2 and $Mn_{0.92}Pd_{0.08}O_2$ catalysts were tested under the influence of moisture to see the effect of moisture. The results are shown in Fig. 5.38.

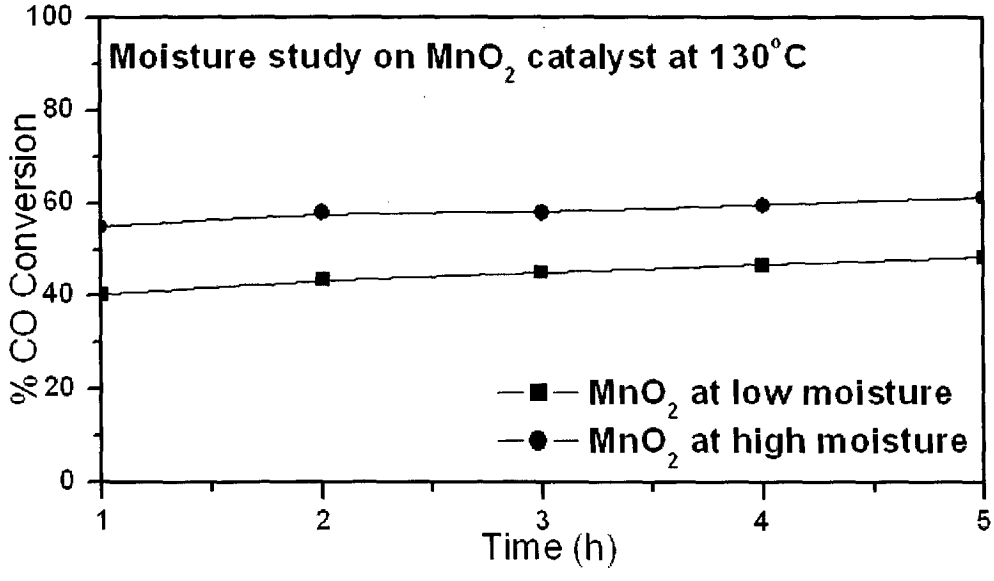

Fig. 5.38 Moisture study on pristine MnO_2.

MnO_2 catalyst was kept at a fixed temperature of 130 °C, and then the mixture of feed gases coming from the water trap was allowed to pass through the catalyst bed. Under the influence of low moisture, after 1 h, nearly 52% CO conversion was observed. Later CO conversion was found to increase and after 5 h 58% CO conversion was observed as seen in Fig. 5.38. This illustrates that the catalyst retains its activity under the influence of moisture and the results obtained in the presence of moisture are much better than in its absence. With increasing time of the reaction there was an increase in activity of the

catalyst indicating optimistic effect of moisture on the MnO_2 catalyst. The effect of high moisture content on catalytic activity of MnO_2 showed much better results as compared to low moisture content. More CO conversion was observed under the influence of high moisture content. After 1 h, 55% CO conversion was observed and it goes on increasing with reaction time. Around 61% CO conversion was seen after 5 h, thus by providing more amount of moisture along with feed gases increase in activity for CO conversion was obtained as seen in Fig. 5.38.

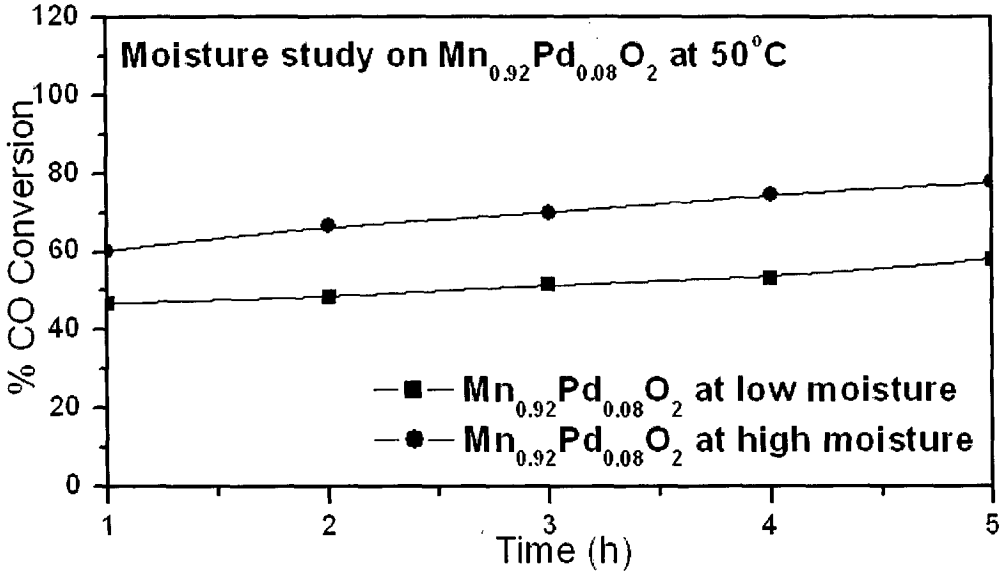

Fig. 5.39 Moisture study on $Mn_{0.92}Pd_{0.08}O_2$.

The $Mn_{0.92}Pd_{0.08}O_2$ catalyst was also tested to see the effect of moisture and results are shown in Fig. 5.39. This catalyst was kept at fixed temperature at 50 °C. Under the influence of low moisture, after 1h, 47% CO conversion was observed as shown in Fig. 5.39 and after 5 h it increases to about 58% showing increase in activity by roughly 10% after 5h. The $Mn_{0.92}Pd_{0.08}O_2$ showed excellent CO conversion activity with higher moisture content. Around 60% CO conversion was seen after 1 h and with increase in time of reaction, it reaches to 78% after 5 h as seen in Fig. 5.39. Consequently the activity of Pd

doped MnO_2 was also highly influenced by passing moisture along with the feed gases and with more moisture it gave much better result.

From these findings it is seen that the presence of moisture strongly affects the CO conversion activities over these catalysts. No deactivation is observed for CO oxidation reaction. Obviously, the reaction mechanism of CO oxidation by O_2 over these catalysts under the influence of moisture is likely to be different. Due to hydration of the adsorbed CO molecule, the CO bond is weakened significantly [206], which facilitates its oxidation and presence of Pd highly influences this activity. Also water may be increasing the acidic sites on the surface of the catalyst [247] enhancing CO adsorption thus leading to higher activity.

The effect of moisture on the activities of MnO_2 (Ag-series) and $Mn_{0.95}Ag_{0.05}O_2$ catalysts was also tested. The activity was tested in presence of low and high moisture content.

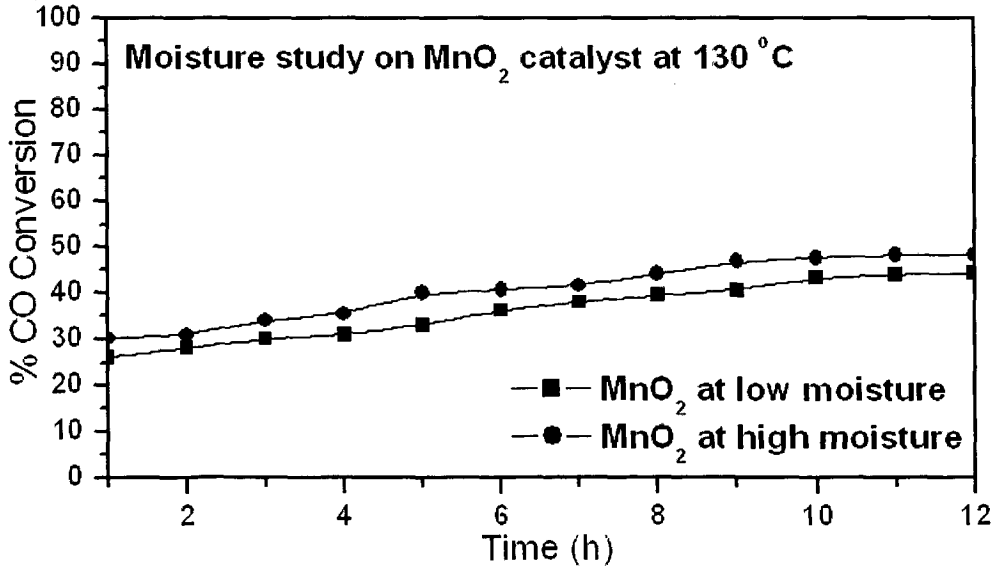

Fig. 5.40 Moisture study on MnO_2 (Ag-series).

MnO_2 catalyst was maintained at 130 °C. Under the influence of low moisture, MnO_2 catalyst is stable and showed increase in activity with time as seen in Fig. 5.40. The effect

of high moisture content on catalytic activity of MnO_2 showed much better results as compared to low moisture content. More CO conversion was observed, as shown in Fig. 5.40.

The $Mn_{0.95}Ag_{0.05}O_2$ catalyst was maintained at 60 °C. Under the influence of low moisture, catalyst is stable showing increase in activity by roughly 11% after 12 h. Under influence of high moisture it showed much better results, as seen in Fig. 5.41.

One interesting phenomenon was observed during stability test, the activity of both the catalysts increased with time either in presence (Figs. 5.40 and 5.41) or in absence of moisture (Fig 5.31). The catalysts were maintained at a lower operating temperature during the stability test (approximately near to its 50% CO conversion). At this low operating temperature the surface active sites which are responsible for CO adsorption may not be totally activated. With increase in time the surface active sites may get activated resulting in more CO conversion. But for longer time period this trend may not continue and expected to reach a plateau region of CO conversion.

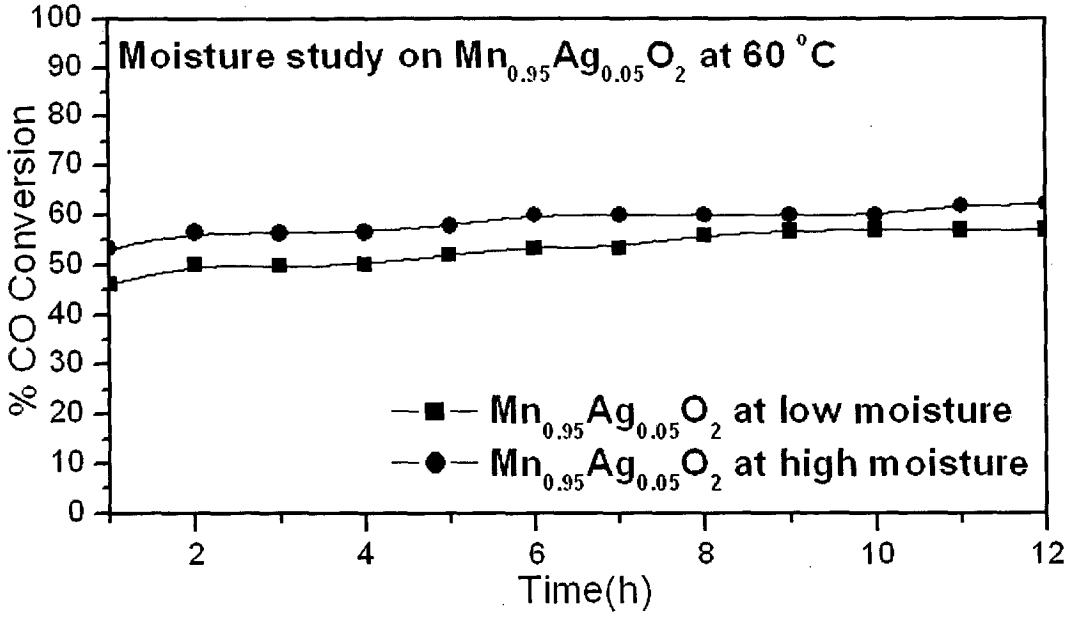

Fig. 5.41 Moisture study on $Mn_{0.95}Ag_{0.05}O_2$.

From Figs. 5.40 and 5.41 (and Fig. 5.31) it is clear that the activity increases for both the catalysts with increase in time either in presence or in absence of moisture. Activity of catalyst is stable for CO oxidation, and under the influence of moisture catalysts shows higher activity. This gives evidence that moisture does participate in catalytic oxidation of CO. In addition to normal catalytic reaction of CO with oxygen to produce CO_2, there is a possibility of adsorbed CO reacting with adsorbed OH^- [199]. Water adsorbs dissociatively on catalyst surface as OH^- and H^+, and then the hydroxyl group may combine with CO to form an intermediate, which then decomposes giving CO_2 and hydrogen. Also there may be a possibility of formation of Bronsted acid sites due to the adsorption of moisture on surface of the catalysts [247]. These acid sites will favour more adsorption of CO on surface of the catalyst which results in more CO_2 production, thus showing better activity.

The time on stream studies were performed in presence of moisture for rhodium doped MnO_2 catalysts. The Fig. 5.42 depicts the results of the moisture study. $Mn_{0.98}Rh_{0.02}O_2$ and $Mn_{0.95}Rh_{0.05}O_2$ catalyst were kept at fixed temperature 60 °C. Both this catalysts are highly stable for CO oxidation reaction in moisture condition for longer period. The $Mn_{0.95}Rh_{0.05}O_2$ catalyst showed around 75% CO conversion initially which reaches to 95% after 10 h under low moisture content. It showed almost similar trend in presence of high moisture, but showed little higher activity. At 60 °C temperature which is operating temperature of this catalyst, the surface active sites which are responsible for CO adsorption may not be totally activated. With increase in time the surface active sites may get activated resulting in more CO conversion. But this may not be continuing for longer period of time.

The $Mn_{0.98}Rh_{0.02}O_2$ catalysts showed around 60% conversion and is stable for longer period under influence both low and high moisture conditions.

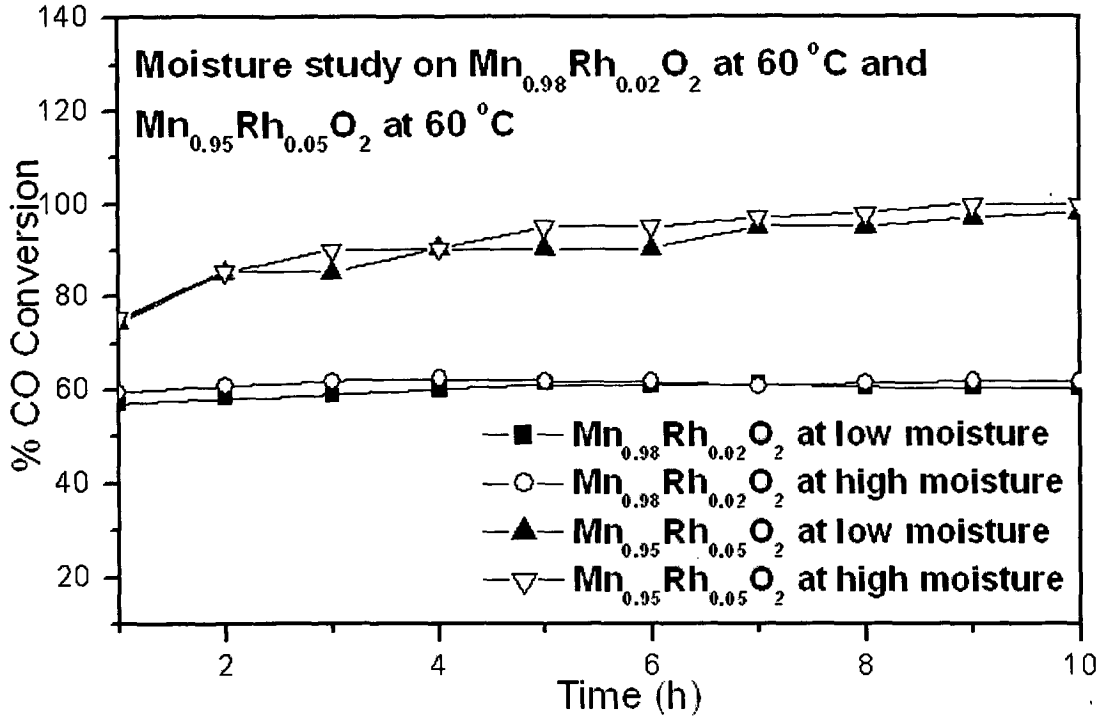

Fig. 5.42 Moisture study on Rh doped MnO_2 catalysts.

The Fig. 5.43 shows moisture study for CuPd/MnO_2 catalyst. $Mn_{0.90}Cu_{0.05}Pd_{0.05}O_2$ catalyst was maintained at 60 °C under the influence of both low and high moisture, the catalyst was stable with time as seen in Fig. 5.43.

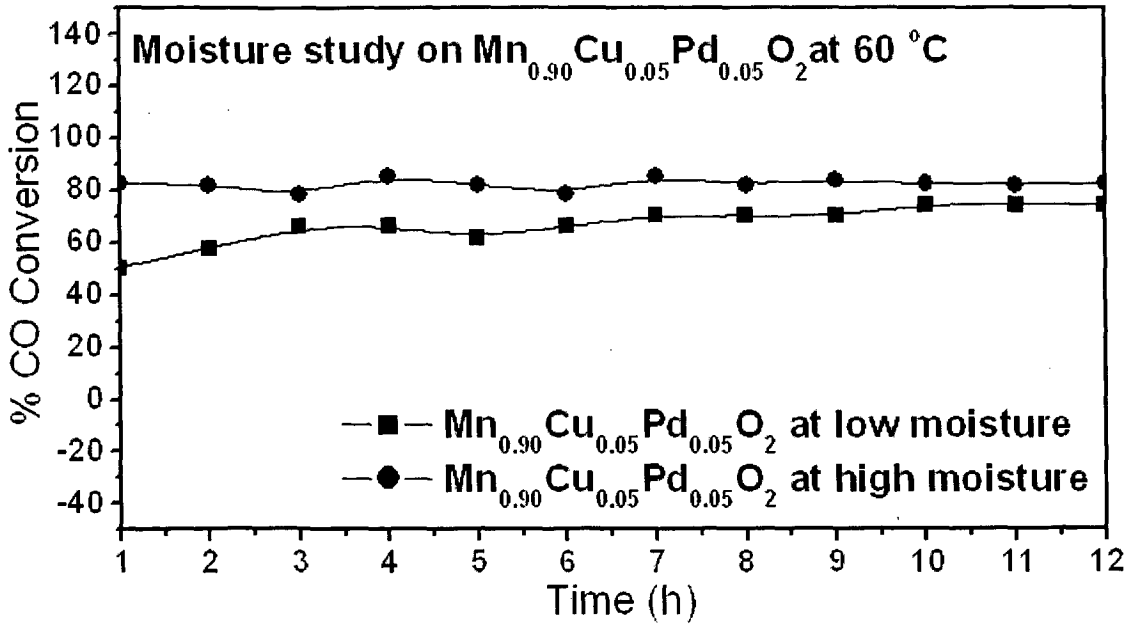

Fig. 5.43 Moisture study on $Mn_{0.95}Cu_{0.05}Pd_{0.05}O_2$ catalyst.

The catalyst also showed more CO conversion in presence of low and high moisture content in the feed as compared to without moisture (Fig. 5.33). Thus by providing the moisture along with the feed gases, increase in CO oxidation activity of the catalyst has been observed. Under the influence of low as well as high moisture content in feed, catalysts showed increase in activity for CO conversion reaction. From this study it is evident that the presence of moisture in the feed gas affects the catalytic activity for CO oxidation reaction.

Thus from time on stream studies (Fig. 5.43) it is clear that $Mn_{0.90}Cu_{0.05}Pd_{0.05}O_2$ catalyst is stable for CO oxidation reaction under the influence of moisture. They showed higher catalytic activity in presence of moisture as compared to activity without moisture and showed increase in activity with increase in moisture content. It is known that due to hydration of adsorbed CO molecule, the CO bond is weakened significantly which facilitates its oxidation [206].

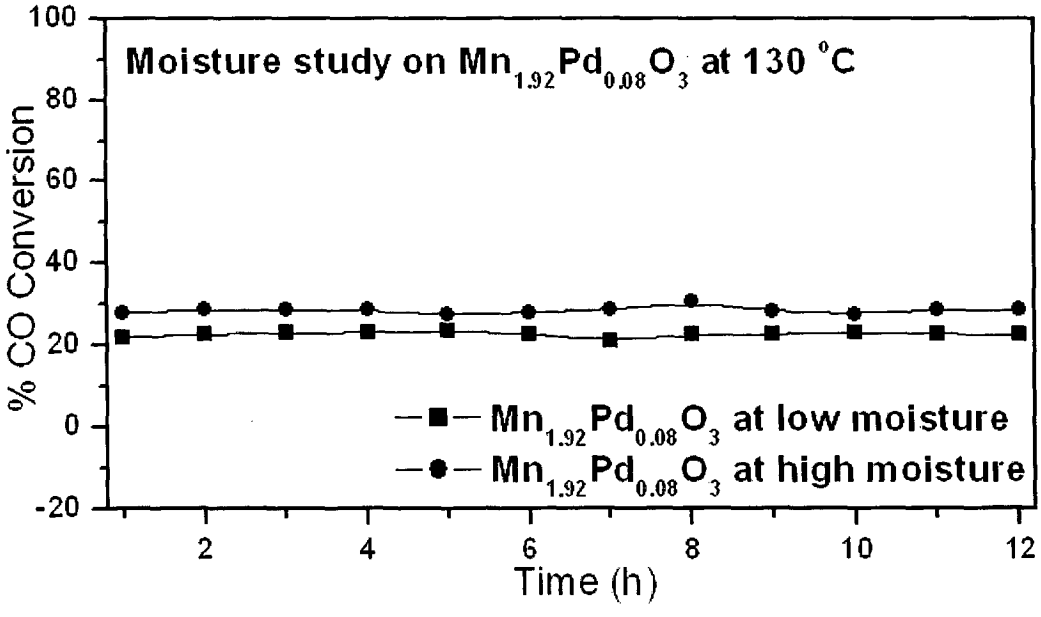

Fig. 5.44 Moisture study on $Mn_{1.92}Pd_{0.08}O_3$ catalyst.

$Mn_{1.92}Pd_{0.08}O_3$ catalyst was maintained at 130 °C. Under the influence of low moisture, the catalytic activity is stable with time as seen in Fig. 5.44. The catalyst also shows good

CO conversion activity in presence of high moisture content in the feed. No decline in activity is observed during the time on stream studies signifying that Pd doped Mn_2O_3 catalysts are stable for CO oxidation reaction in presence of moisture for longer period.

The effect of moisture was also verified on the activity of some of the selected supported catalysts. The time on stream experiments were carried out and activity was tested in both the conditions (under the influence of low and high moisture).

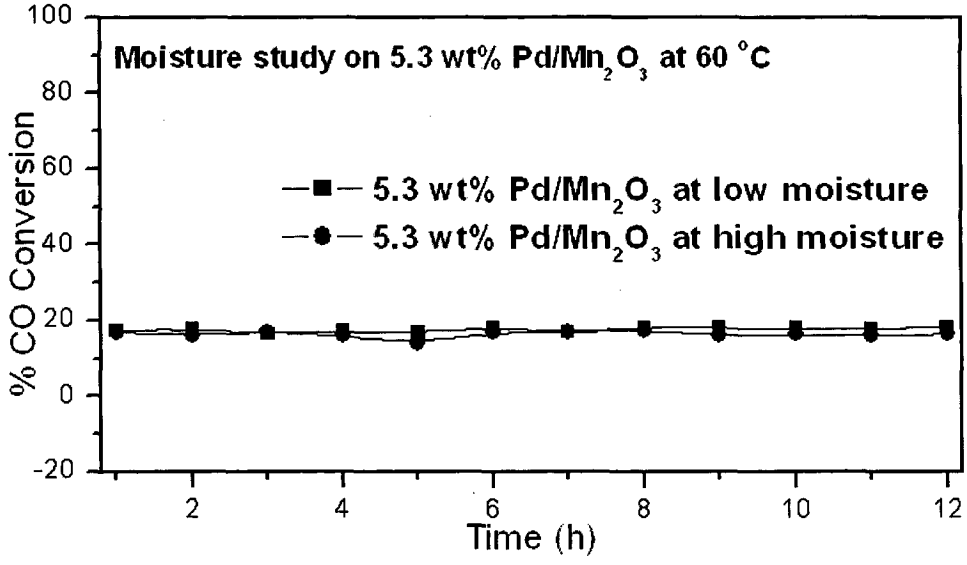

Fig. 5.45 Moisture study on 5.3 wt% Pd/Mn_2O_3 catalyst.

The effect of moisture on CO oxidation activity of 5.3 wt% Pd/Mn_2O_3 catalyst was tested, the results are shown in Fig. 5.45. The 5.3 wt% Pd/Mn_2O_3 catalyst was maintained at fixed temperature of 60 °C. Under the influence of low moisture as well as high moisture content in feed, no change in the CO conversion activity was accounted indicating good stability of this catalyst for CO conversion. From this study it is evident that, presence of moisture in the feed gas does not affect the catalytic activity for CO oxidation reaction.

Fig. 5.46 shows the moisture study for $CuPd/MnO_2$ catalyst. The 3.5 wt% Cu 5.3 wt% Pd/MnO_2 catalyst was maintained at 80 °C, this catalyst also showed good activity in

presence of moisture. Under the influence of low moisture, after 1 h, 68% CO conversion was observed as shown in Fig. 5.46 which remained almost stable up to 12 h. Under the influence of low as well as high moisture content in the feed, catalysts showed increase in activity for CO conversion reaction. From this study it is evident that the presence of moisture in the feed gas affects the catalytic activity for CO oxidation reaction.

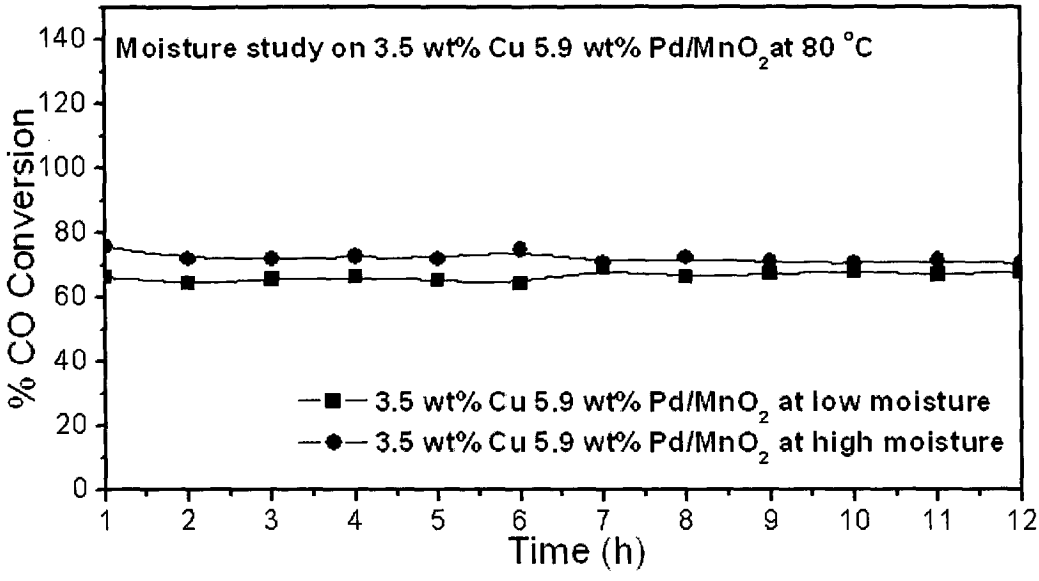

Fig. 5.46 Moisture study on 3.5 wt% Cu 5.3 wt% Pd/MnO_2 catalyst.

It is suggested that water has two possible roles during CO oxidation [200]. First, it may promote the reaction by activating molecular oxygen on the surface to enhance CO_2 production. The second possible role of water is assisting in the decomposition of carbonates that may accumulate on the surface in order to accommodate additional reactants on the surface during CO oxidation. All these hypotheses propose that water promotes CO oxidation but there is no direct involvement in the reaction.

The effect of moisture on the on catalytic activity of 5.9 wt% Pd/MnO_2 catalyst was studied. This is done to verify the activity of this catalyst in moisture condition and Fig. 5.47 shows the results. The 5.9 wt% Pd/MnO_2 in presence of low moisture showed around 80% conversion initially after 1 h, further with increase in reaction time the catalysts is

almost found to be stable up to 10 h. The similar behavior is observed in presence of high moisture. Hence the presence of moisture does not affect the catalytic activity of this catalyst.

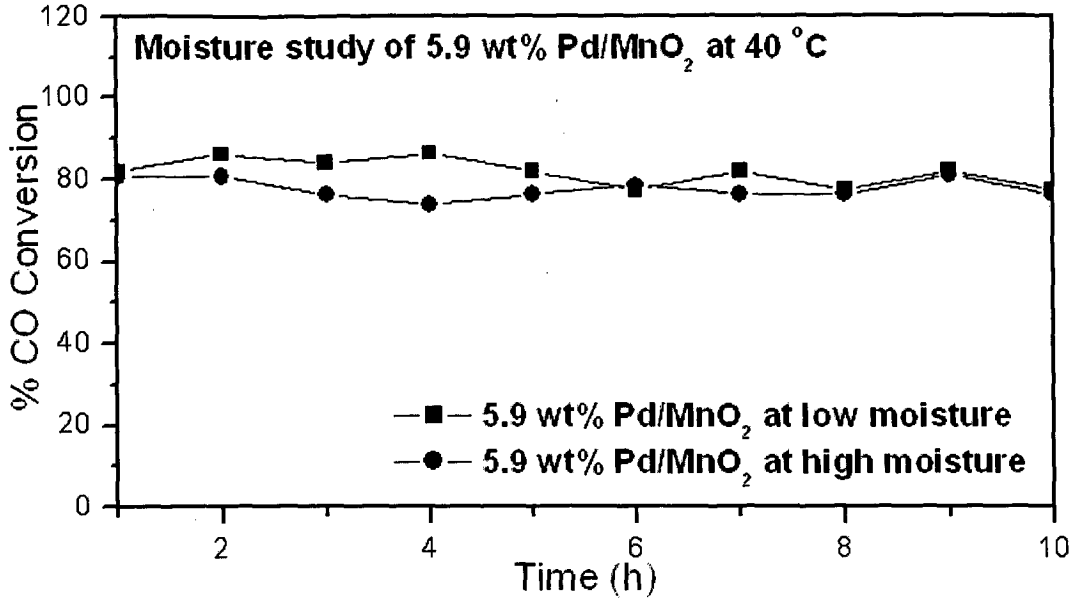

Fig. 5.47 Moisture study on 5.9 wt% Pd/MnO_2 catalyst.

5.9 Influence of acid and base treatment on CO oxidation

The influence of acid and base treatment was done on MnO_2 and Ag doped MnO_2 catalysts.

Influence of Acid treatment

Acid treatment was done on the catalysts basically to increase the acidic sites on catalysts surface. In this case 0.9 g of catalyst was mixed with 5 ml of 0.01 M HNO_3 solution with stirring this was dried at 200 °C for nearly 3 h, these catalysts were then used for CO oxidation reaction. Fig. 5.48a depicts the activity of acid treated catalysts for CO oxidation reaction.

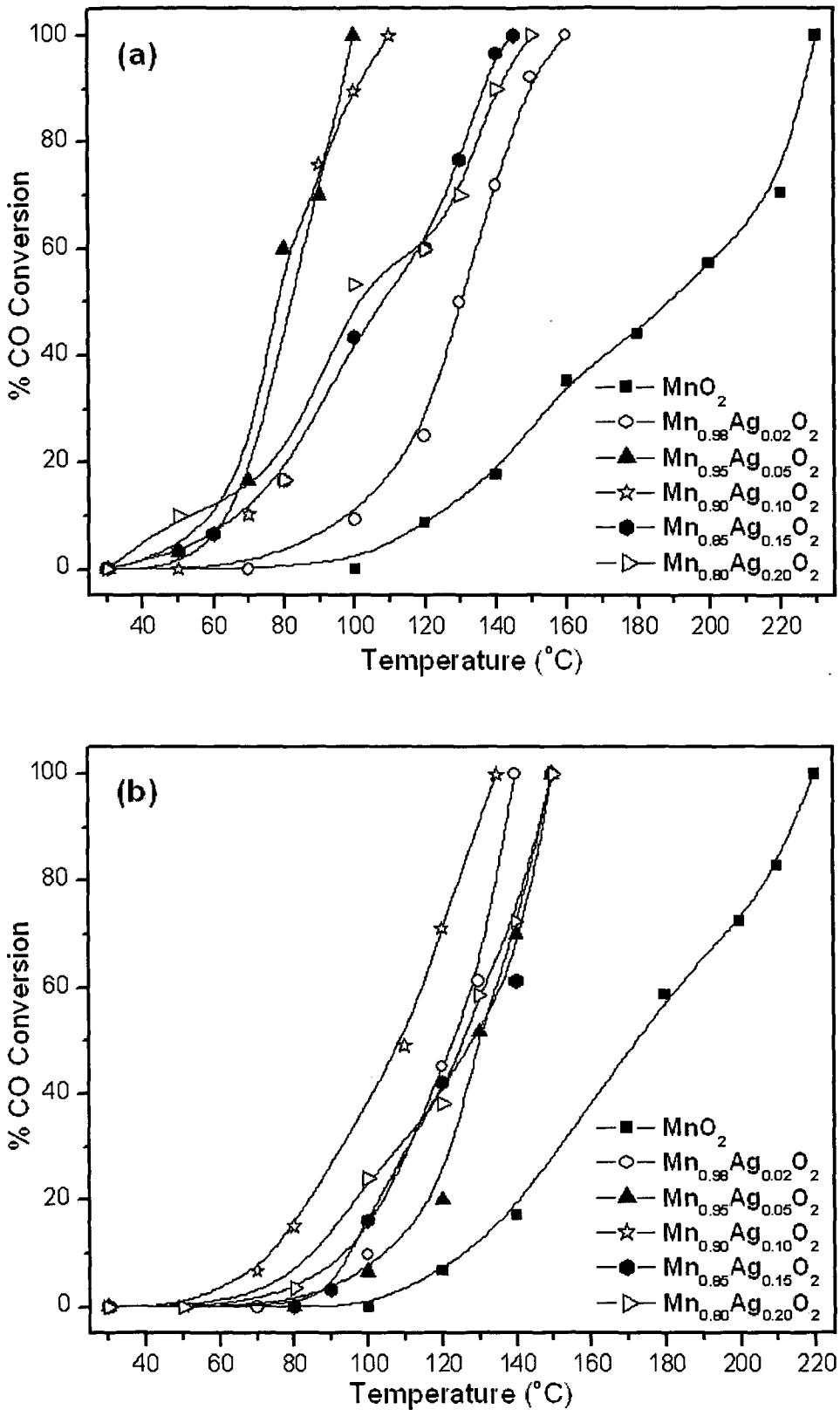

Fig. 5.48 Light–off curves for CO oxidation over different catalysts under (a) Acid treatment and (b) Base treatment, Conditions: 5% CO and 5% O_2 in nitrogen at a rate of 5000 ml h^{-1}.

Acid treated catalysts showed lower activity as compared to the activity of catalysts without acid treatment (Fig. 5.4), T_{100} for all the catalysts was found to be higher. Due to acid treatment, catalyst gets deactivated. It may decreases the basic sites due to which CO adsorption on surface increases but adsorption of oxygen decreases. Moreover, it is also evident from NH_3 TPD data of $Mn_{0.95}Ag_{0.05}O_2$ catalyst that this catalyst has strong acidic sites which are important for CO oxidation reaction. Thus by giving acid treatment there is increase in acid sites and decrease in basic sites. But in some cases acid treated catalysts showed enhanced CO oxidation ability. Catalysts such as CoFe-tungstates [248] which shows very poor activity for CO oxidation, however when enriched with dilute acid shows drastic increase in activity.

Influence of Base treatment

Base treatment on catalysts was done mainly to increase the basic sites on catalysts surface. In this case 0.9 g of catalyst was mixed with 0.01 M NH_3 solution with stirring this was dried at 200 °C for nearly 3 h, these catalysts was then used for CO oxidation reaction. Like acid treated catalysts, base treated catalysts also showed lower CO oxidation activity as compared to the activity of catalysts without base treatment (Fig. 5.4). 100% CO conversion temperature is comparatively higher than untreated catalysts. Fig. 5.48b depicts the activity of base treated catalysts. Acidic sites may get reduced due to base treatment thus reducing the adsorption of CO on surface of catalysts.

For the catalytic oxidation reaction both reactants should adsorb over the catalyst surface. It is found that the carbon monoxide has excess electrons and it requires acidic sites to get adsorb, similarly for oxygen basic sites are needed. Therefore, for complete oxidation both acidic and basic sites on the catalyst surface are essential for CO and O_2 adsorption [248].

CHAPTER 6

SUMMARY AND CONCLUSIONS

SUMMARY AND CONCLUSIONS

The Thesis describes the preparation of doped manganese oxides and supported manganese oxides catalysts. These prepared catalysts were characterized by various instrumental techniques. The solid state studies were carried out on doped manganese dioxide catalysts. All these catalysts were tested for carbon monoxide oxidation reaction. Various parameters like effect of partial pressure oxygen, influence of moisture in the feed on the catalytic activity of the catalysts were studied. This chapter will present a brief summary of the work described in the previous chapters and the general conclusions arrived from these chapters.

Chapter 1 gives the brief introduction regarding the CO oxidation catalysts along with the organization of the thesis, aims and objectives.

Chapter 2 briefly describes the literature survey regarding the carbon monoxide, catalysis in general and nanotechnology in catalysis. It gives information on manganese oxides, their crystallographic structures and various method of preparation by different routes. The brief survey of CO oxidation reaction over manganese oxide based catalysts was also presented. In addition, the influence of moisture and excess oxygen in the feed for the CO oxidation reaction over catalyst surface was also shown.

Chapter 3 describes the method of preparation of catalysts, the doped manganese oxides (MnO_2 and Mn_2O_3) were prepared by co-precipitation method and the supported catalysts were prepared by wet impregnation method. These prepared compounds were characterized by various instrumental technique such as XRD, Thermal analysis (TG/DTA), FTIR spectroscopy, SEM, TEM, BET surface area etc. The solid state studies

such as magnetic susceptibility and electrical resistivity were carried out on the doped manganese oxide compounds.

Chapter 4 describes the spectroscopic and solid state studies of all the prepared compounds. X-ray diffraction technique was used to investigate the structure as well as the phase of the synthesized catalyst. The XRD patterns authenticate the formation of MnO_2 and Mn_2O_3 phases, the data obtained from XRD agree well with the reported data (ICDD card and JCPDS card).

Thermal analysis (TG/DTA) was preformed for all the samples. MnO_2 decomposes at a temperature above 550 °C with loss of oxygen and there is a conversion of the MnO_2 phase to Mn_2O_3 with corresponding endothermic peak. Further, Mn_2O_3 converts to give Mn_3O_4 phase with the loss of oxygen at a temperature above 950 °C. This shows that MnO_2 is stable up to a temperature of around 550 °C. Mn_2O_3 shows the major weight loss above 950 °C with an endothermic peak, this weight loss is due to the loss of oxygen and conversion of the phase from Mn_2O_3 to Mn_3O_4.

FTIR spectra gives the characteristic Mn-O vibrations of Mn oxides. The MnO_2 shows characteristic broad peaks at ~525 and 630 cm^{-1}, which are attributed to the antisymmetric stretching mode of MnO_6 octahedra. These peaks are also prominent in doped MnO_2 catalysts indicating that the MnO_2 phase is stable even after doping. The Mn_2O_3 gave peak at ~ 665 cm^{-1} which is attributed to Mn–O stretching vibration of Mn_2O_3 and at ~ 528 cm^{-1} is due to Mn–O bending vibration of Mn_2O_3. Similar features are also shown by the doped Mn_2O_3 samples.

The DC Electrical resistivity (ρ) of different samples at various temperatures were measured in conductivity unit cell by two probe method in air and in temperature range from room temperature to 400 °C. Initially at lower temperature, all the samples show low

conductivity, but there is a raise in conductivity with increase in temperature. Thus all the samples show decrease in resistivity with increase in temperature indicating that these samples are semiconducting type. In some samples dopants also play a role in the conductivity, an increase in conductivity of MnO_2 is observed after doping.

Magnetic studies show that all these samples are paramagnetic in nature. Magnetic moment value of the doped MnO_2 catalysts is almost above 3 B.M. This confirmed that the Mn^{4+} ion in MnO_2 has three unpaired electrons, whereas the magnetic moment value of doped Mn_2O_3 shows values above 4 B.M. indicating that Mn is present in 3+ oxidation state having four unpaired electrons. The pristine MnO_2 and Mn_2O_3 showed higher values of magnetic susceptibility and magnetic moment as compared to the doped samples, with increasing concentration of dopants the magnetic susceptibility and magnetic moment values found to decrease due to the influence of dopants in the lattice structure of MnO_2 and Mn_2O_3.

The diffuse reflectance spectra (DRS) for all the samples were recorded in the range 400 to 800 nm wavelength and the % reflectance was measured against wavelength. The band gap was calculated for all the samples. The band gap calculated was found to be in the semiconducting range.

From the XPS data of pristine MnO_2 it is evident that manganese is present in 4+ oxidation state. The data also shows the presence of two types of oxygen species, one is lattice oxygen and other is the surface oxygen.

Chapter 5 describes the CO oxidation reaction over all the prepared catalysts. Doped MnO_2 samples showed good surface area than the undoped MnO_2. The Mn_2O_3 samples exhibits lower surface area as compared to MnO_2 samples, this may be due to higher calcination temperature. Pd supported MnO_2 and Rh supported MnO_2 catalysts showed

higher surface area among all supported samples. Catalytic activity also depends on the surface area, higher surface area corresponds to more surface available for adsorption of reactant molecules giving better activity.

The surface morphology and particle nature of the prepared catalysts were investigated by SEM. All these samples are nano-sized with spherical morphology, some samples also showed rod-like elongated morphologies. The doped MnO_2 samples showed smaller particle size as compared to doped Mn_2O_3 samples. The TEM images of doped MnO_2 samples show particle size in the range 20-40 nm, whereas those of doped Mn_2O_3 samples are in the range 50-80 nm.

NH_3-TPD (temperature programmed desorption) was performed to explore the adsorption sites over these catalysts. Basically, presence of acidic sites is needed on the surface of the catalysts for adsorption of CO molecules. NH_3-TPD was employed to monitor the acidity of the surface.

Catalytic oxidation of CO was performed on all the catalysts. The catalytic activity was determined using a feed gas composition of 5% CO and 5% O_2 in nitrogen. The mixture of gases was then allowed to pass over the catalyst at a rate of 5000 ml h^{-1}. The feed gases and the products were analyzed employing an online Gas Chromatograph with molecular sieve 13X and Porapak Q columns. H_2 was used as a carrier gas. The doped catalyst showed higher activity for CO oxidation and complete conversion was achieved at a much lower temperature as compared to undoped MnO_2 and Mn_2O_3 catalyst. Doped MnO_2 catalysts gave total CO oxidation at a much lower temperature as compared to doped Mn_2O_3 catalysts and showed conversion even at room temperature. Whereas the Ni and Ce doped MnO_2 showed poor activity, incorporation of Ni and Ce did not improve the catalytic activity of MnO_2 for CO oxidation reaction. Doping of Ni in MnO_2 may decrease

the adsorption capability of MnO_2 resulting in lower activity. Supported catalysts also showed good activity at lower temperature and activity was seen even at room temperature.

The stability of the catalyst for CO oxidation reaction was verified by performing time on stream experiments, by maintaining the catalyst at a constant temperature. No decline in activity for CO oxidation was accounted during this period signifying good stability of these catalysts. Influence of excess oxygen on activity of catalysts was carried out by increasing O_2 partial pressure in the feed gas compositions. Under the influence of excess oxygen catalysts are stable and show good activity. Further, time on stream analysis was performed to check the influence of moisture on activity of the catalyst for CO oxidation with low and high moisture contents. All the catalysts showed good activity in presence of moisture. In some cases increase in activity was observed in presence of moisture which indicates that moisture may participate in the catalytic CO oxidation process giving higher activity. Water may furthermore increase the acidic sites on the surface of the catalyst enhancing CO adsorption thus leading to higher activity. Also the effect of excess acidity and basicity was studied for CO oxidation by treating catalyst with dilute acid and base. From this study it may be concluded that both acidic as well as basic sites are important for CO and O_2 adsorption.

Conclusions

Finally it is concluded that, the co-precipitation method was employed to prepare the nano-sized doped MnO_2 and Mn_2O_3 catalysts. This method is a green process wherein no toxic by-products are evolved. Supported catalysts have been prepared by wet impregnation method. XRD substantiates the formation of MnO_2 and Mn_2O_3 phase. XRD also reveals that these catalysts are highly nano-sized particles. Thermal analysis gives the

significant evidence of phase change of MnO_2 to Mn_2O_3 above 550 °C and Mn_2O_3 to Mn_3O_4 phase above 950 °C. The FTIR spectra of manganese oxides showed some characteristic vibrations in 700-400 cm^{-1}. These vibrations are also seen in doped samples indicating that the phase is stable even after doping. DC electrical resistivity measurements for all doped samples reveal the semiconducting nature of these oxides. Magnetic susceptibility measurements showed that these samples are paramagnetic in nature. The pristine MnO_2 and Mn_2O_3 showed higher values of magnetic susceptibility and magnetic moment as compared to the doped samples. Band gap calculated from DRS was found to be in semiconducting range. The XPS data of pure MnO_2 shows that Mn is present in 4+ oxidation state. SEM/TEM images confirmed that these catalysts are nano-sized, most of the samples showed spherical morphology and are agglomerated in appearance. The doped MnO_2 samples showed smaller particle size as compared to doped Mn_2O_3 samples. The supported catalysts show higher agglomeration as compared to doped samples. NH_3-TPD data indicates the presence of acidic sites on catalyst surface which are important for CO adsorption.

The doped MnO_2 catalysts showed better activity than pristine MnO_2 catalysts. In case of Pd, Ag and Rh doped MnO_2 catalysts complete conversion was obtained at a much lower temperature. These catalysts even showed room temperature conversion. Drastic decrease in the total conversion temperature was observed due to the synergistic effect. The doping of Ni and Ce in MnO_2 does not improve the catalytic activity of MnO_2. Doped Mn_2O_3 catalysts shows better activity than pristine Mn_2O_3, but as compared to doped MnO_2 catalysts they showed lower activity. Among all doped Mn_2O_3, Pd doped Mn_2O_3 showed interesting results, total CO conversion was seen at a much lower temperature as compared to undoped Mn_2O_3. Supported catalysts also showed good activity for CO oxidation reaction. Pd/MnO_2 showed activity even at room temperature and total CO

conversion was obtained at much lower temperature. Pd/Mn_2O_3 catalysts also showed good activity for CO conversion. The stability test for the catalysts at fixed temperature showed that activity remains constant with time for longer period, and some catalysts even showed increased in percentage conversion with time. No change in catalytic activity for CO conversion was observed under the influence of excess oxygen. Higher oxygen in feed gas does not affect the CO oxidation activity of the catalysts, however it showed good activity. From time on stream experiments for moisture study, it is clear that the catalysts are highly stable for CO oxidation for longer period in presence of moisture in feed gas. Some of the catalysts showed higher activity for CO conversion in presence of moisture, indicating that moisture facilitates CO oxidation reaction on the catalyst surface. Both acidic as well as basic sites are needed for CO and O_2 adsorption for better CO oxidation reaction.

REFERENCES

[1] S. Royer, D. Duprez, Chem. Cat. Chem. 3 (2011) 24–65.

[2] M.A. Newton, A.J. Dent, S. Diaz-Moreno, S.G. Fiddy, B. Jyoti, J. Evans, Chem. Eur. J. 12 (2006) 1975–1985.

[3] D. Na-Ranong, A. Jaree, R.R. Hudgins, H.M. Budman, P.L. Silveston, M. Menzinger, Canadian J. Chem. Eng. 81 (2003) 1215–1221.

[4] A.A. Herzing, C.J. Kiely, A.F. Carley, P. Landon, G.J. Hutchings, Sci. 321 (2008) 1331–1335.

[5] M. Bonn, S. Funk, C. Hess, D.N. Denzler, C. Stampfl, M. Scheffler, M. Wolf, G. Ertl, Sci. 285 (1999) 1042–1045.

[6] C. Galletti, S. Specchia, G. Saracco, V. Specchia, Int. J. Hydrogen Energy 33 (2008) 3045–3048.

[7] B. Yoon, H. Hakkinen, U. Landman, A.S. Worz, J.M. Antonietti, S. Abbet, K. Judai, U. Heiz, Sci. 307 (2005) 403–407.

[8] A.V. Salker, D.K. Chakrabarty, H.V. Keer, Ind. J. Chem. 28A (1989) 458–462.

[9] F. Somodi, I. Borbath, M. Hegedus, K. Lazar, I.E. Sajo, O. Geszti, S. Rojas, J.L.G. Fierro, J.L. Margitfalvi, Appl. Surf. Sci. 256 (2009) 726–736.

[10] T.H.M. Housmans, J. M. Feliu, R. Gmez, M.T.M. Koper, Chem. Phys. Chem. 6 (2008) 1522–1529.

[11] P. Nolte, A. Stierle, N.Y. Jin-Phillipp, N. Kasper, T.U. Schulli, H. Dosch, Sci. 321 (2008) 1654–1659.

[12] A.D. Sarkar, B.C. Khanra, J. Mol. Catal. A: Chem. 229 (2005) 25–29.

[13] J. Schoiswohl, S. Eck, M.G. Ramsey, J.N. Andersen, S. Surnev, F.P. Netzer, Surf. Sci. 580 (2005) 122–136.

[14] J. Haber, M. Wojciechowska, M. Zielinski, W. Przystajko, Catal. Lett. 113 (2007) 46–53.

[15] W. Zhang, Z. Yang, X. Wang, Y. Zhang, X. Wen, S. Yang, Catal. Commun. 7 (2006) 408–412.

[16] G.A. Somorjai, Y.G. Borodko, Catal. Lett. 76 (2001) 1.

[17] H.H. Kung, M.C. Kung, Appl. Catal. A: Gen. 246 (2003) 193.

[18] M.S. Chen, Y. Cai, Z. Yan, K.K. Gath, S. Axnanda, D.W. Goodman, Surf. Sci 601 (2007) 5326–5331.

[19] M. Jeguirim, K. Villani, J.F. Brilhac, J.A. Martens, Appl. Catal. B: Environ. 96 (2010) 34–40.

[20] A.B. Mhadeshwar, D.G. Vlachos, J. Catal. 234 (2005) 48–63.

[21] S.H. Oh, G.B. Hoflund, J. Catal. 245 (2007) 35–44.

[22] F. Marino, C. Descorme, D. Duprez, Appl. Catal. B: Environ. 54 (2004) 59–66.

[23] S.M. Gurav, A.V. Salker, Indian J. Chem. Technol. 5 (1998) 286–292.

[24] A.V. Salker, T. Vaz, Indian J. Chem. 43A (2004) 710–714.

[25] U.R. Pallai, S. Deevi, Appl. Catal. B: Environ. 65 (2006) 110–117.

[26] X.C. Zheng, S.H. Wu, S.P. Wang, S.R. Wang, S.M. Zhang, W.P. Huang, Appl. Catal. A 283 (2005) 217–223.

[27] C.F. Gautrelet, J.M. Krafft, G.D. Mariadassou, C. Thomas, J. Catal. 247 (2007) 34–42.

[28] J. Xu, D.R. Mullins, S.H. Overbury, J. Catal. 243 (2006) 158–164.

[29] U.R. Pallai, S. Deevi, Appl. Catal. A: Gen. 299 (2006) 266–273.

[30] J.Y. Luo, M. Meng, X. Li, X.G. Li, Y.Q. Zha, T.D. Hu, Y.N. Xie, J. Zhang, J. Catal. 254 (2008) 310-324.

[31] N. Russo, D. Fino, G. Saracco, V. Specchia, Catal. Today 117 (2006) 214–219.

[32] G. Arzamendi, V.A. de la Pena O'Shea, M.C. Alvarez-Galvan, J.L.G. Fierro, P.L. Arias, L.M. Gandía, J. Catal. 261 (2009) 50–5.

[33] Y.F. Han, L. Chen, K. Ramesh, E. Widjaja, S. Chilukoti, I.K. Surjami, J. Chen, J. Catal. 253 (2008) 261–268.

[34] R. Kumar, S. Sithambaram, S.L. Suib, J. Catal. 262 (2009) 304–313.

[35] V.D. Makwana, Y.C. Son, A.R. Howell, S.L. Suib, J. Catal. 210 (2002) 46-52.

[36] K. Tomita, Y. Oshima, Ind. Eng. Chem. Res. 43 (2004) 7740–7743.

[37] S. Devaraj, N. Munichandraiah, J. Phys. Chem. C 112 (2008) 4406–4417.

[38] S. Liang, F. Teng, G. Bulgan, R. Zong, Y. Zhu, J. Phys. Chem. C 112 (2008) 5307–5315.

[39] S. L. Suib, Accounts Chem. Res. (ACS) 41 No. 4 (2008) 479–487.

[40] S.L. Brock, N. Duan, Z.R. Tian, O. Giraldo, H. Zhou, S.L. Suib, Chem. Mater. 10 (1998) 2619–2628.

[41] K. Ramesh, L. Chen, F. Chen, Y. Liu, Z. Wang, Y.F. Han, Catal. Today 131 (2008) 477–482.

[42] M. Kramer, T. Schmidt, K. Stowe, W.F. Maier, Appl. Catal. A 302 (2006) 257–263.

[43] S. Imamura, H. Sawada, K. Uemura, S. Ishida, J. Catal. 109 (1988) 198–205.

[44] L.H. Chang, N. Sasirekha, B. Rajesh, Yu-Wen Chen, Separation Purification Technol. 58 (2007) 211–218.

[45] X. Wu, Q. Liang, D. Weng, J. Fan, R. Ran, Catal. Today 126 (2007) 430–435.

[46] G. B. Hoflund, S. D. Gardner, D. R. Schryer, B. T. Upchurch, E. J. Kielin, Appl. Catal. B: Environ. 6 (1995) 117–126.

[47] L.H. Chang, N. Sasirekha, Y.W. Chen, Catal. Commun. 8 (2007) 1702–1710.

[48] L.C. Wang, X.S. Huang, Q. Liu, Y.M. Liu, Y. Cao, H.Y. He, K.N. Fan, J.H. Zhuang, J. Catal. 259 (2008) 66–74.

[49] I. Blumenthal, J. R. Soc. Med. 94 (2001) 270–272.

[50] L.D. Prockop, R.I. Chichkova, J. Neurol. Sci. 262 (2007) 122–130.

[51] O.R. Gilliam, C.M. Johnson, W. Gordy, Phys. Review 78 (1950) 140.

[52] S.E. Gustavo, M.D. Miller, F.G. Jensen, J. Chem. Phys. 94 (1991) 6660–6665.

[53] S. Thorsten, J. Rudolf, J. Mole. Modeling 6 (2000) 282–288.

[54] F. Blanco, I. Alkorta, M. Solimannejad, J. Elguero, J. Phys. Chem. A 113 (2009) 3237–3244.

[55] E.Z. Eisenmeser, D.A. Bosco, M. Akke, D. Kern, Sci. 295 (2002) 1520–1525.

[56] U. Heiz, A. Sanchez, S. Abbet, W.D. Schneider, Chem. Phys. 262 (2000) 189–194.

[57] B.C. Gates, J. Molec, A. Catal, Chem. 163 (2000) 55–65.

[58] K. Hojrup Hansen, Z. Sljivancanin, E. Laegsgaard, F. Besenbacher, I. Stensgaard, Surf. Sci. 505 (2002) 25.

[59] H. Graoui, S. Giorgio, C.R. Henry, Surf. Sci. 417 (1998) 350.

[60] T. Shimoboji, E. Larenas, T. Fowler, A.S. Hoffman, P.S. Stayton, Bioconjugate Chem. 14 (2003) 517.

[61] M.J. Figurski, W. Arabczyk, Z.L. Bielun, S. Lenart, Appl. Catal. A: Gen. 266 (2004) 11–20.

[62] A.A. Mirzaei, H.R. Shaterian, R.W. Joyner, M. Stockenhuber, S.H. Taylor, G.J. Hutchings, Catal. Commun. 4 (2003) 17–20.

[63] W. Gac, Appl. Catal. B: Environ. 75 (2007) 107–117.

[64] J.L. Ayastuy, M.P. Gonzalez-Marcos, J.R. Gonzalez-Velasco, M.A. Gutierrez-Ortiz, Appl. Catal. B: Environ. 70 (2007) 532–541.

[65] Z.Y. Ding, L. Li, D. Wade, E.F. Gloyna, Ind. Eng. Chem. Res. 37 (1998) 1707–1716.

[66] K.T. Li, I. Wang, K.R. Chang, Ind. Eng. Chem. Res. 32 (1993) 1007–1011.

[67] M.S. Islam, R.A. Davies, J.D. Gale, Chem. Mater. 15 (2003) 4280–4286.

[68] M.S. Wu, P.C.J. Chiang, J.T. Lee, J.C. Lin, J. Phys. Chem. B 109 (2005) 23279–23284.

[69] W. Jantscher, L. Binder, D.A. Fiedler, R. Andreaus, K. Kordesch, J. Power Sources 79 (1999) 9–18.

[70] J. Dai, S.F.Y. Li, K.S. Siow, Z. Gao, Electrochemica Acta 45 (2000) 2211–2217.

[71] G.Q. Zhang, X.G. Zhang, Y.G. Wang, Carbon 42 (2004) 3097–3102.

[72] C.S. Johnson, D.W. Dees, M.F. Mansuetto, M.M. Thackeray, D.R. Vissers, D. Argyriou, C.K. Loong, L. Christensen, J. Power Sources 68 (1997) 570–577.

[73] V. Iablokov, K. Frey, O. Geszti, N. Kruse, Catal. Lett. 134 (2010) 210–216.

[74] C.M. Julien, M. Massot, C. Poinsignon, Spectrochemica Acta A 60 (2004) 689–700.

[75] D.E. Simon, R.W. Morton, J.J. Gislason, Adv. X-ray Analysis 47 (2004) 267–279.

[76] S. Foss, O. Nilsen, A. Olsen, J. Tafto, Philosophical Magazine, 85 (2005) 2689–2705.

[77] M. Kang, E.D. Park, J.M. Kim, J.E. Yie, Appl. Catal. A: Gen. 327 (2007) 361–369.

[78] N. Chandra, S. Bhasin, M. Sharma, D. Pal, Mater. Lett. 61 (2007) 3728–3732.

[79] M. Anilkumar, V. Ravi, Mater. Res. Bulletin 40 (2005) 605–609.

[80] S. Jana, S. Basu, S. Pande, S.K. Ghosh, T. Pal, J. Phys. Chem. C (2007) 16272–16277.

[81] S.P. Jiang, W.R. Ashton, A.C.C. Tseung, J. Catal. 131 (1991) 88–93.

[82] G.J. Hutchings, A.A. Mirzaei, R.W. Joyner, M.R.H. Siddique, S.H. Taylor, Appl. Catal. A: Gen. 166 (1998) 143–152.

[83] M. Kang, E.D. Park, J.M. Kim, J.E. Yie, Catal. Today 111 (2006) 236–241.

[84] C. Jones, S.H. Taylor, A. Burrows, M.J. Crudace, C.J. Kiely, G.J. Hutchings, Chem. Commun. (2008) 1707–1709.

[85] C. Jones, K.J. Cole, S.H. Taylor, M.J. Crudace, G.J. Hutchings, J. Mole. Catal. A: Chem. 305 (2005) 121–124.

[86] S. Colley, R.G. Copperthwaite, G.J. Hutchings, M. ven der Rite, Ind. Eng. Chem. Res. 27 (1998) 1339–1344.

[87] G. Qi, R.T. Yang, R. Chang, Appl. Catal. B: Environ. 51 (2004) 93–106.

[88] F. Arena, G. Trunfio, J. Negro, B. Fazio, L. Spadaro, Chem. Mater. 19 (2007) 2269–2276.

[89] Y.Z. Steenwinkel, J. Beckers, A. Bliek, Appl. Catal. A Gen. 235 (2002) 79–92.

[90] S.D. Gardner, G.B. Hoflund, M.R. Davidson, H.A. Laitinen, D.R. Schryer, B.T. Upchurch, Langmuir 7 (1991) 2140–2145.

[91] J. Pan, Y. Sun, P. Wan, Z. Wang, X. Liu, Electrochem. Acta 51 (2006) 3118–3124.

[92] D.B. Akolekar, S.K. Bhargava, G. Foran, M. Takahashi, J. Mole. Catal. A: Chem. 238 (2005) 78–87.

[93] J. Wen, X. Ruan, Z. Zhou, J. Phys. Chem. Solids 70 (2009) 816–820.

[94] S. Hamoudi, F. Larachi, G. Cerrella, M. Cassanello, Ind. Eng. Chem. Res. 37 (1998) 3561–3566.

[95] Z.R. Tian, Y.G. Yin, S.L. Suib, Chem. Mater. 9 (1997) 1126–1133.

[96] G.P. Osorio, F. Castillon, A. Simakov, H. Tiznado, F. Zaera, S. Fuentes, Appl. Catal. B: Environ. 69 (2007) 219–225.

[97] X. Wang, A. Yuan, Y. Wang, J. Power Sources 172 (2007) 1007–1011.

[98] S. Kobayashi, I.R.M. Kottegoda, Y. Uchimoto, M. Wakihara, J. Mater. Chem. 14 (2004) 1843–1848.

[99] Y. Matsuo, Y. Miyamoto, T. Fukutsuka, Y. Sugie, J. Power Sources 146 (2005) 300–303.

[100] C. Shao, H. Guan, Y. Liu, X. Li, X. Yang, J. Solid State Chem. 177 (2004) 2628–2631.

[101] J. Liu, J. Cai, Y.C. Son, Q. Gao, S.L. Suib, M. Aindow, J. Phys. Chem. B 106 (2002) 9761–9768.

[102] C.H. Lu, S.K. Saha, J. Sol-Gel Sci. Technol. 20 (2001) 27–34.

[103] M.A. Gulgun, M.H. Nguyen, W.M. Kriven, J. Am. Ceram. Soc. 82 (1999) 556–562.

[104] M.H. Nguyen, S.J. Lee, W.M. Kriven, J. Mater. Res. 14 (1999) 3417.

[105] L. Li, Y. Pan, L. Chen, G. Li, J. Solid State Chem.180 (2007) 2896–2902.

[106] B. Tang, G. Wang, L. Zhuo, J. Ge, Nanotechnol. 17 (2006) 947–957.

[107] X.F. Shen, Y.S. Ding, J.C. Hanson, M. Aindow, S.L. Suib, J. Am. Chem. Soc. 128 (2006) 4570–4577.

[108] V. Subramanian, H. Zhu, R. Vajtai, P.M. Ajayan, B. Wei, J. Phys. Chem. B 109 (2005) 20207.

[109] W.N. Li, J. Yuan, S. Gomez-Mower, S. Sithambaram, S.L. Suib, J. Phys. Chem. B 110 (2006) 3066–3073.

[110] X. Wang, Y. Li, Chem. Eur. J. 9 (2003) 300–306.

[111] M. Wei, Y. Konishi, H Zhou, H. Sugihara, H. Arakawa, Nanotechnol. 16 (2005) 245–254.

[112] D.K. Walanda, G.A. Lawrance, S.W. Donne, J. Power Sources 139 (2005) 325–341.

[113] T. Gao, H. Fjellvag, P. Norby, Nanotechnol. 20 (2009) 055610 (7 pages).

[114] X.Y. Xue, L.L. Xing, Y.G. Wang, T.H. Wang, Solid State Sci. 11 (2006) 2106–2110.

[115] D. Zheng, S. Sun, W. Fan, H. Yu, C. Fan, G Cao, Z. Yin, X. Song, J. Phys. Chem. B 109 (2005) 16439–16443.

[116] Y.S. Ding, X.F. Shen, S. Gomez, H. Luo, M. Aindow, S.L. Suib, Adv. Funct. Mater. 16 (2006) 549–555.

[117] X. Li, W. Li, X. Chen, C. Shi, J. Crystal Growth 297 (2006) 387–389.

[118] Z.Y. Yuan, T.Z. Ren, G. Du, B.L. Su, Chem. Phys. Lett. 389 (2004) 83–86.

[119] Y. Cai, S. Liu, X. Yin, Q. Hao, M. Zhang, T. Wang, Physica E 43 (2010) 70–75.

[120] Y. Chen, Y. Zhang, Q.Z. Yao, G.T. Zhou, S. Fu, H. Fan, J. Solid State Chem. 180 (2007) 1218–1223.

[121] H. Pang, L. Jiang, G. Li, .H. Peng, Z. Zhang, J. Dispersion Sci. Technol. 27 (2006) 1161–1163.

[122] R. Xu, X. Wang, D. Wang, K. Zhou, Y. Li, J. Catal. 237 (2006) 426–430.

[123] M.W. Xu, G.Y. Gao, W.J. Zhou, K.F. Zhang, H.L. Li, J. Power Sources 175 (2008) 217–220.

[124] M. Liu, G.J. Zhang, Z.R. Shen, P.C. Sun, D.T. Ding, T.H. Chen, Solid State Sci. 11 (2009) 118–128.

[125] F.C. Buciuman, F. Patcas, T. Hahn, Chem. Engg. Processing 38 (1999) 563–569.

[126] W. Zhang, Z. Yang, X. Wang, Y. Zhang, X. Wen, S. Yang, Catal. Commun. 7 . (2006) 408–412.

[127] Y. Ren, Q. Liu, J. Wang, H. Wang, D. Xue, Mater. Lett. 63 (2009) 661–663.

[128] A. Gil, L.M. Gandia, S.A. Korili, Appl. Catal. A: Gen. 274 (2004) 229–235.

[129] X.M. Wu, Z.Q. He, S. Chen, M.Y. Ma, Z.B. Xiao, J.B. Liu, Mater. Lett. 60 (2006) 2497–2500.

[130] P. Lavela, L. Sanchez, J.L. Tirado, S. Bach, J.P.P. Ramos, J. Power Sources 84 (1999) 75–79.

[131] J. Li, J. Chen, R. Ke, C. Luo, J. Hao, Catal. Commun. 8 (2007) 1896–1900.

[132] R.D. Monte, J. Kaspar, P. Fornasiero, M. Graziani, C. Paze, G. Gubitosa, Inorg. Chem. Acta 334 (2002) 318–326.

[133] L.F. Chen, G. Gonzalez, J.A. Wang, L.E. Norena, A. Toledo, S. Castillo, M.M. Pineda, Appl. Surf. Sci. 243 (2005) 319–328.

[134] M.F. Luo, Z.Y. Pu, M. He, J. Jin, L.Y. Jin, J. Mole. Catal. A: Chem. 260 (2006) 152–156.

[135] P.V. Snytnikov, M.M. Popova, Y. Men, E.V. Rebrov, G. Kolb, V. Hessel, V.A. Sobyanin, Appl. Catal. A: Gen. 350 (2008) 53–62.

[136] J. Okal, M. Zawadzki, Appl. Catal. B: Environ. 89 (2009) 22–32.

[137] C. Reed, Y.K. Lee, S.T. Oyama, J. Phys. Chem. B 110 (2006) 4207–4216.

[138] Q. Tang, X. Huang, C. Wu, P. Zhao, Y. Chen, Y. Yang, J. Mole. Catal. A: Chem. 306 (2009) 48–53.

[139] R. Jothiramalingam, B. Viswanathan, T.K. Varadarajan, Catal. Commun. 6 (2005) 41–45.

[140] J.S. Park, D.S. Doh, K.Y. Lee, Topics Catal. 10 (2000) 127–131.

[141] M.C. Alvarez-Galvan, B. Pawelec, V.A. de la Pena O'Shea, J.L.G. Fierro, P.L. Arias, Appl. Catal. B: Environ. 51 (2004) 83–91.

[142] J. Requies, M.C. Alvarez-Galvan, V.L. Barrio, P.L. Arias, A.M. Carrera, V.A. de la Pena O'Shea, J.L.G. Fierro, Appl. Catal. B: Environ. 79 (2008) 122–131.

[143] M.F. Luo, X.X. Yuan, X.M. Zheng, Appl. Catal. A: Gen. 175 (1998) 121–129.

[144] M. Ferrandon, J. Carno, S. Jaras, E. Bjornbom, Appl. Catal. A: Gen. 180 (1999) 141–151.

[145] Y.C. Son, V.D. Makwana, A.R. Howell, S.L. Suib, Angew. Chem. Int. Ed. 40 No.22 (2001) 4280–4282.

[146] A.R. Gandhe, J.S. Rebello, J.L. Figueiredo, J.B. Fernandes, Appl. Catal. B: Environ. 72 (2007) 129–135.

[147] X. Tang, Y. Li, J. Chen, Y. Xu, W. Shen, Microporous Mesoporous Mater. 103 (2007) 250–256.

[148] X.S. Liu, Z.N. Jin, J.Q. Lu, X.X. Wang, M.F. Luo, Chem. Engg. J. 162 (2010) 151–157.

[149] X. Yang, J. Han, Z. Du, H. Yuan, F. Jin, Y. Wu, Catal. Commun. 11 (2010) 643–646.

[150] J.S. Rebello, P.V. Samant, J.L. Figueiredo, J.B. Fernandes, J. Power Sources 153 (2006) 36–40.

[151] G.G. Xia, Y.G. Yin, W.S. Willis, J.Y. Wang, S.L. Suib, J. Catal. 185 (1999) 91–105.

[152] R. Jothiramalingam, M.K. Wang, J. Hazardous Mater. 147 (2007) 562–569.

[153] H. Rongrong, C. Yi, X. Lanying, W. Dezheng, Chin J. Catal. 28(5) (2007) 463–468.

[154] X.M. Liu, S.Y. Fu, C.J. Huang, Powder Technol. 154 (2005) 120–124.

[155] M. Ghaemi, A. Ghaolami, R.B. Moghaddam, Electrochem. Acta 53 (200) 3250–3256.

[156] M.S. Niasari, F. Mohandes, F. Davar, K. Saberyan, Appl. Surf. Sci. 256 (2009) 1476–1480.

[157] J. Park, E. Kang, C.J. Bae, J.G. Park, H.J. Noh, J.Y. Kim, J.H. Park, T. Hyeon, J. Phys. Chem. B 108 (2004) 13594–13598.

[158] C. Laberty, C. Marquez-Alvarez, C. Drouet, P. Alphonse, C. Mirodatos, J. Catal. 198 (2001) 266–276.

[159] A.D. Poali, A.A. Barresi, Ind. Eng. Chem. Res. 40 (2001) 1460–1464.

[160] M.F. Luo, X.M. Zheng, Y.J. Zhong, Ind. J. Chem. 38A (1999) 703–707.

[161] L.C. Wang, L. He, Y.M. Liu, Y. Cao, H.Y. He, K.N. Fan, J.H. Zhuang, J. Catal. 264 (2009) 145–153.

[162] J. Cao, Y. Zhu, L. Shi, L. Zhu, K. Bao, S. Liu, Y. Qian, Eur. J. Inorg. Chem. (2010) 1172–1176.

[163] W.N. Li, L. Zhang, S. Sithambaram, J. Yuan, X.F. Shen, M. Aindow, S.L. Suib, J. Phys. Chem. C 111 (2007) 14694–14697.

[164] L. Liu, H. Liang, H. Yang, J. Wei, Y. Yang, Nanotechnol. 22 (2011) 015603 (8 pages).

[165] B. Ji, X. Jiao, N. Sui, Y. Duan, D. Chen, Cryst. Eng. Comm. 12 (2010) 3229–3234.

[166] V.G. Kumar, K.B. Kim, Ultrasonics Sonochem. 13 (2006) 549–556.

[167] A. Zolfaghari, F. Ataherian, M. Ghaemi, A. Gholami, Electrochem. Acta 52 (2007) 2806–2814.

[168] I.S. Yakovleva, L.A. Isupova, V.A. Rogov, V.A. Sadykov, Kinetics Catal. 49No.2 (2008) 261–270.

[169] Z.Q. Zou, M. Meng, Y.Q. Zha, J. Phys. Chem. C 114 (2010) 468–477.

[170] S.H. Ju, Y.C. Kang, Mater. Res. Bulletin 43 (2008) 590–600.

[171] M.I. Dominguez, P. Navarro, F. Romero-Sarria, J.J. Delgado, M.A. Centeno, M. Montes, J.A. Odriozola, J. Nanosci. Nanotechnol. 9 (2009) 3837.

[172] Y. Ding, X. Shen, S. Sithambaram, S. Gomez, R. Kumar, V. Mark, V. Crisostomo, S.L. Suib, M. Aindow, Chem. Mater. 17 (2005) 5382–5389.

[173] W.Y. Hernández, M.A. Centeno, F. Romero-Sarria, S. Ivanova, M. Montes, J.A. Odriozola, Catal. Today 157 (2010) 160–165.

[174] S.J. Yuan, K. Xu, L.M. Yu, S.X. Cao, J.C. Zhang, J. Magnetism Magnetic Mater. 314 (2007) 100–104.

[175] B. Murugan, A.V. Ramaswamy, Chem. Mater. 17 (2005) 3983–3993.

[176] M. Wei, Y. Konishi, H. Zhou, H. Sugihara, H. Arakawa, Nanotechnol. 16 (2005) 245–249.

[177] H. Cao, S.L. Suib, J. Am. Chem. Soc. 116 (1994) 5334–5342.

[178] H. Yagi, T. Ichikawa, A. Hirano, S. Ogawa, Y. Takeda, Ionics 8 (2002) 1–5.

[179] L. Yuan, Z. Li, J. Sun, K. Zhang, Y. Zhou, Mater. Lett. (2003) 1945–1948.

[180] J, Chen, J, Li, H, Li, X, Huang, W, Shen, Microporous Mesoporous Mater. 116 (2008) 586–592.

[181] Y.F. Han, F. Chen, Z.Y. Zhong, K. Ramesh, E. Widjaja, L.W. Chen, Catal. Commun. 7 (2006) 739–744.

[182] Z. Aifei, L. Jiping, L. Guangshu, Front. Chem. Eng. China 1 (2007) 55–58.

[183] P. Billik, M. Caplovicova, J. Janata, V.S. Fajnor, Mater. Lett. 62 (2008) 1052–1054.

[184] Q. Li, G. Luo, J. Li, X. Xia, J. Mater. Processing Technol. 137 (2003) 25–29.

[185] Y.-F. Yu Yao, J. Catal. 87 (1984) 152–162.

[186] G. Ertl, Sci. 245 (1991) 1750–1755.

[187] J. Barbier Jr, D. Duprez, Appl. Catal. B: Environ. 3 (1993) 61–83.

[188] N. D. Ivanova, S. V. Ivanov, E. I. Boldyrev, G. V. Sokol'skii, I. S. Makeeva, Russian J. Appl. Chem. 75No.9 (2002) 1420–1423.

[189] Z.R. Tang, C.D. Jones, J.K.W. Aldridge, T.E. Davies, M.J. Rosseinsky, J.B. Claridge, Z. Xu, M.J. Crudace, G.J. Hutchings, Chem. Cat. Chem. 1 (2009) 247–251.

[190] A. Dyer, M. Pillinger, J. Newton, R. Harjula, T. Moller, S. Amin, Chem. Mater. 12 (2000) 3798–3804.

[191] R. Hu, C. Yan, L. Xie, Y. Cheng, D. Wang, Int. J. Hydrogen Energy 36 (2011) 64–71.

[192] M.M. Schubert, S. Hackenberg, A.C. Van Veen, M. Muhler, R.J. Behm, J. Catal. 197 (2001) 113.

[193] A. Longo, L.F. Liotta, G.D. Carlo, F. Giannici, A.M. Venezia, A. Martorana, Chem. Mater. 22 (2010) 3952–3960.

[194] H. Zou, S. Chen, Z. Liu, W. Lin, Powder Technol. 207 (2011) 238–244.

[195] V.N. Sanin, D.E. Andreev, E.V. Pugacheva, S.Ya. Zhuk, V.N. Borshch, V.I. Yukhvid, Inorganic Mater. 45No.7 (2009) 777–784.

[196] K. S. Abdel Halim, A. M. Ismail, M. H. Khedr, M. F. Abadir, Top Catal. 47 (2008) 66–72.

[197] P. Mars, D.W. Van Krevelen, Chem. Eng. Sci. Spec. Suppl. 3 (1954) 41–59.

[198] J. Gong, R.A. Ojifinni, T.S. Kim, J.D. Stiehl, S.M. Mcclure, J.M. White, C.B. Mullins, Topics Catal. 44No.1-2 (2007) 57–63.

[199] R.A. Ojifinni, N.S. Froemming, J. Gong, M. Pan, T.S. Kim, J.M. White, G. Henkelman, C.B. Mullins, J. Am. Chem. Soc. 130 (2008) 6801–6812.

[200] M. Date, M. Okumura, S. Tsubota, M. Haruta, Angew. Chem. Int. Ed. 43 (2004) 2129–2132.

[201] M. Date, H. Imai, S. Tsubota, M. Haruta, Catal. Today 122 (2007) 222–225.

[202] H.H. Kung, M.C. Kung, C.K. Costello, J. Catal. 216 (2003) 425–432.

[203] A. Luengnaruemitchai, D.T.K. Thoa, S. Osuwan, E. Gulari, Int. Association Hydrogen Energy (2005).

[204] M. Date, M. Haruta, J. Catal. 201 (2001) 221–224.

[205] T. Yan, J. Gong, D.W. Flaherty, C.B. Mullins, J. Phys. Chem. C 115 (2011) 2057–2065.

[206] S.D. Ebbesen, B.L. Mojet, L. Lefferts, J. Catal. 246 (2007) 66–73.

[207] S. Monyanon, S. Pongstabodee, A. Luengnaruemitchai, J. Power Sources 163 (2006) 547–554.

[208] S.H. Cho, J.S. Park, S.H. Choi, S.K. Lee, S.H. Kim, Catal. Lett. 103No.3-4 (2005) 257–261.

[209] M. Okumura, N. Masuyama, E. Konishi, S. Ichikawa, T. Akita, J. Catal. 208 (2002) 485–489.

[210] E.C. Njagi, C.H. Chen, H. Genuino, H. Galindo, H. Huang, S.L. Suib, Appl. Catal. B: Environ. 99 (2010) 103–110.

[211] C.H. Chen, E.C. Njagi, S.P. Sun, H. Genuino, B. Hu, S.L. Suib, Chem. Mater. 22 (2010) 3313–3315.

[212] X. Xie, Y. Li, Z.Q. Liu, M. Haruta, W. Shen, Nature 458 (2009) 746–749

[213] T. Visser, T.A. Nijhuis, A.M.J. van der Eerden, K. Jenken, Y. Ji, W. Bras, S. Nikitenko, Y. Ikeda, M. Lepage, B.M. Weckhuysen, J. Phys. Chem. B 109 (2005) 3822–3831.

[214] H.I. Leed, J.M. White, J. Catal. 63 (1980) 261–264.

[215] G.W. Coulston, G.L. Haller, J. Chem. Phys. 95 (1991) 6932–6938.

[216] Y.D. Kim, H.Over, G. Krabbes, G. Ertl, Topics in Catalysis 14 No. 1-4 (2001) 95–100.

[217] C.H.F. Peden, D.W. Goodman, J. Phys. Chem. 90 (1986) 1360–1367.

[218] C. Stampfl, S. Schwegmann, H. Over, M. Scheffler, G. Ertl, Phys. Rev. Lett. 77 (1996) 3371.

[219] A. Bottcher, M. Rogazia, H. Niehus, H. Over, G. Ertl, J. Phys. Chem. 103 (1999) 6267–6272.

[220] P.V. Snytnikov, M.M. Popova, Y. Men, E.V. Rebrov, G. Kolb, V. Hessel, J.C. Schouten, V.A. Sobyanin, Appl. Catal. A: Gen. 350 (2008) 53–62.

[221] Y.F. Han, M.J. Kahlich, M. Kinne, R.J. Behm, Phys. Chem. Chem. Phys. 4 (2002) 389–397.

[222] D. W. Goodman, C. H. F. Peden, J. Phys. Chem. 90 (1986) 4839.

[223] A.R. West, Solid State Chemistry and its Applications, John Wiley and Sons, Singapore, 2003, p. 115.

[224] A.R. West, Solid State Chemistry and its Applications, John Wiley and Sons, Singapore, 2003, p. 102.

[225] R.L. Dutta, A. Syamal, Elements of Magnetochemistry, East-West Press, New Delhi, 1993, p. 44.

[226] V. L. J. Joly, P. A. Joy, S. K. Date and C. S. Gopinath, J. Phys. Condens. Matt. 13 (2001) 649.

[227] D.K. Chakrabarty, B. Vishvanathan, Heterogeneous Catalysis, New Age publishers, India, p. 231.

[228] A.M.A. Hashem, H.A. Mohamed, A. Bahloul, A.E. Eid, C.M. Julien, Ionics 14 (2008) 7–14.

[229] A. Kayan, E. Tarcan, U. Kadiroglu, K. Esmer. Mater. Lett. 58 (2004) 2170–2174.

[230] B. Banov, A. Momchilov, M. Massot, C. M. Julien. Mater. Sci. Engg. B 100 (2003) 87–92.

[231] N. Dharmaraj, P. Prabu, S. Nagarajan, C. H. Kim, J. H. Park, H. Y. Kim. Mater. Sci. Engg. B 128 (2006) 111–114.

[232] Q. Dong, H. Su, F. Song, D. Zhang, N. Wang, J. Am. Ceram. Soc. 90 (2007) 376–380.

[233] Y. Chen, Y. Zhang, Q.Z. Yao, G.T. Zhou, S. Fu, H. Fan, J. Solid State Chem. 180 (2007) 1218–1223.

[234] X.Y. Xue, L.L. Xing, Y.G. Wang, T.H. Wang, Solid State Sci. 11 (2009) 2106–2110.

[235] R.L. Mary, B. Jeyaraj, K.S. Nagaraja, Sens. Transducers J. 101 (2009) 42–51.

[236] A. H. Gemeay, I. A. Mansour, R. G. El-Sharkawy, A. B. Zaki, Eur. Poly. J. 41 (2005) 2575–2583.

[237] A.B. Murphy, Solar Energy Mater. Solar Cells 91 (2007) 1326–1337.

[238] S. Jana, S. Pande, A.K. Sinha, S. Sarkar, M. Pradhan, M. Basu, S. Saha, T. Pal, J. Phys. Chem. C (2009) 1386–1392.

[239] S. Ponce, M.A. Pana, J.L.G. Fierro, Appl. Catal. B: Environ. 24 (2000) 193–205.

[240] A. Machochi, T. Ioannides, B. Stasinska, W. Gac, W. Grzegorezyk, S. Pasieczna, J. Catal. 227 (2004) 282–296.

[241] R.J. Iwanowski, M.H. Heinonen, W. Paszkowicz, T. Story, B. Witkowska, Appl. Surf. Sci. 252 (2006) 3632–3641.

[242] M.V.R. Rao, T. Shripathi, J. Electron Spectrosc. Relat. Phenom. 87 (1997) 121.

[243] A. Simmons, J. Yang, J.J. Xu, Rutgers Scholar 4 (2002).

[244] A.V. Salker, N.J. Choi, J.H. Kwak, B.S. Joo, D.D. Lee, Sens. Actuators B 106 (2005) 461–467.

[245] M.F. Luo, X.X. Yuan, X.M. Zheng, Appl. Catal. A 175 (1998) 121–129.

[246] S.H. Oh, G. B. Hoflund, J. Catal. 245 (2007) 44–35.

[247] A.V. Salker, Indian J. Chem. Technol. 11 (2004) 683–687.

[248] A.V. Salker, S.J. Naik, Appl. Catal. B: Environ. 89 (2009) 246–254.

APPENDIX - I

PUBLICATIONS

Palladium doped manganese dioxide catalysts for low temperature carbon monoxide oxidation

A. V. Salker and R. K. Kunkalekar

Catalysis Communication 10 (2009) 1776–1780.

Low temperature carbon monoxide oxidation over nanosized silver doped manganese dioxide catalysts

R. K. Kunkalekar and A. V. Salker

Catalysis Communication 12 (2010) 193–196.

Activity of Pd doped and supported Mn_2O_3 for CO oxidation reaction

R. K. Kunkalekar and A. V. Salker

Communicated

Nano-sized Cu-Pd doped and supported MnO_2 catalysts for lower temperature catalytic CO oxidation reaction

R. K. Kunkalekar and A. V. Salker

Communicated

APPENDIX - II

CONFERENCE PUBLICATIONS

Preparation, characterization and solid state studies on Ni doped Mn_2O_3 nanomaterials

R. K. Kunkalekar and A. V. Salker

Second International Conference on Frontiers in Nano Science and Technology (Cochin Nano 2009), January 3–6, 2009. CUSAT, Cochin – Kerala.

Preparation of Ce doped Mn_2O_3 catalysts for CO oxidation

R. K. Kunkalekar and A. V. Salker

19th National Symposium on Catalysis (CATSYMP-19), catalysis for sustainable energy and chemicals, January 18–21, 2009. NCL – Pune.

Preparation characterization of Ni doped MnO_2 nanomaterials

R. K. Kunkalekar and A. V. Salker

International Conference on Materials for the Millennium (MATCON 2010), January 11–13, 2010. CUSAT, Cochin – Kerala.

Preparation and characterization of Ag doped Mn_2O_3 catalysts for CO oxidation

R. K. Kunkalekar and A. V. Salker

RSC-West India section Ph. D. Student Symposium, September 3–4, 2010. Goa University – Goa.

Carbon monoxide oxidation over doped manganese dioxide catalysts

R. K. Kunkalekar and A. V. Salker

DAE-BRNS 3rd International Symposium on Materials Chemistry (ISMC-2010), December 7-11, 2010. BARC – Mumbai.

Preparation and characterization of Pd doped Mn_2O_3 catalysts for CO oxidation

R. K. Kunkalekar and A. V. Salker

20th National Symposium on Catalysis for Energy Conversion and Conservation of Environment, December 19-22, 2010. IIT – Madras.

Preparation and characterization of doped manganese dioxide materials and their catalytic activity for CO oxidation reaction

R. K. Kunkalekar and A. V. Salker

Third International Conference on Frontiers in Nano Science and Technology (Cochin Nano 2011), August 14–17, 2011. CUSAT, Cochin – Kerala. (accepted)

Catalysis Communications 10 (2009) 1776–1780

Contents lists available at ScienceDirect

Catalysis Communications

journal homepage: www.elsevier.com/locate/catcom

Palladium doped manganese dioxide catalysts for low temperature carbon monoxide oxidation

A.V. Salker *, R.K. Kunkalekar

Department of Chemistry, Goa University, Goa 403206, India

ARTICLE INFO

Article history:
Received 31 January 2009
Received in revised form 21 May 2009
Accepted 29 May 2009
Available online 6 June 2009

Keywords:
MnO_2
$Mn_{1-x}Pd_xO_2$
Carbon monoxide oxidation
Co-precipitation
Influence of moisture

ABSTRACT

Nano-sized palladium doped manganese dioxide catalysts with varying compositions were prepared by the co-precipitation method. Palladium doped manganese dioxide catalysts show markedly enhanced CO oxidation activity, and CO conversion even at 35 °C. Strong interaction occurs between palladium and manganese dioxide which results in high catalytic activity and total CO conversion occurs at a lower temperature. Activity test carried out at fixed temperature indicate that the catalysts retain their activity with increasing time. The moisture influenced the catalytic activities considerably. The SEM study shows that particles are nano-sized and almost spherical in shape.

1. Introduction

Carbon monoxide (CO) is one of the toxic components of industrial waste gases and exhaust gases from automobiles. It is also formed in the regeneration of hydrocarbon cracking catalysts. It causes potential harmful effects on living beings and environment. Thus complete elimination or abatement below the permissible levels fixed by environmental regulations is a major concern. In recent years many methods have been used to reduce the emissions of CO. The catalytic technologies are attractive because of their low cost and high efficiency. Nanotechnology has recently experienced a rapid escalation owing to the unique physical and chemical properties of nanoparticles compared with the bulk solids [1–4].

Many different catalysts have been prepared and tested for the low temperature carbon monoxide oxidation activity. Precious metals like Pt, Pd, Au, Rh, Ru are active catalyst for CO conversion [5–7]. They generally allow low operating temperatures and higher space velocities than the transition metal oxide based catalysts. However, due to the high cost of noble metals and their less availability as well as sublimation and sintering problems, considerable part of the research has been devoted to the development of suitable catalyst among the transition metal oxides [8–10]. Appropriate combination of oxides and some mixed metal oxides exhibit greater activity and thermal stability then the single oxides. Combination of noble metals with transition metal oxides result in materials with high catalytic activity, stability and also require less quantity of the noble metals [11–14]. Few reports are available on palladium supported catalysts, indicating that they are very active and stable. Palladium is used as catalyst in various types of reactions [15–18]. Manganese dioxide is an important material widely used as a catalyst [19–22], cathodic material in batteries [23,24] and in organic synthesis. The properties of MnO_2 are influenced significantly by its structure, morphology and preparative methods. The basic building block of manganese oxide is MnO_6 octahedra, these octahedra share their corners or edges into variety of different structural arrangements [25,26]. A great deal of attention has been paid to the preparation of MnO_2 with different crystallographic structures and morphologies [25–28].

In the present investigation, a series of nano-sized Pd doped MnO_2 catalyst were prepared by dextrose aided co-precipitation technique. The prepared catalysts were tested for CO oxidation reaction and other studies. The interaction of Pd with MnO_2 results in a good catalytic activity. The effect of moisture was studied to see the performance of the catalyst for CO conversion along with activity test.

2. Experimental

2.1. Catalyst preparation

The solid catalysts of composition $Mn_{1-x}Pd_xO_2$ (where $X = 0$, 0.02, 0.05, 0.08) were prepared by dextrose aided co-precipitation technique. All reagents used were of analytical grade. Appropriate amount of manganese (II) acetate was dissolved in distilled water at room temperature, calculated amount of palladium (II) chloride

* Corresponding author. Tel.: +91 832 6519315; fax: +91 832 2452889.
E-mail address: sal_arun@rediffmail.com (A.V. Salker).

1566-7367/$ - see front matter © 2009 Elsevier B.V. All rights reserved.
doi:10.1016/j.catcom.2009.05.028

was taken in a separate beaker, to this distilled water and concentrated nitric acid was added and heated with stirring to dissolve completely. Both these solutions were mixed together at room temperature to get a clear homogeneous solution. This solution was added to 2% dextrose solution at 100 °C with stirring, dextrose solution was added to avoid agglomeration. The precipitation was carried out by adding drop by drop solution of sodium hydroxide (10%) to the above solution under vigorous stirring. Subsequently, the suspension of precipitated metal hydroxide mixture (at pH 9) was subjected to oxidation by drop wise addition of 30% H_2O_2 solution with constant stirring in order to adjust the appropriate oxidation state of the metal ions. The precipitate was then digested on a water bath for three hours, filtered and dried in air at 120 °C for 10 h. Finally the dried precipitate was homogenized well in mortar and calcined in air at 400 °C for 5 h.

2.2. Catalyst characterization

The X-ray powder diffraction (XRD) measurement was carried out on RIGAKU diffractometer, using Cu Kα radiation (λ = 1.5418 Å). The BET surface area was measured by nitrogen adsorption at liquid nitrogen temperature using a SMART SORB-91 surface area analyzer. The samples were degassed at 200 °C for 4 h prior to the adsorption experiments. The surface morphology was determined with JSM-5800LV scanning electron microscope (SEM) instrument operating at 20 kV. Thermal analysis was carried out on a NETZCH STA 409 PC TG/DSC instrument in air at a heating rate of 10 K min^{-1} and heated from ambient to 1100 °C.

2.3. Catalytic activity

The catalytic tests for CO oxidation by O_2 were carried out in a continuous flow, fixed bed glass reactor. The catalyst powder of 0.9 g was supported between glass wool plugs in a glass reactor which was placed in an electric furnace. The catalytic activity was determined using a feed gas composition of 5% CO and 5% O_2 in nitrogen. All these three gases were first mixed in a mixing bulb. The individual gas flow rates were controlled using flow meters and precision needle valves, previously calibrated for each specific gas. The mixture of gases was then allowed to pass over the catalyst at a rate of 5000 ml h^{-1}. The temperature of the furnace was raised slowly from room temperature to the temperature at which 100% CO conversion is achieved. The feed gases and the products were analyzed employing an online Gas Chromatograph with molecular sieve 13X and Porapak Q columns. H_2 was used as a carrier gas. The CO was prepared in the laboratory by standard procedure and further purified by passing through alkali and molecular sieve traps. Oxygen, nitrogen and hydrogen gases were used from pure commercial cylinders.

The activity of the catalysts was tested for CO oxidation continuously for 5 h, by keeping the catalyst at a constant temperature. Also the effect of moisture on the catalytic activity was studied with low and high moisture contents at a fixed temperature.

3. Results and discussion

3.1. Characteristic properties

Fig. 1 shows the XRD pattern for MnO_2 and $Mn_{0.92}Pd_{0.08}O_2$. The peaks were assigned for MnO_2 at the 2θ angles of 37.34° (1 3 1), 38.42° (2 3 0), 42.3° (3 0 0), 56.22° (1 6 0) and 65.04° (4 2 1) shown in Fig. 1a. All the reflections of the XRD patterns can be readily indexed to MnO_2 which agrees well with the values reported in literature (ICDD Card No. 14-0644). Whereas the XRD phase identification of $Mn_{0.92}Pd_{0.08}O_2$ revealed characteristic signals at

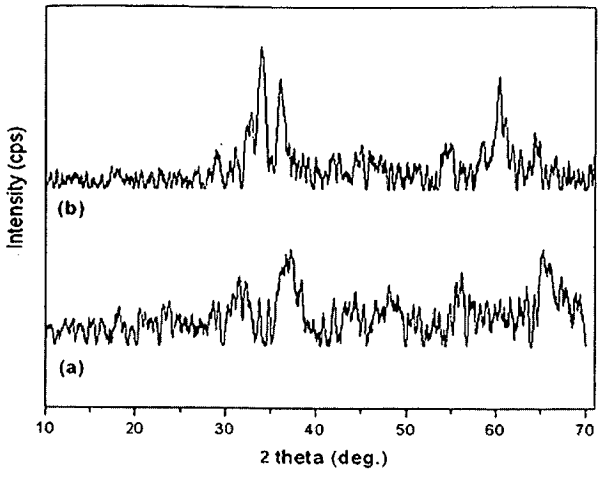

Fig. 1. XRD pattern of (a) MnO_2 and (b) $Mn_{0.92}Pd_{0.08}O_2$.

2θ values of 34.04° (1 3 0), 36.04° (0 2 1), 55.03° (2 2 1) and 60.34° (2 3 1) which is shown in Fig. 1b and these reflections correspond to the ramsdellite structure of MnO_2 (ICDD Card No. 05-0600). Pd doped samples exhibits ramsdellite structure of MnO_2.

The BET surface area of prepared samples is listed in Table 1. MnO_2 shows surface area 44 m^2g^{-1}. There is no decrease in surface area when palladium is doped in MnO_2.

The surface morphology of the prepared catalysts was investigated by SEM and is shown in Fig. 2. From the SEM images it is observed that the particles are nano sized and in the range of 30–50 nm. Preparation of catalysts by co-precipitation technique in dextrose solution may highly influence the particle size, also not much agglomeration of particles is seen. Due to the addition of dextrose solution during preparation, the precipitated mixture does not get settled easily and they remain suspended in the solution. As a result, the particles got separated thus resulting in ultra fine, spherical nanoparticles.

Thermogravimetry (TG) and differential scanning calorimetry (DSC) of MnO_2 and $Mn_{0.92}Pd_{0.08}O_2$ were carried out. All the samples showed the initial weight loss at 80–120 °C region which is generally due to loss of adsorbed water [28]. The weight loss in the region 560–700 °C is attributed solely to the loss of oxygen and this weight loss is generally considered due to the transformation of MnO_2 to Mn_2O_3 phase [29]. Further weight loss in the temperature range 880–1050 °C is due to the conversion of Mn_2O_3 to Mn_3O_4 phase.

3.2. Catalytic performance

Fig. 3 shows the catalytic performance for CO oxidation of the MnO_2 and Pd doped MnO_2 samples. From the figure it is clear that Pd doped catalysts show high activity for CO oxidation. It is observed that the light-off temperature (T_{50}) of Pd doped MnO_2 catalysts are at a much lower temperature than that of MnO_2

Table 1
BET surface area and catalytic activity of the samples.

Sample	SA ($m^2 g^{-1}$)	T_{50} (°C)	T_{100} (°C)
MnO_2	44	130	200
$Mn_{0.98}Pd_{0.02}O_2$	55	87	110
$Mn_{0.95}Pd_{0.05}O_2$	48	76	115
$Mn_{0.92}Pd_{0.08}O_2$	45	69	90

T_{50} Temperature for 50% conversion for CO oxidation.
T_{100} Temperature for 100% conversion for CO oxidation.

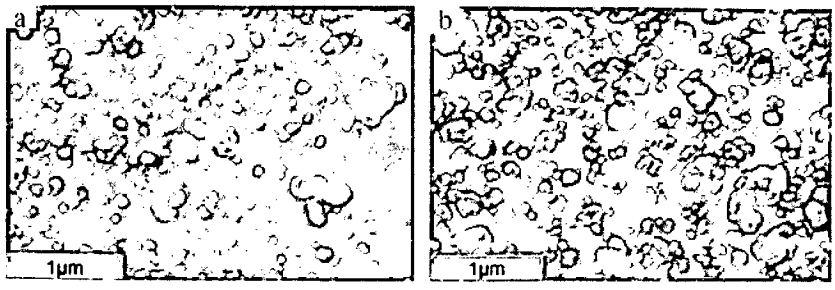

Fig. 2. SEM images of the catalysts: (a) $Mn_{0.98}Pd_{0.02}O_2$ and (b) $Mn_{0.92}Pd_{0.08}O_2$.

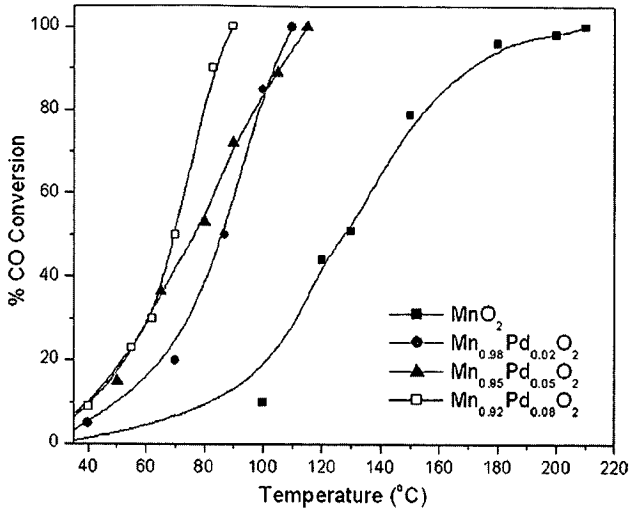

Fig. 3. CO conversion against catalyst temperature over different catalysts.

catalyst. The light-off temperatures of 50% CO conversion (T_{50}) and 100% CO conversion (T_{100}) over different catalysts are presented in Table 1. The addition of Pd in MnO_2 facilitates the adsorption of CO as well O_2 which in turn shows higher activity. The $Mn_{0.92}Pd_{0.08}O_2$ gave total conversion at around 90 °C which is to a great extent much lower as compared to MnO_2, indicating that Pd doped MnO_2 is an excellent catalyst for CO oxidation reaction.

Generally CO oxidation on transition metal oxides follows a mechanism proposed by Mars–Van Krevelen [30], implying that the lattice oxygen incorporation occurs during CO oxidation and that the reduced surface of the metal oxide is rejuvenated by taking up oxygen from the feed mixture [31]. On the other hand, it is well known that the reactivity for the structure sensitive reaction depends on the particle size, surface morphology and crystal plane of the catalyst [1]. Thus surface structure of the catalyst also influences catalytic performance.

Maximum CO conversion over metal oxide catalyst greatly depends on the method of preparation. The surface area largely depends on the preparative methods and higher the surface area generally corresponds to higher oxidation activity. Inspite of $Mn_{0.92}Pd_{0.08}O_2$ having lower surface area it showed highest activity because Pd–MnO_2 interaction might have resulted into more active sites per unit surface area compared to other catalysts. It is seen that by introducing Pd in MnO_2 influences the activity of MnO_2 and 100% CO conversion is obtained at temperature of 90 °C, this gives evidence that by introducing Pd in MnO_2 produces a strong Pd–MnO_2 interaction which may be similar like the interaction in Ag–MnO_2 [1] and this interaction results in more favorable surface active sites which gives higher CO conversion at low temperature.

3.3. Activity test for the catalysts and effect of moisture on its activity

The activities of the catalysts MnO_2 and $Mn_{0.92}Pd_{0.08}O_2$ were tested for CO oxidation continuously for 5 h by maintaining the temperature of the catalyst near to its 50% CO conversion temperature (T_{50}).

MnO_2 catalyst was maintained at a fixed temperature of 130 °C to check the activity. Around 50% CO conversion was observed in 1 h. After 5 h nearly 55% CO conversion is observed, indicating increase in activity with time. Fig. 4a depicts the results of the activity test. No decrease in activity of the catalyst was accounted during this period, signifying that MnO_2 catalyst is a good catalyst for CO conversion.

The activity of $Mn_{0.92}Pd_{0.08}O_2$ was also tested for 5 h continuously. This test was performed to ascertain whether the activity of the catalyst retains with increasing reaction time or not. The catalyst was kept at a fixed temperature of 50 °C. With increase in the reaction time, the CO conversion remains almost constant with a slight increase. Fig. 5a shows the results of activity test. It was reported that palladium oxide powder shows high activity for CO oxidation even at room temperature [32], but its activity decreases with increasing temperature. But when MnO_2 was doped with Pd, a strong interaction occurs between Pd and MnO_2 which results in high catalytic activity. Even catalyst like Ag doped OMS-2 shows very low activity at 100 °C and its activity goes on decreasing with time [26].

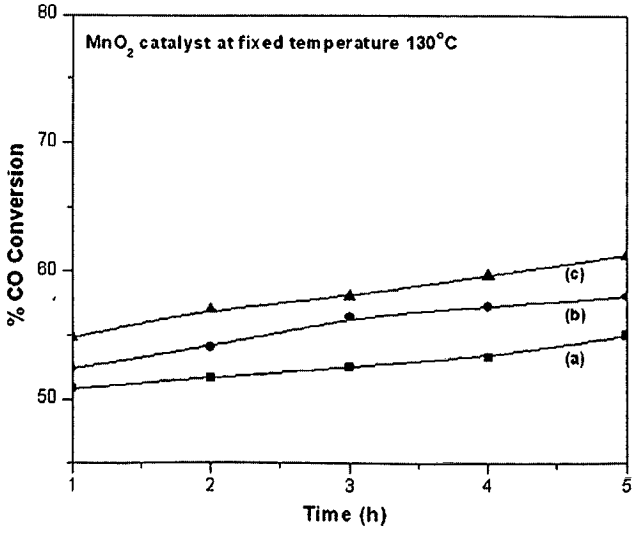

Fig. 4. Activity study of MnO_2 catalyst at 130 °C for 5 h for CO conversion (a) activity without moisture, (b) effect of low moisture content on activity and (c) effect of high moisture content on activity.

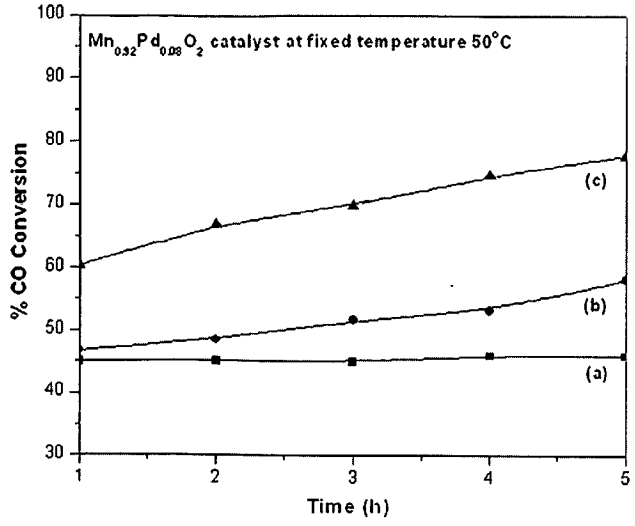

Fig. 5. Activity study of $Mn_{0.92}Pd_{0.08}O_2$ catalyst at 50 °C for 5 h for CO conversion. (a) Activity without moisture, (b) effect of low moisture content on activity and (c) effect of high moisture content on activity.

The effect of moisture on the activities of MnO_2 and $Mn_{0.92}Pd_{0.08}O_2$ catalysts were tested. The activity was tested in the presence of low and high moisture content. The activity of the catalyst in the presence of low moisture content was tested by allowing the mixture of feed gases to pass through water trap (maintained at room temperature) before passing through the catalyst bed. At room temperature the number of water molecules passing along with feed gases is around 1.6730×10^{21} molecules h^{-1}. Also the activity of the catalyst was tested with high moisture content by allowing the mixture of feed gases to pass through water trap (maintained at 50 °C temperature) before passing through the catalyst, at 50 °C the number of water molecules passing along with feed gases is around 8.3117×10^{21} molecules h^{-1}. In both the studies catalyst temperature was kept constant and activity was tested for 5 h continuously.

MnO_2 catalyst was kept at a fixed temperature of 130 °C, and then the mixture of feed gases coming from the water trap was allowed to pass through the catalyst bed. Under the influence of low moisture, after 1 h, nearly 52% CO conversion was observed. Later CO conversion was found to increase and after 5 h 58% CO conversion was observed as seen in Fig. 4b. This illustrates that the catalyst retains its activity under the influence of moisture and the results obtained in presence of moisture are much better then in absence of moisture. With increasing time of the reaction there is an increase in activity of the catalyst indicating optimistic effect of moisture on the MnO_2 catalyst. The effect of high moisture content on catalytic activity of MnO_2 shows much better results as compared to low moisture content. More CO conversion was observed under the influence of higher moisture content. After 1 h, 55% CO conversion was observed and it goes on increasing with reaction time. Around 61% CO conversion was seen after 5 h, thus by providing more amount of moisture along with feed gases, the activity for CO conversion was seen to increase as shown in Fig. 4c.

The $Mn_{0.92}Pd_{0.08}O_2$ catalyst was also tested to see the effect of moisture. The catalyst was kept at a fixed temperature of 50 °C. Under the influence of low moisture, after 1 h, 47% CO conversion was observed as shown in Fig. 5b and after 5 h it increases to about 58% showing increase in activity by roughly 10% after 5 h. The $Mn_{0.92}Pd_{0.08}O_2$ shows excellent CO conversion activity with higher moisture content. Around 60% CO conversion was seen after 1 h and with increase in the time of reaction, it reaches to 78% after 5 h as seen in Fig. 5c. Consequently the activity of Pd doped MnO_2 is also highly influenced by passing moisture along with the feed gases and with more moisture it gives much better result.

From these findings it is seen that the presence of moisture strongly influences the CO conversion activities over these catalysts. No deactivation is observed for CO oxidation reaction. Obviously, the reaction mechanism of CO oxidation by O_2 over these catalysts under the influence of moisture is likely to be different. Due to hydration of the adsorbed CO molecule, the CO bond is weakened significantly, which facilitates its oxidation [33] and presence of Pd highly influence this activity. Also water may increase the acidic sites on the surface of the catalyst [34] enhancing CO adsorption thus leading to higher activity.

4. Conclusions

The Pd doped MnO_2 catalysts showed high activity for CO oxidation and complete conversion was achieved at a much lower temperature as compared to MnO_2. The XRD pattern confirmed the formation of MnO_2 phase. SEM images shows that particles are nano sized and in the range of 30–50 nm. Thermal analysis gives evidence for the phase change of MnO_2 to Mn_2O_3 and Mn_3O_4 with increase in temperature. The activity test carried out at fixed temperature showed that the activity does not fall with time but show slight increase in the percentage conversions. The influence of moisture has enhanced the activity over these catalysts.

Acknowledgement

This work is financially supported by University Grant Commission, New Delhi.

References

[1] R. Xu, X. Wang, D. Wang, K. Zhou, Y. Li, J. Catal. 237 (2006) 426–430.
[2] Li.H. Chang, N. Sasirekha, Y.W. Chen, Catal. Commun. 8 (2007) 1702–1710.
[3] J.Y. Luo, M. Meng, X. Li, X.G. Li, Y.Q. Zha, T.D. Hu, Y.N. Xie, J. Zhang, J. Catal. 254 (2008) 310–324.
[4] S. Kobayashi, I.R.M. Kottegoda, Y. Uchimoto, M. Wakihara, J. Mater. Chem. 14 (2004) 1843–1848.
[5] F. Mariño, C. Descorme, D. Duprez, Appl. Catal. B 54 (2004) 59–66.
[6] N. Russo, D. Fino, G. Saracco, V. Specchia, Catal. Today 117 (2006) 214–219.
[7] U.R. Pillai, S. Deevi, Appl. Catal. A 299 (2006) 266–273.
[8] M. Kramer, T. Schmidt, K. Stowe, W.F. Maier, Appl. Catal. A 302 (2006) 257–263.
[9] C. Laberty, C. Marquez-Alvarez, C. Drouet, P. Alphonse, C. Mirodatos, J. Catal. 198 (2001) 266–276.
[10] U.R. Pillai, S. Deevi, Appl. Catal. B 65 (2006) 110–117.
[11] S. Monyanon, S. Pongstabodee, A. Luengnaruemitchai, J. Power Sources 163 (2006) 547–554.
[12] H. Rongrong, C. Yi, X. Lanying, W. Dezheng, Chin. J. Catal. 28 (5) (2007) 463–468.
[13] U.G. Singh, J. Li, J.W. Bennett, A.M. Rappe, R. Seshadri, S.L. Scott, J. Catal. 249 (2007) 349–358.
[14] M. Jeguirim, V. Tschamber, P. Ehrburger, Appl. Catal. B 76 (2007) 235–240.
[15] J. Requies, M.C. Alvarez-Galvan, V.L. Barrio, P.L. Arias, J.F. Cambra, M.B. Guemez, A.M. Carrera, V.A. de la Pena O'Shea, J.L.G. Fierro, Appl. Catal. B 79 (2008) 122–131.
[16] A. Gniewek, J.J. Ziółkowski, A.M. Trzeciak, M. Zawadzki, H. Grabowska, J. Wrzyszcz, J. Catal. 254 (2008) 121–130.
[17] Y. Matsumura, W.J. Shen, Y. Ichihashi, M. Okumura, J. Catal. 197 (2001) 267–272.
[18] M.F. Luo, Z.Y. Pu, M. He, J. Jin, L.Y. Jin, J. Mol. Catal. A 260 (2006) 152–156.
[19] N.D. Ivanova, S.V. Ivanov, E.I. Boldyrev, G.V. Sokol'skii, I.S. Makeeva, Russ. J. Appl. Chem. 75 (9) (2002) 1420–1423.
[20] M. Kang, E.D. Park, J.M. Kim, J.E. Yie, Catal. Today 111 (2006) 236–241.
[21] M.W. Xu, G.Y. Gao, W.J. Zhou, K.F. Zhang, H.L. Li, J. Power Sources 175 (2008) 217–220.
[22] R. Jothiramalingam, M.K. Wang, J. Hazard. Mater. 147 (2007) 562–569.
[23] M.S. Islam, R.A. Davies, J.D. Gale, Chem. Mater. 15 (2003) 4280–4286.
[24] X. Wang, A. Yuan, Y. Wang, J. Power Sources 172 (2007) 1007–1011.
[25] S.L. Brock, N. Duan, Z.R. Tian, O. Giraldo, H. Zhou, S.L. Suib, Chem. Mater. 10 (1998) 2619–2628.
[26] G.G. Xia, Y.G. Yin, W.S. Willis, J.Y. Wang, S.L. Suib, J. Catal. 185 (1999) 91–105.

[27] V.D. Makwana, Y.C. Son, A.R. Howell, S.L. Suib, J. Catal. 210 (2002) 46–52.
[28] J. Liu, J. Cai, Y.C. Son, Q. Gao, S.L. Suib, M. Aindow, J. Phys. Chem. B 106 (2002) 9761–9768.
[29] J. Li, J. Chen, R. Ke, C. Luo, J. Hao, Catal. Commun. 8 (2007) 1896–1900.
[30] P. Mars, D.W. Van Krevelen, Chem. Eng. Sci. Spec. (Suppl. 3) (1954) 41.
[31] A.V. Salker, N.J. Choi, J.H. Kwak, B.S. Joo, D.D. Lee, Sens. Actuators B 106 (2005) 461–467.
[32] S.H. Oh, G.B. Hoflund, J. Catal. 245 (2007) 35–44.
[33] S.D. Ebbesen, B.L. Mojet, L. Lefferts, J. Catal. 246 (2007) 66–73.
[34] A.V. Salker, Indian J. Chem. Technol. 11 (2004) 683–687.

Catalysis Communications 12 (2010) 193–196

Contents lists available at ScienceDirect

Catalysis Communications

journal homepage: www.elsevier.com/locate/catcom

Low temperature carbon monoxide oxidation over nanosized silver doped manganese dioxide catalysts

R.K. Kunkalekar, A.V. Salker *

Department of Chemistry, Goa University, Goa 403206, India

ARTICLE INFO

Article history:
Received 10 July 2010
Received in revised form 13 August 2010
Accepted 8 September 2010
Available online xxxx

Keywords:
Manganese dioxide
Silver doped manganese dioxide
Carbon monoxide oxidation
Influence of moisture
Partial pressure oxygen

ABSTRACT

Nanosized silver doped manganese dioxide catalysts have been prepared and tested for CO oxidation reaction at lower temperature. Silver doped manganese dioxide catalysts show higher CO conversion as compared to undoped manganese dioxide. Under the influence of excess oxygen catalysts are stable and show good activity. From time on stream experiments it is clear that the catalysts are highly stable for CO oxidation for a longer period in absence of moisture as well as in presence of moisture in the feed gas. The catalysts show higher activity for CO conversion in presence of moisture, indicating that moisture facilitates CO oxidation reaction on the catalyst surface.

1. Introduction

The carbon monoxide is one of the main toxic gaseous pollutants which is generally produced and released from the combustion process of fossil fuels. Catalytic oxidation of carbon monoxide to carbon dioxide at low temperature has been of considerable interest due to its significance in many industrial applications as well as to meet stringent environmental regulations. Last several years various catalysts have been prepared and tested for lower temperature CO oxidation. Mixed metal oxides such as hopcalite [1,2], mixed cobalt-cerium oxides [3,4] and supported metal oxides have been found to be highly active for CO oxidation reaction.

Manganese oxides (MnO_x) have long been used as highly active, durable, low cost and environmental friendly catalysts for the combustion of various volatile organic substances [5–7]. Various types of manganese oxide, mixed manganese oxide, noble metal doped/supported Mn oxides [8,9] are widely used for CO oxidation reaction. Among all manganese oxides, MnO_2 is most important due to its unique properties and has wide applications in different fields. It is generally accepted that phase structure can significantly influence the catalytic activity of MnO_2 [10,11].

Presence of moisture in feed stream highly influences the activity of catalysts for CO oxidation reaction. Catalysts such as $PtAu/CeO_2$ [12] deactivates in the presence of moisture while catalysts like Au/TiO_2, Ir/TiO_2 [13,14] show good activity and stability in presence of moisture. In the present work, the development of a new efficient nanosized Ag doped MnO_2 catalyst exhibiting exceptionally high activity and enhanced stability for CO oxidation reaction is being discussed.

2. Experimental

2.1. Catalysts preparation

Nanosized Ag doped MnO_2 catalysts of the type $Mn_{1-x}Ag_xO_2$ (where $x = 0$, 0.02, 0.05, 0.10, 0.15 and 0.20) were prepared by co-precipitation and drying method. Stoichiometric amount of manganese acetate and silver nitrate were dissolved in distilled water. Both this solutions were added to 200 ml distilled water at 100 °C with stirring. Liquid ammonia solution was added till pH = 9. Subsequently, the suspension was subjected to oxidation by drop wise addition of 30% H_2O_2 solution with constant stirring [15]. The suspension was then stirred continuously at 100 °C till dryness. The resulting product was dried at 150 °C for 6 h and calcined in air at 400 °C for 10 h.

2.2. Catalysts characterization

The phase composition of the calcined samples was analyzed by X-ray diffraction (XRD) using RIGAKU Ultima IV diffractometer. Transmission electron microscope (TEM) images were recorded on a PHILIPS CM 200 electron microscope. Elemental analysis was performed using energy-dispersive X-ray (EDX) on JEOL JSM 6360-LV scanning electron microscope and atomic absorption spectroscopy (AAS) on AA-6300 SHIMADZU. The BET surface area was measured by nitrogen adsorption at liquid nitrogen temperature using a SMART SORB 91 surface area analyzer.

* Corresponding author. Tel.: +92 832 6519071; fax: +91 832 2452889.
E-mail address: sal_arun@rediffmail.com (A.V. Salker).

1566-7367/$ - see front matter © 2010 Elsevier B.V. All rights reserved.
doi:10.1016/j.catcom.2010.09.013

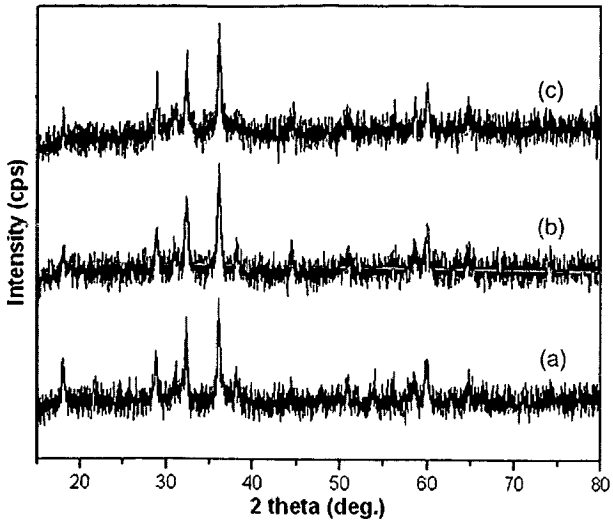

Fig. 1. XRD pattern of (a) MnO_2, (b) $Mn_{0.95}Ag_{0.05}O_2$ and (c) $Mn_{0.90}Ag_{0.10}O_2$.

2.3. Catalytic performance

The catalytic tests for CO oxidation by O_2 were performed in a continuous flow, fixed bed glass reactor. The catalyst powder of 0.9 g was supported between glass wool plugs in a glass reactor. The catalytic activity was determined using a feed gas composition of 5% CO and 5% O_2 in nitrogen and pass over the catalyst at a rate of 5000 ml h^{-1}. Prior to the CO oxidation reaction the catalyst was activated by passing O_2 at 100 °C for 30 min. The feed gases and the products were analyzed employing an online gas chromatograph with molecular sieve 13X and Porapak Q columns. H_2 was used as a carrier gas.

3. Results and discussion

3.1. Catalysts characterization

The XRD pattern of MnO_2 (Fig. 1a) shows well defined diffraction features characteristics of nanocrystalline MnO_2, indexed to tetragonal phase. After doping of Ag, an almost identical pattern was obtained for Ag doped MnO_2 samples as that of pristine MnO_2 indicating well maintaining of the crystal structure of MnO_2. Fig. 1b and c shows the XRD patterns for $Mn_{0.95}Ag_{0.05}O_2$ and $Mn_{0.90}Ag_{0.10}O_2$ catalysts. No distinct Ag reflections are visible in the XRD patterns of any sample indicating that Ag is well incorporated in MnO_2.

Representative TEM images of MnO_2 and $Mn_{0.95}Ag_{0.05}O_2$ catalysts are shown in Fig. 2. From the figure it is clear that the particles are nanosized and in the range 25–50 nm, the particles are agglomerated in appearance and spherical in nature. Inset in the figure shows electron diffraction patterns; Fig. 2a shows that rings are made of discrete spots signifying crystalline nature of MnO_2. But in contrast, Ag doped MnO_2 catalysts (Fig. 2b) exhibited clear continuous ring patterns demonstrating that Ag doped catalysts are polycrystalline in nature. From the EDX and AAS analysis of $Mn_{0.95}Ag_{0.05}O_2$ it is confirmed that Mn and Ag are present in appropriate ratio. The weight % ratio of Mn/Ag found to be 9.9 which is almost close to theoretical value.

The specific BET surface area of all the catalysts has been summarized in Table 1. After incorporation of Ag in MnO_2 the surface area found to be almost in the same range, but in the case of higher doped samples the surface area found to be decreased monotonously.

3.2. Catalytic activity

Fig. 3 displays the temperature dependence of the CO oxidation over various catalysts. It is clear that activity of the Ag doped MnO_2 catalysts are much higher than that for the pure MnO_2 catalysts. The T_{50} and T_{100} (light-off temperature of 50% and 100% CO conversion) values are given in Table 1. The pure MnO_2 shows complete CO oxidation at 180 °C whereas Ag doped MnO_2 catalysts show complete conversion below 125 °C. Moreover one can see that complete oxidation of CO could be attained at temperature 80 °C over $Mn_{0.95}Ag_{0.05}O_2$ catalyst. Even the catalyst like Ag/MnO_2 and Ag-Mn composite oxide shows complete CO conversion at higher temperature [16,17] than the present catalyst. The data in Fig. 3 also indicate that oxidation activity per catalysts increased monotonously with Ag doping, but for higher Ag doped samples the catalytic activity found to be decreasing.

As an electron donor, when CO molecule adsorbed on the surface of Ag, the C = O bond is activated by the back donation electrons from the filled d orbitals of Ag to CO $2\pi^*$ antibonding molecular orbitals. In addition, incorporation of Ag produces a strong Ag–MnO_2 interaction [16] which also promotes CO adsorption. XRD and TEM studies suggest that Ag is highly incorporated in MnO_2 and probably interact strongly with MnO_2.

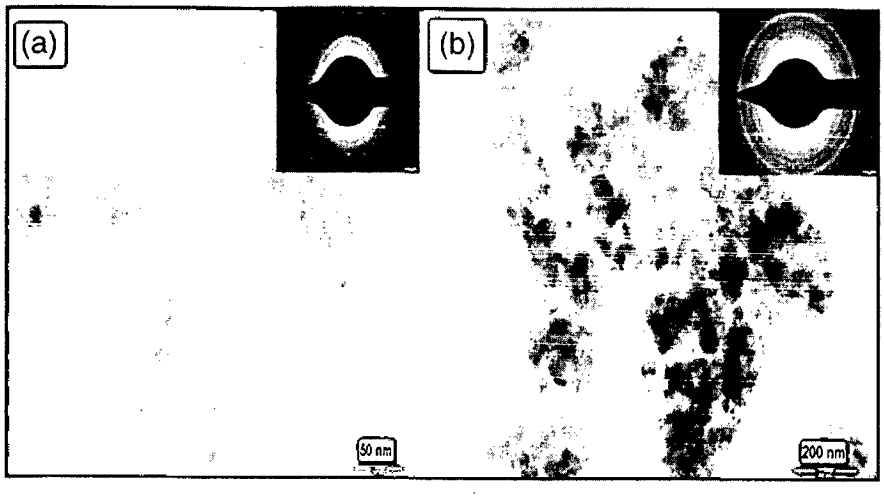

Fig. 2. TEM images of the catalysts: (a) MnO_2 and (b) $Mn_{0.95}Ag_{0.05}O_2$.

Table 1
BET surface area and catalytic activity at different temperatures

Sample	SA ($m^2\ g^{-1}$)	T_{50} (°C)	T_{100} (°C)
MnO_2	24	147	185
$Mn_{0.98}Ag_{0.02}O_2$	26	94	120
$Mn_{0.95}Ag_{0.05}O_2$	23	60	80
$Mn_{0.90}Ag_{0.10}O_2$	24	61	90
$Mn_{0.85}Ag_{0.15}O_2$	12	84	125
$Mn_{0.80}Ag_{0.20}O_2$	10	80	100

T_{50} and T_{100} (temperature for 50% and 100% CO conversion).

3.3. CO oxidation in excess oxygen

Performance of the catalysts for CO oxidation under the influence of excess oxygen i.e. 20% O_2 (5% CO and 20% O_2 in nitrogen) and 40% O_2 (5% CO and 40% O_2 in nitrogen) in feed gas mixture maintaining the same total flow rate of 5000 ml h^{-1} was studied. No decrease in activity for CO conversion was observed under influence of 20% O_2, but instead it showed slight increase in activity. Also in case of 40% O_2, slight increase in activity was observed than that of 20% O_2. Thus the influence of excess oxygen favours CO oxidation reaction and shows better activity. The possibility of blocking of active sites for CO adsorption over the surface due to excess oxygen is not encountered.

3.4. Stability test for the catalysts

Time on stream studies were carried out on MnO_2 and $Mn_{0.95}Ag_{0.05}O_2$ catalysts for oxidation of CO continuously for 12 h. MnO_2 catalyst was maintained at 130 °C; from Fig. 4a it is clear that the catalyst is stable for CO oxidation for longer period and also increase in activity was observed. The $Mn_{0.95}Ag_{0.05}O_2$ catalyst was maintained at 60 °C, it also shows good stability and increase in activity (Fig. 5a). Comparatively, the Ag doped OMS-2 catalyst shows low activity at 100 °C and whose activity declines with increase in reaction time [18,19].

Thus the results of stability test shows that MnO_2 and Ag doped MnO_2 catalysts are highly stable for CO oxidation reaction. The basic building block for most of the manganese oxide is the MnO_6 octahedra [11], they are generally porous material and often crystallizes as microporous tunnel structures. This tunnel structure is necessary for high CO oxidation activity [18] and incorporation of Ag ions and their mobility may also play important role in CO oxidation.

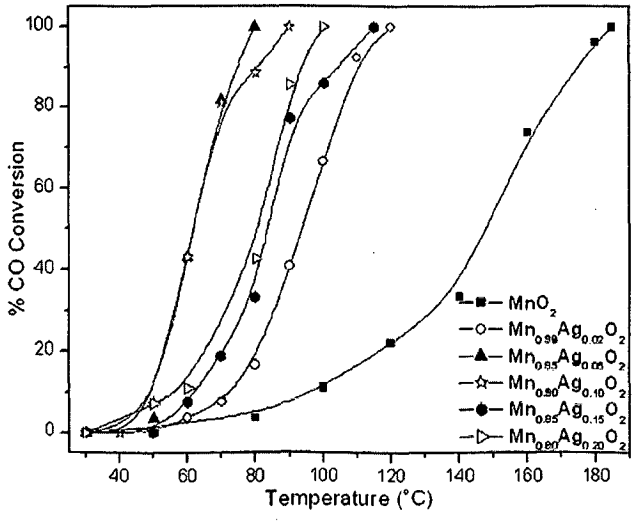

Fig. 3. Light-off curves for CO oxidation over different catalysts.

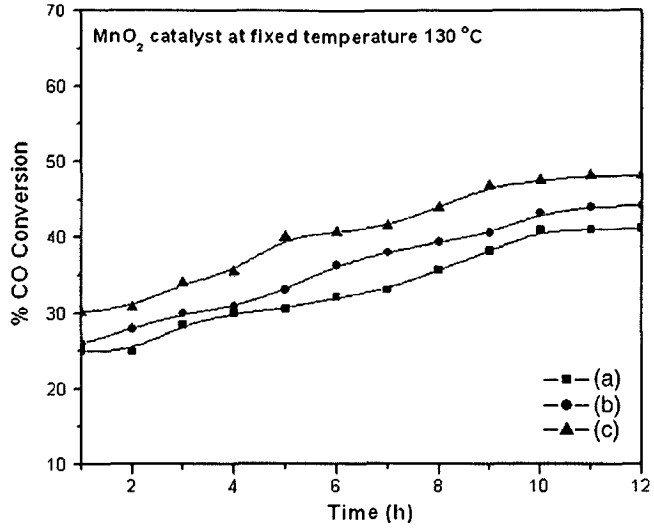

Fig. 4. Stability study of MnO_2 catalyst at 130 °C for 12 h. (a) Activity without moisture, (b) effect of low moisture and (c) effect of high moisture.

3.5. Influence of moisture on activity of catalyst

The effect of moisture on the activities of MnO_2 and $Mn_{0.95}Ag_{0.05}O_2$ catalysts was also tested. The activity was tested in presence of low and high moisture content [15]. The activity of the catalyst in the presence of low moisture content was tested by allowing the mixture of feed gases to pass through water trap (maintained at room temperature) and in the presence of high moisture content by allowing the mixture of feed gases to pass through water trap (maintained at 50 °C) before passing through the catalyst bed.

MnO_2 catalyst was maintained at 130 °C. Under the influence of low moisture, MnO_2 catalyst is stable and shows increase in activity with time as seen in Fig. 4b. The effect of high moisture content on catalytic activity of MnO_2 shows much better results as compared to low moisture content. More CO conversion was observed, as shown in Fig. 4c.

The $Mn_{0.95}Ag_{0.05}O_2$ catalyst was maintained at 60 °C. Under the influence of low moisture, catalyst is stable showing increase in activity by roughly 11% after 12 h shown in Fig. 5b. Under influence of high moisture it shows much better results, as seen in Fig. 5c.

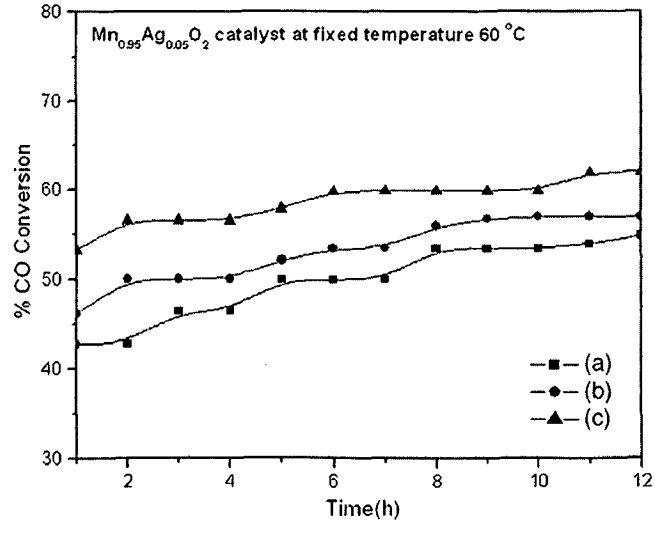

Fig. 5. Stability study of $Mn_{0.95}Ag_{0.05}O_2$ catalyst at 60 °C for 12 h. (a) Activity without moisture, (b) effect of low moisture and (c) effect of high moisture.

One interesting phenomenon was observed during stability test, the activity of both the catalysts increases with time (Figs. 4 and 5) either in presence or in absence of moisture. The catalysts were maintained at lower operating temperature during the stability test (approximately near to its 50% CO conversion). At this low operating temperature the surface active sites which are responsible for CO adsorption may not be totally activated. With increase in time the surface active sites may get activated resulting in more CO conversion. But for longer time period this trend may not continue and expected to reach a plateau region of CO conversion.

From Figs. 4 and 5 it is clear that catalysts are stable for CO oxidation, and under the influence of moisture catalysts show higher activity. This gives evidence that moisture does participate in catalytic CO oxidation. In addition to normal catalytic reaction of CO with oxygen to produce CO_2, there is a possibility of adsorbed CO reacting with adsorbed OH^- [20]. Water adsorbs dissociatively on catalyst surface as OH^- and H^+, and then the hydroxyl group may combine with CO to form an intermediate, which then decomposes giving CO_2 and hydrogen. Also there may be a possibility of formation of Bronsted acid sites due to the adsorption of moisture on surface of the catalysts [21]. These acid sites will favour more adsorption of CO on surface of the catalyst which results in more CO_2 formation, thus showing better activity.

4. Conclusion

Ag doped MnO_2 catalysts showed high catalytic activity for CO oxidation reaction as compared to pristine MnO_2 and these catalysts are highly stable. Presence of moisture in the feed facilitates catalytic CO oxidation. X-ray diffraction patterns of silver doped manganese dioxides are almost similar to pure manganese dioxide indicating Ag is well incorporated in MnO_2. TEM images confirmed that the particles are nanosized.

Acknowledgements

Authors are grateful to University Grant Commission, New-Delhi, for the financial support.

References

[1] G.J. Hutchings, A.A. Mirzaei, R.W. Joyner, M.R.H. Siddiqui, S.H. Taylor, Appl. Catal. A Gen. 166 (1998) 143–152.
[2] C. Jones, K.J. Cole, S.H. Taylor, M.J. Crudace, G.J. Hutchings, J. Mol. Catal. A Chem. 305 (2009) 121–124.
[3] U.R. Pillai, S. Deevi, Appl. Catal. B Environ. 65 (2006) 110–117.
[4] X.C. Zheng, S.H. Wu, S.P. Wang, S.R. Wang, S.M. Zhang, W.P. Huang, Appl. Catal. A Gen. 283 (2005) 217–223.
[5] N.D. Ivanova, S.V. Ivanov, E.I. Boldyrev, G.V. Sokol'skii, I.S. Makeeva, Russian J. Appl. Chem. 75 (9) (2002) 1420–1423.
[6] R. Kumar, S. Sithambaram, S.L. Suib, J. Catal. 262 (2009) 304–313.
[7] Y.C. Son, V.D. Makwana, A.R. Howell, S.L. Suib, Angew. Chem. Intl. Ed. 40 (2001) 4280–4282.
[8] C. Jones, S.H. Taylor, A. Burrows, M.J. Crudace, C.J. Kiely, G.J. Hutchings, Chem. Commun. (2008) 1707–1709.
[9] L.H. Chang, N. Sasirekha, Y.W. Chen, Catal. Commun. 8 (2007) 1702–1710.
[10] S. Liang, F. Teng, G. Bulgan, R. Zong, Y. Zhu, J. Phys. Chem. C 112 (2008) 5307–5315.
[11] S.L. Brock, N. Duan, Z.R. Tian, O. Giraldo, H. Zhou, S.L. Suib, Chem. Mater. 10 (1998) 2619–2628.
[12] S. Monyanon, S. Pongstabodee, A. Luengnaruemitchai, J. Power Sources 163 (2006) 547–554.
[13] M. Date, M. Okumura, S. Tsubota, M. Haruta, Angew. Chem. Intl. Ed. 43 (2004) 2129–2132.
[14] M. Okumura, N. Masuyama, E. Konishi, S. Ichikawa, T. Akita, J. Catal. 208 (2002) 485–489.
[15] A.V. Salker, R.K. Kunkalekar, Catal. Commun. 10 (2009) 1776–1780.
[16] R. Xu, X. Wang, D. Wang, K. Zhou, Y. Li, J. Catal. 237 (2006) 426–430.
[17] S. Imamura, H. Sawada, K. Uemura, S. Ishida, J. Catal. 109 (1988) 198–205.
[18] G.G. Xia, Y.G. Yin, W.S. Willis, J.Y. Wang, S.L. Suib, J. Catal. 185 (1999) 91–105.
[19] H. Rongrong, C. Yi, X. Lanying, W. Dezheng, Chin. J. Catal. 28 (5) (2007) 463–468.
[20] R.A. Ojifinni, N.S. Froemming, J. Gong, M. Pan, T.S. Kim, J.M. White, G. Henkelman, C.B. Mullins, J. Am. Chem. Soc. 130 (2008) 6801–6812.
[21] A.V. Salker, Indian J. Chem. Technol. 11 (2004) 683–687.